

# **Acoustic singularities in interfacial fluid dynamics**

by

Hamed Habibi Khoshmehr

A thesis submitted in partial fulfillment of the requirements for the degree of

Doctor of Philosophy

in

Applied Mathematics

Department of Mathematical and Statistical Sciences

University of Alberta

© Hamed Habibi Khoshmehr, 2020

# Abstract

Formation of singularities in physical phenomena has always fascinated scientists and stimulated both development of mathematical theories accounting for observations and further experimental scrutiny of the governing physics with the goal to resolve the singular behavior. The underlying theme of this Dissertation is to unify the appearance of cavitation phenomena in an impulse-driven drop sitting on a membrane and of folds on a retracting soap film, studied here both experimentally and theoretically, under the umbrella of geometric acoustics and singularity theories. A fundamental difference between wave propagation in two and three dimensions proved to be instrumental in elucidating the phenomena at hand.

The Dissertation consists of two parts. In the first part, we explore impulse-driven drop phenomena. Drop deformation and disintegration regimes have been studied in many contexts ranging from an impact on a solid surface or a liquid layer of varying thickness to a liquid drop suspended in air and hit by a propagating aerodynamic shock wave. As a counterpart, deformation and disintegration of an initially static drop of controlled shape and size sitting on an impulsively driven stiff membrane are explored here experimentally. A significant amount of collected experimental data is used here to map the possible drop morphological changes along with the transitions between them. In order to elucidate the effects of impulse intensity, viscosity, surface tension, and wetting, we measured the crown height and radius in the drop deformation regimes, as well as the drop detachment and breakup times along with probability density functions of the secondary droplets in the drop disintegration regimes. With the goal to convey the physical mechanisms behind these transient responses, the observations are interpreted with phenomenological models, scalings, and estimates highlighting the rich multiscale physics of the impulse-driven drop phenomena. To provide a theo-

retical background for the cavitation phenomena responsible for the most energetic regimes of drop disintegration, we will explore the behavior of the pressure field near the most singular region – the cusp – and then near the caustic with the goal to demonstrate qualitatively that the pressure field develops significant amplitudes capable of leading to cavitation as observed experimentally.

In the second part, we will study the acoustic singularities – the folds – on soap films. Soap films have been not only the object of children’s play, but also the subject of scientific research since the time of Leonardo Da Vinci. Earlier systematic experimental studies of bursting soap films using high-speed flash photography revealed a precursor wave preceding the expanding hole, with a disturbed region of shrinking film material in between. In 1969 Mysels, famous for his work on soap films, referred to this wave and the disturbed region as the “shock wave” and the “aureole”, respectively. These observations have overturned some misconceptions regarding the bursting process in earlier theoretical and experimental works, which concluded that a rolled up rim collected all of the disappearing film, leaving the rest of the film undisturbed. Also in 1969, Frankel and coworkers qualitatively interpreted this as a shock wave in the surfactant film and showed that any significant aureole preceding the rim of the expanding hole in a punctured soap film is related to large changes in surface tension as the film shrinks and thickens. In this part of the Dissertation, we will report and interpret new phenomena associated with the aureole and accidentally discovered in our laboratory. On the theoretical side, first we will use the basics of geometric acoustics to deduce qualitatively the behavior of acoustic waves on the soap film and to explain the origin of folds along the diagonal of a collapsing soap film. Given the experimental observation that there is an areola – a wave preceding the retracting soap film edge – we will revisit the classical theory in order to develop proper equations governing the velocity and thickness of the collapsing soap film, since these variables are crucial for the proper interpretation of the wave propagation superimposed on the evolving in time base state, which will lead to a succinct understanding of the origin of the observed folds.

# Preface

This research is an original work by Hamed Habibi Khoshmehr. The research has been done under supervision of Professor Krechetnikov at the University of Alberta, Department of Mathematical and Statistical Sciences.

A version of chapter 2 is published in the *Journal of Fluid Mechanics* under the authorship of Hamed K. Habibi and Rouslan Krechetnikov. All experiments were conducted in Krechetnikov Fluid Physics Laboratory (KFPL). Hamed K. Habibi was responsible for building the experimental platform, conducting the experiments, and analyzing the acquired data. All steps have been done under supervision of Professor Krechetnikov. Both authors wrote the manuscript and revised it.

A version of chapter 3 will be submitted for publication under the authorship of Hamed K. Habibi and Rouslan Krechetnikov. All experiments were conducted in KFPL. Hamed K. Habibi was responsible for building the experimental platform, conducting the experiments, and analyzing the acquired data. All steps have been done under supervision of Professor Krechetnikov. Both authors will write the manuscript and revise it.

# Acknowledgements

To begin, I would like to express my deepest gratitude to my supervisor, Professor Rouslan Krechetnikov, who expertly guided me through my Ph.D. journey. You provided me with research assistant funding, teaching assistant support, and the opportunity to work in the lab with access to all required facilities. I have learned a lot from all of these resources. Thank you, Rouslan, for being generous with your time and patient during the course of my learning. Without your persistent help and consistent guidance, this dissertation would have never come to a successful completion.

Also, I would like to thank my supervisory committee members, Professor Bob Koch and Professor Sina Ghaemi for their advice and guidance during my Ph.D. Furthermore, I would also like to thank Professor G. M. Bud Homsy who supported my research with his advice and helpful comments.

In the last six years that I spent in my Ph.D. program, I was blessed in many ways by so many people in the Mathematics department at the University of Alberta. It is hard to list them all. However, I thank them all. I would also like to acknowledge the Physics department at the University of Alberta. They provided me with access to the machine shop and advanced machining facilities. Special thanks to Mr. Tony Vinagreiro for teaching me machining skills.

I would like to deeply acknowledge friends who supported me. I would thank Quinton Farr and Alain Gervais for sharing their experiences with me and for spending their time to read my paper and dissertation. I want to thank Pedram Emami who stood beside me in all ups and downs of this long journey.

Among all my supporters, my family was outstanding. They supported and cared for me from thousands of miles away. Lastly, I would appreciate my fiancée, Sahar, who I have been blessed to have. Without Sahar, it would have been impossible to complete this page of my life.

# Contents

<b>List of Tables</b>	<b>xi</b>
<b>List of Figures</b>	<b>xii</b>
<b>1 Introduction: acoustics and singularity theory</b>	<b>1</b>
1.1 Basic notions: eikonal and ray equations . . . . .	1
1.2 Caustics . . . . .	5
1.2.1 The ray surface and Lagrange’s manifold . . . . .	5
1.2.2 Example: coffee cup caustic . . . . .	8
1.2.3 Thom’s theorem . . . . .	10
1.3 Wave propagation in 2D vs 3D . . . . .	11
<b>2 Impulse-driven drop</b>	<b>14</b>
2.1 Experiments . . . . .	16
2.1.1 Experimental setup and procedure . . . . .	16
2.1.1.1 Apparatus . . . . .	16
2.1.1.2 Fluid properties and membrane kinematics . . . . .	18
2.1.2 Results: overview of key morphologies . . . . .	20
2.1.3 Results: drop deformation regimes . . . . .	22
2.1.3.1 Crown precursors . . . . .	24
2.1.3.2 Key crown regimes and transitions . . . . .	26
2.1.3.3 On the crown formation: basic physical processes . . . . .	31

2.1.3.4	Effects of viscosity, surface tension, and impact intensity on the crown dynamics . . . . .	34
2.1.3.5	Wettability effects . . . . .	38
2.1.3.6	Crown forming instability . . . . .	40
2.1.4	Results: drop disintegration regimes . . . . .	45
2.1.4.1	Key disintegration regimes and transitions . . . . .	45
2.1.4.2	On the origin of cupola . . . . .	48
2.1.4.3	Detachment and disintegration times . . . . .	53
2.1.4.4	On the secondary droplet size distribution . . . . .	55
2.1.5	Discussion . . . . .	59
2.1.5.1	Comparison of morphologies with other drop impact phenomena	59
2.1.5.2	Key findings of the present study . . . . .	62
2.2	Theory . . . . .	65
2.2.1	Acoustic wave focusing . . . . .	65
2.2.1.1	Caustic geometry . . . . .	65
2.2.1.2	The characteristic length-scales of the caustic boundary layer . .	68
2.2.1.3	Pressure near the caustic cusp . . . . .	69
2.2.2	Near caustic behavior . . . . .	72
2.2.2.1	Coordinate systems . . . . .	72
2.2.2.2	Application to barotropic fluid: inner solution near the caustic . .	75
2.2.2.3	Linear geometric acoustics: outer solution and matching . . . . .	77
Appendix 2.A	Analogy between geometric acoustic and Hamiltonian mechanics . . . .	80
Appendix 2.B	Electromagnetic shock wave generator . . . . .	83
Appendix 2.C	Summary of characteristic time and length scales . . . . .	86
Appendix 2.D	SW reflection from plane interface . . . . .	87
Appendix 2.E	Image processing . . . . .	88
Appendix 2.F	Data fit . . . . .	91

Appendix 2.G	Acoustic reflection and refraction . . . . .	92
Appendix 2.H	On identification of detachment and disintegration times . . . . .	94
Appendix 2.I	Stain detection via image processing . . . . .	96
<b>3</b>	<b>Folds on soap films</b>	<b>99</b>
3.1	Experiments . . . . .	99
3.1.1	Materials and methods . . . . .	99
3.1.1.1	Experimental setup components . . . . .	100
3.1.1.2	Soap solutions . . . . .	106
3.1.2	Experimental results . . . . .	107
3.1.2.1	Mapping of the regimes . . . . .	108
3.1.2.2	Key velocities . . . . .	110
3.1.2.3	The corner effect . . . . .	115
3.2	Theory . . . . .	116
3.2.1	Soap film dynamics . . . . .	116
3.2.1.1	Classical theory of Taylor (1959c) . . . . .	116
3.2.1.2	Generalized theory . . . . .	121
3.2.1.3	Numerical solution of one and two dimensional shock wave propagation models . . . . .	125
3.2.2	Waves on soap films . . . . .	129
3.2.2.1	Taylor's inviscid analysis . . . . .	129
3.2.2.2	Surfactant surface kinetics and material behavior . . . . .	133
3.2.2.3	Soap film elasticity . . . . .	135
3.2.2.4	Elasticity waves in soap films: phenomenological model . . . . .	138
3.2.2.5	Effect of viscosity and elasticity on soap film waves . . . . .	139
3.2.2.6	Symmetric modes . . . . .	143
3.2.2.7	Soap film dynamics: problem statement . . . . .	145
3.2.2.8	Soap film dynamics: non-dimensional equations . . . . .	148

3.2.2.9 Soap film dynamics: asymptotic expansion . . . . . 150

3.2.3 Acoustics on soap film: eikonal equation and key findings . . . . . 153

Appendix 3.A Optical film thickness measurements . . . . . 159

Appendix 3.B Method of characteristics . . . . . 161

**4 Conclusions** . . . . . **165**

**Bibliography** . . . . . **166**

# List of Tables

- 2.1 Properties of working fluids in the course of experiments. . . . . 18
- A2.2 Analogy to mechanics. . . . . 80
- A2.3 Characteristic time and spatial scales for a liquid drop. . . . . 87
  
- 3.1 Properties of NiChrome 60 wires. . . . . 101
- 3.2 Properties of sodium dodecyl sulfate surfactant (SDS). . . . . 107
- 3.3 Analogy between soap film and compressible flow dynamics. . . . . 139

# List of Figures

1.1	Wavefront. . . . .	2
1.2	On the caustic theory. . . . .	5
1.3	Illustration of the origin of a caustic. . . . .	7
1.4	Caustic in a coffee cup. . . . .	8
1.5	Structurally stable caustics with codimension $n \leq 2$ . . . . .	11
1.6	On Huygens' principle. . . . .	11
2.1	Schematics of the capturing part of the experimental setup and typical membrane kinematics. . . . .	17
2.2	Maximum deflection $h_{\max}$ , velocity $V_{\max}$ , acceleration $a_{\max}$ for each membrane thickness for five different initial energies $E = 250, 390, 500, 750,$ and $1000\text{J}$ . . . . .	19
2.3	High resolution images of the key observed morphologies. . . . .	21
2.4	Top view of crown forming regimes: crown without splash, crown splash, and microdroplet crown splash. . . . .	23
2.5	Regimes' transitions for different impact intensities: ripple waves, ejecta, non-monotonic crown, monotonic crown. . . . .	24
2.6	Ripple wave pattern in DI water. . . . .	25
2.7	Ejecta pattern in DI water. . . . .	26
2.8	Crown forming regimes time sequence images: crown without splash, crown splash, and microdroplet crown splash. . . . .	27
2.9	Map of the impact intensity effect. . . . .	29

2.10	Map of the observed crown regimes on both stainless steel and copper substrate. . . . .	32
2.11	Impact of a liquid cylinder on a solid surface. . . . .	33
2.12	Sequence of events illustrating the crown formation (a) relative to the membrane motion in the impulse-driven drop and (b) relative to the stationary solid surface in the drop impact experiments. . . . .	34
2.13	Log-log plots of non-dimensional rim radius and height for 1000 J fixed initial energy.	35
2.14	Time sequence images of non-monotonic and monotonic crown evolution. . . . .	37
2.15	(a) Maximum non-dimensional radius $R_{\max}$ and height $H_{\max}$ achieved during the process of crown evolution. (b) The powers of the fitted curves ( $\alpha_R$ and $\alpha_H$ ) to non-dimensional radius and height. . . . .	38
2.16	Non-dimensional log-log plots of crown radius and height for different impact intensities. . . . .	39
2.17	Maximum non-dimensional radius (a) and height (c) of the crown. The power of the fitted curve to non-dimensional radius $\alpha_R$ (b) and height $\alpha_H$ (d). . . . .	40
2.18	Time sequence of images to demonstrate the effect of contact angle on the crown formation pattern. . . . .	41
2.19	Crown evolution in 10% wt sucrose from top and side views. . . . .	42
2.20	Log-log plots of wavelength of the fingerings on the crown rim versus non-dimensional time. . . . .	44
2.21	Time sequence images of the butterfly crown splash, cupola, and direct atomization regimes. . . . .	46
2.22	Map of high intensity impulse cases when a liquid drop was placed directly on the copper membrane. . . . .	47
2.23	Schematics of shock wave propagation through an impulsively-driven drop sitting on a membrane. . . . .	48
2.24	Supersonic (a) and subsonic (b) regimes of the drop-solid interaction with initial contact angle $\theta_0 > 90^\circ$ . . . . .	50

2.25	The time of detachment from the membrane for six liquids in the cupola and atomization regimes. . . . .	54
2.26	The time of disintegration of six liquids in the cupola and atomization regimes. . .	54
2.27	PDFs of secondary droplet radii in the direct atomization experiments on 0.034 mm copper membrane. . . . .	57
2.28	The comparison between the mean of the experimental data and of the fitted curves of the PDFs presented in figure 2.27. . . . .	57
2.29	Schematics of the patterns shown in figure 2.3. . . . .	60
2.30	Breakup regimes when shock wave passes through a liquid drop. . . . .	61
2.31	Breakup regimes when a liquid drop hits dry surface. . . . .	62
2.32	Summary of the influence of each parameter on the regimes and sequence of regimes as impact intensity increases. . . . .	63
2.33	(a) Caustics formation; (b) near cusp geometry. . . . .	65
2.34	Caustic coordinate systems: (a) polar, (b) normal. . . . .	72
A2.1	A geometric view of an advancing front. . . . .	82
A2.2	Schematics of the experimental setup and electrical circuit. . . . .	83
A2.3	Reflection of a shock wave from a free surface. . . . .	87
A2.4	An example of Edge-detection image processing. . . . .	89
A2.5	Procedure of curve fitting for non-dimensional height. . . . .	91
A2.6	Shadowgraph images of a shock wave hitting a water column. . . . .	92
A2.7	Disintegration time of different liquids in the cupola regime. . . . .	94
A2.8	Disintegration time of different liquids in the direct atomization regime. . . . .	95
A2.9	50% wt water-sucrose liquid dropl detachment from the membrane in the cupola regime. . . . .	96
A2.10	Hough transform on stains to determine the radii of the microdroplets. . . . .	96
3.1	Frame configuration used for holding and releasing soap films. . . . .	101
3.2	Experimental setup for soap film experiments. . . . .	103

3.3	Soap film pulling. . . . .	104
3.4	Schematic of the electrical circuit used for the controlled release of flat soap films. .	106
3.5	Time sequence of the soap film retraction with and without developing shock pattern on the surface of the film. . . . .	109
3.6	Maps of shock wave and no shock wave patterns for different concentrations of surfactant and glycerol. . . . .	111
3.7	A time sequence of images showing the formation of a bridge in a rectangular soap film geometry. . . . .	112
3.8	Time sequence of the soap film retraction with and without developing shock pattern on the surface of the film with the camera zoomed on a quarter of the soap film area.	113
3.9	Wave propagation velocity $c_0$ and soap film retraction velocity $U_{TC}$ for different soap films. . . . .	114
3.10	Time sequence of the soap film retraction to show the appearance of dark region on the soap film surface with the camera zoomed on a quarter of the soap film area. . .	115
3.11	Time sequence of the soap film retraction to show the effect of frame corner with the camera zoomed on a quarter of the soap film area. . . . .	117
3.12	Taylor's derivation and new configuration for one dimensional soap film retracting problem. . . . .	118
3.13	Schematics of steady and unsteady flows. . . . .	121
3.14	Element of an evolving soap film. . . . .	122
3.15	One dimensional shock wave and velocity field distribution on the soap film. . . . .	126
3.16	(a) Numerical result for the velocity field on the soap film in presence of a shock wave. (b) Changes of the soap film thickness due to the shock wave propagation in the soap film. (c) The PIV image of the flow field in the soap film in presence of the shock wave. . . . .	128
3.17	Coordinate setup, symmetric and antisymmetric waves on a soap film. . . . .	129
3.18	Evolution of a soap film under an increase of the applied tension. . . . .	135

3.19 (a) Adsorption isotherm: the surface concentration $\Gamma_1$ of soap molecules adsorbed at the interface as a function of the volumetric concentration $c_1$ in the bulk of the fluid. (b) The isothermal dependence of the surface tension $\sigma$ on the concentration $c_0$ of the solution. . . . .	136
3.20 antisymmetric, Taylor symmetric ,and elastic symmetric waves in a soap film. . . .	144
3.21 Mach cone. . . . .	154
3.22 Velocity field in a soap film. . . . .	157
3.23 The bridge formation in a soap film. . . . .	158
A3.1 Light transmission through soap films. . . . .	160
A3.2 Soap film thickness based on light transmission data. . . . .	161
A3.3 Method of characteristics for nonlinear first-order PDEs. . . . .	161

# Chapter 1

## Introduction: acoustics and singularity theory

Appearance of singularities in physical phenomena has always been a stimulus for the development of mathematical theories accounting for observations and further investigation of the physics in order to resolve the singular behavior. In this Dissertation I attempted to unify the occurrence of cavitation phenomena in an impulse-driven drop sitting on a membrane and of folds on a retracting soap film with the help of geometric acoustics (§1.1) and singularity (§1.2) theories. In this introduction we provide the reader with the necessary elements of these two general theories and, since, there is also a fundamental difference between wave propagation in two dimensions (2D) versus three dimensions (3D), we will address it as well in §1.3. The discussion of the physics pertinent to the phenomena under consideration will be provided at the beginning of the corresponding chapters 2 and 3, with the background literature reviewed in the body of these chapters. The key new findings and comparison with previous work will be done in §§2.1.5.1, 2.1.5.2 and 3.2.3.

### 1.1 Basic notions: eikonal and ray equations

First, we will develop a heuristic view of geometric acoustics, which will highlight the basic physics before taking a more formal approach, which will highlight the mathematical aspects of the matter. The basic assumption of geometric acoustics (Landau & Lifshitz, 1987) is that locally, a sound wave

$$\phi(t, \mathbf{r}) = A(t, \mathbf{r})e^{i\psi(t, \mathbf{r})} \tag{1.1}$$

can be considered plane (cf. figure 1.1) – for that it is necessary that the amplitude  $A$  and the wave direction do not change appreciably over the sound wavelength  $\lambda$ , i.e. geometric acoustics requires  $\lambda/L \ll 1$  relative to the characteristic length scale  $L$  of the phenomena being studied. Then, it is possible to introduce the notion of sound rays, the tangent to which at each point coincides with the direction of the wave propagation. Therefore, since the phase in plane wave with wavevector  $\mathbf{k}$  and frequency  $\omega$  is  $\psi = \mathbf{k} \cdot \mathbf{r} - \omega t + \psi_0$  and, by assumption, a sound wave in geometric acoustics approximation is locally plane as well, one can Taylor expand the phase  $\psi(t, \mathbf{r}) = \psi_0 + \mathbf{r} \cdot \nabla\psi + t \partial\psi/\partial t$  and by comparison find the corresponding wavevector (wavenumber if in 1D or modulus considered)  $\mathbf{k}$  and frequency  $\omega$ :

$$\mathbf{k} = \nabla\psi, \quad \omega = -\frac{\partial\psi}{\partial t}; \quad (1.2)$$

here  $\mathbf{k}$  and  $\omega$  are related via the dispersion relation  $k^2 = \omega^2/c^2$  in the plane wave approximation, where the sound speed  $c$  may be a function of spatial coordinate. The above relation leads to the eikonal equation:

$$k^2 = \frac{\omega^2}{c^2} \Rightarrow (\psi_t)^2 - c^2 (\nabla\psi)^2 = 0, \quad (1.3)$$

which defines how the surface of constant phase  $\psi = \text{const}$  moves in the physical  $\mathbf{r}$  space; the surface over which  $\psi(\mathbf{r})$  is constant is defined as the wavefront. The unit normal to the surface  $\psi$  is  $\mathbf{n} = \nabla\psi/|\nabla\psi|$ . We can also calculate the velocity normal to that surface by considering two neighboring points  $(\mathbf{r}_0, t_0) = 0$  and  $(\mathbf{r}_0 + \mathbf{n} \delta s, t_0 + \delta t) = 0$ , the Taylor expansion of which leads to the expression for the normal velocity, cf. figure 1.1:

$$\lim_{\delta t \rightarrow 0} \frac{\delta s}{\delta t} = \frac{\psi_t}{|\nabla\psi|} = c. \quad (1.4)$$

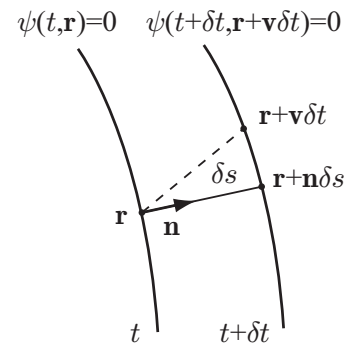


**Figure 1.1:** Wavefront.

Therefore, the eikonal equation simply states that the wavefront propagates with normal velocity  $c$ .

If the properties of the media through which the sound propagates do not change over time, the frequency of the wave stays constant along the ray. Indeed,

$$\frac{d\omega}{dt} = \frac{\partial\omega}{\partial t} + \frac{\partial\omega}{\partial\mathbf{r}} \cdot \dot{\mathbf{r}} + \frac{\partial\omega}{\partial\mathbf{k}} \cdot \dot{\mathbf{k}} \quad (1.5)$$

where using (1.2)

$$\frac{\partial\omega}{\partial\mathbf{r}} = -\frac{\partial^2\psi}{\partial\mathbf{r}\partial t} = -\frac{\partial}{\partial t} \left( \frac{\partial\psi}{\partial\mathbf{r}} \right) = -\dot{\mathbf{k}}, \quad (1.6)$$

while  $\partial\omega/\partial\mathbf{k}$  is the group speed<sup>1</sup>, which along the ray coincides with speed of a point  $\dot{\mathbf{r}}$  on a ray, i.e.  $\partial\omega/\partial\mathbf{k} = \dot{\mathbf{r}}$ . As a result, equation (1.5) gives  $d\omega/dt = \partial\omega/\partial t$ , which is zero in the case of stationary propagation, and the evolution of the wavenumber and the point on the ray obey:

$$\dot{\mathbf{k}} = -\frac{\partial\omega}{\partial\mathbf{r}}, \quad \dot{\mathbf{r}} = \frac{\partial\omega}{\partial\mathbf{k}}, \quad (1.7)$$

respectively, strikingly analogous to Hamiltonian equations for particle dynamics in classical mechanics (Appendix 2.A). The ray (1.7) and eikonal (1.3) will be central for our subsequent interpretation of the observed and discovered physical phenomena.

On a formal side, the ansatz (1.1), which is of the WKB type (Bender & Orszag, 1999), for the sound wave representation must satisfy the wave equation

$$\left[ \partial_t^2 - c^2 \nabla^2 \right] \phi = 0, \quad (1.8)$$

---

<sup>1</sup>Any smooth wave traveling in physical space  $x$  can be represented in the Fourier decomposition form  $a(t, x) = \int_{-\infty}^{+\infty} A(k) e^{i(kx - \omega(k)t)} dk$ , where  $A(k)$  is the amplitude distribution of the wave across wavenumbers  $k$  and  $\omega(k)$  is the dispersion relation defining the harmonic frequency dependence on the wavelength  $\lambda = k/2\pi$ . If the wave  $a(t, x)$  is almost monochromatic, i.e. represents a wavepacket meaning that in the Fourier space  $A(k)$  is sharply peaked around a central wavenumber  $k_0$ , the expression for the wave can be simplified after Taylor expanding the dispersion relation  $\omega(k)$  around  $k_0$  to  $a(t, x) = e^{i(k_0 x - \omega_0 t)} \int_{-\infty}^{+\infty} A(k) e^{i(k-k_0)(x - \omega'(k_0)t)} dk$ , which tells us that the wave consists of a monochromatic wave with wavenumber  $k_0$  with peaks and troughs moving at the phase velocity  $\omega_0/k_0 \equiv \omega(k_0)/k_0$  within the envelope of the wavepacket, which in turn travel at velocity  $\omega'(k_0)$ .

at least approximately. Since now we know that the frequency  $\omega$  remains constant, which mathematically is due to that the wave equation does not have time-dependent coefficients and hence is amenable to separation of variables leading to the exponential form, we can represent  $\phi(t, \mathbf{r})$  in (1.1) equivalently in the form

$$\phi(t, \mathbf{r}) = U(\mathbf{r})e^{-i\omega t}, \quad (1.9)$$

hence, by incorporating the phase into the new amplitude  $U(\mathbf{r})$ , the substitution of which into the wave equation (1.8) produces the (reduced wave) Helmholtz equation

$$[\nabla^2 + k_0^2 n^2(\mathbf{r})] U(\mathbf{r}) = 0, \quad (1.10)$$

where, for convenience, we introduced the refractive index  $n(\mathbf{r}) = k/k_0$  with  $k_0 = \omega/c_0 = \text{const}$  for some reference sound speed  $c_0$ . Next, in order to connect wave and geometric acoustics, let us assume that the field  $U(\mathbf{r})$  consists of a slowly-varying amplitude  $a(\mathbf{r})$  and a rapidly-oscillating phase  $\psi(\mathbf{r})$  proportional to the wavenumber:

$$U(\mathbf{r}) = a(\mathbf{r})e^{ik_0\psi(\mathbf{r})}, \quad (1.11)$$

the substitution of which into the Helmholtz equation (1.10) yields

$$k_0^2 a (n^2 - \nabla\psi \cdot \nabla\psi) + ik_0 (2\nabla a \cdot \nabla\psi + a\nabla^2\psi) + \nabla^2 a = 0. \quad (1.12)$$

Equation (1.12) can also be analyzed asymptotically using Debye series  $a(\mathbf{r}) = \sum_{j=0}^{\infty} a_j(\mathbf{r})/(ik_0)^j$ . Indeed, to view the high frequency nature of the geometric acoustics approximation, let us rewrite the Helmholtz equation (1.10) in the equivalent form

$$\left[ \nabla^2 + \frac{\omega^2}{c^2(\mathbf{r})} \right] U(\mathbf{r}) = 0, \quad (1.13)$$

the solution of which can be sought in the form of the following asymptotic (WKBJ) expansion, which automatically takes into account the oscillations:

$$U = \left( a + \frac{a_1}{i\omega} + \frac{a_2}{(i\omega)^2} + \dots \right) e^{i\omega\psi}, \quad (1.14)$$

the plugging of which and collecting terms of the leading significant orders  $\omega^2$  and  $\omega$ , we get the system (1.15) of the eikonal equation for the phase  $\psi$  (without the Bohmian correction) and the transport equation for the amplitude  $a$ :

$$\nabla\psi \cdot \nabla\psi = n^2, \quad (1.15a)$$

$$\nabla \cdot (a^2 \nabla\psi) = 0, \quad (1.15b)$$

where the first of the found relations is a stationary variant of the eikonal equation (1.3), while the second relation is known as the transport equation (conservation of energy of the field).

## 1.2 Caustics

### 1.2.1 The ray surface and Lagrange's manifold

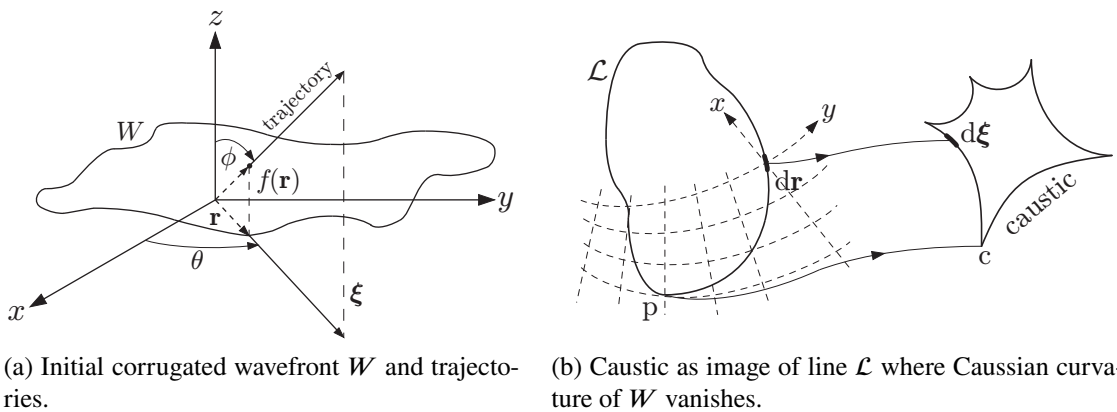


**Figure 1.2:** On the caustic theory (Berry, 1976).

Following [Berry \(1976\)](#), consider a monochromatic plane wave travelling along the positive direction  $z$  in a homogeneous isotropic medium. Let the wavefront at  $z = 0$  be deformed into a surface  $W$  by lifting the part at  $\mathbf{r} \equiv (x, y)$  from  $z = 0$  to  $z = f(\mathbf{r})$ , cf. [figure 1.2a](#) and assume that all radii of curvature of  $W$  are large in comparison with the wavelength  $\lambda$ , so that the assumption of geometric acoustics is applicable. We are interested in the far field of the waves from  $W$ , the directions of the trajectories of which contribute to the far field and can be specified by projections  $\xi$  on the  $xy$  plane ([figure 1.2a](#)), i.e. by  $\xi_x = \sin \theta \cos \phi$ ,  $\xi_y = \sin \theta \sin \phi$ , where  $\theta$  and  $\phi$  are the polar angles with  $x$  and  $z$  axes, respectively. The intensity  $I(\xi)$  is defined by the flux through  $d\xi$  far from  $W$  for a unit flux through unit area of  $W$  itself.

Each point  $\mathbf{r}$  on  $W$  gives rise to a trajectory normal to  $W$  with the direction

$$\xi(\mathbf{r}) = -\nabla f(\mathbf{r}). \quad (1.16)$$

For given  $\xi$  there may be several points  $\mathbf{r}$  satisfying this equation, which we label  $\mathbf{r}_i(\xi)$ . Then the intensity  $I$  on the trajectory picture is

$$I(\xi) = \sum_i \left| J(\mathbf{r}_i, \xi)^{-1} \right|, \quad (1.17)$$

where  $J(\mathbf{r}_i, \xi)$  is the Jacobian of the mapping (1.16) from the Cartesian  $\mathbf{r}$  to the ray  $\xi$  coordinates:

$$\left| \frac{d\xi}{d\mathbf{r}} \right| = \left| \frac{\partial^2 f}{\partial x^2} \frac{\partial^2 f}{\partial y^2} - \left( \frac{\partial^2 f}{\partial x \partial y} \right)^2 \right| \equiv |\mathcal{K}(\mathbf{r})|, \quad (1.18)$$

where  $\mathcal{K}(\mathbf{r})$  is the Gaussian curvature of  $W$  at  $\mathbf{r}$ .

The caustics of the set of trajectories travelling from  $W$  represent the singularities of the mapping  $\mathbf{r} \rightarrow \xi$ , i.e. they occur where  $J(\mathbf{r}, \xi)$  vanishes and  $I$  is infinite. Therefore caustics are the images in  $\xi$  of the lines  $\mathcal{L}$  on  $W$  where the Gaussian  $\mathcal{K}$  vanishes ([figure 1.2b](#)).

To illustrate the above ideas, let us write the equations of the family of rays leaving an initial surface (figure 1.3a) in a parametric form:

$$x = x(\tau, \xi, \eta), \quad y = y(\tau, \xi, \eta), \quad z = z(\tau, \xi, \eta), \quad (1.19)$$

or, equivalently, in the vector form  $\mathbf{r} = \mathbf{r}(\xi)$  with  $\xi = (\tau, \xi, \eta)$ . At  $\tau = 0$  these equations describe the initial surface  $Q$  and for  $\tau > 0$ , a smooth three-dimensional hypersurface  $S_r$  in the extended six-dimensional space  $\{\mathbf{r}, \xi\} = \{x, y, z, \tau, \xi, \eta\}$ , which is referred to as a *ray surface* as it is formed by rays. Projecting a ray surface  $S_r$  from the extended space  $\{\mathbf{r}, \xi\}$  onto the configurational space  $\mathbf{r} = \{x, y, z\}$  brings about singularities identified with caustics, as these singularities are where the Jacobian of the transformation from Cartesian to ray coordinates vanishes.

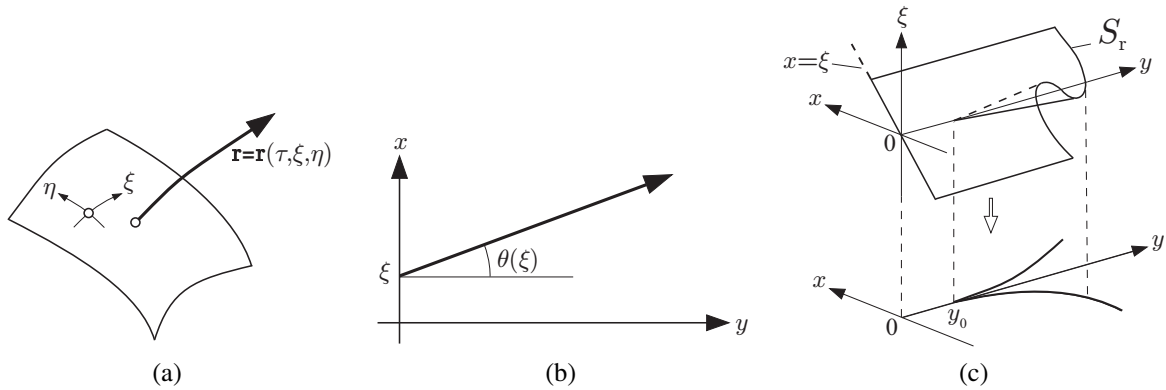


**Figure 1.3:** Illustration of the origin of a caustic: (a) ray path bearing ray coordinates; (b) ray path in the  $(x, y)$ -plane; (c) ray surface  $S_r$  in the extended space  $(x, y, \xi)$  when mapped onto the physical  $(x, y)$ -plane gives rise to a cusp.

For example, let  $\xi$  be the coordinate of the emanation point on the  $x$  axis, and  $\theta(\xi)$  the angle, measured from the  $y$  axis, at which the ray is launched in the  $(x, y)$  plane, as shown in figure 1.3b. With this notation the equation (1.19) of the ray family in the  $(x, y)$  plane becomes

$$x = \xi + y \tan \theta(\xi). \quad (1.20)$$

In the extended 3D space  $\{x, y, \xi\}$  this equation describes a two-dimensional ray surface  $S_r : \xi = \xi(x, y)$ . Figure 1.3c shows schematically such a surface for ray slope varying by the law  $\tan \theta = \beta \xi / (\xi^2 + a^2)$ . Projecting the ray surface  $S_r$ , which experiences a gradient catastrophe ( $\nabla S_r \rightarrow \infty$ ), onto the physical plane  $\{x, y\}$  gives rise to caustics corresponding to the singularities of the mapping. In figure 1.3c the caustic has the form of a cusp and the corresponding singularity of  $S_r$  is known as a fold.

### 1.2.2 Example: coffee cup caustic

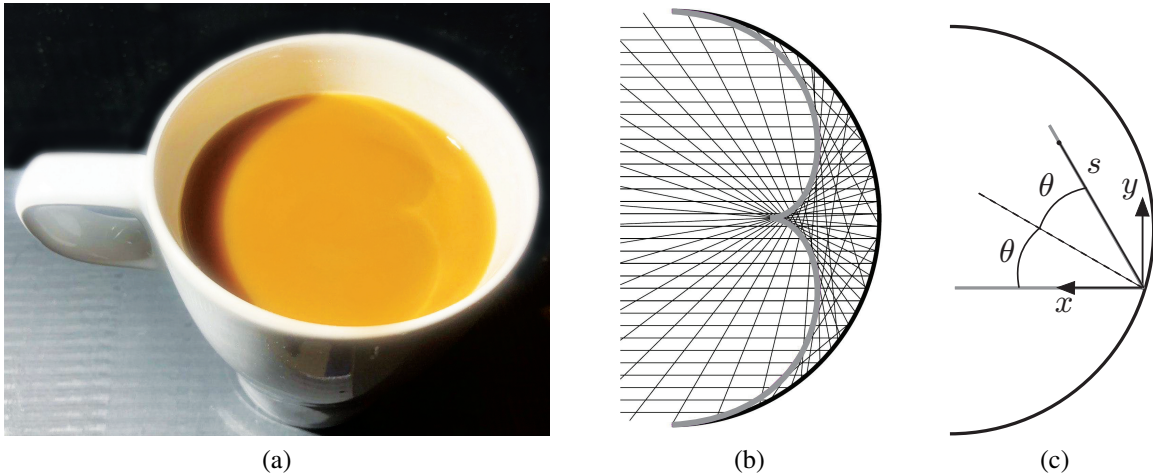


**Figure 1.4:** Caustic in a coffee cup.

The coffee cup caustic appears when parallel rays are reflected by a concave surface and hit a flat surface of the coffee or the cup bottom, cf. figure 1.4a. In figure 1.4b two curves that meet in a bright tip aka “cusp” and are called “folds”.

In order to construct the caustic mathematically, we can parametrize incident ray by the impact parameter  $b = R \sin \theta$  or, equivalently, the angle  $\theta$  of the impact point measured with respect to the direction of the incident rays; here  $R$  is the radius of the cup. The reflected ray makes an angle  $2\theta$  with respect to the incident direction. Along the reflected ray we can introduce the ray length  $s$

measured from the cup surface towards the inside. Therefore, the reflected rays are represented as

$$x = R \cos \theta - s \cos 2\theta, \quad (1.21a)$$

$$y = R \sin \theta - s \sin 2\theta, \quad (1.21b)$$

where the coordinate  $x$  points along the incident direction, and  $y$  is perpendicular to it. Equations (1.21) represent a mapping from the parameter space  $(s, \theta)$  to the coordinate space  $(x, y)$ . If a family of rays is traced, they form a curved envelope – the caustic (thick grey curve in figure 1.4b). According to §1.1, it can be found from the condition that the mapping  $(s, \theta) \mapsto (x, y)$  is singular. Since the Jacobian of this coordinate transformation is

$$J = \begin{pmatrix} \frac{\partial x}{\partial s} & \frac{\partial x}{\partial \theta} \\ \frac{\partial y}{\partial s} & \frac{\partial y}{\partial \theta} \end{pmatrix} = \begin{pmatrix} -\cos 2\theta & -R \sin \theta + 2s \sin 2\theta \\ -\sin 2\theta & R \cos \theta - 2s \cos 2\theta \end{pmatrix} \quad (1.22)$$

and its determinant  $\det J = 2s - R \cos \theta$ , in the parameter space, the coffee cup caustic is therefore given by an arclength  $s = \frac{1}{2}R \cos \theta$  measured from the reflection point of the ray. The caustic in coordinate space is then given by:

$$x = R \cos \theta - \frac{R}{2} \cos \theta \cos 2\theta, \quad (1.23a)$$

$$y = R \sin \theta - \frac{R}{2} \cos \theta \sin 2\theta. \quad (1.23b)$$

In particular, by taking  $\theta = 0$  we find that the cusp is located at  $s = R/2$ , half-way between the rim and the center of the cup. The behaviour near the cusp is found by expanding for small  $\theta$ :

$$x = \frac{R}{2} + \frac{3}{4}R \theta^2, \quad y = \frac{7}{6}R \theta^3, \quad (1.24)$$

which illustrates that the cusp is the fractional-power parabola  $y \sim \pm |x - x_c|^{3/2}$  with  $x_c = R/2$ .

### 1.2.3 Thom's theorem

Thom's transversality theorem (Thom, 1954, 1956), responsible for the development of catastrophe theory (Arnold, 2003) describing how continuous action produces a discontinuous result (Aubin, 2004), tells us, in particular, about the forms the caustics may take. The application of Thom's theorem is made convenient by the fact that the trajectories (1.16) can be derived from a *generating function* of the form

$$\Phi(\mathbf{r}, \xi) = \xi \cdot \mathbf{r} + f(\mathbf{r}), \quad (1.25)$$

by the gradient conditions

$$\nabla_{\mathbf{r}} \Phi = 0; \quad (1.26)$$

then the caustics are singularities of gradient maps of the form (1.26) derived from generating functions  $\Phi(\mathbf{r}, \xi)$ . Thom's theorem concerns generic caustics, i.e. structurally stable in the dynamical systems sense (Wiggins, 2003) meaning that a perturbation leaves the local structure of the caustic unchanged: the perturbed and unperturbed caustics are related by a diffeomorphism (a smooth reversible transformation). Structurally unstable caustics are therefore those, whose topological type is changed by perturbation.

Thom's theorem states (Wassermann, 1974) that there exists only a finite number of structurally stable caustic types (named as the "elementary catastrophes" by Thom) for a given value of the control parameter space  $\xi$  dimension  $n$ , called the co-dimension of the caustic, and it gives explicit standard forms for the generating functions when  $n$  is less than 7. Of immediate interest to us are only the first two generating functions:

$$n = 1 : \Phi = x^3/3 + \xi_1 x \text{ (fold)}, \quad (1.27a)$$

$$n = 2 : \Phi = x^4/4 + \xi_1 x^2/2 + \xi_2 x \text{ (cusp)}, \quad (1.27b)$$

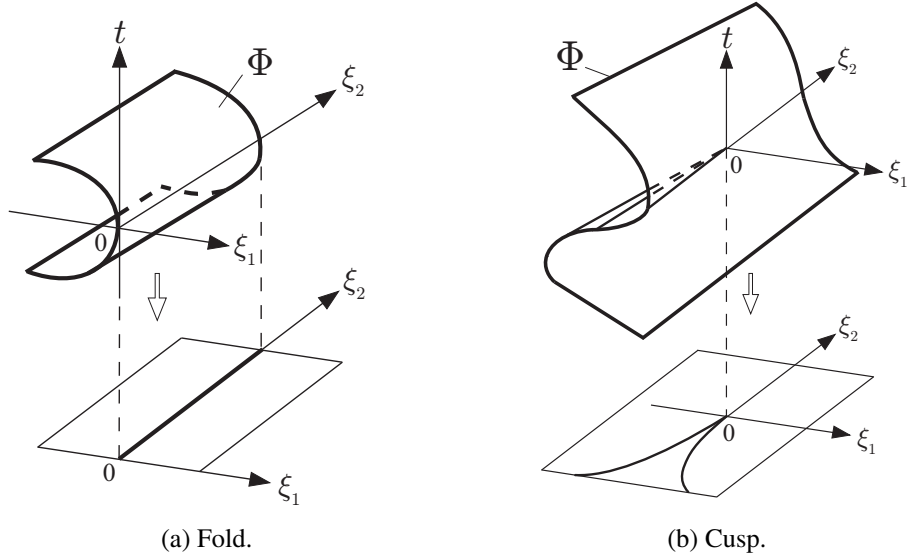
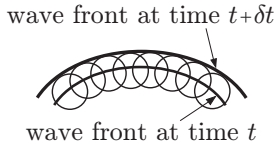


**Figure 1.5:** Structurally stable caustics with codimension  $n \leq 2$ .

illustrated in figures 1.5a and 1.5b, respectively; in terms of projection from extended onto physical space, the origin of these singularities is shown in figures 1.5a and 1.5b, respectively.

### 1.3 Wave propagation in 2D vs 3D



Huygens' principle states that the wavefront of a propagating wave at any instant of time conforms to the envelope of wavelets emitted from the wavefront at the previous time instant, cf. figure 1.6.

**Figure 1.6:** On Huygens' principle.

While we are going to appeal to Huygens's principle in both 2D and 3D situations, strictly speaking, it is not valid in 2D because sharp signals exist only in 3D (this statement can be generalized to odd dimensions higher than three). To show that, consider, for simplicity, the spherically symmetric wave equation, which in the corresponding radial coordinate  $r$  takes the form

$$\frac{\partial^2 \psi}{\partial t^2} = \frac{\partial^2 \psi}{\partial r^2} + \frac{n-1}{2} \frac{\partial \psi}{\partial r}, \quad (1.28)$$

where  $n$  is the dimension of the problem. With the transformation  $\phi(t, r) = r^{(1-n)/2}\psi(t, r)$  we can absorb the first derivative:

$$\frac{\partial^2 \phi}{\partial t^2} = \frac{\partial^2 \phi}{\partial r^2} - \frac{(n-1)(n-3)}{4r^2} \phi. \quad (1.29)$$

Hence, if  $n = 1$ , then  $\phi = \psi$  with the general solution of the form

$$\psi(t, r) = f(r-t) + g(r+t) \quad (1.30)$$

for arbitrary functions  $f$  and  $g$ . Also, if  $n = 3$ , then the general solution reads

$$\psi(t, r) = \frac{f(r-t)}{r} + \frac{g(r+t)}{r}. \quad (1.31)$$

In both 1D and 3D cases the solution depends on  $r \pm t$  meaning that a single pulse will propagate with the unit speed (on the Mach cone).

In two dimensions, however, the solution of the linear wave equation is, without loss of generality,

$$\psi \sim \cos(ct)J_0(r), \quad (1.32)$$

where the Bessel function can be represented in the integral form  $J_0(r) = \frac{2}{\pi} \int_0^\infty \sin[\cosh(\theta r)] d\theta$  (Abramowitz & Stegun, 1965). Multiplying  $J_0(r)$  by  $\cos(ct)$ , we find that the solution of the wave equation has the form

$$\psi(t, r) \sim \frac{1}{\pi} \int_0^\infty \{ \sin[\cosh(\theta r) - ct] + \sin[\cosh(\theta r) + ct] \} d\theta, \quad (1.33)$$

where each value of  $\theta$  corresponds to a propagation speed  $c/\cosh\theta$ , i.e. it varies from  $c$  to zero. This indicates that the solution to the wave equation at any event is correlated not just with the solution on its ‘‘Mach cone’’, but with the every event inside its Mach cone. From experience we

know that if one drops a pebble in a quiescent pond, a circular wave on the two-dimensional water surface will propagate outward. Should Huygens' principle be valid in 2D, the pond surface would be perfectly flat both outside and inside the expanding spherical wave. However, even after the wave has propagated through, the water surface inside of the expanding wave remains excited indefinitely, although with the magnitude diminishing in time.

While figure 1.6 depicts the propagation of the wave "front", Huygens' principle applies equally to any locus of constant phase propagating at the same wave speed  $c$ . This implies that there is no diffusion of waves. However, this is not true in 2D as we just concluded. Of course, the leading edge of a wave in 2D always propagates at the wave speed  $c$ , regardless of whether Huygens' principle is valid or not, but behind the leading edge of the disturbance this principle does apply in 2D.

# Chapter 2

## Impulse-driven drop

The breakup of drops into secondary ones is an important multiphase process with a variety of applications from atomization, combustion instability of sprays, heterogeneous detonations of gas/liquid mixtures, dispersed multiphase flows, agricultural and environmental spraying, aerosol formation, steam turbine blade erosion, ablation in space technology, and interactions between high-speed aircraft and raindrops, to name a few (Lefebvre & McDonell, 2017; Ashgriz, 2011). Among the key objectives in this secondary atomization of liquid drops is the increase of surface area and the enhancement of heat and mass transfer, for example between the fuel and the ambient gas.

There are three basic situations in which a drop may experience the secondary breakup – shock wave (SW) passing through a suspended drop known as aerobreakup, a drop impinging on a solid or liquid surface, and a solid surface impulsively accelerating into the drop sitting on it – all necessarily involving a sudden impact, which provides enough energy to overcome surface tension forces holding the drop together and the viscous resistance opposing the stresses required to break up the drop. The latter configuration, while occurring in a number of aforementioned applications, is also fundamental to diesel engine technology, sensor resonators, condensation on resonators in thermoacoustic engines and heat exchangers.

While aerobreakup is characterized by a non-uniform pressure distribution due to aerodynamic forces and contribution of thermodynamic effects (Joseph *et al.*, 1996), since at the earliest stages of drop fragmentation copious amounts of mist are formed due to flash evaporation of the low-pressure hot liquid on the drop leeside, none of these complications occur in the case of impulsively accel-

erated drops sitting on a solid substrate. As for distinctions from the drop impact on solid, besides the obvious fact that in the latter situation the drop is an oblate spheroid before the impact while in our case the sessile drop shape is dictated by the wetting properties of the solid substrate, they come to two key factors drastically differentiating the system under consideration. First, we naturally do not need to deal with air entrapment effects, which occur in the drop impact problem (Josserand & Thoroddsen, 2016). Second, the coordinate transformation from a drop impinging a solid to a drop driven by a nearly impulsive acceleration  $a$  of the substrate requires a transition to a non-inertial frame of reference and therefore lacks a Gallilean invariance: hence one cannot necessarily infer the behavior of one phenomenon from the other (§2.1.3.3) as evidenced by the different metamorphoses a drop experiences (§§2.1.2,2.1.5.1). In this regard, to our knowledge, the effect of a finite acceleration  $a$  on the response of a liquid drop of density  $\rho$  and dynamic viscosity  $\mu$  has not been studied, which is apparent even from the governing velocity  $V_{\max}$ -based non-dimensional parameters – Reynolds  $Re = \rho V_{\max} R_0 / \mu$  and Weber  $We = \rho V_{\max}^2 R_0 / \sigma$  numbers – used to characterize the aerobreakup (Pilch & Erdman, 1987) and drop impact on solid phenomena (Yarin, 2006). However, as we will show, despite substantial magnitudes of acceleration, its variation (along with the associated intensity of the SW induced in the drop by a sudden displacement of the substrate) proves to be responsible for the diversity of drop responses.

Similar to the above mentioned sister problems, analytical progress on understanding the impulse-driven drop phenomena is impeded by the fact that the drop distortion is comparable to its initial size thus requiring fully nonlinear analysis. Reliable numerical progress is hindered as well in view of severe changes in the drop topology due to cavitation, detachment from the substrate, and eventual disintegration – all amounting to the multiscale nature of the phenomena. For that reason we approach the problem with experimental tools here (§2.1.1) in order to uncover the key morphologies (§2.1.2), which prove to be strikingly different from those in aerobreakup and drop impact on solid as discussed in §2.1.5.1. As will be shown, our experiments revealed two primary regimes of drop response which we denote as *deformation* and *disintegration*, respectively, within which there is a great variety of sub-regime responses overviewed in §2.1.2. In the subsequent sections we highlight

the underlying physical mechanisms either qualitatively or with appropriate scalings and estimates in the detailed studies of both the drop deformation (§2.1.3) and disintegration (§2.1.4) regimes organized in the order of increasing impact intensity. Starting with quantifying the crown-precursors and the physics behind them (§2.1.3.1), we explore the different crown regimes (§2.1.3.2), the governing mechanisms of impulse-driven drop deformation (§2.1.3.3) and then crown dynamics along with the viscosity and surface tension effects on it (§2.1.3.4). In the drop disintegration regimes (§2.1.4.1), we explore the fluid dynamics behind them (§2.1.4.2), drop detachment and disintegration times (§2.1.4.3), as well as the effects of viscosity, surface tension, and compressibility on the secondary droplet size distributions (§2.1.4.4). Throughout the paper, we identify proper time scales and non-dimensional parameters which help one to understand the nature of various drop deformation (§2.1.3.2) and disintegration (§2.1.4.1) morphologies along with the transitions between them.

## 2.1 Experiments

### 2.1.1 Experimental setup and procedure

#### 2.1.1.1 Apparatus

Methods for generating shock waves in liquids – explosive, electromagnetic, piezoelectric and piezodispersive – were recently reviewed and compared by [Dion \*et al.\* \(2009\)](#). Despite the key disadvantage of the electromagnetic piston method – namely, high voltage components – we have chosen it over other approaches due to easy adjustability, in particular the ability to control the signal shape by varying resistance and inductance and to produce shocks of large amplitudes compared to, say, the piezoelectric method. To study shock wave-drop interaction phenomena, we built an electromagnetic shock wave generator (EMSWG) originally invented by [Eisenmenger \(1962\)](#) for the production of plane shock waves in water and used in subsequent works, e.g. by [Mortimer & Skews \(1996\)](#) and [Kedrinskii \*et al.\* \(2005\)](#). The physics of EMSWG and its electroacoustic efficiency are now reasonably well understood ([Roi, 1970](#)).

While the mechanical and electric components of the setup – an electromagnetic shock tube assembly as well as charging, triggering, and measuring units – are detailed in Appendix 2.B, the capturing part, schematized in figure 2.1a, resorts to conventional high-speed photography visualization techniques. A pulse required to stop/record the phenomena with a camera is provided by a linear Hall effect sensor (TT Electronics, OHS3150U). Once this sensor detects the electromagnetic (EM) field, it sends a signal to a pulse/delay generator *BNC* (Berkeley Nucleonics Corp, Model 575). After some delay precisely set by the *BNC*, a pulse is sent to a camera and a strobe to start or stop recording. Two cameras were used in these experiments: high resolution (Vieworks VA-8MC-C16A0) and high speed (Phantom V5.2) ones. In the case of a high resolution camera a light strobe (IDT-19LED-2nd Gen) was employed and synchronized with it. In the case of the high speed camera a hand made LED source ( $\sim 14000$  lumens) was used to provide a continuous lighting during the recording. Exposure time of recording with the Phantom was set at  $\leq 10 \mu\text{s}$  and with the Vieworks down to  $1 \mu\text{s}$ . Frame size of the Vieworks camera was  $1920 \times 1080$  pixels and in the case of the Phantom camera was adjusted depending on the frame rate.

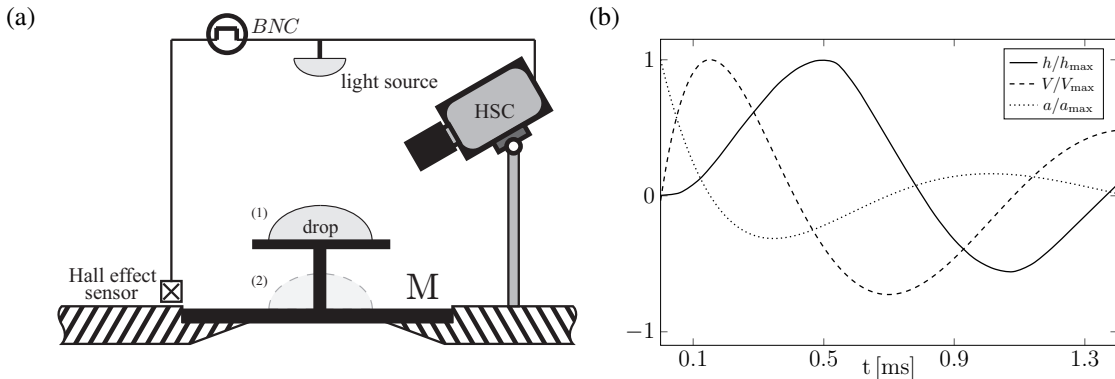


**Figure 2.1:** (a) Schematics of the capturing part of the experimental setup indicating two studied configurations: drop sitting on (1) a pedestal circular ( $\varnothing 20$  mm and 0.5 mm thick) plate mounted on membrane M and (2) the membrane directly. (b) Typical membrane kinematics shown for the initial energy 390 J and membrane thickness 0.1 mm: scaled by maximum values are the membrane deflection  $h/h_{\text{max}}$  (solid), velocity  $V/V_{\text{max}}$  (dashed), and acceleration  $a/a_{\text{max}}$  (dotted).

Impulse energy of the EMSWG varied between 250 – 1000 J. In the low impulse intensities a drop was placed on a pedestal – a circular plate mounted on the post (configuration 1 in figure

2.1a), which is fixed at the center of the 0.5 mm copper membrane<sup>1</sup> clamped along its periphery and agitated by the EMSWG. In the high impulse-intensities a drop is positioned directly on thinner copper membranes of thicknesses  $h_0 = 0.17, 0.1, \text{ and } 0.034 \text{ mm}$  (configuration 2). A slight difference between these two configurations is that the pedestal top plate remains perfectly flat, while the membrane deforms (cf. figure 2.2a), though stays essentially flat near its center where the drop is placed since the deformations are much smaller than the membrane radius.

### 2.1.1.2 Fluid properties and membrane kinematics

water-glycerol					water-sucrose					water-ethanol				
$c$	$\mu$	$\sigma$	$\theta_{ss}$	$\theta_c$	$c$	$\mu$	$\sigma$	$\theta_{ss}$	$\theta_c$	$c$	$\mu$	$\sigma$	$\theta_{ss}$	$\theta_c$
45	4.7	67.7	82	92	0	0.89	72	89	86	2	1.1	64.1	87	86
67	17.6	66.7	79	105	10	1.33	73.5	88	84	6	1.5	57.3	83	82
75	37.6	66.1	71	103	20	1.7	74.7	88	86	12	1.95	45.6	68	73
80	59.9	65.7	71	83	30	2.8	75.9	86	97	22	2.3	36.9	62	57
88	147.5	64.7	80	82	40	5.3	77.1	86	100	35	2.2	31.5	47	43
90	266	64.5	85	82	50	12.8	78.3	86	103					
99.5	934	62.5	86	81										

properties variation		
glycerol	$\mu \uparrow$ (a lot)	$\sigma \downarrow$ (a little)
sucrose	$\mu \uparrow$ (a lot)	$\sigma \uparrow$ (a little)
ethanol	$\mu \uparrow$ (a little)	$\sigma \downarrow$ (a lot)

**Table 2.1:** Working fluids: each of the five columns for the glycerol-, sucrose-, and ethanol-water mixtures represents concentration  $c$  [% wt], dynamic viscosity  $\mu$  [mPa·s], surface tension  $\sigma$  [mN m<sup>-1</sup>], as well as contact angles with stainless steel  $\theta_{ss}$  and copper  $\theta_c$ , accordingly. Encircled are the properties of water.

To investigate the effect of surface tension and viscosity on SW-drop interaction, we used various concentrations of 7 water-glycerol, 5 water-sucrose, 5 water-ethanol solutions and also deionized (DI) water: their thermophysical properties and contact angles  $\theta$  on both stainless steel and copper substrates are summarized in table 2.1. These three types of mixtures with water were deliberately chosen in order to achieve a wide range of the viscosities, surface tensions, and contact angle variations between wetting and non-wetting across  $\theta = 90^\circ$ . This enables us to work in the range in which viscous and interfacial forces are the dominant factors controlling the physical system.

<sup>1</sup>While we refer to the load-bearing element as a *membrane* following the convention in the literature, the caveat is that in elasticity theory (Landau & Lifshitz, 1986) it should be referred to as a plate since membrane is subject to large external stretching forces applied at its circumference, which is not the case here.

Contact angles were measured in our laboratory, as actual values often vary from those reported in the literature. The sound speed for pure ethanol, pure glycerol, and DI water at 20 °C are 1170, 1923, and 1479 m s<sup>-1</sup>, respectively (Giacomini, 1947; Association, 1963; Pryor & Roscoe, 1954). In the case of sucrose, 50% wt solution is considered as a reference for the speed of sound, which is 1720 m s<sup>-1</sup> (Pryor & Roscoe, 1954). Sound speeds for all other solutions, for which data are not available, were found by interpolation as appropriate for liquid mixtures (Matheson, 1971). Liquid drop volumes were changed between 25, 50, 75, and 100 μl.

To measure the membrane kinematics, cf. figure 2.1b, a needle was fixed at the membrane center, where maximum values of deflection are experienced; the displacement of the needle tip was recorded at 60,000 fps and frame size of 256 × 32 pixels. Maximum deflection  $h_{\max}$ , velocity  $V_{\max}$ , and acceleration  $a_{\max}$  for all studied cases are reported in figure 2.2 with the latter two variables corresponding to the early times of the displacement curve, cf. figure 2.1b. While raw data, e.g.  $h_{\max}$  vs  $E$  in the inset of figure 2.2a, are quite scattered, plotting the kinematics variables versus impact intensity  $E/h_0^2$  shows reasonable collapse since the membrane response to EM agitation is dictated not only by the released energy  $E$ , but also by the membrane thickness  $h_0$ .

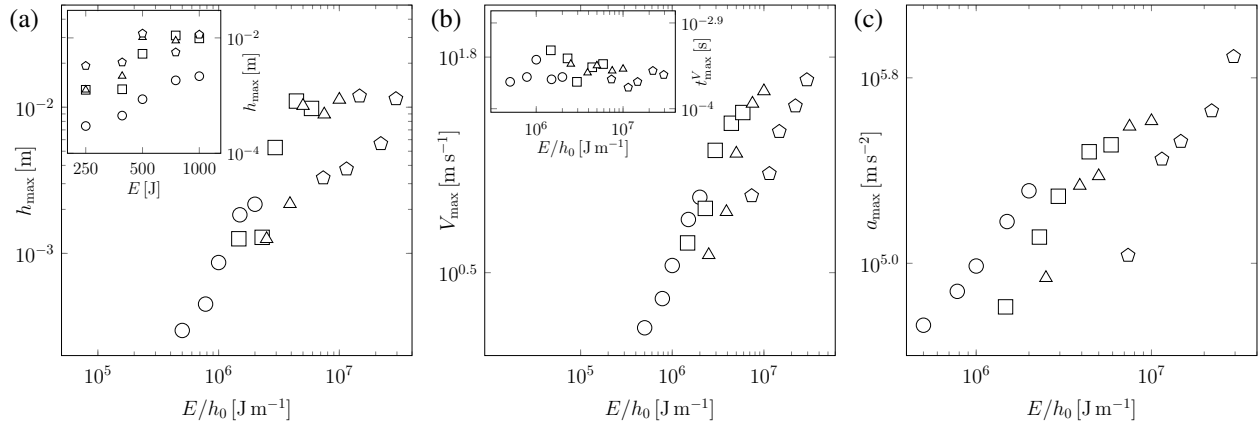


**Figure 2.2:** Maximum deflection  $h_{\max}$  (a), velocity  $V_{\max}$  (b), acceleration  $a_{\max}$  (c) for each membrane thickness  $h_0 = 0.5, 0.17, 0.1,$  and  $0.034$  mm (denoted by  $\circ, \square, \triangle,$  and  $\diamond$ , respectively) for five different initial energies  $E = 250, 390, 500, 750,$  and  $1000$  J. Inset on (b) shows the time  $t_{V_{\max}}$  when  $V_{\max}$  is registered.

<sup>2</sup>The choice of  $E/h_0$  follows from the fact that it is the pressure  $p \sim E/(h_0 D^2)$  induced on the membrane surface that is important for the phenomena at hand (Roi, 1970). Since the membrane diameter  $D$  is fixed, then  $E/h_0$  accounts for the variation of pressure and also encodes the natural membrane frequency  $\omega_M$ .

Lastly, the magnitudes of acceleration  $a_{\max}$  in figure 2.2c are comparable with  $O(10^5 - 10^6) \text{ m s}^{-2}$  in the SW-drop interactions experiments by Joseph *et al.* (1999), but much lower than  $O(10^7 - 10^8) \text{ m s}^{-2}$  in Simpkins & Bales (1972) for incident-shock Mach numbers 6 – 10. On the other hand, accelerations in our experiments are several orders of magnitude higher than in the recent studies of drop trampoline by Chantelot *et al.* (2018a,b), who looked at the drop-membrane interaction in the relatively low acceleration regime of  $O(10^2) \text{ m s}^{-2}$ . The patterns found by Chantelot *et al.* (2018b) are analogous to ours reported earlier (Habibi & Krechetnikov, 2015).

## 2.1.2 Results: overview of key morphologies

First, experiments were carried out to identify the key morphologies, illustrated and defined in figure 2.3<sup>3</sup>, as well as to map out the regimes and the corresponding transition boundaries between them discussed below in §§2.1.3.2, 2.1.4.1. In the *ripple wave* regime (rw), apparently, the driving velocity of the substrate  $V_{\max}$  is below the interfacial wave velocity  $c_p$ : as a result, the capillary waves induced by membrane deflection are capable of propagating along the drop surface and forming a staircase structure. Once the ‘supersonic’ regime is achieved  $V_{\max} > c_p$  upon increasing the membrane driving intensity, one observes hydraulic jump type phenomena leading to *ejecta* formation (e). This is confirmed by comparing the phase velocity of capillary waves  $c_p$  with  $V_{\max}$  in §2.1.3.1. In the *ejecta* regime the rim stays flat, i.e. does not develop an along-the-rim instability. In the crown regimes (cns, cs, md) the drop initially flattens into a pancake and the same mechanism as that responsible for the *ejecta* formation is intensified thus feeding more fluid into the *ejecta*. In the *crown without splash* (cns) regime the rim mostly stays flat, but may experience an instability at a later stage of development though without secondary droplet detachment. Upon increasing the impulse intensity and reaching the *crown with splash* regime (cs), a Rayleigh-Taylor (RT) instability

<sup>3</sup>Test conditions – liquid, drop volume, capacitor energy, exposure time, delay, physical image size, viewing angle – are as follows: (rw) DI water, 50  $\mu\text{l}$ , 250 J, 0.5 mm, 10  $\mu\text{s}$ , 3000  $\mu\text{s}$ ,  $10.9 \times 7.3 \text{ mm}^2$ , 5°; (e) DI water, 50  $\mu\text{l}$ , 390 J, 0.5 mm, 10  $\mu\text{s}$ , 700  $\mu\text{s}$ ,  $10.9 \times 7.3 \text{ mm}^2$ , 5°; (cns) 75% wt glycerol, 50  $\mu\text{l}$ , 1000 J, 0.5 mm, 10  $\mu\text{s}$ , 1000  $\mu\text{s}$ ,  $20.7 \times 13.8 \text{ mm}^2$ , 40°; (cs) DI water, 50  $\mu\text{l}$ , 1000 J, 0.5 mm, 10  $\mu\text{s}$ , 1200  $\mu\text{s}$ ,  $20.7 \times 13.8 \text{ mm}^2$ , 40°; (md) 35% wt ethanol, 50  $\mu\text{l}$ , 500 J, 0.034 mm, 1  $\mu\text{s}$ , 632  $\mu\text{s}$ ,  $13.8 \times 9.2 \text{ mm}^2$ , 30°; (bcs) 67% wt glycerol, 50  $\mu\text{l}$ , 390 J, 0.17 mm, 10  $\mu\text{s}$ , 1800  $\mu\text{s}$ ,  $18.2 \times 12.2 \text{ mm}^2$ , 30°; (c) 50% wt sucrose, 50  $\mu\text{l}$ , 500 J, 0.1 mm, 5  $\mu\text{s}$ , 1700  $\mu\text{s}$ ,  $71.7 \times 47.9 \text{ mm}^2$ , 30°; (da) DI water, 50  $\mu\text{l}$ , 1000 J, 0.034 mm, 3  $\mu\text{s}$ , 800  $\mu\text{s}$ ,  $71.7 \times 47.9 \text{ mm}^2$ , 30°.

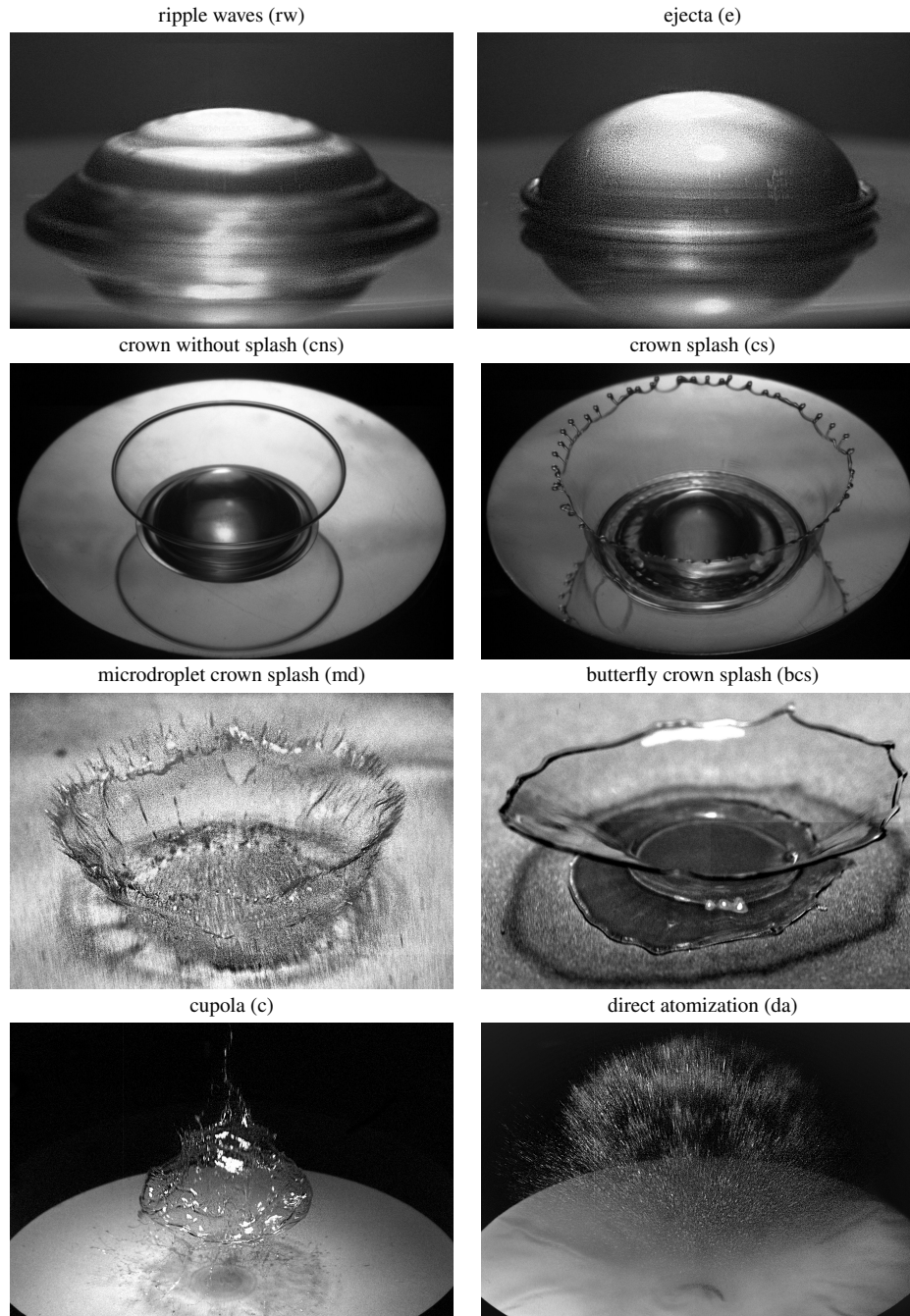


**Figure 2.3:** High resolution images of the key observed morphologies.

of accelerating interface overcomes the stabilizing role of surface tension: acceleration becomes significant enough to produce fingers, which eventually break up via a Rayleigh-Plateau (RP) instability, i.e. drops pinch off from the end of each jet and the rim develops cusps similar to crown formation in other drop impact phenomena (Yarin & Weiss, 1995). We refer to this regime as a crown

with splash irrespective of its regularity (Krechetnikov & Homsy, 2009). In the *microdroplet crown* regime (md) the ejecta becomes thinner, which is essentially due to enhanced flattening of the drop. As a consequence, the thinner ejecta breaks initially into smaller droplets (see also the right column in figure 2.4), but as ejecta thickens the emitted drop size increases. Once ejecta becomes too thin with increasing impact intensity, there emerges the *butterfly crown* (bcs) regime characterized by larger crowns and more substantial sidewise deflection of the crown liquid sheet, which we believe is due to the resistance of the surrounding air and membrane deformations much larger compared to that in the previous regimes<sup>4</sup>. Such crowns have a Hatazori-gata (curving lip) cup shape, which experiences an instability along its wall (sheet) perimeter leading to a butterfly pattern. In the *cupola* regime (c) a new type of phenomena appears, which is due to above-critical cavitation bubble density leading to a fast formation of a void comparable to the drop size and responsible for the drop detachment from the membrane and eventual disintegration. At even higher intensity impulses the drop experiences an immediate break-up – the *direct atomization* regime (da). In what follows we disentangle these observations by considering drop deformation (§2.1.3) and disintegration (§2.1.4) regimes separately.

### 2.1.3 Results: drop deformation regimes

For drops of all liquid types on the 0.5 mm thick membrane (pedestal configuration), by increasing impulse energy and hence intensity the patterns change from ripple waves to monotonic crown, as per figure 2.5. The ripple wave pattern is observed when the initial energy was 250 J. Upon increasing the initial energy to 390 J, the pattern transitions to ejecta. By further increase of the initial energy to 500 J the non-monotonic crown is formed, meaning that radius of the crown first increases to a maximum value and then decreases with time (figure 2.5c); this non-monotonic pattern is also observed for the 35% wt ethanol-water solution when the initial energy was set to 750 J. For the rest of liquid types at 750 J and for all liquids at 1000 J initial energy the crown radius increases

---

<sup>4</sup>Regimes, starting with the butterfly crowns, were observed on thin membranes only, which deform substantially more compared to the experiments on thick membranes, cf. figure 2.2a.

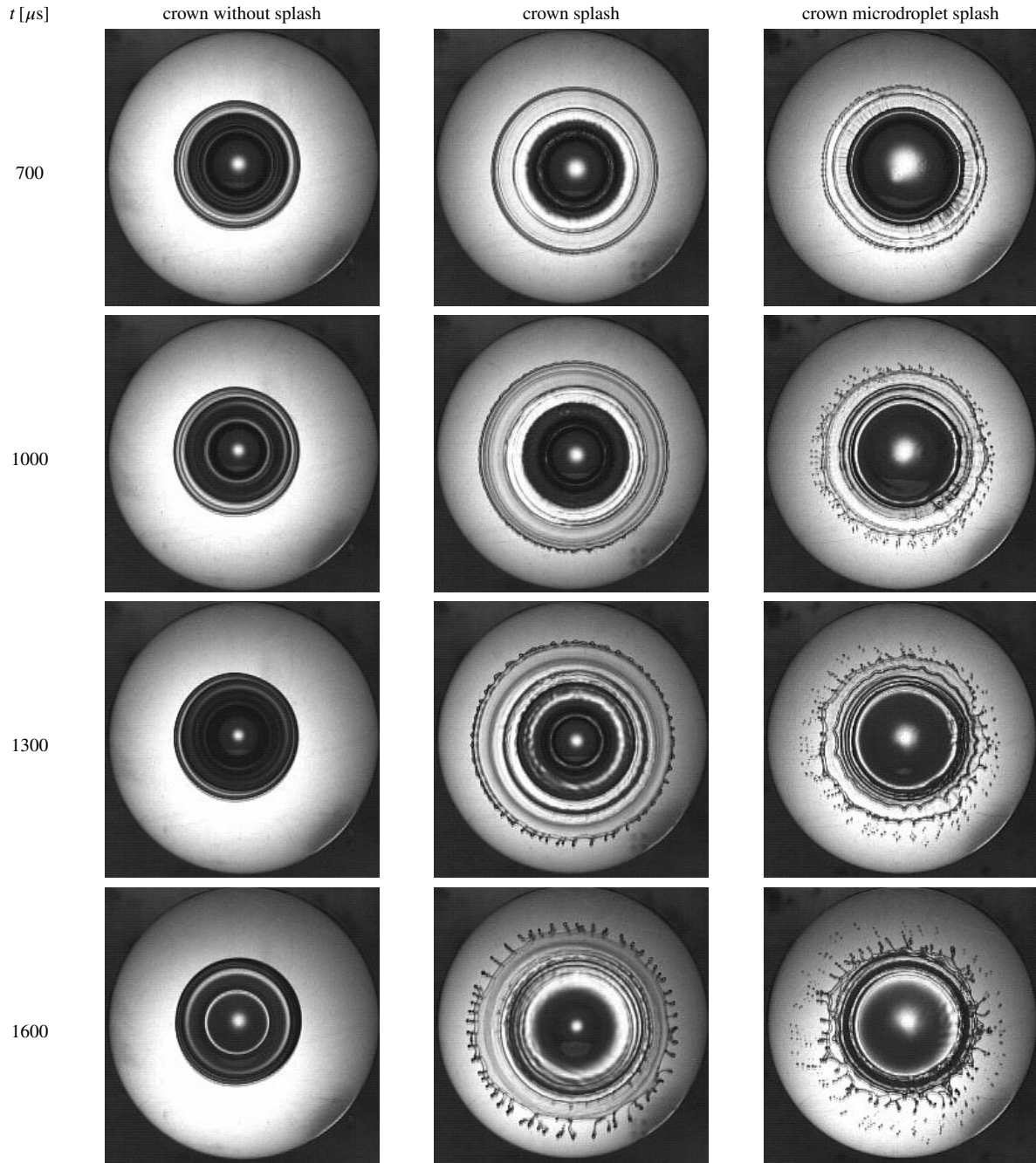


**Figure 2.4:** Top view: crown without splash (99.5% wt glycerol), crown splash (DI water), and crown microdroplet splash (35% wt ethanol) on the 0.5 mm stainless steel membrane driven by 1000J initial energy. Physical image size is  $20.0 \times 20.0 \text{ mm}^2$ . Diameter of the fingers at time stamp 1600  $\mu\text{s}$  is  $\sim 0.55 \text{ mm}$  and the diameter of the initially ejected microdroplets at the same time stamp is  $< 0.18 \text{ mm}$ , which are much smaller than the droplets emitted in the crown splash regime and which are followed by larger droplets as is evident from the photograph. The frame size and rate are the same as in figure 2.8.

monotonically with time (figure 2.5d). The interplay of monotonic vs non-monotonic crowns is discussed further in §2.1.3.4.

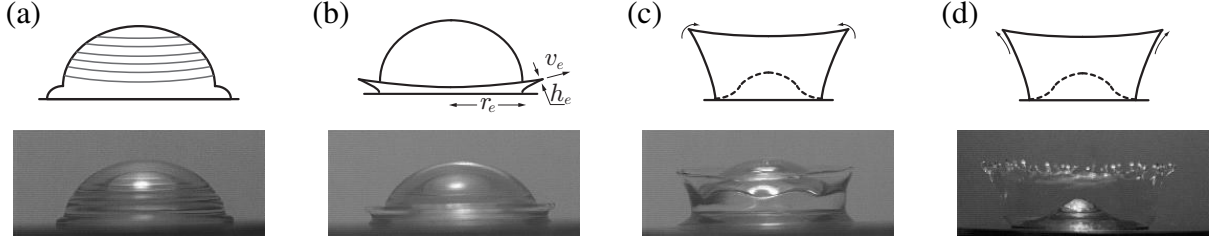


**Figure 2.5:** Regimes' transitions for different impact intensities: (a) ripple waves, (b) ejecta characterized by velocity  $v_e$ , thickness  $h_e$ , and the root radius  $r_e$ , (c) non-monotonic crown, (d) monotonic crown.

### 2.1.3.1 Crown precursors

As mentioned above, at the lower impulse intensities we first observe ripple waves and ejecta, cf. figures 2.6 and 2.7. By running experiments with all the liquids reported in table 2.1, we noticed that increasing viscosity from water to glycerol and sucrose solutions decreases the number of observed ripple waves on the liquid drop surface at an earlier stage meaning that the speed of their propagation is reduced. The same effect occurs if we decrease surface tension by going from water to ethanol solution. These two effects can be understood from the consideration of linear dissipative deep water waves (Lamb, 1932; Plesset & Whipple, 1974). Namely, given the linear evolution equation for the free surface deformation  $\zeta(t, \mathbf{x})$  in the wavenumber  $k$  space  $\widehat{\zeta}_{tt} + 4\nu k^2 \widehat{\zeta}_t + \omega_0^2 \widehat{\zeta} = 0$ , where  $\omega_0^2 = a k + \sigma k^3 / \rho$  and  $\nu \equiv \mu / \rho$  is the kinematic viscosity, we find the frequency of the ripple waves in the limits of the capillary waves and low viscosity

$$\omega(k) \approx (\sigma k^3 / \rho)^{1/2} [1 - 2\rho\nu^2 k / \sigma] + 2i\nu k^2 + \dots \quad (2.1)$$

Since the dominant wavenumber  $k$  is dictated by the form of the initial perturbation  $\zeta(0, \mathbf{x})$  – the maximum displacement of the membrane – we can perform further analysis in terms of the phase speed  $c_p = \omega(k)/k$  for this concrete wavenumber. As follows from (2.1),  $c_p$  decreases with increasing viscosity  $\nu$  and with decreasing surface tension  $\sigma$  (as long as the viscosity is small).

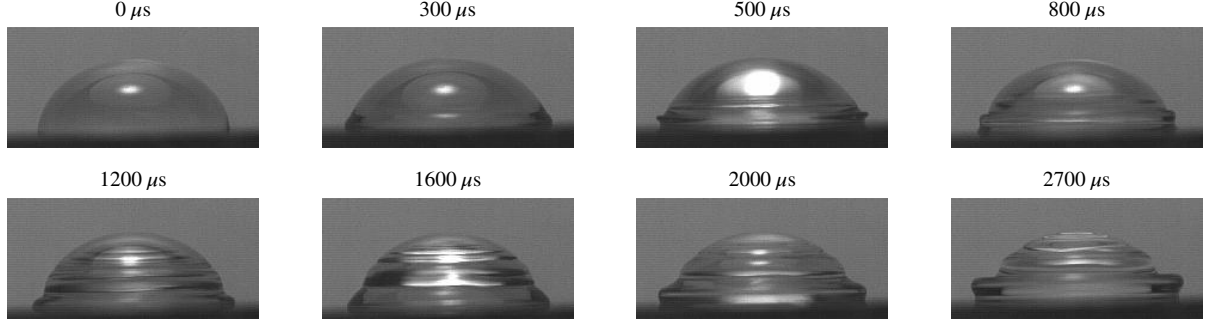


**Figure 2.6:** Ripple wave pattern in DI water. The drop volume, the initial energy, maximum velocity and deflection of the stainless steel membrane, and the membrane thickness are  $50 \mu\text{l}$ ,  $250 \text{ J}$ ,  $1.47 \text{ m s}^{-1}$ ,  $0.3 \text{ mm}$ , and  $0.5 \text{ mm}$ , respectively. Physical image size is  $11.0 \times 5.3 \text{ mm}^2$ .

Ripple wave patterns in figure 2.6 are analogous to the staircase structure observed by Renardy *et al.* (2003) and Roux & Cooper-White (2004) in drop impacts on a solid surface. To explain the existence of the staircase phenomenon, one must appeal to capillary waves. Since the capillary wave of maximal amplification has a phase speed equal to the impulse speed, its wavelength is  $\lambda \sim \sigma / \rho V_{\text{max}}^2$ . Clearly, waves are observed if  $\lambda < R_0$ , i.e.  $We > 1$ . Also, in order to observe the staircase structures the distance of decay  $l$  of a wave of length  $\lambda$  propagating with speed  $V_{\text{max}}$  must be  $l \sim \rho \lambda^2 V_{\text{max}} \mu > R_0$ , thus implying  $We Ca < 1$ , where  $Ca = \mu V_{\text{max}} / \sigma$  is the capillary number. Altogether, the range of speeds in which the staircase structures are observable is

$$\left(\frac{\sigma}{\rho R_0}\right)^{1/2} < V_{\text{max}} < \left(\frac{\sigma^2}{\rho \mu R_0}\right)^{1/3}, \quad (2.2)$$

where each of the (lower and upper) limits would correspond in the drop impact on solid experiments to the transition to spreading (figure 2.31a) and ‘fried egg’ (figure 2.31c) regimes, respectively. In our case, equation (2.2) yields  $O(0.1) \text{ m s}^{-1} < V_{\text{max}} < O(1.0) \text{ m s}^{-1}$ , which indeed explains the existence of the patterns in figure 2.6 at the measured  $V_{\text{max}} = 1.47 \text{ m s}^{-1}$ .

To understand the transition from the ripple waves in figure 2.6 to ejecta in figure 2.7, note that the capillary waves generated on the drop surface have a wavelength comparable to the corresponding membrane deflection. Since the minimum velocity wavenumber in our case is  $k_m = (\rho g / \sigma)^{1/2} \approx 400 \text{ m}^{-1}$  with the corresponding  $\lambda_m = 2\pi / k_m \sim 1 \text{ cm}$  and we are therefore in the limit  $k / k_m \gg 1$ ,

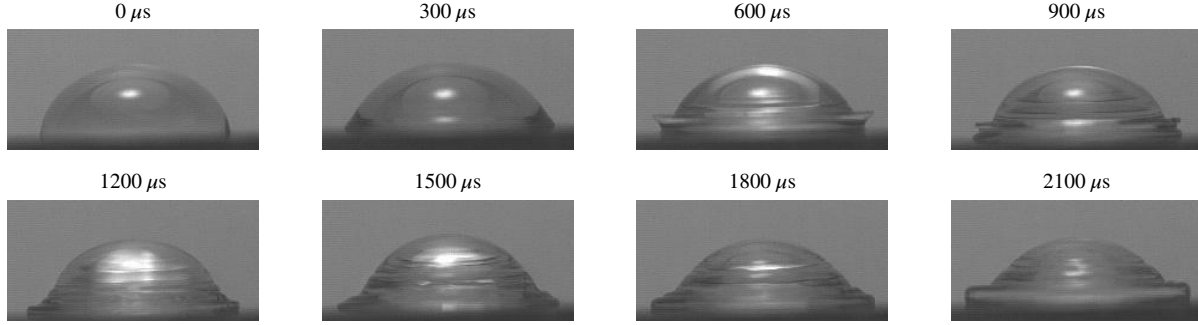


**Figure 2.7:** Ejecta pattern in DI water. The drop volume, the initial energy, maximum velocity and deflection of the stainless steel membrane, and the membrane thickness are  $50 \mu\text{l}$ ,  $390 \text{ J}$ ,  $2.21 \text{ ms}^{-1}$ ,  $0.45 \text{ mm}$ , and  $0.5 \text{ mm}$ , respectively. Physical image size is  $11.0 \times 5.3 \text{ mm}^2$ .

then the phase velocity is  $c_p \sim (\sigma k / \rho)^{1/2} \approx 0.6 - 1.8 \text{ m s}^{-1}$  for the impulse intensities in figures 2.6 and 2.7, which is in the range of the measured  $V_{\text{max}} = 1.47 - 2.21 \text{ m s}^{-1}$  reported in these figures. Hence it is the hydraulic jump which is responsible for the ripple wave to ejecta transition in the same way as SWs are formed in the media when the flow velocity exceeds the speed at which perturbations can propagate – acoustic as opposed to capillary waves in our case – so that faster fluid particles push the slower ones leading to wave steepening and eventually to ejecta.

### 2.1.3.2 Key crown regimes and transitions

Upon increasing the impulse intensity  $E/h_0$  beyond that required for the ejecta regime, there are three types of crowns – no splash, splash, and microdroplet splash – as is evident from figures 2.8 and 2.4. While the no splash regime is characterized by absence of secondary emitted droplets, the splash and microdroplet splash are distinguished by the size of emitted droplets: in the latter case they are much smaller, on the order of tens of microns in diameter. It is also remarkable that the microdroplet crown regime exhibits an instability of the thin crown sheet, cf. figure 2.8c. To study the radius change in the crown evolution process, the phenomena were recorded from top view using a semitransparent mirror placed at  $45^\circ$  in between the target and the light source positioned vertically above the target. Also, to investigate the crown height change, a set of recordings was performed from a side view.

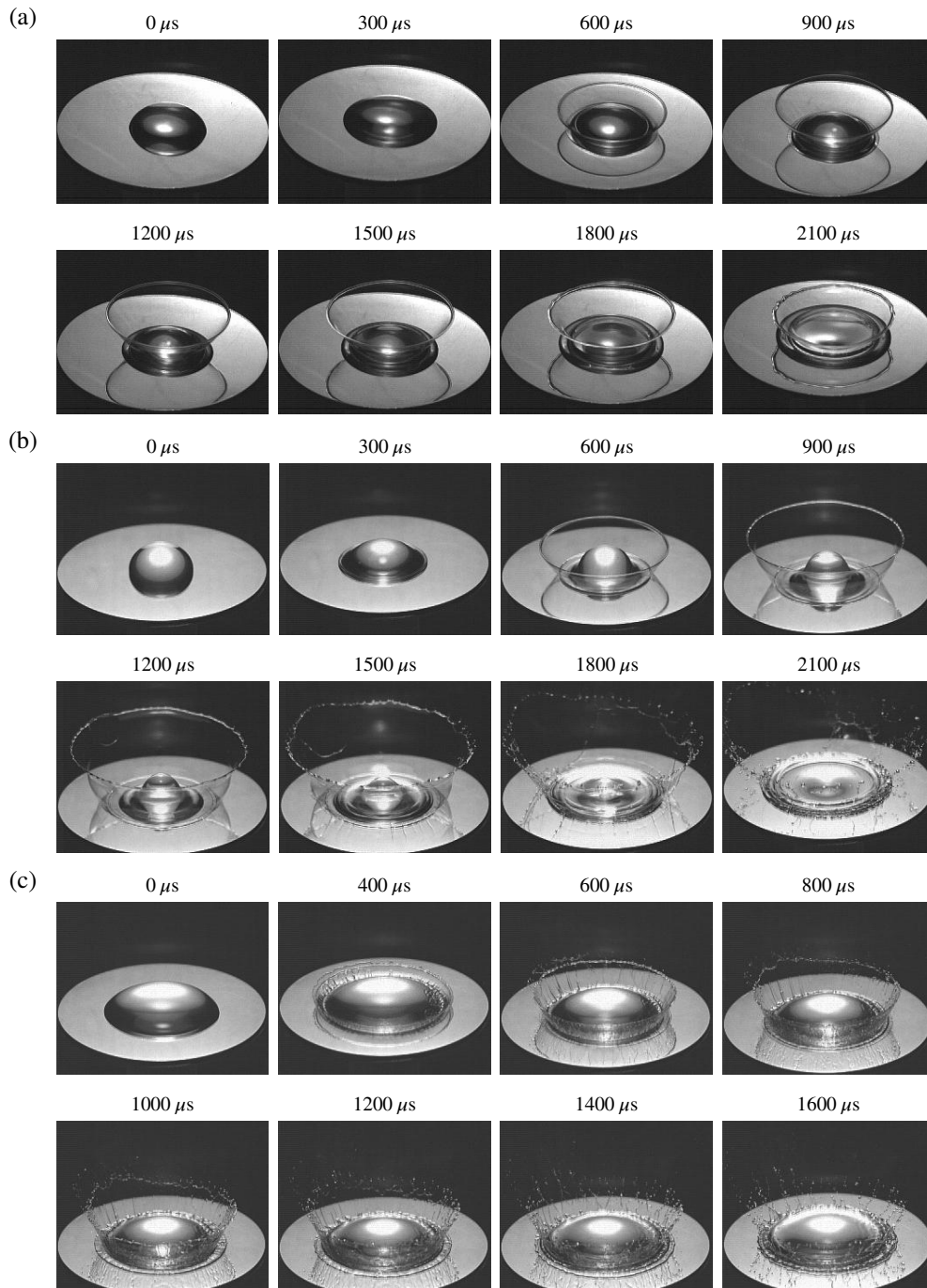


**Figure 2.8:** (a) Crown without splash of 80% wt water-glycerol solution. (b) Crown with splash of 10% wt water-sucrose solution. (c) Microdroplet crown splash of 35% wt water-ethanol solution. In all cases the initial energy and the membrane thickness were 1000 J and 0.5 mm, respectively; drop volume in (a,b) was  $50 \mu\text{l}$  and in (c)  $100 \mu\text{l}$ . Frame size and frame rate were  $256 \times 256$  pixels and 10,000 fps, respectively; physical image size is  $20.6 \times 16.1 \text{ mm}^2$ . Since the interrogation window was fixed in space, the images show the actual motion of the pedestal.

The complete map of all the drop deformation regimes observed in our experiments is summarized in figure 2.9a. While the energy and membrane thickness were varied in getting all these data points, they are not used in plotting as both  $We$  and  $Re$  numbers are built from the associated membrane kinematics data controlled by the impulse intensity  $E/h_0$ , cf. figure 2.2.

To study the effect of impact intensity and drop liquid properties, in the experiments presented in figure 2.9 various solutions were employed and the initial energy varied. A map of the observed regimes in these experiments provided in figure 2.9a is replotted in terms of  $We$  and  $Re$  numbers and in figure 2.9b in terms of the splashing parameter  $K \equiv Re^{1/2}We$ , which puts the data in the monotonic order with microdroplet crown splash on the extreme side of the parameter  $K$  value. Figure 2.9b also highlights the role of acceleration  $a_{\max}$  in organizing the transitions in a monotonic order: for the lowest magnitudes the regime is ripple waves, while for the largest magnitudes the regimes change from crown without splash to microdroplet splash as  $K$  increases for  $a_{\max}$  fixed. The complexity of the curves separating the regimes in figure 2.9a suggests that the  $(We, Re)$ -plane does not form appropriate coordinates as the transitions should be scalable, but the  $(a_{\max}/g, K)$  coordinates make the transition curves monotonic.

To understand the origin and relevance of the splashing parameter  $K$  to our phenomena, let us consider an impulsively driven drop on a membrane in the large  $We$  and  $Re$  number regime neglecting the effects of compressibility, in analogy with the considerations by Josserrand & Zaleski (2003) for the impact of a drop on liquid surface. We know that depending upon physical conditions two types of patterns may exist with and without ejecta as illustrated in figures 2.5a and 2.5b. Since the viscous length scale  $l_v = (\nu t)^{1/2}$ , dictated by the solution of the first Stokes problem, exceeds the vertical one  $V_{\max} t$  for  $t < t_v = \tau_0 Re^{-1}$  with  $\tau_0 = R_0/V_{\max}$ , this defines a region of size  $l_v$  near the jet neck, where the vorticity is concentrated. Hence, the jet thickness  $h_e$ , cf. figure 2.5b, in the viscous stage must match the viscous length scale  $h_e \simeq l_v$ . The jet velocity  $v_e$  can be obtained by a mass conservation argument: mass coming from the deformed part of the drop due to impulsive motion of the membrane per unit time  $\rho V_{\max} \pi r_e^2$  must be equal to the mass flux through the jet  $2\pi \rho r_e h_e v_e$ , thus producing  $v_e \simeq (t/\tau_0)^{-1/2} V_{\max} Re^{1/2}$ , which obviously diverges as  $t \rightarrow 0$  in this

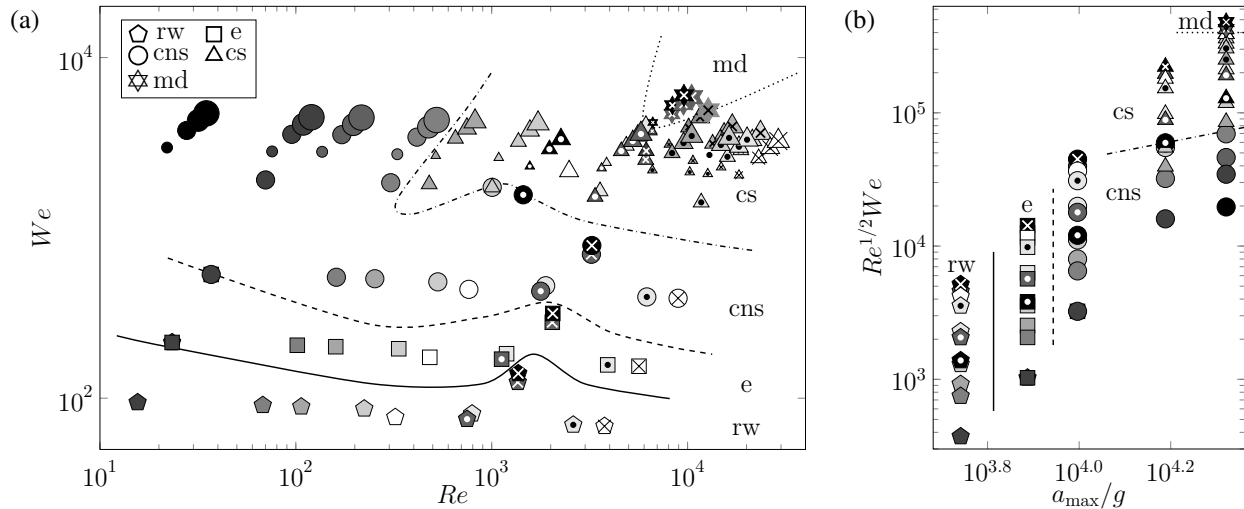


**Figure 2.9:** (a) Map of the impact intensity effect with dashed lines denoting transitions between regimes (to guide the eye); for the regime definitions refer to figure 2.3. The substrate was made out of stainless steel of 0.5 mm thickness. Six liquids (67 % wt glycerol, 80 % wt glycerol, 90 % wt glycerol, 50 % wt sucrose, 22 % wt ethanol, and DI water) in four different volumes were chosen for tests at five initial energies (250, 390, 500, 750, and 1000 J). Liquid *drop volumes* are denoted by relative symbol sizes:  $\circ$  25  $\mu\text{l}$ ,  $\bigcirc$  50  $\mu\text{l}$ ,  $\bigcirc$  75  $\mu\text{l}$ ,  $\bigcirc$  100  $\mu\text{l}$ ; *concentrations* by different shadings:  $\bullet$  45% wt glycerol, 10% wt sucrose, 2% wt ethanol;  $\bullet$  67% wt glycerol, 20% wt sucrose, 6% wt ethanol;  $\bullet$  75% wt glycerol, 30% wt sucrose, 12% wt ethanol;  $\bullet$  80% wt glycerol;  $\bullet$  88% wt glycerol, 40% wt sucrose, 22% wt ethanol;  $\bullet$  90% wt glycerol;  $\bullet$  99.5% wt glycerol, 50% wt sucrose, 35% wt ethanol; type of *solutions* by different symbols: white  $\bigcirc$  – water, symbols with a black dot inside light shading  $\odot$  and a white dot inside dark shading  $\bullet$  – sucrose solutions, simple symbols  $\bullet$  – glycerol solutions, symbols with a black cross inside light shading  $\otimes$  and a white cross inside dark shading  $\otimes$  – ethanol solutions. (b) Map of the impact intensity effect shown for the 50  $\mu\text{l}$  liquid drop only (to avoid data cluttering) in terms of the splashing parameter  $K$  and acceleration  $a_{max}$  scaled by gravity  $g$ .

incompressible flow analysis. When the jet forms, its rim recedes due to surface tension with the Taylor (1959a)-Culick (1960) velocity

$$v_{TC} \simeq (2\sigma/\rho h_e)^{1/2} = (t/\tau_0)^{-1/2} V_{max} We^{-1/2} Re^{1/4}. \quad (2.3)$$

If  $v_{TC} < v_e$ , the jet length increases; if, on the other hand,  $v_{TC} > v_e$ , the jet cannot form. Thus, a necessary condition for the jet formation is that the Weber number is large enough. The condition  $v_{TC} < v_e$  for ejecta formation translates into  $t/\tau_0 < K^2$ , where  $K = Re^{1/2} We$  is the splashing parameter originally identified experimentally by Stow & Hadfield (1981).

The observed crown regime map for these sets of experiments is presented in figure 2.10a. Effects of viscosity and surface tension are exemplified in figure 2.10b, indicating that decreasing surface tension while keeping viscosity constant brings us to the microdroplet splash regime, while increasing surface tension leads to the crown splash. Conversely, increasing viscosity while maintaining surface tension constant suppresses the splash leading to the crown without splash. Replotting figure 2.10a in terms of the splashing parameter  $K$  again organizes the data in a monotonic order, cf. figure 2.10c. Comparison between the observed regimes and those in the drop impact on a thin liquid layer is presented in figure 2.10d, showing substantial qualitative and quantitative differences. While in the drop splash on a thin film (Deegan *et al.*, 2008) the transition from crown with splash to without splash happens at the boundary, which scales as  $We \sim Re^{-1/2}$  similar to the splashing parameter criterion  $K \gtrsim 3330$  in the drop splash on solid surface (Mundo *et al.*, 1995), in our case not only the value  $K = 3330$  is far exceeded, but this transition boundary also scales as  $We \sim Re$  as per figure 2.10a. That is, apparently, the splashing parameter  $K = Re^{1/2}We$  varies along the transition boundary, cf. figure 2.10c, which again indicates that acceleration  $a_{\max}$  must be a governing parameter consistent with the earlier observation in figure 2.9b. Also, considerably elevated values of  $Re$  and  $We$  required for crowns with splash to form in the impulsively driven drop experiments compared to those in drop impact on thin films, cf. figure 2.10d, suggest that splashing is made more difficult in the case of an accelerating substrate – the effect somewhat analogous to the fact that it is harder to splash on soft substrates (Howland *et al.*, 2016).

Next, using the time scales identified from a dimensional analysis (summarized in table A2.3 of Appendix 2.C), first note that the crown without splash in figure 2.3(cns) is characterized by the time scale  $\tau_a^v = (v/a^2)^{1/3} = O(10^{-5})$  s dictated by full dissipation of hydrostatic energy due to acceleration  $a$  into heat, i.e.  $\rho a l^4 \sim \tau \mu (V/l)^2 l^3$  with  $V \sim V_v^l \sim v/l$  and  $\tau \sim l/V_v^l$ . These values of  $\tau_a^v$  imply that undulations driven, for example, by acceleration-induced instabilities (including those due to SW-free interface interactions leading to a Richtmyer-Meshkov instability) are suppressed by viscous dissipation because  $\tau_a^v \ll \tau_a^d$ , where  $\tau_a^d = (R_0/a)^{1/2}$  is the loading time scale it would take for a drop to be smashed by the membrane provided all other forces are negligible. Second,

the time scale of full dissipation of the surface energy into heat<sup>5</sup> is  $\tau_\sigma^v = \nu^3/\gamma^2 = O(10^{-5})$  s, i.e. short-wave capillary undulations are quickly suppressed by viscous dissipation; here  $\gamma \equiv \sigma/\rho$ . In the crown without splash regime viscous dissipation effects on the capillary-induced undulations and velocity defects persist to later times as suggested by the time scale  $\tau_\sigma^{v,d} = \nu R_0/\gamma = O(10^{-3})$  s it takes for the velocity defect  $\gamma/\nu$  to propagate through the drop of size  $R_0$  compared to that of  $\tau_\sigma^v$  required to propagate through a boundary layer  $l_\sigma^v$ . This explains why the crown stays smooth, despite that dissipation of inertia into heat on the drop lengthscale  $R_0$  is still too slow since  $\tau_\sigma^d = R_0^2/\nu \sim O(10^{-1})$  s.

### 2.1.3.3 On the crown formation: basic physical processes

In addition to the hydraulic jump phenomena leading to ejecta as a precursor of the crown formation discussed in §2.1.3.1, to understand the origin of the various observed drop deformation regimes, let us start with the simpler, seemingly naive, question as to why a drop spreads out in sidewise motion, cf. figure 2.5b. To that end let us consider first a simpler situation when a liquid cylinder of radius  $r$  strikes a rigid solid as in figure 2.11. First, using Newton's second law the characteristic pressure experienced is determined from the fact that the mass  $\rho \pi r^2 c dt$  accelerates in time  $dt$ , and thus the force acting during time  $dt$  (momentum change) is  $\rho \pi r^2 c V dt$ , producing the initial water hammering pressure on the order of  $\rho c V$  (Joukowsky, 1899; von Karman, 1929)<sup>6</sup>, which is the same pressure as that in an acoustic wave (Landau & Lifshitz, 1987). The high pressures result from the fact that, although the whole area of the head of the cylinder impacts against the solid, only the liquid at the edge is free to flow initially, and the liquid at the center remains compressed until

---

<sup>5</sup>To find  $\tau_\sigma^v$  note that from the normal dynamic boundary condition at the free interface we find  $\sigma/l \sim \mu V/l$ , which for the velocity change due to viscosity  $V \sim V_\nu^l \sim \nu/l$  over some distance  $l$  yields the length scale  $l_\sigma^v$  which can be interpreted as follows. If surface energy equilibrates with the viscous dissipation  $\sigma l^2 \sim \tau \mu (V/l)^2 l^3$ , where we estimated viscous dissipation rate as  $dE/dt \sim \mu |\nabla \mathbf{v}|^2 \times \text{Volume}$  and took  $V \sim V_\nu^l \sim \nu/l$  along with  $\tau \sim l/V_\nu^l$ , then  $l = l_\sigma^v$  is the size at which surface energy completely dissipates into heat (namely, one takes the initial state at rest,  $V = 0$ , deforms the liquid body of size  $l_\sigma^v$ , and then surface tension deforms the liquid body into an equilibrium shape dissipating energy into heat). Also  $l_\sigma^v$  shows the thickness of the layer where the velocity defect  $V_\sigma^v = l_\sigma^v/\tau_\sigma^v = \gamma/\nu$ , i.e. when the velocity changes from that in the bulk to the interface, is observed. The associated time scale  $\tau_\sigma^v = l_\sigma^v/V_\sigma^v$  is the time required for the surface energy to fully dissipate into heat.

<sup>6</sup>The use of von Karman's formula is justified as opposed to water hammer and drop impact experiments where entrapped air leads to the air cushioning effect lowering the impact pressures.

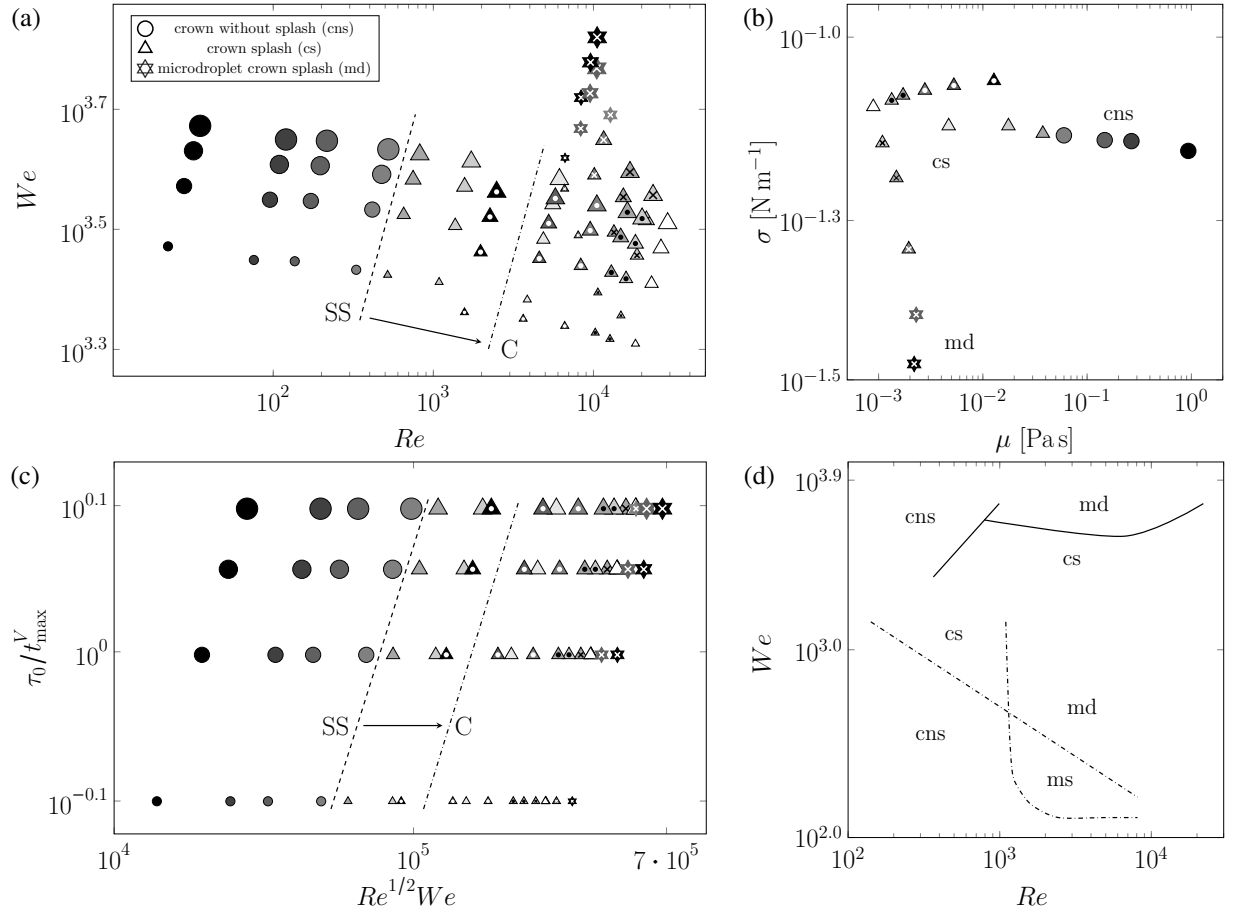


**Figure 2.10:** (a) Map of the observed crown regimes. Thickness of the stainless steel membrane and initial energy were fixed at 0.5 mm and 1000 J, respectively. The shift in the transition boundary between crown without splash and crown splash when the substrate is changed from stainless steel (SS) to copper (C) is indicated by the arrow and the location of a new transition. The liquid drop thermophysical properties were changed as per table 2.1 and volumes were 25, 50, 75 and 100  $\mu\text{l}$ . The leftmost set of data points scales as  $We \approx 134.5 Re$ . (b) The changes in the regimes due to viscosity and surface tension of the utilized liquids. (c) Map of the observed regimes in the non-dimensional time vs  $Re^{1/2} We$ . (d) Regime's boundary map. Solid lines correspond to the boundaries of regimes in the present study. Dashed lines correspond to the boundary of regimes reported by Deegan *et al.* (2008) for drop impact on a thin film.

reached by the release waves from the sides, cf. figure 2.11. As a result, the compressible effects are instrumental in the ability of the fluid initially moving in the direction of the membrane deflection to divert in the membrane plane. If the membrane is smooth, the initial energy can be converted into a radial flow on the surface, in which case a crown fails to form unless the resistance of the surrounding air impedes the radial flow of the liquid (Yakimov, 1973).

To compare and contrast an impulsively driven drop on a membrane with drop impact on solid, let us consider the basic sequence of events with a particular focus on the accelerations experienced

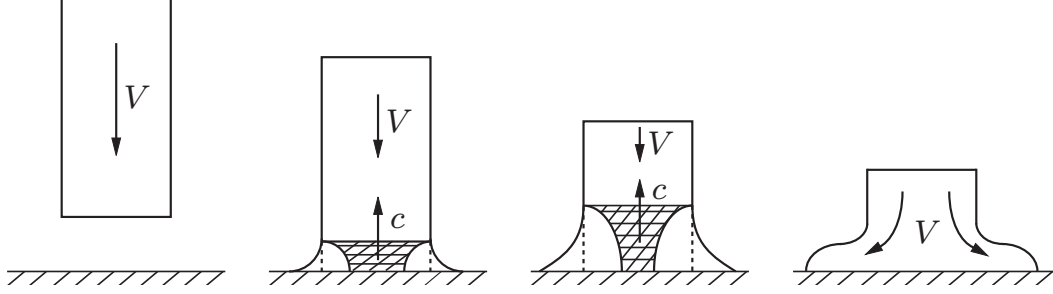


**Figure 2.11:** Impact of a liquid cylinder on solid surface with the shaded areas denoting the liquid still under compression, which is a corrected version due to [Gonor & Rivkind \(1982\)](#) of that originally given by [Bowden & Field \(1964\)](#): the interface of the released liquid should not be convex, but concave as shown in figure 2.11. It can be shown that the release wavelets, which travel inward from the sides at velocity  $c$ , add up to give a curved wavefront, and the released liquid flows out at velocity  $\sim V$  as per the solution of the wave equation for the liquid cylinder impacting with a membrane developed by [Kononkov \(1975\)](#).

by the liquid in both cases, cf. figure 2.12. The initial remarkable observation is that due to a well-developed crown wall (also known as a Peregrine sheet) the splashes occurring in the impulse-driven drops are more typical of crowns in the drop impacts on (thicker) films ([Worthington, 1895](#); [Wang & Chen, 2000](#); [Deegan \*et al.\*, 2008](#)) rather than on solids ([Worthington, 1877a,b](#); [Rioboo \*et al.\*, 2001](#); [Liu \*et al.\*, 2010](#)). First, when the membrane is being accelerated upwards ( $a > 0$ ), the liquid drop flattens into a ‘pancake’ under the action of a suddenly enhanced hydrostatics (figure 2.12a). It is at this stage that the water hammering pressure  $p \sim \rho V_{\max} c$  is experienced by the drop. The pancake thickness  $\eta$ , under the equilibrium conditions  $a = \text{const}$ , would be determined by the balance of hydrostatic and surface energies  $\pi R^2 \eta \frac{1}{2} \rho \eta \sim 2\pi R^2 \sigma$ , i.e. the capillary length  $\eta \sim 2(\sigma/\rho a)^{1/2}$ , which is  $O(10^{-4} - 10^{-5})$  m in our experiments and would result in substantial size pancakes. However, since the acceleration  $a$  is impulsive, the drop does not have time to flatten to such an extent. Next, at the stage of deceleration ( $a < 0$ ), which is important only in the crown regimes as in the higher impulse intensity cases (§2.1.4) the drop attains independence from the membrane, the liquid inertia together with the friction at the contact line and resistance of the surrounding air lead to the pancake deflection at its edge, i.e. ejecta formation which moves at some angle to the substrate. The fluid mass flux into the ejecta is intensified as the membrane moves downward leading to the crown formation. The origin of ejecta can also be understood from the fact that the substrate vertical displacement necessarily moves the fluid upwards with velocity  $V$ , while the built up pressure

$p \sim \rho V c$  at the center of the drop contact with the membrane pushes the fluid sidewise. This explains why the ejecta travels with the speed  $v_e$  exceeding that of impact  $V_{\max}$ , e.g. for the impact conditions in figures 2.13a and 2.13b (45% glycerol solution)  $V_{\max} \approx 9 \text{ m s}^{-1}$ , while  $v_e \approx 17 \text{ m s}^{-1}$ . The same phenomena also occur in the drop impact on a liquid layer (Thoroddsen, 2002).

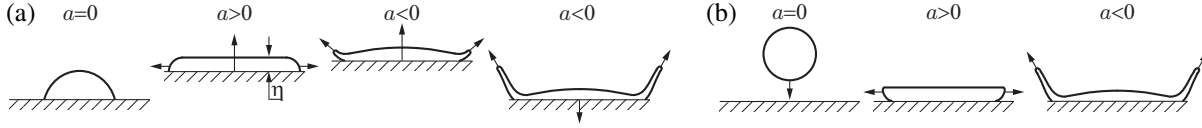


**Figure 2.12:** Sequence of events illustrating the crown formation (a) relative to the membrane motion in the impulse-driven drop and (b) relative to the stationary solid surface in the drop impact experiments.

In the case of impact of a drop of radius  $R_0$  on solid with velocity  $V$  (figure 2.12b), the liquid first experiences crashing ( $a > 0$ ), which flattens it similar to the drop on membrane, and water hammering pressure  $p \sim \rho V c$  develops. In the absence of air phase, the deceleration  $a$  during crashing is dictated by the liquid compressibility  $a \sim cV/R_0$ . However, in reality this deceleration is substantially reduced and the time instant of its maximum value  $a_{\max}$  is varied due to air trapped between the drop and solid surfaces, as is also known in water impact experiments (Mayer & Krechetnikov, 2018). Thus the time scale of acceleration  $a(t)$  in the drop impact is determined by air cushioning, while in the impulse-driven drop by the impulse intensity  $E/h_0$  and the membrane natural frequency  $\omega_M$ .

#### 2.1.3.4 Effects of viscosity, surface tension, and impact intensity on the crown dynamics

To study quantitative changes of the radius  $R$ , height  $H$ , and instability wavelength  $\lambda$  of the crown, image processing codes were developed, which automatically detect the edge and process it into the dynamical data. To investigate the radius changes of the crown, we used the top view as in figure 2.4. Representative choices of liquid mixtures and energies leading to the crown regimes are shown in figures 2.13 and 2.16. To understand the effects of viscosity and surface tension in the stage of crown evolution, changes of the non-dimensional rim radius with respect to non-dimensional time are demonstrated in figures 2.13a, 2.13c and the crown height in figures 2.13b, 2.13d. The crown height trajectory – the distance from the rim edge to the substrate – was measured only up to its

reaching the maximum, since we analyzed the crown dynamics only in the first impact period, cf. figure 2.12a. The subsequent crown height decrease is due to a combination of two factors: decrease in the crown height and upward substrate movement (second oscillation). In the case of the crown radius measurement we extracted data until the complete collapse of the crown wall. Notably, figure 2.13d shows substantial variation in achieved maxima between water and ethanol as opposed to figure 2.13b for glycerol solutions.

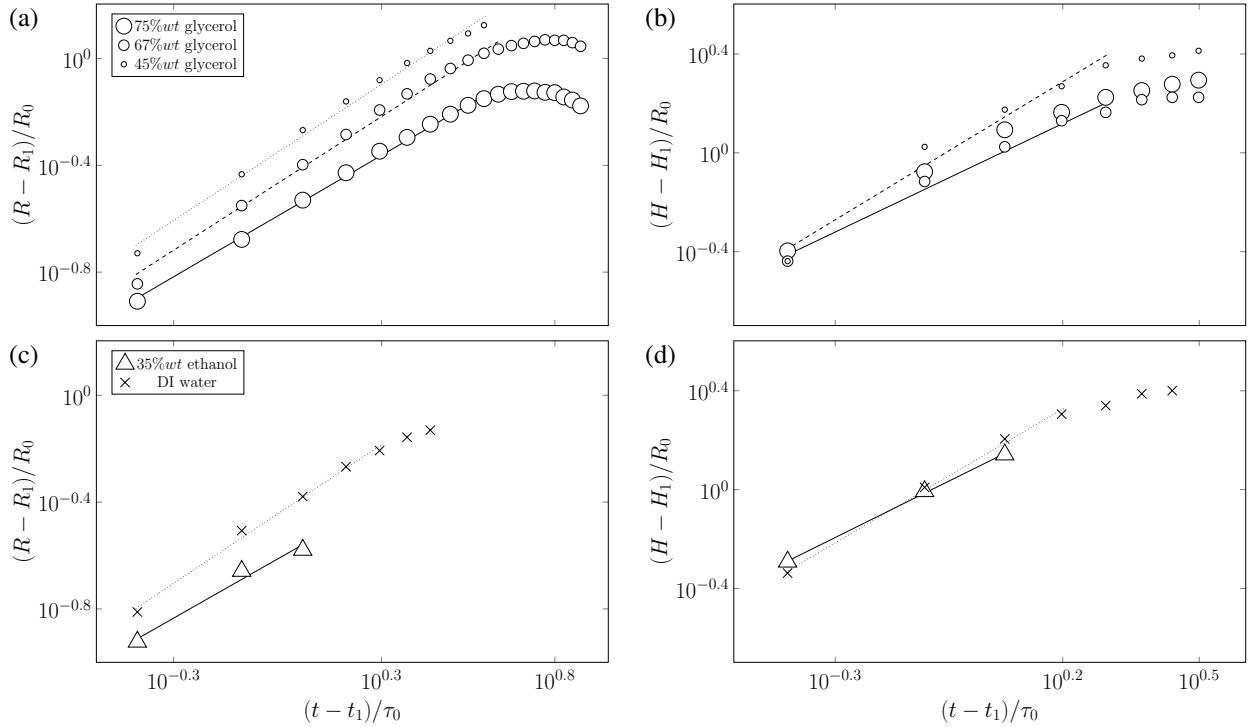


**Figure 2.13:** Log-log plots of non-dimensional rim radius (left) and height (right) vs non-dimensional time for water-glycerol solutions (a,b), and 35% wt water-ethanol and DI water (c,d). Recording of the crown radius was stopped at the disintegration of the crown wall. In the cases when the crown radius evolution with respect to time is non-monotonic (a), data fits were performed up to the end of the monotonic regime before reaching the maximum radius. For the crown height measurement, data were recorded up to the end of the first impact period, cf. figure 2.12a. The thickness of the stainless steel membrane, the initial energy, and liquid drop volume were fixed and equal to 0.5 mm, 1000 J and 50  $\mu$ l, respectively. In (a,b) patterns are cs for all concentrations, in (c,d) cs in DI water and md in 35% wt water-ethanol solutions. All curves are shifted to the origin by subtracting first data point ( $t_1/\tau_0$ ,  $R_1/R_0$ , and  $H_1/R_0$ ) in each set. The crown height dynamics are shown only up the maximum point since after that the membrane is in its second oscillation.

Data acquired from experiments seem to follow a power-law, but simple plotting in log-log axes would not work as the fit function  $y = ax^b$  is applicable only when the data either pass through the origin or behave hyperbolically, i.e. when  $b < 0$ . Therefore, only after shifting to the origin by

subtracting the first data point from each data set, data were fitted with a power-law function  $y = ax^b$ , where the values of  $a$  and  $b$  are found through the least square fit procedure. Fittings in figures 2.13a,2.13c were performed for the data points, which follow the power-law behavior. Similarly, in figures 2.13b,2.13d fittings were performed before the bend at the end of each data set. It is notable that, as per figure 2.15b, radius  $R(t)$  evolves closer to a linear fashion  $\alpha_R = 1$  characteristic of a ballistic regime as predicted by Peregrine (1981), though in a different context (drop impact on a solid surface), but with increase of viscosity or decrease of surface tension  $\alpha_R$  reduces closer to  $1/2$  empirically suggested by Yarin & Weiss (1995) in the drop impact experiments. The ballistic limit comes simply from the horizontal trajectory of the ejected (with non-zero initial velocity  $U_0$ ) fluid particles in the gravity field, when other forces are negligible. As for the limit  $\alpha_R = 1/2$ , it can be explained by the dynamics of the liquid sheet, whose mass is increasing with time, i.e. increasing inertia of the crown liquid sheet slows down its evolution. As a model, let us consider the 1D liquid sheet of thickness  $h_\infty$  at the rim of which there is a blob of mass  $M_r(t) = M_{r0} + \rho h_\infty x(t)$ , i.e. growing with time due to accumulation of the film mass into the blob as it travels the distance  $x(t)$  from the initial position. This growth may be due to surface tension forces pulling the blob towards the sheet as in the retracting soap film problem (Taylor, 1959b; Culick, 1960) and/or due to mass flux into the ejecta sheet due to splash as in the drop impact. Newton's second law then leads to the following initial value problem:

$$\frac{d}{dt} \left[ M_r(t) \frac{dx}{dt} \right] = 2\sigma; \quad x(0) = 0, \quad \frac{dx}{dt} = U_0, \quad (2.4)$$

the solution of which is  $x(t) = \left[ -M_{r0} + (M_{r0}^2 + 2\rho h_\infty M_{r0} U_0 t + v_{TC}^2 t^2 \rho^2 h_\infty^2)^{1/2} \right] / \rho h_\infty$ , reducing to the form assumed by Yarin & Weiss (1995) if  $\sigma = 0$ . Also, if  $t \gg M_{r0}/(\rho h_\infty U_0)$ , the trajectory reduces to a pure power-law  $\sim t^{1/2}$ . Therefore, decreasing surface tension, by replacing a water drop with a 35%-ethanol one, makes  $\alpha_R$  approach the value  $1/2$  as in figure 2.17b. If  $M_{r0}$  is negligible, then  $x(t) \sim v_{TC} t$  in accordance with the Taylor (1959b)-Culick (1960) theory.

As follows from figure 2.13a, increasing viscosity allows the rim radius  $R$  to reach a maximum value  $R_{\max}$  and then to decrease with time before the crown disintegrates. This non-monotonic

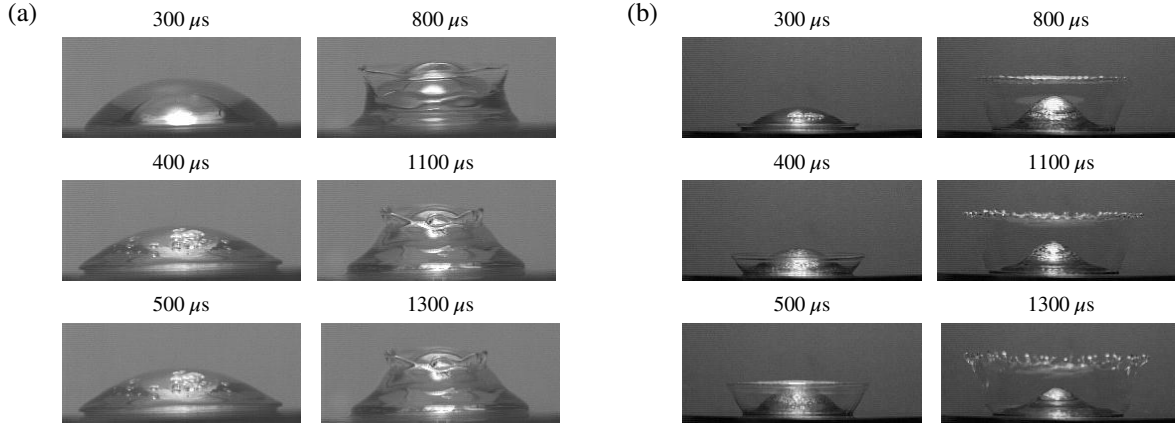


**Figure 2.14:** Non-monotonic (a) and monotonic (b) crowns. Physical image size:  $12.6 \times 5.3 \text{ mm}^2$  (the left column) and  $21.8 \times 9.1 \text{ mm}^2$  (the right column). In both cases initial energy, stainless steel membrane thickness, and liquid drop volume were 1000 J, 0.5 mm, and  $50 \mu\text{l}$ , respectively. Time sequence in (a) corresponds to experiment with 99.5% glycerol and (b) to 10% wt water-sucrose solution.

crown regime (figure 2.14a) implies that after some time the radius of the lower part of the crown, which is laid on the substrate, is larger than the rim radius thus making it optically difficult to precisely detect the position of the rim edge. In the other cases the rim radius is monotonically increasing with time until the crown wall has collapsed (figure 2.14b). It should be mentioned that non-monotonic crowns are also observed in 80% wt, 88% wt, 90% wt, and 99.5% wt water-glycerol solutions. At the physical level, the origin of the non-monotonic crowns is due to surface tension forces overcoming the liquid inertia and tending to minimize the crown surface area.

Evolution of the crown height  $H$  shown in figures 2.13b and 2.13d demonstrates monotonic increase with time. To summarize the effects of viscosity and surface tension, maximum non-dimensional radius and height with respect to the splashing parameter  $Re^{1/2}We$  are presented in figure 2.15a. The glycerol solutions in figure 2.15 suggest a retarding effect of higher viscosities compared to the lower viscosity liquids (water) operating in the ballistic regime, when  $\alpha_R$  is closer to one, cf. figure 2.15b. Lower surface tension of the 35% ethanol solution also brings  $\alpha_R$  down and hence  $R_{\max}$  as well, which is explained by the model (2.4).

The effect of impulse intensity on crown dynamics is shown in figure 2.16. Maximum non-dimensionalized crown radius  $R_{\max}$  and height  $H_{\max}$  with respect to  $Re^{1/2}We$  are summarized in figures 2.17a and 2.17c, respectively. Figure 2.17a indicates that, compared to water, higher viscos-

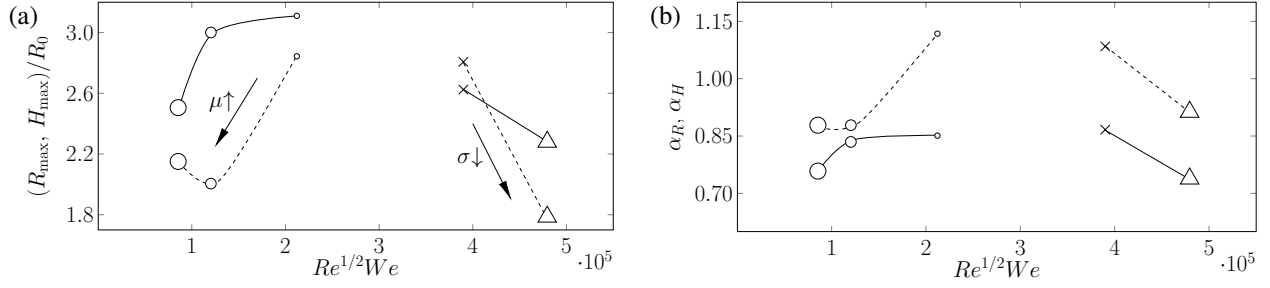


**Figure 2.15:** (a) Maximum non-dimensional radius  $R_{\max}$  (solid) and height  $H_{\max}$  (dashed) achieved during the process of crown evolution vs  $Re^{1/2}We$ . (b) Exponents  $\alpha_R$  and  $\alpha_H$  are the powers of the fitted curves to non-dimensional radius and height:  $\hat{R} = \hat{R}_1 + \beta_R(\hat{t} - \hat{t}_1)^{\alpha_R}$ ,  $\hat{H} = \hat{H}_1 + \beta_H(\hat{t} - \hat{t}_1)^{\alpha_H}$  in figure 2.13. The thickness of the stainless steel membrane, the initial energy, and liquid drop volume were fixed and equal to 0.5 mm, 1000J, and 50  $\mu$ l, respectively. For symbols description see figure 2.13. Solid lines connect the data points for the crown radius and dashed ones for the crown height.

ity leads to larger  $R_{\max}$ , while lowering surface tension decreases it. The same trend is exhibited by  $H_{\max}$  in figure 2.17c. Clearly, both viscosity and surface tension play a significant role in the crown dynamics. Also, as per figure 2.17b, higher energies bring the exponent  $\alpha_R$  closer to one, which is the ballistic limit, while lower energies make  $\alpha_R$  approach the value 1/2. Previous considerations based on model (2.4) explain the lower values of  $R_{\max}$  and  $H_{\max}$  in figures 2.17a and 2.17c. Higher viscosity, on the other hand, slows down the mass flux into the crown sheet thus enabling the ballistic limit  $\alpha_{R,H} \sim 1$ , and therefore higher values of both  $R_{\max}$  and  $H_{\max}$ . However, too high viscosity (at a fixed impulse intensity) retards the crown dynamics as per figure 2.15.

### 2.1.3.5 Wettability effects

The use of different substrates enabled the study of wettability effects. Observation of different regimes for stainless steel and copper membranes at the same  $We$  and  $Re$  numbers indicates a remarkable dependence on the wetting properties of the substrate (membrane) as per figures 2.9a and 2.22a. Figures 2.10a and 2.10c demonstrate a noticeable shift of the transition boundary between crown with and without splash regimes when substrate material changes from stainless steel to copper. Also, experiments showed that increasing the static contact angle  $\theta$  in the microdroplet crown regime drives away from this regime towards the crown with splash regime. Next, figure 2.18 illustrates the effect of the static contact angle on the crown formation pattern for two liquids: 75% wt water-glycerol and 50% wt water-sucrose. The reason for choosing these two solutions is a

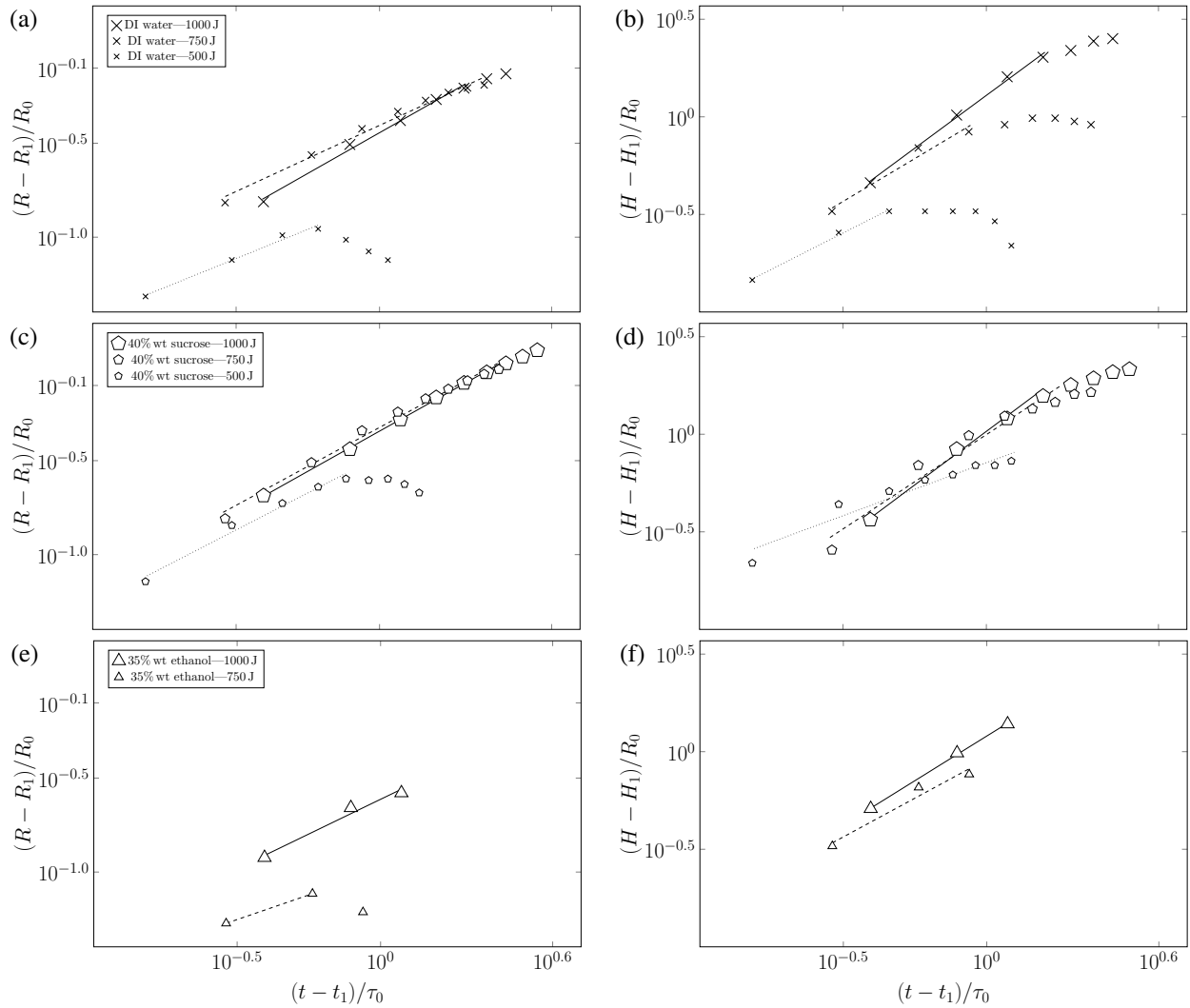


**Figure 2.16:** Non-dimensional log-log plots of crown radius and height for DI water (a,b), 40% wt water-sucrose (c,d), and 35% wt water-ethanol (e,f) vs time for initial energies 500, 750, and 1000J. The stainless steel membrane thickness and liquid drop volume were equal to 0.5 mm and 50  $\mu$ l, respectively. Regimes: (a,b) cns in 500 J and cs in 750 and 1000J, (c,d) cns in 500 J and cs in 750 and 1000J, (e,f) cs in 750 J and md in 1000J. All curves are shifted to the origin by subtracting the first data point in each set.

considerable difference in their contact angle being  $< 90^\circ$  on the stainless steel substrate ( $71^\circ$  for 75% wt water-glycerol and  $86^\circ$  for 50% wt water-sucrose) compared with being  $> 90^\circ$  on the copper substrate ( $103^\circ$  for 75% wt water-glycerol and  $103^\circ$  for 50% wt water-sucrose), cf. table 2.1. On the stainless steel substrate, the crown reaches a larger maximum radius compared to the same liquid on the copper substrate, cf. figure 2.18. Also, on the stainless steel substrate the crown splashes while on the copper substrate it does not. Since, except for the substrate material, all experimental conditions are the same, the considerable difference in the contact angles is deemed responsible

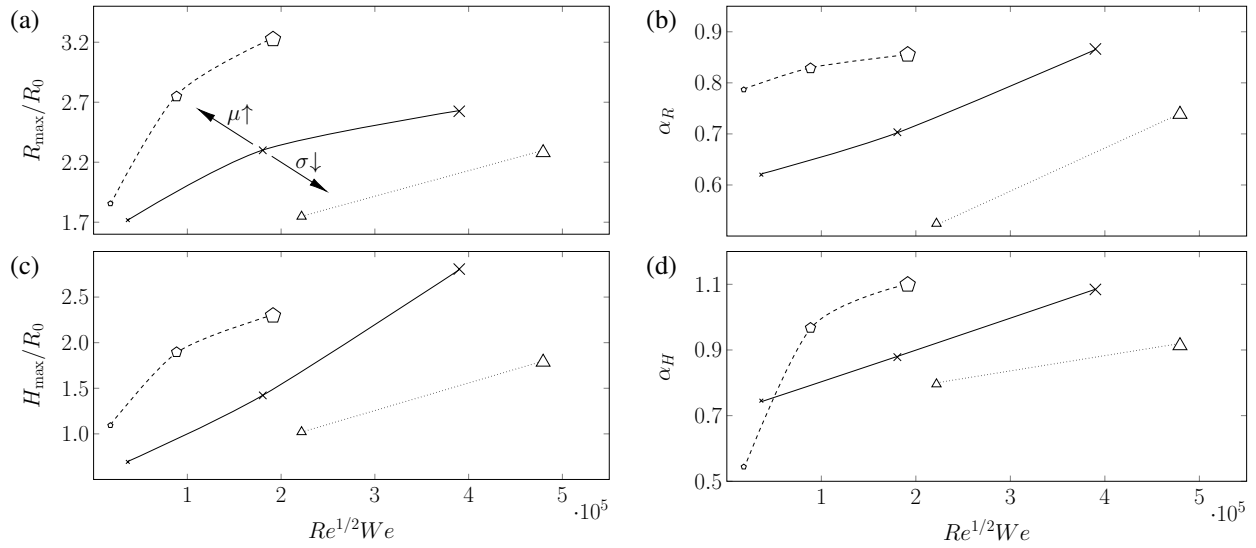


**Figure 2.17:** (a) Maximum non-dimensional radius of the crown vs  $Re^{1/2}We$ . (b) Exponent  $\alpha_R$  is the power of the fitted curve to non-dimensional radius  $\hat{R} = \hat{R}_1 + \beta_R(\hat{t} - \hat{t}_1)^{\alpha_R}$  in figure 2.16, where  $\hat{R} = R/R_0$  and  $\hat{t} = t/\tau_0$ . (c) Maximum non-dimensional height vs  $Re^{1/2}We$ . (d) Exponent  $\alpha_H$  is the power of the fitted curve to non-dimensional height  $\hat{H} = \hat{H}_1 + \beta_H(\hat{t} - \hat{t}_1)^{\alpha_H}$  in figure 2.16. The stainless steel membrane thickness and the liquid drop volume were fixed and equal to 0.5 mm and 50  $\mu\text{l}$ , respectively. The initial energy and the liquid thermophysical properties (with the corresponding symbols) were changed as described in figure 2.16. Connecting lines are provided just to guide the eye.

for the observed effects. Namely, the underlying physical reasons follow from the distinction in the compressible processes at the initial stage of the drop deformation depending upon the contact angle being smaller or larger than  $90^\circ$ , as will be discussed in §2.1.4.2.

The effect of wetting on splashing characteristics has been observed in other situations such as impact of spheres studied by [Duez et al. \(2007\)](#), who established a dependence between a threshold impact velocity for air entrainment and the wetting contact angle. Despite the fact that the contact angle is dictated by microscopic phenomena, the latter have an effect on the macroscopic behavior of the problem, in particular global splashing characteristics as in our case.

### 2.1.3.6 Crown forming instability

As shown in figure 2.19, in early stages of the crown evolution fingers on the rim are very small (400 – 700  $\mu\text{s}$ ). With time, these small fingers detected by our image processing code (cf. Appendix 2.E) merge together and form larger ones (800 – 1100  $\mu\text{s}$ ). Furthermore, close examination of top and side views shows that the crown radius and height grow fast in early stages after impact (400 –

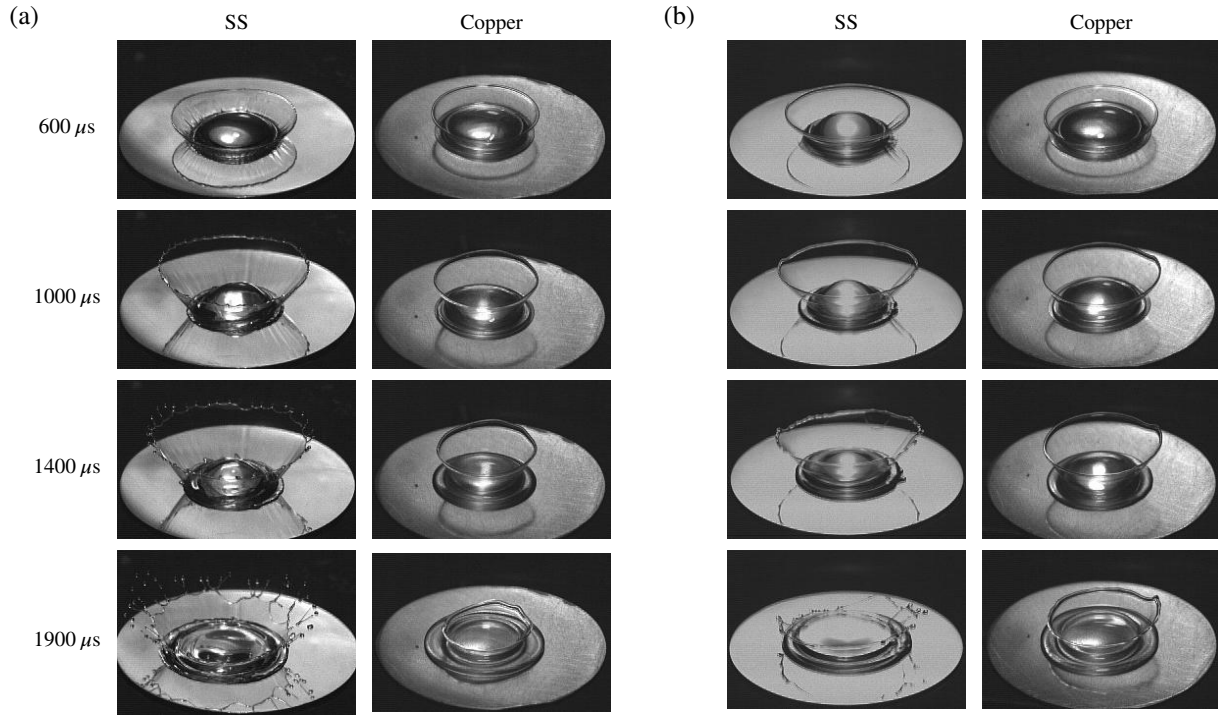


**Figure 2.18:** The effect of contact angle on the crown formation pattern. Figure (a) corresponds to 75% wt water-glycerol and (b) to 50% wt water-sucrose solutions. Left and right columns in each figure show crown evolution on stainless steel and copper substrate, respectively. Thickness of the membrane, initial energy of the capacitors, and liquid drop volume were fixed and equal to 0.5 mm, 1000J, and 50  $\mu$ l, respectively. Physical image size is  $20.3 \times 13.4 \text{ mm}^2$ .

700  $\mu$ s) and remain almost constant in late stages (800 – 1100  $\mu$ s) with the transition happening around 800  $\mu$ s, though the transition time varies for different liquids and test conditions. After this transition, fingers merge to make larger ones while the crown radius does not change considerably. Also, the relatively small rate of change of wavelength  $\lambda = 2\pi R/N$  in early stages (cf. figure 2.20a) seems to result from the change in the number of fingers  $N$  being nearly compensated by growth of the crown radius  $R(t)$ . The latter makes it the problem of pattern formation on a time-dependent domain (Knobloch & Krechetnikov, 2015) – the growing rim of radius  $R(t)$  – with the mechanism responsible for the changes in the number of spikes being the Eckhaus instability. Curve fitting to  $\lambda(t)$  in figure 2.20 was performed for time stamps after the transition time, so that wavelength changes are mainly due to the changes in the number of fingers, but not due to the time-dependence of  $R(t)$ .

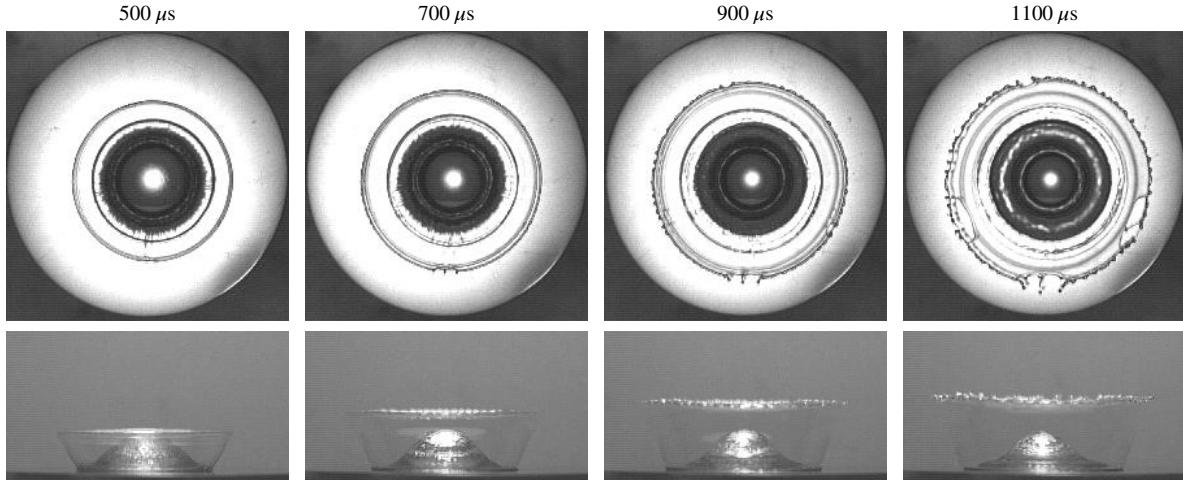


**Figure 2.19:** Crown evolution in 10% wt sucrose from top and side views. The drop volume, the initial energy, and the membrane thickness are  $50 \mu\text{l}$ ,  $1000\text{J}$ , and  $0.5 \text{ mm}$ , respectively. Physical image size in top view images is  $20.0 \times 20.0 \text{ mm}^2$  and in side view images is  $21.8 \times 9.1 \text{ mm}^2$ .

Wavelength evolution in time is presented in figures 2.20a–2.20c. Close examination of these figures shows that in most cases the wavelength is monotonically increasing with the crown radius. In the cases of 67% wt and 75% wt water-glycerol solutions, changes of wavelength with respect to non-dimensional time are slightly nonmonotonic around the times when the maximum radius is achieved per figure 2.13a. As for the impulse intensity effects, notably wavelengths in figures 2.20b and 2.20c show considerable variation as the energy varied twice thus indicating that RT instability due to its dependence on  $a_{\text{max}}$  must be a major player in setting the spike structure.

As discussed in §2.1.3.3, the crowns observed in our experiments are more like the crowns in the drop impacts on thin films rather than on solids. From figure 2.3(cs) we can estimate that the rim radius is  $r_b \sim 0.1 \text{ mm}$ , resulting in the most amplified RP wavelength  $\lambda_{\text{RP}} \approx 2.87\pi r_b = O(1) \text{ mm}$ , i.e. of the order of the measured average wavelength  $\lambda = 0.7 \text{ mm}$  in the same figure. Direct comparison with the instability wavelength measured in the drop impact on a thin layer experiments by Krechetnikov & Homsy (2009) or Zhang *et al.* (2010) is not possible as, for example, in the latter study the measurements were performed at  $Re = 1060$  and  $We = 760$  (and nondimensional film thickness  $h/D_0 = 0.2$ , which is the ratio of the film thickness  $h = 0.35 \text{ mm}$  and the drop diameter  $D_0 = 1.72 \text{ mm}$ ): our experiment with the closest values of  $Re = 1046$  and  $We = 816$  corre-

sponds to the butterfly crown regime instead (50% wt water-sucrose solution, membrane thickness 0.17 mm, and the capacitors energy 250 J).

At the time scale level, the characteristic time of the RP instability  $\tau_{\text{RP}} \sim (\rho r^3 / \sigma)^{1/2} = O(10^{-5})$  s is faster than the crown formation time in figure 2.3(cs) thus enabling the crown spikes to form. Next, the most amplified wavelength of the RT instability  $\lambda_{\text{RT}} = 2\pi (3\sigma / \rho a)^{1/2} = O(10^{-1} - 10^0)$  mm with the associated characteristic time  $\tau_{\text{RT}} \sim (\sigma / \rho a^3)^{1/4} = O(10^{-4} - 10^{-5})$  s also indicate the feasibility of the RT mechanism being responsible for the crown formation. In our context, a RT instability arises when the acceleration  $a$  is directed from the relatively heavy liquid to air<sup>7</sup>. In fact, there are two scenarios when a RT instability may contribute to crown spike formation: when the rim accelerates towards air or when it decelerates from a non-zero initial velocity away from air. In general, the wavelengths estimated above from the RP and RT dispersion relations are within the range of wavelengths reported in figure 2.20. Locally, the crown wall with a rim can be considered as an accelerating liquid sheet experiencing an along-the-edge instability: due to the Einstein equivalence principle the freely accelerating fluid body does not feel the acceleration and hence no hydrostatic pressure is built up, which leads to the stability analysis of [Krechetnikov \(2010\)](#) showing that both RP and RT mechanisms play a role in setting the instability wavelength and cannot be considered as a linear superposition of non-interacting modes. Also, the effects of curvature ([Krechetnikov, 2009](#)) and unsteady acceleration on RT instability as well as the effect of time-dependence of the base state (growing rim) on RP instability ([Krechetnikov, 2017](#)) make the problem less quantitatively compliant with the above scalings, which are adequate only for flat interfaces (RT) and steady circular cylinders (RP).

$$k_{\text{RT}} = k_{\text{RT}}^0 + \nu \rho \sigma^{-1} (32 a k_{\text{RT}}^0 / 27)^{1/2} + \dots, \text{ where } k_{\text{RT}}^0 = (a \rho / 3 \sigma)^{1/2}. \quad (2.5)$$

---

<sup>7</sup>As an example, one can think of a water layer plastered to a ceiling and supported by the atmospheric pressure, but due to the gravity pointing down (towards air) the interface experiences a RT instability ([Sharp, 1984](#)).

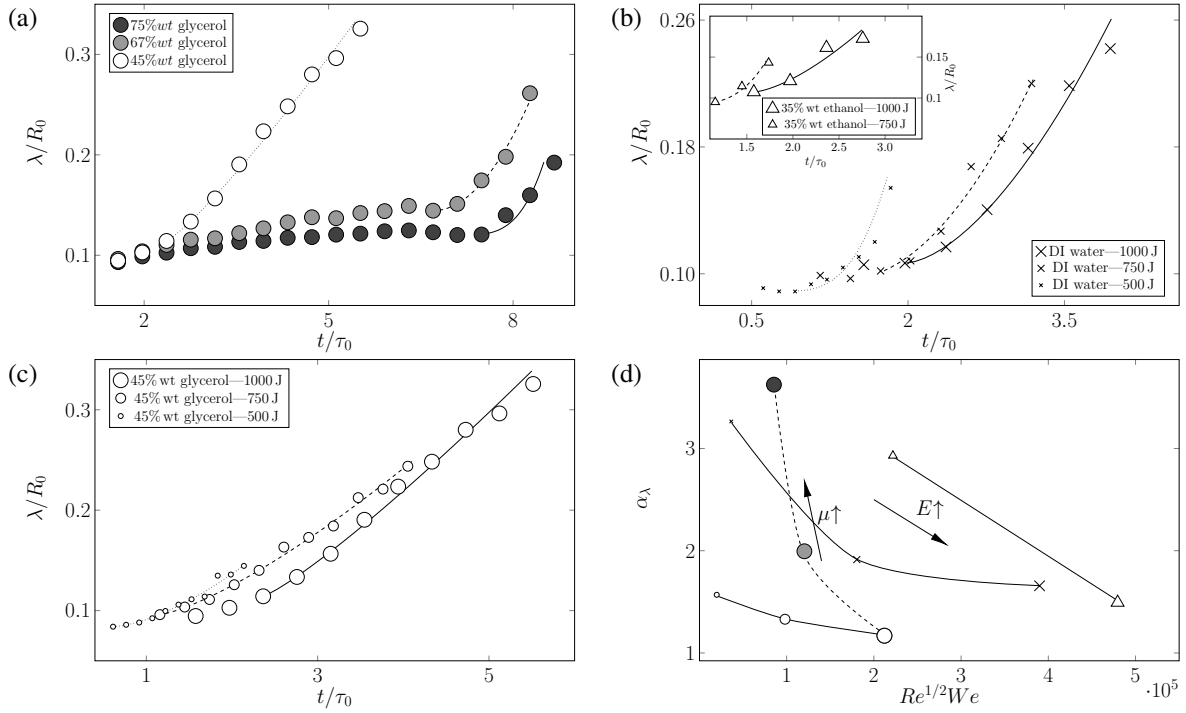


**Figure 2.20:** (a) Log-log plots of wavelength  $\lambda$  scaled with  $R_0 = 2.3$  mm vs non-dimensional time for water-glycerol solution. The initial energy was 1000J. Crown splash was observed in all cases. (b) Log-log plots of wavelength  $\lambda$  vs non-dimensional time for DI water and water-ethanol solutions (inset) for different initial energies. The observed patterns: cns in 500J and cs in 750 and 1000J; inset: cs in 750J and md in 1000J. (c) Log-log plots of wavelength  $\lambda$  vs non-dimensional time for water-glycerol solutions for different initial energies. The observed patterns: cns in 500J and cs in 750 and 1000J. (d) The power  $\alpha_\lambda$  of the fitted curve  $\hat{\lambda} = \beta_\lambda (\hat{t} - \hat{t}_1)^{\alpha_\lambda} + \hat{\lambda}_1$  vs  $Re^{1/2}We$ , where symbols  $\hat{\lambda}$  and  $\hat{t}$  correspond to non-dimensional wavelength  $\lambda/R_0$  and time  $t/\tau_0$ , respectively. Symbols connected by a dashed line correspond to the water-glycerol solutions shown in (a), in which concentration was varied, and symbols connected by a solid line correspond to the cases shown in (b,c), in which energy was varied. In all experiments substrate was made of stainless steel.

For example, the time-dependence of  $\lambda$  apparent from figure 2.20 is a departure from these classical theories. Next, the inset in figure 2.20b for ethanol shows shorter wavelengths compared to water in accordance with the RT mechanism, since  $\lambda_{RT} \sim \sigma^{1/2}$ . However, increase of  $\lambda$  with impulse intensity and hence with  $a_{\max}$  does not conform with  $\lambda_{RT} \sim a^{-1/2}$  for a flat interface base state, suggesting that the base state time-dependence, curvature and interaction with the RP mechanism are the dominant factors. Finally, increasing viscosity shortens the instability wavelength, cf. figure 2.20a, which is similar to the RT instability in the presence of viscosity enlarging the most amplified wavenumber  $k_{RT} = 2\pi/\lambda_{RT}$  (Plesset & Whipple, 1974). Indeed, the analysis of the dispersion

relation from §2.1.3.1 in the case when both acceleration and capillarity are important yields the following (positive) correction to the most unstable wavenumber:

## 2.1.4 Results: drop disintegration regimes

### 2.1.4.1 Key disintegration regimes and transitions

Increasing the impulse intensity even more brings us to the drop disintegration regimes, in which we include butterfly crown splash (figure 2.21a) when more than half of the original drop disintegrates, as well as cupola (figures 2.21b and 2.21c) and direct atomization (figure 2.21d) both characterized by complete disintegration of the drop. The retarding effects of viscosity become especially pronounced in the most intense regime: as evidenced in first column of figure 2.21d, increasing the viscosity reduces the number of microdroplets in early stages and consequently the drop breaks into microdroplets in later stages. As noted by Kedrinskii *et al.* (2005), on the one hand it is known that the presence of viscosity leads to the dissipation of energy in a liquid, but on the other hand it is still a question what precisely changes in the structure of the flow as viscosity varies: e.g. compare the atomization patterns for different liquids in figure 2.21d.

Next, let us apply the time scales following from a dimensional analysis (table A2.3 of Appendix 2.C) to the transitions in the higher impulse intensity regimes in figure 2.9b. Clearly, both the viscous  $\tau_v^d = R_0^2/\nu$  time scale required for viscous effects to propagate through the drop and the surface tension  $\tau_\sigma^d = (R_0^3/\gamma)^{1/2}$  time scale of small<sup>8</sup> (natural) oscillations of the drop do not play a role in our phenomena, because they are longer than the loading time scale  $\tau_a^d$ . This suggests that acceleration  $a$  should be a governing variable, which leads to the time scale  $\tau_a^\sigma = (\gamma/a^3)^{1/4}$  it takes to transfer hydrostatic energy (due to acceleration) into surface energy<sup>9</sup> (i.e.  $\rho a l^4 \sim \sigma l^2$  naturally yielding the associated capillary length  $l = l_a^\sigma \sim (\gamma/a)^{1/2}$  and time  $\tau_a^\sigma$  scales) and the time scale  $\tau_a^\nu = (\nu/a^2)^{1/3}$  introduced earlier, plotted in figures 2.22b and 2.22c, respectively. These figures,

<sup>8</sup>so that the actual kinetic energy value is not important;  $\tau_\sigma^d$  is also a period of capillary waves of wavelength  $R_0$  driven by surface tension alone and, coincidentally, the RP instability time scale.

<sup>9</sup>or sets the period of small oscillations when kinetic energy magnitude is not important; notably,  $\tau_a^\sigma$  is also the RT instability time scale.

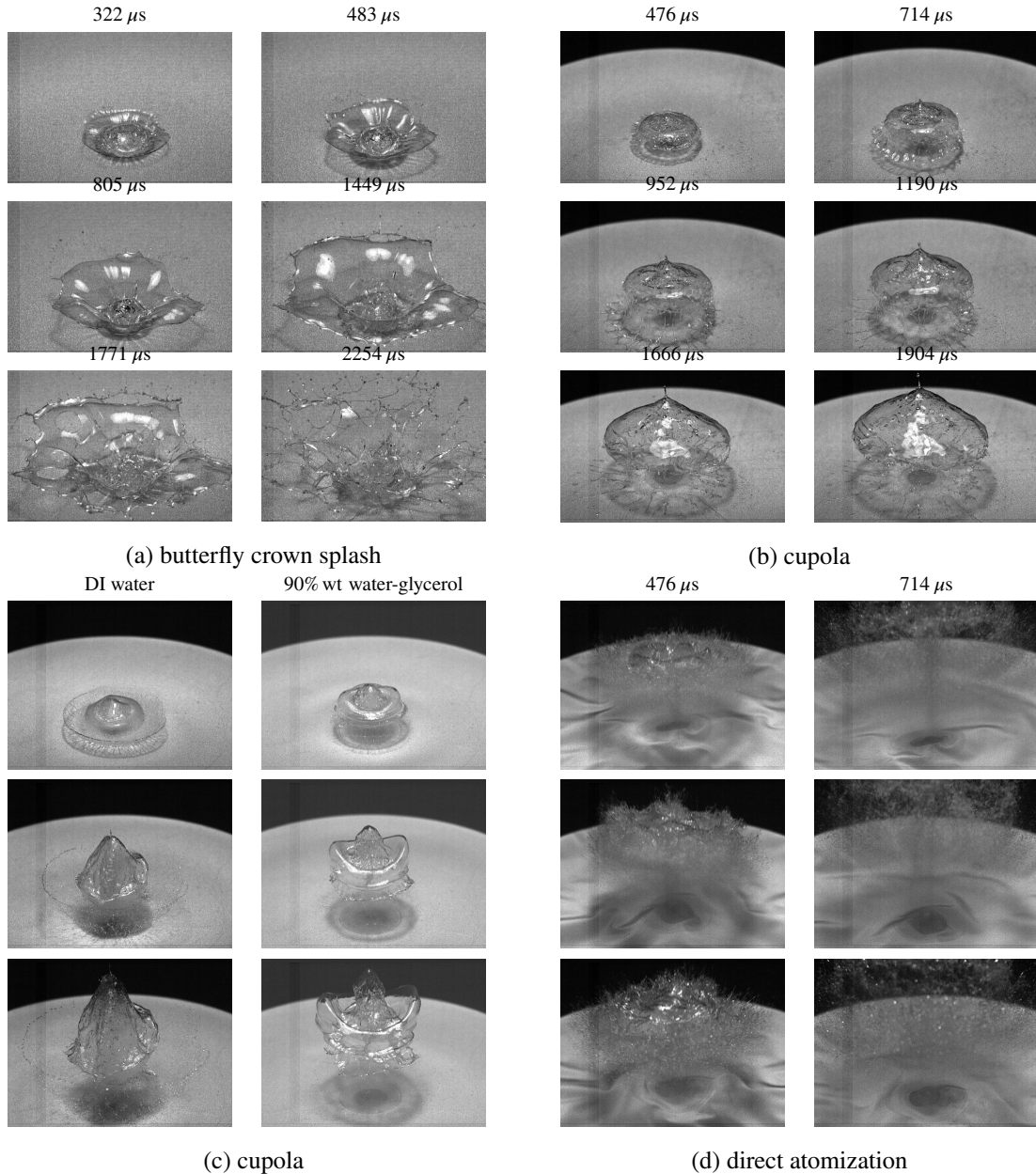


**Figure 2.21:** (a) Butterfly crown splash pattern observed for 67% wt water-glycerol solution. The drop volume, the initial energy, and the membrane thickness are  $50 \mu\text{l}$ ,  $390 \text{ J}$ , and  $0.17 \text{ mm}$ , respectively. Physical image size is  $37.2 \times 25.1 \text{ mm}^2$ . (b) Cupola pattern in 50% wt water-sucrose solution. The drop volume, the initial energy, and the membrane thickness are  $50 \mu\text{l}$ ,  $500 \text{ J}$ , and  $0.17 \text{ mm}$ , respectively. Physical image size is  $47.0 \times 31.7 \text{ mm}^2$ . (c) Cupola patterns observed in different experiments. First to third rows correspond to  $476$ ,  $714$ , and  $952 \mu\text{s}$ , respectively. In both cases the liquid drop volume, the initial energy, and the membrane thickness are  $50 \mu\text{l}$ ,  $500 \text{ J}$  and  $0.1 \text{ mm}$ , respectively. Physical image size is  $47.0 \times 35.3 \text{ mm}^2$ . (d) Direct atomization patterns observed in different experiments. First to third rows correspond to DI water, 22% wt water-ethanol and 67% wt water-glycerol, respectively. In all cases the liquid drop volume, the initial energy, and the membrane thickness are  $50 \mu\text{l}$ ,  $1000 \text{ J}$  and  $0.034 \text{ mm}$ , respectively. Physical image size is  $47.0 \times 35.3 \text{ mm}^2$ .

while indicating that both viscous  $\tau_a^v$  and surface tension  $\tau_a^\sigma$  time scales play a role in defining the transitions between the crown regimes, do not demonstrate a monotonic behavior unless combined

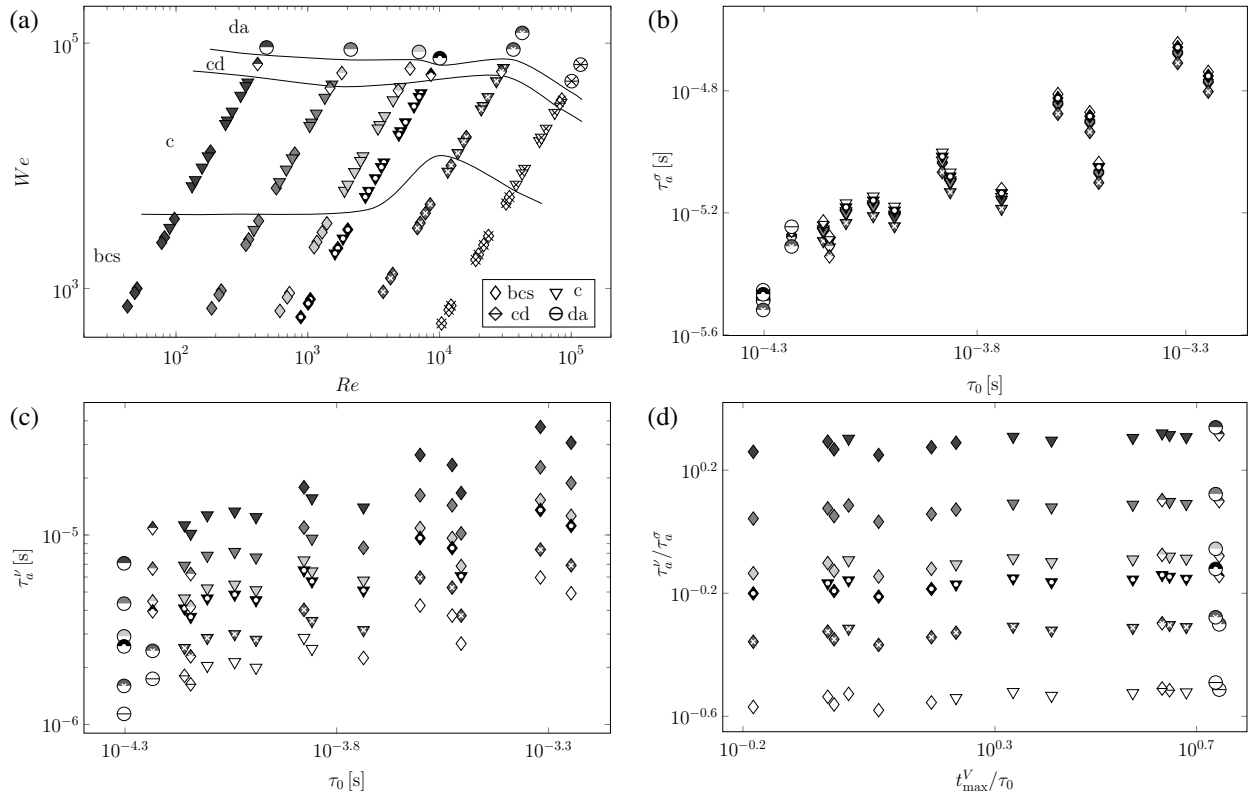


**Figure 2.22:** (a) Map of high intensity impulse cases when a liquid drop of volume  $50 \mu\text{l}$  was placed directly on the copper membrane of three different thicknesses (0.17, 0.1, 0.034 mm) agitated at five initial energies (250, 390, 500, 750, and 1000 J): *patterns* are distinguished by different symbols according to the legend. For the regime definitions and illustrations refer to figure 2.3; cd refers to cupola-to-direct atomization transition. The symbols and shadings used are identical to those defined in figure 2.9a. DI water, 90% wt water-glycerol, 80% wt water-glycerol, 67% wt water-glycerol, 50% wt water-sucrose and 22% wt water-ethanol solutions were employed. The corresponding time scale plots: (b)  $\tau_a^\sigma$  vs  $\tau_0$ , (c)  $\tau_a^\nu$  vs  $\tau_0$ , (d)  $\tau_a^\nu/\tau_a^\sigma$  vs  $t_{\max}^V/\tau_0$ .

as in figure 2.22d: using the ratios  $\tau_a^\nu/\tau_a^\sigma$  and  $t_{\max}^V/\tau_0$  brings in not only reasonably monotonic transitions from the butterfly crown splash to direct atomization through the successive intermediate regimes, but also shows that  $\tau_0 = R_0/V_{\max}$  is of the same order as the measured  $t_{\max}^V$  and thus is an appropriate parameter to be used throughout the discussion. The slight non-monotonic behavior of  $t_{\max}^V$  in the inset of figure 2.2b, which is due to the particularities of the membrane dynamics<sup>10</sup>, proved to be crucial for organizing the data in figure 2.22d in a monotonic order.

Similar to the crown without splash regime, early stages of the butterfly crown splash and cupola, cf. figure 2.3, are characterized by short time scales  $\tau_a^\nu = O(10^{-5})\text{s}$  meaning that undulations

<sup>10</sup>While the pressure on the membrane  $\sim E/h_0$  is monotonic along the abscissa in the inset of figure 2.2b, the membrane response depends on  $h_0$ .

driven, for example, by acceleration-induced instabilities are suppressed by viscous dissipation. Also,  $\tau_\sigma^v = O(10^{-6})$  s, i.e. short-wave capillary undulations are suppressed by viscous dissipation in the butterfly crown regime, but not in the cupola one since the liquid is fractured. As opposed to the crown without splash regime, in which viscous dissipation effects persist to later times as suggested by  $\tau_\sigma^{v,d} = O(10^{-3})$  s, this does not happen in the butterfly crown and cupola regimes. Notably, while hydrostatic (due to acceleration) energy is readily transferred into surface energy in all the regimes, since it happens on relatively short length scales  $l_a^\sigma = O(10^{-5})$  m which are allowed only in the most intense regimes, this process is relevant from the microdroplet generation regime onward, i.e. when small enough droplets are generated. The length scale  $l_a^\sigma$  is analogous to  $l_V^\sigma = \sigma/\rho V^2$ , which is the ratio of surface and kinetic energies, so if  $l_V^\sigma \ll R_0$ , then atomization takes place if permitted by other effects (e.g. if viscous dissipation is insignificant).

#### 2.1.4.2 On the origin of cupola

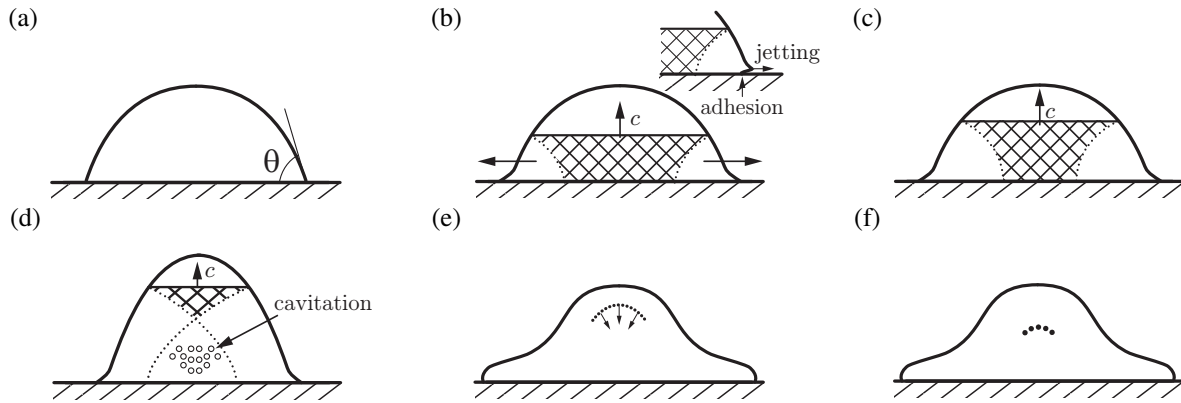


**Figure 2.23:** SW propagation through an impulsively-driven drop sitting on a membrane: (a) initial condition with the contact angle  $\theta < 90^\circ$ , (b) jetting occurs and continues (c) with the liquid next to the membrane being affected by friction/adhesion, (d) cavitation, (e) reflected SW focusing in (f) in analogy to [Camus \(1971\)](#). The SW front is flat in parts (a-d) because the drop is wider at the bottom (hydrophilic case). Note that the top (above SW) in parts (a-d) has the same shape as it is not yet affected by the SW. In the above picture we neglected the shock wave passing around the drop in air, since, as noted by [Joseph et al. \(1999\)](#) in the context of aerobreakup experiments, the passage of the shock over the drop has no important influence on the breakup.

*Early stages.* While compressible effects proved to be instrumental in the initial stages of the drop deformation (§2.1.3.3), upon intensification of the driving impulse new compressible phenomena occur. Figure 2.23 develops a characteristic sequence of events as a SW created by a sudden

motion of the membrane with speed  $V$  propagates through a drop sitting on a dry surface. Initially, the pressure and density in the water drop are dictated by the ambient pressure and the contact angle  $\theta$ , cf. figure 2.23a. Immediately upon impact, a strong shock wave is created and moves upward, cf. figure 2.23b, similar to that when a liquid cylinder strikes a rigid solid, cf. figure 2.11. The SW propagating in the drop compresses it. Next, depending upon the contact angle of the drop with the membrane, there are two possible scenarios. If the drop liquid is not wetting,  $\theta > 90^\circ$ , the edge velocity is higher than the shock speed throughout this initial stage: thus, the SW remains attached to the contact periphery, typically within a few nanoseconds (figure 2.24a).

The pressure at the center of the impact is the “water hammer” pressure  $p = \rho c V$ , which in our experiments reaches  $O(10)$  MPa, consistent with the EM pressure  $p_{\max}$  estimated from the measured current  $I_{\max}$  (Appendix 2.B). However, there are even higher pressures at the expanding contact edge, since the wavelets (see figure 2.24a) bunch up in this region, and these reach a maximum value of about  $3\rho c V$  just before the shock envelope overtakes the contact edge (Lesser, 1981). After this time, the edge velocity decreases below the shock velocity. Once the shock detaches and moves up along the free surface of the drop, cf. figure 2.24b, release waves travel into the drop interior and jetting commences. The elastic energy in the compressed liquid (the shaded areas in figure 2.23) is gradually transformed into kinetic energy of the lateral flow, and the contact pressures must decrease. One important trait of the phenomena is that the high-velocity jet is ejected only from the contact edge, which is not necessarily obvious, since the traveling shock wave carries high pressure along the entire free surface and one might expect that jetting would occur everywhere on the free surface after the shock passage. The latter does not happen due to the mentioned above expansion wave adjacent to the free surface, which rapidly lowers the high pressure carried by the shock and inhibits jetting across the free surface. The only region in the drop where the pressure remains high and can produce sustainable jetting is the zone at the contact edge, cf. figure 2.24b. The release waves superpose when they cross, bringing the liquid into a tensile-stress state, cf. figure 2.23d. The presence of low pressure, indicating strong rarefaction in the middle of the drop, could produce cavitation. In figure 2.23 we considered the case  $\theta < 90^\circ$  and thus assumed regular SW reflection

throughout the entire process of SW propagation, i.e. when rarefaction waves arising on the free surface do not disturb the front of the SW because they cannot outrun their source (Berezin & Grib, 1960), cf. Appendix 2.D. For wetting angles  $\theta > 90^\circ$  reflection initially may be irregular (Mach), but becomes regular at later stages (due to the drop convex shape).

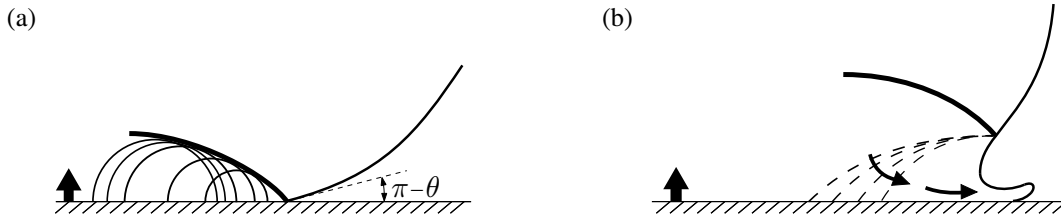


**Figure 2.24:** Supersonic (a) and subsonic (b) regimes of the drop-solid interaction with initial contact angle  $\theta_0 > 90^\circ$ . Initially (a), the perimeter of the liquid/solid interface moves tangentially outward at a speed which exceeds the velocity of propagation of the shock wave (solid) generated by the impact. The resulting shock front, therefore, remains attached to the solid surface and the compressed liquid, being bounded entirely by the solid surface on one side and by the shock front separating it from undisturbed liquid on the other, cannot flow out. It is only when the shock wave overtakes the interface perimeter, and reaches a free surface, i.e., when the shock front becomes detached (b), that lateral flow is able to begin. Namely, when the edge advance falls below the wave speed the shock leaves the impact plane and a system of expansion waves (dashed) now connects the undisturbed regions with the free edge which forms a jetting motion.

*Late stages.* The SW propagating upward reaches the drop upmost point, where it is reflected downward in figure 2.23e and becomes a rarefaction wave (cf. Appendix 2.G), which travels in the compressed drop and unloads it providing a rapid decompression leading to negative pressures and thus to cavitation<sup>11</sup>, e.g. in figures 2.14 and 2.14a. It should be emphasized that at the free surface, the SW is reflected normal to the surface as an expansion (rarefaction) wave, which focuses in the inner region of the water drop, cf. figure 2.23f. Such occurrence of a focused rarefaction wave in the middle of the drop has been observed experimentally by Field *et al.* (1989) in the 2D drop impacts.

<sup>11</sup>While the classical nucleation theory predicts (Caupin, 2005) that water can get to as low a pressure as  $-100$  MPa due to its strong cohesion, the cavitation bubbles are still observable in our experiments despite much lower  $O(10)$  MPa water hammering pressure. Therefore, as to the origin of cavitation, strength of liquid under dynamic loading is not as certain a phenomenon as that of solid strength due to the presence of micro-inhomogeneities in the form of gas bubbles, solid particles, and fluctuating density “holes” (Frenkel, 1955), which serve as cavitation nuclei. For example (Strasberg, 1956), DI water contains about  $10^4 \text{ cm}^{-3}$  of micro-bubbles of characteristic size  $1.5 \mu\text{m}$  with volume fraction of  $10^{-12} - 10^{-8}$ . While presence of these micro-bubbles does not have appreciable effect on shock wave propagation, when there are tensile stresses the cavitation nuclei start expanding increasing the volume fraction by 5 – 6 orders in less than a microsecond. The problem of liquid fracture in intense rarefaction waves formed as a result of explosive loading of a liquid with a free surface reduces to determining a *critical tensile stress*  $p_*$  allowed by the cavitating liquid. For settled tap water  $p_* = -0.85$  MPa, for DI water  $-1.5$  MPa (Wilson *et al.*, 1975), which explains, when compared to the  $O(10)$  MPa pressure experienced in our experiments, the presence of cavitation bubbles.

Also, a contributing factor is a SW curving (§2.1.3.3) which in the cupola regime follows the shape of the drop interface upon approaching it similar to the SW reflection in the 2D experimental studies by Camus (1971) and Field *et al.* (1989), so that when a SW reflects from the liquid-air interface, it does not lead to breakup of the latter. At higher intensity impulses this fine tuning between the SW and the drop shape no longer takes place and SW interaction with the drop surface leads to its immediate breakup, e.g. via a Richtmyer-Meshkov instability – the direct atomization regime.

In experimental studies of a single (hemispherical) drop disintegration under ultrashort loading (Kedrinskii *et al.*, 1997), it was found that the cavitation zone is a system of microbubbles, inertial development of which leads to formation of cellular-type structures different from the foams with spherical and polyhedral cells. The process of disintegration of this cellular structure can be divided into the following stages (Kedrinskii, 1993): growth of microbubbles leading to formation of cavitation clusters, development of the cavitation clusters until the foam stage establishes, and disintegration of foam via atomization. More specifically, as alluded to by Kedrinskii *et al.* (1997), for the SW of 15 MPa amplitude, in about 25  $\mu\text{s}$ , in the center of the drop one observes formation of a cavitation zone as well as near the membrane, where one can see a cavitation layer linked to the drop's detachment from the membrane. At  $\sim 50 \mu\text{s}$  a relatively large cavity is formed in the drop center. In about 70 – 100  $\mu\text{s}$  the drop transforms in a 'boiling' state assuming a distinct cellular-type structure, at the basis of which are large clusters formed by merging bubbles growing in the straining flow of the growing and deforming liquid network. It is notable that by this stage the drop has not changed its size appreciably and has not traveled much from the membrane. Eventually, the cavitation zone grows due to inertia, forms a cupola with cellular structure comprised of liquid threads connected by a thin film forming a net, and detaches from the membrane around 200  $\mu\text{s}$ , as confirmed by our measurements, cf. figure 2.25a. At the end, this liquid network disintegrates into threads and droplets.

A closely related experimental study is by Stebnovskii & Chernobaev (1987) on the process of disintegration of cylindrical liquid shells under impulsive loading in which they varied the time of loading  $\tau_a^d$  defined by the characteristic parameters of explosion, and fixed the time  $\tau_c^d$  it takes for a

rarefaction wave to travel from the free surface to the explosion cavity. They found that if  $\tau_a^d > \tau_c^d$ , then the liquid volume disintegration is due to perturbation growth at the free surfaces. If, on the other hand,  $\tau_a^d \leq \tau_c^d$ , the disintegration stage is preceded by cavitation bubble growth and cluster formation. In our case, however,  $\tau_a^d = O(10^{-5}) \text{ s} \geq \tau_c^d = O(10^{-6}) \text{ s}$ , while we still observe cavitation bubble formation in the bulk, cf. figure 2.14a.

At the same time, growth of bubble concentration  $\alpha$  in a liquid leads to increased relaxation time of tensile stresses, i.e. the liquid attains new rheological properties and behaves as viscoelastic. It is then natural to suppose that disintegration of such a medium is due to accumulation of elastic energy at which the bubbly medium is no longer stable thus leading to spontaneous formation of discontinuities (cavities) in the regions of elevated bubble concentration  $\alpha$ . Understanding when such bubbly media disintegrate requires comparison of the dynamic loading time  $\tau_a^d$  with the relaxation time  $\tau_{\text{tensile}}$  of tensile stresses. If the liquid volume does not contain cavitation nuclei, then under volume stretching it would accumulate elastic energy. In this case, the time of relaxation of tensile stresses can be estimated as  $\tau_{\text{tensile}} = 10^{-10} \text{ s}$ , cf. table A2.3 in Appendix 2.C. If  $\tau_{\text{tensile}} < \tau_a^d$ , which is the case here as  $\tau_a^d = O(10^{-5}) \text{ s}$ , then in the process of deformation cavitation bubbles would grow: elastic energy of the liquid is spent on the work required for cavitation. If stretching stresses are sufficiently high, nonuniformities in the cavitation bubble concentration  $\alpha$  are characterized by larger relaxation time and hence more intense accumulation of elastic energy, which leads to bubble coalescence and thus void formation.

Formation of cracks in the cavitating media (Stebnovskii & Chernobaev, 1986) is also stipulated by shear stresses, which can grow only if the time of their relaxation  $\tau_{\text{shear}}$  is larger than the characteristic time of shear deformation, which in our case can have a number of origins, but the most relevant one is due to minute surface deformations happening on the time scale  $\tau_\sigma^v = O(10^{-9} - 10^{-10}) \text{ s}$  as per table A2.3. The relaxation time scale can be estimated from  $\tau_{\text{shear}} = \mu_{\text{eff}}/G_\infty$ , where  $G_\infty$  is the dynamic shear modulus and  $\mu_{\text{eff}}(\alpha)$  the effective shear viscosity of a cavitating medium, which increases with the volume concentration of bubbles  $\alpha$ . Hence, even for low viscosity Newtonian liquids, due to bubble concentration growth,  $\tau_{\text{shear}}(\alpha)$  may exceed  $\tau_\sigma^v$ , and thus the liquid transitions

into a viscoelastic state: growth of shear stresses leads to accumulation of elastic energy necessary for crack formation. Namely, as bubbles grow and, due to interaction among themselves, deform, they accumulate elastic energy because of surface tension. It is at this stage when the fluid starts behaving as viscoelastic owing to the fact that potential energy of deformed bubbles can transform into kinetic energy only in a finite time equal to the time required for the bubble to restore spherical shape. This time increases with bubble size and concentration  $\alpha$ . While it was claimed earlier (Kedrinskii *et al.*, 2005) that viscosity obstructs formation of cavitation bubbles, the map in figure 2.22a for  $Re < O(10^3)$  does not exhibit any significant viscosity dependence of the transition between the cupola regime, which relies upon cavitation, and the butterfly crown regime, in which cavitation phenomena are not essential. In our opinion, while viscosity indeed impedes the growth of cavitation bubbles, as can be inferred from the Rayleigh-Plesset equation (Brennen, 1995), the associated time scales are still disparate from the loading time and thus no effect on the cupola-crown regimes transition is observed. This implies that the above described process of shear-induced cavitation is not dominant in our case compared to that induced by shock waves.

### 2.1.4.3 Detachment and disintegration times

Both the cupola and direct atomization regimes are characterized by total detachment, while the butterfly crown regime by partial detachment. In the later case, whether any copious amount of liquid is left depends on the competition between adhesion force proportional to  $\sigma \cdot \sin \theta$  and the impulse intensity. As one can see from figure 2.25a the detachment times are expectedly much shorter in the direct atomization than in the cupola regime and increase with adhesion. Despite a significant visual difference between cupola and direct atomization regimes, the detachment times collapse onto one curve when scaled by the loading time  $\tau_0$ , cf. figure 2.25b.

Next, figure 2.26a clearly indicates the retardation effect of viscosity on the drop disintegration time. From a practical viewpoint, e.g. in the context of combustion, the retardation of the drop distortion and breakup due to increased viscosity implies that after the injection of such drops they will penetrate deeper into the surrounding space. Therefore, to attain equal degrees of atomization

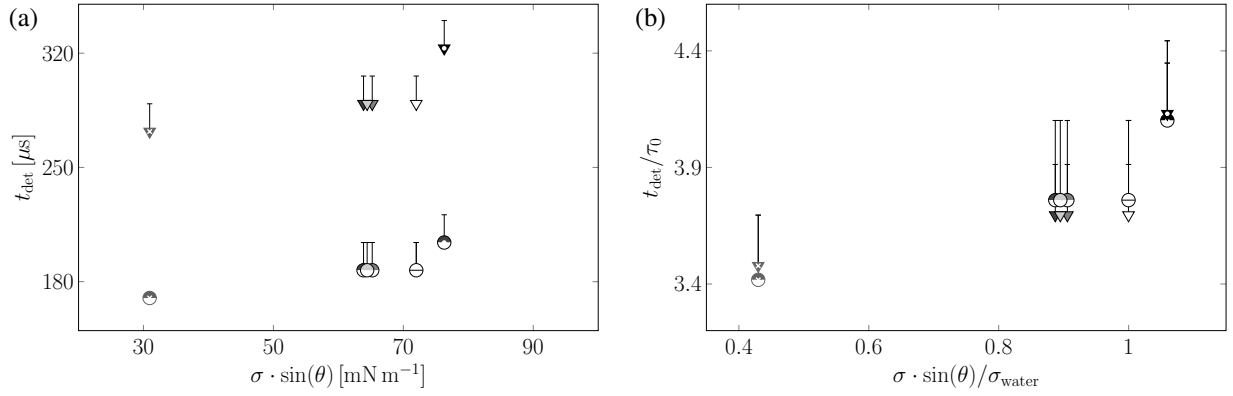


**Figure 2.25:** (a) The time of detachment from the membrane for six liquids in the cupola and atomization regimes with respect to surface tension force projected on the axis normal to the membrane surface (for the criteria on determining detachment times, refer to Appendix 2.H). (b) Non-dimensional detachment time of the liquid drops with respect to nondimensionalized surface tension. Error bars indicate the range of detachment uncertainty. Implemented liquids were DI water, 22% wt water-ethanol, 50% wt water-sucrose, as well as 67% wt, 80% wt, and 90% wt water-glycerol solutions. In all cases initial energy of the capacitors and the liquid drop size were fixed and equal to 1000 J and 50  $\mu\text{l}$ , respectively. In the cupola and direct atomization regimes, the copper membrane thickness was set at 0.17 mm and 0.034 mm, respectively. For symbol and shading definitions see figures 2.9a and 2.22a.

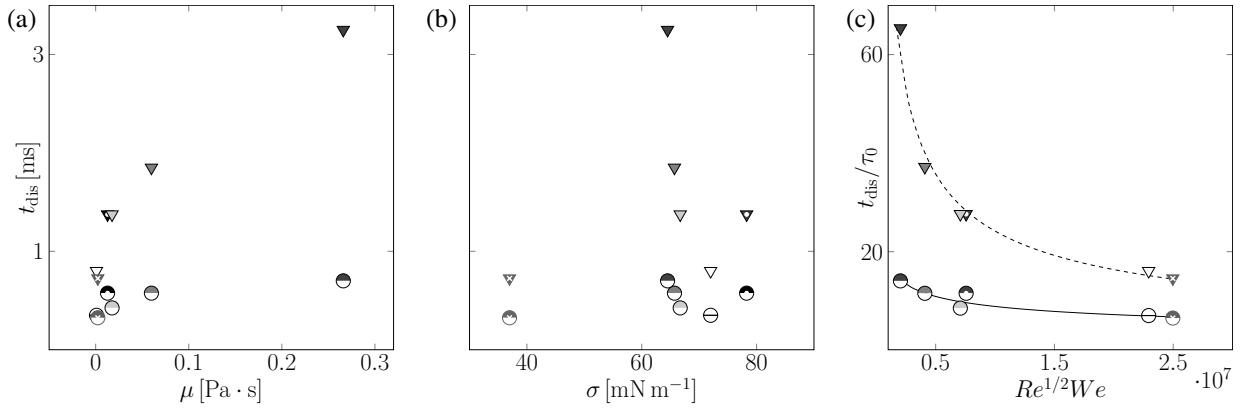


**Figure 2.26:** Disintegration time of liquid drops with respect to (a) viscosity and (b) surface tension (for the criteria on determining disintegration times, refer to Appendix 2.H). (c) Non-dimensional disintegration time of six liquids in the cupola and direct atomization regimes with respect to  $Re^{1/2}We$ . Implemented liquids were DI water, 22% wt water-ethanol, 50% wt water-sucrose, as well as 67% wt, 80% wt, and 90% wt water-glycerol solutions. In all cases, initial energy of the capacitors and the liquid drops size were fixed and equal to 1000 J and 50  $\mu\text{l}$ , respectively. In the cupola and direct atomization regimes, the membrane thickness was set at 0.17 mm and 0.034 mm, respectively. The curve fitted to the cupola regime data points is  $t_{dis}/\tau_0 = 213200 (Re^{1/2}We)^{-0.5636}$  and for the direct atomization regime is  $t_{dis}/\tau_0 = 1064.2 (Re^{1/2}We)^{-0.2969}$ . For symbol and shading definitions see figure 2.9a and 2.22a.

for the viscous components of a fuel it is required to increase the dimensions of the combustion chamber. While surface tension effects do not seem to have a clear trend as per figure 2.26b, the

disintegration times non-dimensionalized with respect to the loading time scales collapse on power-law curves when plotted against the splashing parameter  $K$ , cf. figure 2.26c.

#### 2.1.4.4 On the secondary droplet size distribution

Different liquids were employed to study the effect of viscosity and surface tension on the size of the secondary droplets produced in the direct atomization regime. The droplet sizes were determined using the stain method (Komabayasi *et al.*, 1964; Hall, 1970; Stow & Hadfield, 1981) discussed in Appendix 2.I, which assumes that a droplet impinging upon an absorbent surface produces a stain with the diameter being proportional to that of the droplet. The distribution of droplet sizes is obtained by comparing the stain sizes with those produced by droplets of known diameter. Similar to the originator of the method, German meteorologist Lenard (1904), we added red food-colour to the liquids (< 1% wt). Whatman paper of grade 1 (medium porosity, so that it takes 10.5 seconds to pass 0.155 m<sup>3</sup> of air through 1 m<sup>2</sup> surface area of the paper) was placed 200 mm away from the membrane surface and parallel to it. After each experiment the stained paper was scanned to produce a high resolution image for further processing with the Hough transform used to fit circles to the stains.

The secondary droplet distributions in the direct atomization regime were first compared to different analytic probability distribution functions (PDFs), and it was found that they are best represented by log-normal ones as, in particular, is evidenced by the good match of the mean secondary droplet radii between experimental and fitted log-normal PDFs in figure 2.28b. Accordingly, all experimental data were fitted to a log-normal distribution function; means and standard deviations for both experimental data and fitted curves were recorded and presented in figure 2.28a. The well-distinguished bimodal character of the PDF for 35% ethanol solution in figure 2.27b suggests that there are two dominating processes responsible for the drop atomization producing two different secondary droplet populations and operating on similar length and time scales. Each of these processes leads to a log-normal distribution, the superposition of which gives a bimodal one with two preferred most probable droplet radii. While binomial distributions are not uncommon in atom-

ization (Eroglu & Chigier, 1991; Harari & Sher, 1998; Alekseev *et al.*, 2015), in our case with the primary mechanism being the SW-interface interactions, such a PDF likely results from an increased contribution of cavitation similar to the case of superheated water atomization (Alekseev *et al.*, 2015). The most probable size of secondary droplets summarized in figure 2.28a is of the same order as that in the drop impact on a solid surface, e.g. for ethanol (Yarin & Weiss, 1995) and water-ethanol-sucrose solutions (Mundo *et al.*, 1995), though corresponding to the splashing parameter values  $K = (1.7 - 3.5) \times 10^4$  considerably below the ones we work with here, cf. figure 2.28a.

On the physical side, increase of viscosity both widens the distribution curves and increases the most probable secondary droplet size  $r_{\max}$ , cf. figure 2.27a. Decreasing the impact intensity also widens the distributions and increases  $r_{\max}$ , cf. figure 2.27d. Conversely, surface tension does not seem to have the same distinguished effect, which may be due to being masked by the variation of viscosity of the solutions used, cf. figure 2.27b. Nevertheless, as per figure 2.27c, the PDFs admit reasonable collapse with respect to all the key physical parameters (viscosity, surface tension, and sound speed) in the form favored here to  $r \mu^\alpha \sigma^\beta c^\gamma$  rather than to time or spatial scales, which would obviously provide a non-unique choice. To collapse all PDFs onto a single curve while preserving the total probability to be one, cf. figure 2.27c, a combination of the governing factors  $r \mu^\alpha \sigma^\beta c^\gamma$  was considered with different values of exponents  $\alpha$ ,  $\beta$ , and  $\gamma$  in the range from  $-10$  to  $+10$ . The criterion for the best collapse was the minimum difference between the average of the data sets and the data sets themselves. The substantial dependence of the collapse on the sound speed indicates that the atomization phenomena indeed rely upon compressibility effects. Overall, as summarized in figure 2.28a, the mean radius of secondary droplets exhibits noticeable dependence on both viscosity and surface tension as  $\bar{r}/R_0 \sim (Re^{1/2} We)^{-0.2469}$ .

*Qualitative insights.* Unlike the breakup of a cylindrical liquid column, which is inherently unstable to infinitesimal disturbances having certain wavelengths (Drazin & Reid, 2004), a spherical liquid drop is stable to small disturbances, and, therefore, a finite amount of energy is necessary to cause it to burst because a spherical drop is already at its minimum free energy level. This explains

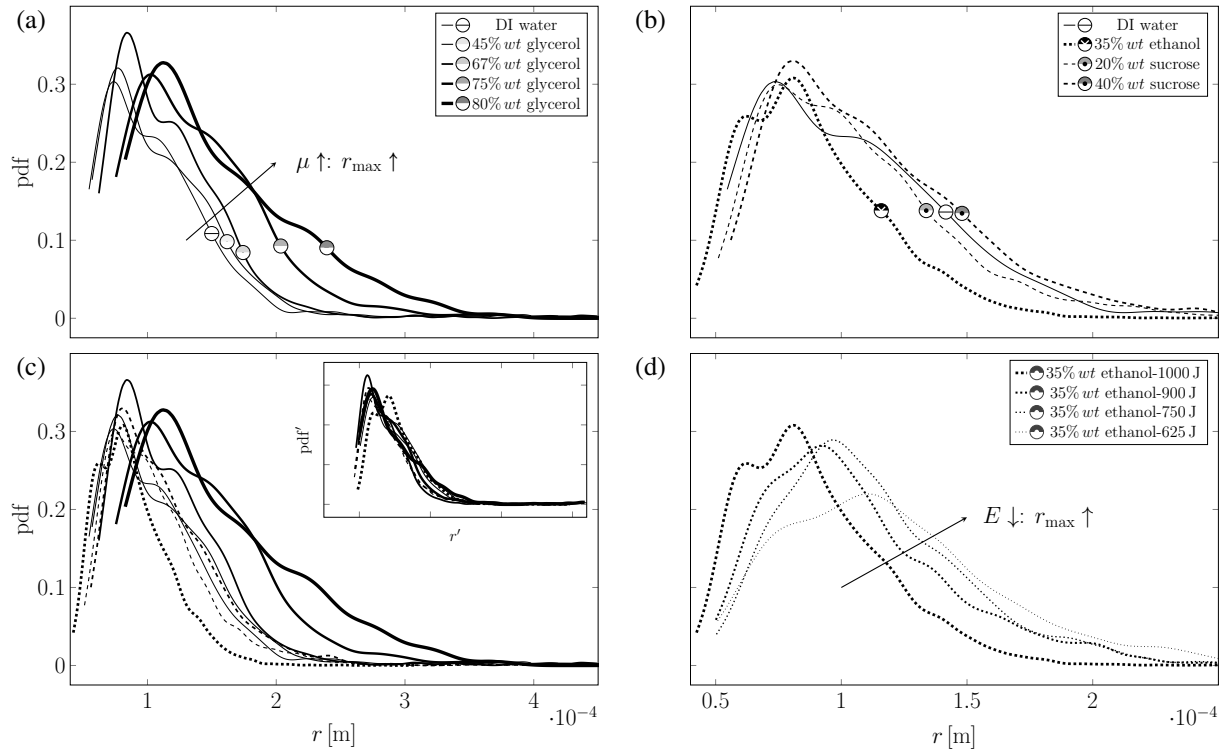


**Figure 2.27:** PDFs of secondary droplet radii in the direct atomization experiments on 0.034 mm copper membrane. (a) The effect of viscosity on the PDF. Implemented liquids are DI water, 45% wt glycerol, 67% wt glycerol, 75% wt glycerol, and 80% wt glycerol. (b) The effect of surface tension on the PDF. Implemented liquids are 35% wt ethanol, DI water, 20% wt sucrose, and 40% wt sucrose. (c) Data in figures (a) and (b) combined to collapse into one PDF curve with respect to the scaled radius  $r' = r \mu^\alpha \sigma^\beta c^\gamma$  in the inset. (d) The effect of impact intensity on PDF in the direct atomization regime for 35% wt ethanol solution. In (a,d),  $r_{\max}$  represents the most probable radius of the microdroplets. Applied energy in (a-c) was 1000 J.

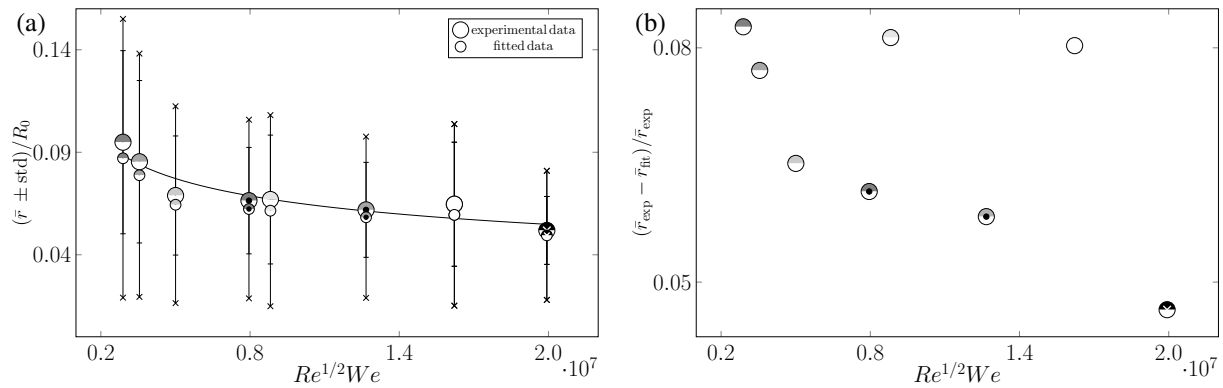


**Figure 2.28:** (a) The comparison between the mean of the experimental data and of the fitted curves of the PDFs presented in figure 2.27. Error bars with "-" and "x" endsymbols correspond to experimental and fitted data, respectively. The curve fitted to the data is given by  $\bar{r}/R_0 = 3.48 (Re^{1/2}We)^{-0.2469}$  with  $R_0 = 1.8$  mm. (b) Normalized difference between mean radii of the experimental data and the fitted curves.

why a critical Weber number (related to the impact energy) is required to break the drop as will be discussed in the context of aerobreakup in §2.1.5.1. Hence, a proper theoretical treatment of the drop breakup would involve more than subjecting a drop to linear perturbations and analyzing the conditions for their growth. Nevertheless, by appealing to the thermodynamic principles, one should be able to deduce certain characteristics of the secondary droplet sizes after the impact. Such an analysis was conducted by [Cohen \(1991\)](#), who showed a power-law probability distribution of the daughter droplet size.

In our case, however, we observe a log-normal distribution, which is characteristic of the interacting droplets situation studied by [Kolmogorov \(1941\)](#). Therefore, despite the seemingly absent droplet interactions in the time-sequence of figure 2.21d and straight trajectories in the direct atomization photo in figure 2.3 in the late stages of the phenomena, the acoustic processes of SW reflection from a free interface (as per figure 2.26c, the SW can turn around many times before the drop disintegrates) and cavitation bubble growth apparently favor a log-normal distribution. The analysis of [Cohen \(1991\)](#) is based on the assumption that daughter droplets do not interact. However, in real applications the interaction is unavoidable. The extreme case, in which droplet interactions are severe, corresponds, for example, to air-blast atomization, the physics of which is very complex: in addition to the breakup induced by gas turbulence, many other random processes such as collision of multiple droplets and turbulence in the liquid contribute to the phenomenon of breakup. As a simplification, the air-blast breakup is treated in the framework of cascade of uncorrelated breakage events in series and independently from the initial size distribution. The idea of cascade breakup originates from the early work of [Kolmogorov \(1941\)](#) on the breakup of solid particles described as a discrete random process, in which the probability of breaking each parent particle into a given number of parts is independent of the size of a parent particle. Based on Lyapunov's central limit theorem ([Billingsley, 1995](#)), such an assumption leads to a log-normal distribution of particle size in the long-time limit. Given the complexity of our phenomena similar to that of aerobreakup, we conclude that the same underlying principles – based on complex interactions of

SWs with free interfaces and among each other along with the cavitation phenomena – lead to a log-normal distribution as well.

*Quantitative estimates.* Inner stresses in the liquid containing bubbles may arise due to the deformation of bubbles which leads to accumulation of excess energy in the bubbles and existence of micro-stresses near the maximum curvature of the bubbles. Moreover, in the cavitation zone small scale pressure nonequilibrium leads to Reynolds-type stresses. When the bubble concentration  $\alpha$  reaches dense packing,  $0.52 < \alpha_* < 0.75$  (Kedrinskii & Chernobaev, 1992) it becomes more energetically preferable to form new free surfaces (discontinuities) in the directions of the maximum deformation of the media. One can estimate the time  $t_*$  required to achieve  $\alpha_*$  from  $t_* \sim \dot{\gamma}^{-1}$ , where  $\dot{\gamma} = \text{div } \mathbf{v}$  is the rate of deformation in the cavitation zone. Equating the kinetic energy of the deformation of a fluid particle of size  $r$  to the surface energy required to create a free surface,  $r^3 \rho (r\dot{\gamma})^2 \sim \sigma r^2$ , we find  $\dot{\gamma} \sim (\sigma/\rho r^3)^{1/2}$  or  $r \sim (\sigma/\rho \dot{\gamma}^2)^{1/3}$ . For water, taking  $10^3 < \dot{\gamma} < 10^5 \text{ s}^{-1}$  we find the range of the droplet sizes  $10^{-5} < r < 10^{-4} \text{ m}$  in accordance with our experimental observations in figure 2.27. Similar estimates follow if RT instability is considered to be governing the break up of the fluid interface in analogy with the RT instability of liquid shells (Bang *et al.*, 2016) as the impulse induces a SW propagating through the drop (cf. figure 2.23) thus accelerating the liquid-air interface: calculating the most amplified wavelength of the RT instability  $\lambda_{\text{RT}} = 2\pi (3\sigma/\rho a)^{1/2}$  (Drazin & Reid, 2004) for the upper end of accelerations  $a$  leading to direct atomization (cf. figure 2.2c), we also find  $r \sim \lambda_{\text{RT}} = O(10^{-5} - 10^{-4}) \text{ m}$ .

## 2.1.5 Discussion

### 2.1.5.1 Comparison of morphologies with other drop impact phenomena

Based on the experimental observations (figure 2.3) we distinguished the outcome patterns in figure 2.29, which schematically highlights the key features in the evolution of each pattern discussed in previous sections, sets the terminology, and provides a counterpart to the outcomes in aerobreakup (figure 2.30) and drop impact on solid (figure 2.31) outlined below.

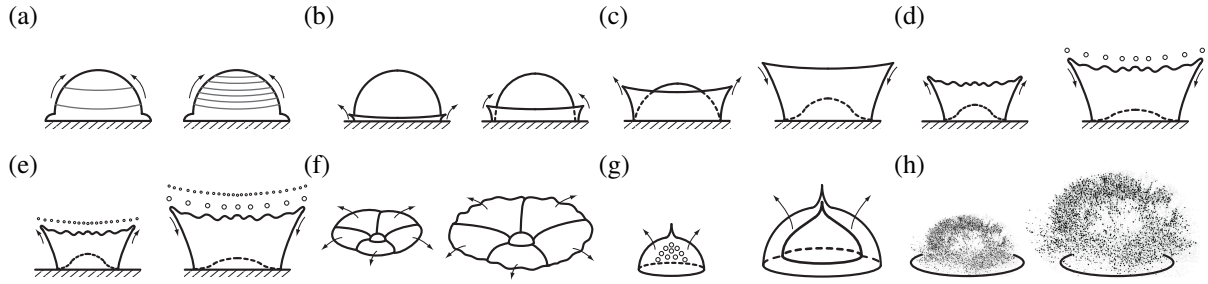


**Figure 2.29:** Schematics of the patterns shown in figure 2.3: (a) rippled waves; (b) ejecta; (c) crown without splash: once substrate is accelerated a crown is formed with the rim either being flat or forming fingers in later times, though without secondary droplet detachment; the crown wall is not disintegrated in this regime; (d) crown splash: after crown formation, fingers are developed at the rim but they may not detach (break into secondary droplets) until the crown wall disintegrates; (e) crown microdroplet splash: after crown formation, fingers are developed at the rim and several microdroplets are detached from the rim while the crown has not disintegrated yet; (f) butterfly crown splash; (g) cupola with cavitation bubbles (left) coalescing to form a void (right); (h) direct atomization.

When a SW in air is passing through a liquid drop at a relative non-zero velocity  $V$ , cf. figure 2.30a, the latter is subject to an impulsive, though finite, acceleration  $a$  and, depending on the SW intensity, may deform or shutter. The drop behavior in such flows is characterized by various modes of appearance, cf. figure 2.30. When viscous forces are negligible, i.e. low Ohnesorge numbers  $Oh = \mu/(\rho R_0 \sigma)^{1/2} \lesssim 0.14$  (Hsiang & Faeth, 1992), transitions between various regimes of deformation and disintegration of an initially spherical drop of radius  $R_0$  and density  $\rho$  happen due to competition between the aerodynamic pressure and restoring surface tension  $\sigma$  forces. The morphological sequence naturally starts with the *vibrational breakup* (b): the flow field interaction with the drop increases the oscillation amplitude, which in turn causes the drop to decompose into a few large fragments. The *bag breakup* (c) emerges from  $We = \rho V^2 R_0 / \sigma = 8 - 13$  and brings about deformation of the drop into a thin disk being normal to the flow direction, followed by distortion of the center of the disk into a thin balloon extending in the downstream direction, while being attached to a more massive toroidal rim. The bag eventually bursts into a large number of small fragments, while the rim disintegrates a short time later producing a small number of comparatively larger fragments. At higher velocities, from about  $We = 30 - 50$ , bag transitions to *umbrella* regime (d), when in addition to the bag breakup morphology, a column of liquid is formed along the drop axis parallel to the approaching flow. The bag bursts first; rim and stamen disintegration follows. Lastly,

the *shear breakup* (e), also known as the stripping regime (Theofanous & Li, 2008) and originally postulated by Taylor (1949), was observed at higher relative velocities, starting with  $We = 40-100$ , and involves continuous stripping of a thin sheet from the periphery of the deforming disk instead of forming a bag. The sheet disintegrates a short distance downstream from the drop. During the entire breakup process a coherent residual drop continues to exist.

As for the regimes of *drop impact on a solid surface*, they were summarized by Rioboo *et al.* (2001) and are similar to those shown in figure 2.31: (a) *deposition*, where the drop during the entire process is only deformed and stays on the surface; (b) *crown (corona) splash*, where a crown is formed during the spreading phase and eventually breaks up into droplets, which develop around the rim of a crown, remote from the solid surface; (c) *prompt splash*, where droplets are ejected directly from the contact line region in the spreading phase of the lamella – this regime is observed only on sufficiently rough surfaces; (d) *receding breakup*, where droplets are left on the surface during the receding phase of the impact – this is a pure wetting phenomenon; (e) complete or partial *rebound*, where either the entire drop or a part thereof rebounds from the substrate.

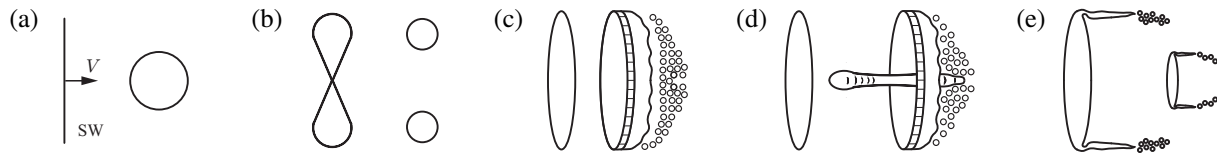


**Figure 2.30:** Breakup regimes (Pilch & Erdman, 1987) when (a) SW passes through a liquid drop: (b) vibrational, (c) bag, (d) umbrella, (e) sheet stripping.

In summary, while ripple waves (figure 2.6) in the impulse-driven drop experiments are analogous to the ones observed in drop impact on solid (Renardy *et al.*, 2003; Roux & Cooper-White, 2004), the lack of a Galilean invariance between these two problems results in different patterns, in particular at higher impulse intensities, compared to those in figure 2.31. Even though the term crown (corona) applies to both experimental configurations – figures 2.29c-2.29f versus figure 2.31b – the splashes in our experiments resemble crowns in the drop impacts on films rather than on solids (cf. §2.1.3.3); also non-monotonic crown behavior (figure 2.14a) and butterfly crowns are signatures of the impulsively-driven drops only. Despite the comparable accelerations experienced in

aerobreakup, the differences in observed morphologies are striking: figure 2.29 versus 2.30. Lastly, quantitative differences on the basis of  $We$  number are also apparent when our experiments are compared to both the drop impact on a thin film (figure 2.10d) as well as to the above discussed transition  $We$  numbers between aerobreak regimes, which are considerably lower than in the impulse-driven drops (figures 2.9a and 2.22a).

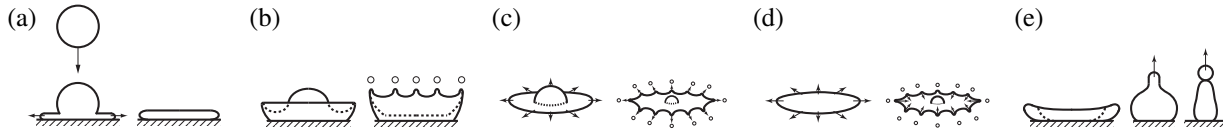


**Figure 2.31:** Breakup regimes when a liquid drop hits dry surface (Rioboo *et al.*, 2001): (a) deposition, (b) corona splash, (c) prompt splash, (d) receding breakup, (e) rebound (partial).

### 2.1.5.2 Key findings of the present study

In the presented experimental study, we highlighted the physics of the multi-scale phenomena of an impulse-driven drop and discussed the differences from along with similarities to aerobreakup as well as drop impact on a solid and a thin liquid layer. Starting with low impulse intensities (§2.1.3) we explored the transitions from ripple waves forming staircase patterns to ejecta occurring due to hydraulic jump phenomena (§2.1.3.1), and from various crown regimes – exhibiting flat rims, regular spike structures, microdroplets, and butterfly patterns (§2.1.3.2) – to drop disintegration ones – cupola formation due to cavitation and direct atomization (§2.1.4). A complete map of the morphological changes an impulse-driven drop undergoes in a wide range of viscosities, surface tensions and impulse intensities was developed (§§2.1.3.2,2.1.4.1), which is found to be quite different, both qualitatively and quantitatively, from aerobreakup and drop impact phenomena (§2.1.5.1); also, as opposed to the latter phenomena, the maximum acceleration, not velocity, proved to be a proper physical variable for data interpretation (figure 2.9).

The effect of each physical parameter – initial intensity reduced here to  $a_{\max}$ , surface tension  $\sigma$ , viscosity  $\mu$ , and contact angle  $\theta$  – on the outcome pattern is summarized in the table of figure 2.32a. The interrelation of the observed morphologies is illustrated in the diagram of figure 2.32b, which in particular shows that the transition from the crown splash regime may either go directly

to butterfly crown splash as the intensity increases while using the same fluid, or to microdroplet splash if the surface tension is decreased, e.g. by using ethanol-water mixtures.

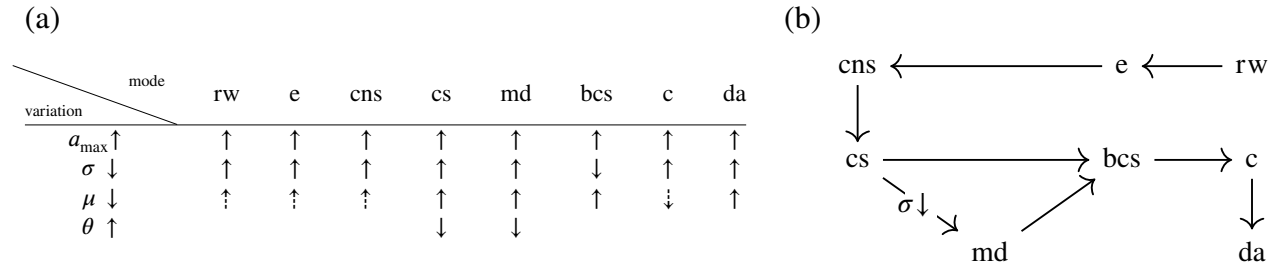


**Figure 2.32:** (a) General trends of how each physical parameter influences the appearance of a regime compared to the previous one in the column on the left; this summary is provided based on observations in figures 2.9, 2.10a,b and 2.22a. Arrow up means that the associated pattern appears from the previous regime and arrow down means that the pattern disappears. Dashed arrows are used when the trends are observed for a narrow range of the parameter. (b) Sequence of regimes as impact intensity increases.

The role of the key time scales in each regime was illuminated as well, culminating in a proper interpretation of the regime maps (§§2.1.3.2, 2.1.4.1) and of the fundamental processes underlying the regimes (§§2.1.3.2, 2.1.4.1, 2.1.4.2). To the best of our knowledge, such an analysis has not been performed in aerobreakup and drop impact problems. The crown dynamics – its radius and height – were explored in detail and contrasted with analogous observations in the drop impact studies (§2.1.3.4), revealing that decreasing surface tension makes the crown radius approach the power-law growth  $R \sim t^{1/2}$ , while lowering viscosity to approach the ballistic regime  $R \sim t$  as opposed to the retarding effect of higher viscosities  $R \sim t^{\alpha_R}$  with  $\alpha_R < 1$ . Non-monotonic crowns, unique to impulse-driven drops, originate from surface tension force competing with liquid inertia.

While SW interaction with the drop interface is instrumental for understanding the early stages of the drop dynamics even in the crown regimes (§2.1.3.3), the most intense impulse regimes – cupola and direct atomization – turned out to strongly rely upon compressible effects such as cavitation and SW-free surface interactions (§2.1.4.2). The key characteristics of the latter two regimes – drop detachment and disintegration times (§2.1.4.3) along with probability distributions of the secondary droplet sizes (§2.1.4.4) – were quantified as well. In all the above studies, the effects of impulse intensity, viscosity, surface tension, and wettability (§2.1.3.5) interplaying with compressibility (§§2.1.3.3, 2.1.4.2) were identified and interpreted. In particular, detachment times were

observed to be much shorter in the direct atomization compared to the cupola regime and increase with adhesion; also disintegration times increase with viscosity. Collapse of these characteristic times on a power-law curve is achieved with the splashing parameter  $K$ . As for secondary droplet PDFs, which prove to be log-normal due to compressible effects, increase of viscosity both widens them and increases the most probable secondary droplet size  $r_{\max}$ . The significant contribution of compressibility to the nature of PDFs is also confirmed by the collapse of the latter when properly scaled with sound speed (§2.1.4.4). Lastly, the discovered bimodal PDF for the 35% ethanol solution is argued to result from an increased contribution of cavitation, to which this particular liquid is more prone.

## 2.2 Theory

To provide a theoretical background for the cavitation phenomena responsible for the most energetic regimes of drop disintegration, we will review the behavior of the pressure field near the most singular region – the cusp (§2.2.1) – and then near the caustic (§2.2.2) with the goal to demonstrate qualitatively that pressure field, should it be positive in the case of shock wave focusing or negative in the case of rarefaction wave focusing, develops significant amplitudes capable of leading to cavitation as observed experimentally.

### 2.2.1 Acoustic wave focusing

#### 2.2.1.1 Caustic geometry

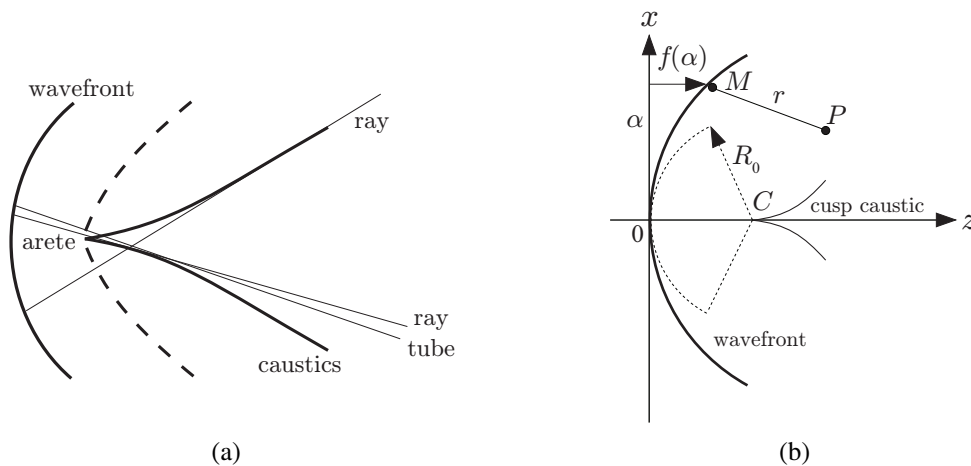


**Figure 2.33:** (a) Caustics formation; (b) near cusp geometry (Coulouvrat, 2000).

A typical focusing wavefront is shown in figure 2.33a: folds are developed as the wavefront moves normal to itself along the rays. The ray envelopes, where the folding occurs, represent the caustics, which typically begin at an arête, that is cusp (1.27b) – the point at which adjacent rays intersect; it also corresponds to the point on the original front with maximal curvature, whose neighborhood is the first to focus and fold. Since the wavefront has a cusp at the point where it touches a

caustic, the assumption that the wavefront everywhere locally looks like a propagating plane wave is no longer valid and the geometrical acoustics is inapplicable. The geometrical-acoustics prediction, of where the caustics occur, as well as the detailed behavior of the state variables close to them are of paramount importance, in particular because at the caustics the wave intensity amplifies enormously due to the wave energy conservation along ray tubes. Thus, formally, in this linear geometric acoustics *outer expansion*, the energy density diverges since the ray tubes collapse into points at a caustic. Therefore, an *inner expansion* becomes indispensable in order to analyze the behavior near caustics.

Let us consider a two dimensional wave propagating in an inviscid homogeneous fluid with sound speed  $c_0$ . Initially, the wave is specified at a concave wavefront, given by  $z = f(x)$ , cf. figure 2.33b. If the radius of curvature of this wavefront has a minimum  $R_0$ , a cusp caustic will appear. The origin  $O$  is positioned at the point of minimum radius of curvature, while the  $Ox$  axis is tangential and the  $Oz$  axis is normal to the wavefront (and directed towards the propagation direction).

As we know from Huygens' principle (§1.3), the acoustic pressure  $p$  wave of frequency  $\omega/2\pi$  can be expressed at an observation point  $P(x, z)$  as a sum of cylindrically diverging waves emanating from the wavefront. If the observation point is far enough from the initial wavefront, the Hankel function  $H_0^\pm(k|\mathbf{r}|)$  can be replaced by its far-field asymptotic expression

$$H_0^\pm(k|\mathbf{r}|) \sim \sqrt{\frac{2}{\pi|\mathbf{r}|}} e^{\pm ik|\mathbf{r}|} \text{ as } k|\mathbf{r}| \rightarrow \infty, \quad (2.6)$$

so that the pressure

$$p(t, x, z) = e^{i\omega t} \int_{-\infty}^{+\infty} r^{-1/2} A(\alpha) e^{ikr} d\alpha, \quad (2.7)$$

where  $r = |\mathbf{r}|$ ,  $k = \omega/c_0$  is the wavenumber,  $A(\alpha)$  is a smooth amplitude function,  $\alpha$  is the  $x$ -coordinate of a current point  $M$  along the wavefront, and  $r$  is the distance between the observation

point  $P$  and the current point  $M$ , cf. figure 2.33b:

$$r = \sqrt{(x - \alpha)^2 + (z - f(\alpha))^2}. \quad (2.8)$$

According to Fermat's principle, among all lines connecting the observation point  $P$  and a wavefront point  $M$ , the acoustic rays are those minimizing the distance  $MP$ , cf. Appendix 2.A:

$$\frac{\partial r}{\partial \alpha} = -\frac{(x - \alpha) + f'(\alpha)(z - f(\alpha))}{r} = 0 \Rightarrow (x - \alpha) + f'(\alpha)(z - f(\alpha)) = 0, \quad (2.9)$$

so that rays are the straight lines normal to the wavefront, each of which can thus be identified by a single parameter ("ray-coordinate")  $\alpha$  – the  $x$ -coordinate of its intersection with the initial wavefront. Caustics are the loci of intersection points of infinitely many adjacent rays, i.e. where the first (2.9) and second derivatives of the phase function

$$\begin{aligned} \frac{\partial^2 r}{\partial \alpha^2} &= -\frac{(1 + f'^2(\alpha))^2 (z - f(\alpha))^2 [f''(\alpha)(z - f(\alpha)) - (1 + f'^2(\alpha))]}{r^3} \\ &\Rightarrow f''(\alpha)[z - f(\alpha)] - [1 + f'^2(\alpha)] = 0. \end{aligned} \quad (2.10)$$

simultaneously vanish. Next, let us now study the caustic geometry near the ray emanating from the origin. With the choice of coordinates as in figure 2.33b we have  $f(0) = 0$ ,  $f' = 0$ ,  $f'' = 1/R_0 > 0$ , and  $f''' = 0$ , where the latter condition comes from the minimal radius of curvature. The intersection point  $C$  between the ray coming from the origin and the caustic is at  $(0, R_0)$ . A point  $Q$  on the caustic has the Cartesian coordinates  $(x, z = R_0 + \delta)$  or, alternatively, can be identified by the ray-coordinate  $\alpha$  pertinent to the ray tangent to the caustic at this point. From equations (2.9,2.10), for small  $\alpha$ 's

$$\delta = \frac{\alpha^2}{2} R_0'' + O(\alpha^3), \quad x = -\frac{\alpha^3}{3} f''(0) R_0'' + O(\alpha^4), \quad (2.11)$$

where the quantity  $R_0'' = 3f''(0) - [f^{(iv)}(0)/f''^2(0)]$  is positive as the radius of curvature has minimum at the origin. As a result, the caustic equations (2.11) can be locally written near the point  $C$  as

$$x = \pm \frac{\delta^{3/2}}{a^{1/2}}, \quad (2.12)$$

where  $a = \frac{9}{8}R_0^2R_0''$  is the parameter determining the local geometry of the caustic.

### 2.2.1.2 The characteristic length-scales of the caustic boundary layer

With the goal to determine the characteristic length-scales of the acoustic field around the cusp, we consider the phase function in the cusp neighborhood. In the geometric acoustics approximation, the phase oscillations in equation (2.7) imply that the main contributions to the acoustic field near the cusp come from the wavefront near the origin  $O$ , i.e. for small values of  $\alpha$ . According to (2.11) the coordinates  $(x, z = R_0 + \delta)$  of the observation point  $P$  near the cusp  $C$  are such that  $x = O(\alpha^3)$  and  $\delta = O(\alpha^2)$ . The phase can then be expanded:

$$r = R_0 + \delta - x \frac{\alpha}{R_0} - \frac{\delta}{2} \left( \frac{\alpha}{R_0} \right)^2 + \frac{a}{27} \left( \frac{\alpha}{R_0} \right)^4 + O(\alpha^5), \quad (2.13)$$

the substitution of which into equation (2.7) leads to the asymptotic expression of the pressure field near the cusp

$$p(t, x, z) \approx \frac{A(0)}{R_0^{1/2}} e^{i(kz - \omega t)} \int_{-\infty}^{+\infty} \exp \left[ -ikx \frac{\alpha}{R_0} - ik \frac{\delta}{2} \left( \frac{\alpha}{R_0} \right)^2 + ik \frac{a}{27} \left( \frac{\alpha}{R_0} \right)^4 \right] d\alpha. \quad (2.14)$$

With the new variable  $\bar{\alpha} = (\alpha/R_0)(ka/27)^{1/4}$ , the above formula yields an analytical expression of the pressure field in terms of the Pearcey function  $P(\bar{x}, \bar{z}) = \int_{-\infty}^{+\infty} \exp(i\bar{x}\bar{\alpha} + i\bar{z}\bar{\alpha}^2 + i\bar{\alpha}^4) d\bar{\alpha}$ , which defines a class of canonical diffraction integrals (Pearcey, 1946):

$$p(t, x, z) \sim e^{i(kz - \omega t)} P(\bar{x}, -\bar{z}). \quad (2.15)$$

The dimensionless variables  $\bar{x}$  and  $\bar{z}$  in the Pearcey function originate from non-dimensionalization of the physical ones by two characteristic length-scales –  $L_x$  transversely to and  $L_z$  along the propagation axis  $Oz$ :

$$\bar{x} = \frac{x}{L_x} = \frac{27}{\epsilon^{3/2}} \frac{x}{a} \text{ with } L_x = \left( \frac{a}{27k^3} \right)^{1/4}, \quad (2.16a)$$

$$\bar{z} = \frac{\delta}{L_z} = \frac{27}{2\epsilon} \frac{\delta}{a} \text{ with } L_z = \left( \frac{4a}{27k} \right)^{1/2}, \quad (2.16b)$$

where the diffraction parameter

$$\epsilon = (27/ka)^{1/2} \quad (2.17)$$

is a measure of the magnitude of diffraction effects near the caustic. The parameter (2.17) is small at sufficiently high frequencies, since the wavelength is small compared to the caustic geometrical parameter  $a$ . From (2.16) it is notable that the transverse length  $L_x$  varies as power  $-\frac{3}{4}$ , while the longitudinal one  $L_z$  varies as power  $-\frac{1}{2}$  of the frequency. With these non-dimensional variables (2.16), the caustic equation (2.12) assumes to the canonical form

$$\bar{x}^2 = \frac{8}{27} \bar{z}^3. \quad (2.18)$$

### 2.2.1.3 Pressure near the caustic cusp

Since we are interested in weakly nonlinear effects near the caustic cusp let us start by deriving the basic equation of nonlinear acoustics (Kuznetsov, 1970) neglecting viscosity and thermal effects, i.e. we will assume that the working fluid is barotropic<sup>12</sup> with the corresponding equation of state being  $p = p(\rho)$  under isentropic (adiabatic) conditions; note that one can also consider the isothermal case, which formally leads to the same functional dependence of the equation of state, but thermodynamically this is a different scenario. Taylor expanding the equation of state around

---

<sup>12</sup>The barotropic equation of state is known to be valid for fluids such as water even at very high pressures (Tait, 1888).

the equilibrium state  $p_0(\rho_0)$ , we get

$$p - p_0 = A \frac{\rho - \rho_0}{\rho_0} + \frac{B}{2!} \left( \frac{\rho - \rho_0}{\rho_0} \right)^2 + \dots, \quad (2.19)$$

where  $A = \rho_0 p'(\rho_0)$  and  $B = \rho_0^2 p''(\rho_0)$ . For example, for the Poisson equation of state  $p/p_0 = (\rho/\rho_0)^\gamma$ , we find  $B/A = \gamma - 1$  and  $c_0^2 = p'(\rho_0) = \gamma p_0/\rho_0$ .

Using the expression for pressure (2.19) in the Euler momentum equation for inviscid and irrotational motion

$$\frac{\partial \mathbf{v}}{\partial t} = -\frac{1}{2} \nabla (v^2) - \frac{c_0^2}{\rho_0} \nabla \left[ (\rho - \rho_0) + \frac{B}{2A\rho_0} (\rho - \rho_0)^2 \right], \quad (2.20)$$

with  $v = |\mathbf{v}|$ , and introducing the scalar velocity potential via  $\mathbf{v} = \nabla \Phi$  and differentiating with respect to time  $t$ , we arrive at

$$-\frac{\partial^2 \Phi}{\partial t^2} = \frac{1}{2} \frac{\partial}{\partial t} (\nabla \Phi)^2 + \frac{c_0^2}{\rho_0} \frac{\partial \rho}{\partial t} + c_0^2 \frac{B}{2A\rho_0^2} \frac{\partial}{\partial t} (\rho - \rho_0)^2. \quad (2.21)$$

Next, with the help of the linearized continuity equation

$$\frac{\partial \rho}{\partial t} + \rho_0 \nabla \cdot \mathbf{v} = 0, \quad (2.22)$$

and linearized version of (2.20) rewritten for the velocity potential  $\Phi$  we arrive at the Kuznetsov equation governing the propagation of weakly nonlinear waves in an inviscid fluid:

$$\frac{\partial^2 \Phi}{\partial t^2} - c_0^2 \Delta \Phi = -\frac{\partial}{\partial t} \left[ \frac{1}{c_0^2} \frac{B}{2A} \left( \frac{\partial \Phi}{\partial t} \right)^2 + (\nabla \Phi)^2 \right], \quad (2.23)$$

with  $B/2A$  being the nonlinearity parameter. According to the pressure far field (2.15), we expect the sound field near the cusp (the inner expansion) to depend on the dimensionless retarded time  $\tilde{t} = \omega(t - z/c_0)$ , describing the axial wave propagation over the wavelength-scale, and on the two variables  $\tilde{x}$  and  $\tilde{z}$  associated with diffraction. When nonlinear effects are taken into account, the

sound field will no longer be monochromatic, so that  $\omega$  is a characteristic frequency only. The dimensionless potential  $\tilde{\Phi}$  is introduced via  $\Phi(t, x, z) = U_0 c_0 \tilde{\Phi}(\tilde{t}, \tilde{x}, \tilde{z})/\omega$ , with  $U_0$  the velocity amplitude of the acoustic field. With this set of variables, the Kuznetsov equation becomes

$$\frac{\partial^2 \tilde{\Phi}}{\partial \tilde{t} \partial \tilde{z}} - \frac{\partial^2 \tilde{\Phi}}{\partial \tilde{x}^2} - \beta \frac{M}{\epsilon} \frac{\partial}{\partial \tilde{t}} \left( \tilde{\Phi}_t^2 \right) = \frac{\epsilon}{4} \frac{\partial^2 \tilde{\Phi}}{\partial \tilde{z}^2} + M \frac{\partial}{\partial \tilde{t}} \left( \tilde{\Phi}_x^2 - \tilde{\Phi}_t \tilde{\Phi}_z + \frac{\epsilon}{4} \tilde{\Phi}_z^2 \right), \quad (2.24)$$

where  $\beta = 1 + B/2A$ . Since the acoustic Mach number  $M = U_0/c_0$  is a small parameter, the right-hand side of (2.24) can be neglected compared to the left-hand side.

With the dimensionless pressure  $\tilde{p} = \partial \tilde{\Phi} / \partial \tilde{t}$ , we immediately deduce that it is a solution of the Khokhlov-Zabolotskaya equation (Rudenko & Khokhlova, 2009)

$$\frac{\partial^2 \tilde{p}}{\partial \tilde{t} \partial \tilde{z}} - \frac{\partial^2 \tilde{p}}{\partial \tilde{x}^2} = \mu \frac{\partial^2 (\tilde{p}^2)}{\partial \tilde{t}^2}, \quad (2.25)$$

where the parameter  $\mu$  measures nonlinear relative to diffraction effects

$$\mu = \frac{\beta M}{\epsilon} = \beta M \left( \frac{ka}{27} \right)^{1/2}. \quad (2.26)$$

The deduced Khokhlov-Zabolotskaya equation for the concrete situation of the pressure field near the cusp governs the nonlinear sound field in the vicinity of the caustic cusp with the power  $\frac{1}{2}$  appearing in the definition of the small diffraction parameter for a caustic cusp. Finally, if we introduce scaling to get rid of the parameter  $\mu$  in (2.25):

$$\tilde{p} = \mu^{-1/3} \hat{p}, \quad \tilde{t} = \mu^{4/3} \hat{t}, \quad \tilde{x} = \mu \hat{x}, \quad \tilde{z} = \mu^{2/3} \hat{z}, \quad (2.27)$$

then all the variables must be  $O(1)$  – this is known as Guiraud’s similitude with respect to the nonlinear parameter (Guiraud, 1965), meaning that pressure evolves as the power  $-\frac{1}{6}$  of the geometric parameter  $a$ .

## 2.2.2 Near caustic behavior

Since the pioneering work of Buchal & Keller (1960) and Ludwig (1966) the caustics of linear waves have been well understood. The analysis by these authors is based on a local multiple-scale expansion near the caustics, where not only the fast scale transversal to the fronts, but also an intermediate scale along the fronts are responsible for the leading order behavior of the acoustic waves. To analyze the acoustic field near the caustic, we will follow Rosales & Tabak (1998).

### 2.2.2.1 Coordinate systems

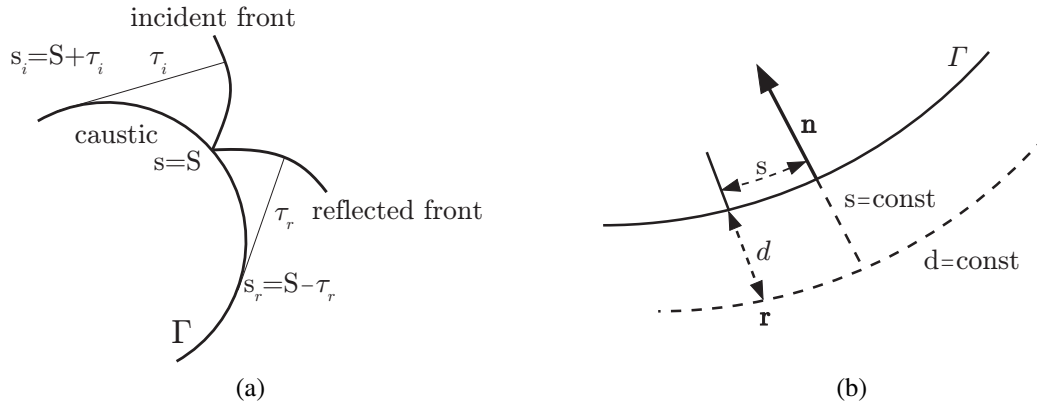


**Figure 2.34:** Caustic coordinate systems: (a) polar, (b) normal (Rosales & Tabak, 1998).

To simplify notations, in this subsection we are going to use non-dimensional variables such that the sound speed  $c = 1$  and the radius of curvature of the wave fronts is  $O(1)$ . Since we deal with high frequency waves corresponding to the limit of geometric optics, the wavelength of the waves is  $2\pi\epsilon/k$  with  $\epsilon \ll 1$  and  $k = O(1)$ . With this choice of variables, the wave fronts are described by the phase:

$$\theta = \frac{\Phi(x, y) - t}{\epsilon}, \quad (2.28)$$

where, as we know from §1.1, the action variable  $\Phi(x, y)$  satisfies the eikonal equation:

$$(\nabla\Phi)^2 = 1, \quad (2.29)$$

which states that the wave fronts ( $\theta = \text{const}$ ) move normal to themselves at speed 1, along straight lines denoted rays.

To describe the caustic, consider a smooth convex caustic  $\Gamma$  in figure 2.34a given parametrically by

$$x = X(s) \text{ and } y = Y(s), \quad (2.30)$$

where  $s$  is the arclength along the caustic, which can be identified with the value of the action variable  $\Phi$  along it:

$$\Phi(X(s), Y(s)) = s. \quad (2.31)$$

Next we introduce the unit vectors

$$\hat{\mathbf{t}}(s) = (\dot{X}(s), \dot{Y}(s))^T \text{ and } \hat{\mathbf{n}}(s) = (-\dot{Y}(s), \dot{X}(s))^T, \quad (2.32)$$

which are respectively tangent and normal to the caustic  $\Gamma$  at  $s$  such that the tangent vector  $\hat{\mathbf{t}}$  is chosen to point in the direction of propagation and the normal vector  $\hat{\mathbf{n}}$  towards the region without waves. The caustic geometry specification is completed with the curvature  $\kappa(s)$  of  $\Gamma$  at the point  $s$ .

If  $\mathbf{R}(s) = (X(s), Y(s))^T$  denotes a point on the caustic, then the incident  $\Phi_i = S$  and reflected  $\Phi_r = S$  waves can be represented parametrically as

$$\mathbf{r}_i = \mathbf{R}(S + \tau_i) - \tau_i \hat{\mathbf{t}}(S + \tau_i), \quad (2.33a)$$

$$\mathbf{r}_r = \mathbf{R}(S - \tau_r) + \tau_r \hat{\mathbf{t}}(S - \tau_r), \quad (2.33b)$$

where  $\tau_i$  ( $\tau_r$ ) specifies the time it takes each point along the front to reach (leave) the caustic; clearly,  $\Phi_i = s_i - \tau_i$  and  $\Phi_r = s_r - \tau_r$ . These systems  $(s_i, \tau_i)$  and  $(s_r, \tau_r)$  describe the incident and reflected fronts, respectively, cf. figure 2.34a.

However, the above introduced coordinate systems become singular and fold into each other in a neighborhood of the caustic, which requires an introduction of the normal to the caustic coordinate system, cf. figure 2.34b:

$$\mathbf{r}(s, d) = (x, y)^T = \mathbf{R}(s) - d \mathbf{n}(s), \quad (2.34)$$

where  $d$  is the signed distance to the caustic with  $d > 0$  corresponding to the wavefront region. While the incident and reflected wavefronts  $\Phi_i$  and  $\Phi_r$  do not have a closed form in this new coordinate system, they can be expanded in powers of  $d^{1/2}$  near the caustic:

$$s = S \pm \frac{2}{3} \sqrt{2\kappa(S)} d^{3/2} + O(d^2). \quad (2.35)$$

Given the above considerations, it appears natural to introduce two fast variables near the caustic: an imperfect phase  $\psi$  accounting for the fast dependence normal to the fronts:

$$\psi = \frac{s - t}{\epsilon}, \quad (2.36)$$

and a transversal variable  $\eta$  accounting for the fast variation along the fronts near the caustic, where their curvature diverges

$$\eta = \frac{d}{\epsilon^{2/3}}. \quad (2.37)$$

Then the phase (2.28) near the caustic can be expanded as

$$\theta = \psi \mp \frac{2}{3} \sqrt{2\kappa(S)} \eta^{3/2} + O(\epsilon^{1/3} \eta^2), \quad (2.38)$$

for the incident and reflected waves, respectively.

### 2.2.2.2 Application to barotropic fluid: inner solution near the caustic

Given that water equation of state can be approximated as barotropic, i.e.  $p = p(\rho)$ , we can consider the acoustic wave propagation in a barotropic medium. The corresponding dimensional linearized Euler equations read

$$\rho_t + \rho_0(u_x + v_y) = 0, \quad (2.39a)$$

$$u_t = -\frac{dp}{d\rho}\rho_x = -c_0^2\rho_x, \quad (2.39b)$$

$$v_t = -\frac{dp}{d\rho}\rho_y = -c_0^2\rho_y, \quad (2.39c)$$

or, in the adopted non-dimensional variables (or, equivalently, putting  $\rho_0 = 1$  and  $c_0 = 1$ ), this system assumes the form

$$\rho_t + u_x + v_y = 0, \quad (2.40a)$$

$$u_t + \rho_x = 0, \quad (2.40b)$$

$$v_t + \rho_y = 0. \quad (2.40c)$$

Transforming these equations to the coordinates  $(s, d)$  such that the velocity components parallel  $\tilde{u}$  and normal  $\tilde{v}$  to the caustic

$$\tilde{u} = u \cos \phi + v \sin \phi, \quad (2.41a)$$

$$\tilde{v} = -u \sin \phi + v \cos \phi, \quad (2.41b)$$

where  $\phi(s)$  is the caustic angle defined via  $\dot{X} = \cos \phi$  and  $\dot{Y} = \sin \phi$ , the Euler equations become

$$[1 + \kappa(s)d] \rho_t + \tilde{u}_s - [(1 + \kappa(s)d)\tilde{v}]_d = 0, \quad (2.42a)$$

$$[1 + \kappa(s)d] \tilde{u}_t + \rho_s = 0, \quad (2.42b)$$

$$\tilde{v}_t - \rho_d = 0, \quad (2.42c)$$

where the caustic curvature can be expressed in terms of the caustic angle  $\kappa(s) = \dot{\phi}$ .

Representing the solution to system (2.42) in terms of the fast variables  $(\psi, \eta)$  instead of  $(s, d)$  and in terms of expansion with respect to the small parameter  $\epsilon$ , valid for  $|d| \ll \epsilon^{1/2}$  (or, equivalently,  $|\eta| \ll \epsilon^{-1/6}$ ):

$$\rho = \rho_0(\psi, \eta, s) + \epsilon^{1/3} \rho_1(\psi, \eta, s) + \dots, \quad (2.43a)$$

$$\tilde{u} = \tilde{u}_0(\psi, \eta, s) + \epsilon^{1/3} \tilde{u}_1(\psi, \eta, s) + \dots, \quad (2.43b)$$

$$\tilde{v} = \tilde{v}_0(\psi, \eta, s) + \epsilon^{1/3} \tilde{v}_1(\psi, \eta, s) + \dots, \quad (2.43c)$$

we find that at the leading order  $\tilde{u}_0 = \rho_0$ ,  $\tilde{v}_0$  does not depend on  $\psi$  and  $\eta$ , while the variables  $\rho_0$  and  $\tilde{v}_1$  satisfy the following system of equations

$$2 \kappa(s) \eta \rho_{0\psi} + \tilde{v}_{1\eta} = 0, \quad (2.44a)$$

$$\tilde{v}_{1\psi} + \rho_{0\eta} = 0, \quad (2.44b)$$

reducing to the Tricomi equation arising in transonic aerodynamics (Cole & Cook, 1986)

$$\rho_{0\eta\eta} - 2 \kappa(s) \eta \rho_{0\psi\psi} = 0, \quad (2.45)$$

which is a second-order partial differential equation of mixed type meaning that it is elliptic for  $\eta < 0$ , hyperbolic for  $\eta > 0$ , and parabolic on the line  $\eta = 0$ .

Since the Tricomi equation (2.45) is linear and does not contain coefficients dependent of  $\psi$ , the dependence of  $\psi$  must be exponential:

$$\rho_0 = \hat{\rho}_0(\eta, s) e^{ik\psi}, \quad (2.46)$$

substitution of which into (2.45) produces

$$\rho_0 = f(s) \text{Ai}(-\alpha\eta) e^{ik\psi}, \quad (2.47)$$

where  $\alpha = [2\kappa(s)k^2]^{1/3}$  and  $\text{Ai}(z)$  is the Airy function which decays as  $z \rightarrow \infty$ .

### 2.2.2.3 Linear geometric acoustics: outer solution and matching

The outer solution, which is valid outside the caustic is sought as a formal series

$$\rho = [a_0(x, y) + \epsilon a_1(x, y) + \dots] e^{ik\theta}, \quad (2.48a)$$

$$u = [u_0(x, y) + \epsilon u_1(x, y) + \dots] e^{ik\theta}, \quad (2.48b)$$

$$v = [v_0(x, y) + \epsilon v_1(x, y) + \dots] e^{ik\theta}, \quad (2.48c)$$

where the phase  $\theta$  is given by (2.28), and the leading order velocity components are expressed as  $u_0 = \Phi_x a_0$ , and  $v_0 = \Phi_y a_0$ . While the action variable  $\Phi$  satisfies the eikonal equation (2.29), the leading order amplitude  $a_0$  satisfies the transport equation (1.15b)

$$2\nabla\Phi \cdot \nabla a_0 + \Delta\Phi a_0 = 0. \quad (2.49)$$

Naturally, it is more convenient to work in the coordinates corresponding to the characteristics of the eikonal equation (2.29): the corresponding ray equations read

$$\frac{dx}{d\tau} = \Phi_x, \quad \frac{dy}{d\tau} = \Phi_y, \quad (2.50)$$

along which the eikonal equation takes the form:

$$\frac{d\Phi_x}{d\tau} = \frac{d\Phi_y}{d\tau} = 0 \text{ and } \frac{d\Phi}{d\tau} = 1. \quad (2.51)$$

Because of the eikonal equation (2.29),  $\Phi_x^2 + \Phi_y^2 = 1$ , the parameter  $\tau$  is the arclength along rays with  $\tau = 0$  at the caustic as per figure 2.34a and  $\tau < 0$  for the incident wave and  $\tau > 0$  for the reflected one. Altogether, the rays and the action variable  $\Phi$  are represented as

$$\Phi_x = \dot{X}(s), \quad \Phi_y = \dot{Y}(s), \quad \Phi = s + \tau, \quad x = X(s) + \Phi_x \tau, \quad y = Y(s) + \Phi_y \tau. \quad (2.52)$$

Since  $\Delta\Phi = 1/\tau$ , the transport equation (2.49) in the characteristic form simplifies to

$$2\frac{da_0}{d\tau} + \frac{1}{\tau}a_0 = 0, \quad (2.53)$$

with the solutions for

$$\text{incident wave : } a_0 = \frac{1}{-\tau} \mathcal{I}(s), \quad (2.54a)$$

$$\text{reflected wave : } a_0 = \frac{1}{\tau} \mathcal{R}(s), \quad (2.54b)$$

where the function  $\mathcal{I}(s)$  is determined by the wave focusing at the caustic and  $\mathcal{R}(s)$  from  $\mathcal{I}(s)$  by matching across the caustic layer (inner solution). Thus, along any ray tangent to the caustic:

$$\rho \sim \frac{1}{\sqrt{|\tau|}} \begin{bmatrix} \mathcal{I} \\ \mathcal{R} \end{bmatrix} \exp \left[ \frac{ik}{\epsilon} (s + \tau - t) \right]; \quad (2.55)$$

the total solution is then a combination of the incident and reflected waves.

In order to perform matching between inner and outer solutions, we have to rewrite the outer solution in the caustic normal coordinates:

$$\rho_i \sim \left( \frac{2d}{\kappa(s)} \right)^{-1/4} \mathcal{I}(s) \exp \left[ ik \left( \psi - \frac{2}{3} \sqrt{2\kappa(s)} \eta^{3/2} \right) \right], \quad (2.56a)$$

$$\rho_r \sim \left( \frac{2d}{\kappa(s)} \right)^{-1/4} \mathcal{R}(s) \exp \left[ ik \left( \psi + \frac{2}{3} \sqrt{2\kappa(s)} \eta^{3/2} \right) \right], \quad (2.56b)$$

and expand the inner solution (2.47) for large values of the argument:

$$\rho_0 \sim 2 \epsilon^{1/6} d^{-1/4} F(s) \cos \left( \frac{2}{3} \sqrt{2\kappa(s)} |k| \eta^{3/2} - \frac{\pi}{4} \right) e^{ik\psi}, \quad (2.57)$$

where  $F(s) = \frac{\sqrt{\pi}}{2} f(s) [2\kappa(s)k^2]^{-1/12}$ . By matching the outer and inner solutions we find

$$\left( \frac{2}{\kappa(s)} \right)^{-1/4} \mathcal{R}(s) = \epsilon^{1/6} F(s) \exp \left( -i \frac{\pi}{4} \text{sign}(k) \right), \quad (2.58a)$$

$$\left( \frac{2}{\kappa(s)} \right)^{-1/4} \mathcal{I}(s) = \epsilon^{1/6} F(s) \exp \left( i \frac{\pi}{4} \text{sign}(k) \right), \quad (2.58b)$$

i.e. the amplitudes of incident and reflected waves are related by

$$\mathcal{R}(s) = -i \text{sign}(k) \mathcal{I}(s). \quad (2.59)$$

The constructed solution (2.58) indicates that the amplitude of the linear acoustics solution is amplified by a factor of  $\epsilon^{-1/6}$  in the caustic (boundary layer) region of width  $\epsilon^{2/3}$  as per the scaling (2.37).

# Appendices

## 2.A Analogy between geometric acoustic and Hamiltonian mechanics

Notably, the eikonal (1.3) and ray (1.7) equations bring about the direct analogy to mechanics as summarized in table A2.2 – here we revised the logic of (Landau & Lifshitz, 1987), who arrived at the ray equations (1.7) by drawing an analogy to mechanics. However, given that the geometric acoustic corresponds to the limit of short wavelengths, the wave nature of the phenomena becomes subdominant to the particle one and therefore the Hamilton’s equations from particle mechanics applied to the phonon of acoustics is not only not surprising, but also expected thus providing a nice interpretation of geometric acoustics limit.

From the Hamilton’s equations in mechanics shown in table A2.2, it follows that  $dH = \frac{\partial H}{\partial \mathbf{p}} d\mathbf{p} + \frac{\partial H}{\partial \mathbf{r}} d\mathbf{r} + \frac{\partial H}{\partial t} dt = \frac{\partial H}{\partial t} dt$ , i.e. the Hamiltonian  $H$  in mechanics is analogous to the frequency  $\omega$  in geometric acoustics. The action  $S$  is the function of the upper limit of the integral taken along the minimal action trajectory of the system with the Lagrangian  $\mathcal{L}$ :

$$S(t, \mathbf{r}) = \int_{t_0}^t \mathcal{L} dt; \tag{A2.1}$$

variable	action $S$	eikonal $\psi$
Hamilton-Jacobi equation	$\frac{\partial S}{\partial t} + H(t, \mathbf{r}, \nabla S) = 0$	$(\psi_t)^2 - c^2 (\nabla \psi)^2 = 0$
Hamilton’s equations	$\dot{\mathbf{p}} = -\frac{\partial H}{\partial \mathbf{r}}, \mathbf{v} = \dot{\mathbf{r}} = \frac{\partial H}{\partial \mathbf{p}}$	$\dot{\mathbf{k}} = -\frac{\partial \omega}{\partial \mathbf{r}}, \dot{\mathbf{r}} = \frac{\partial \omega}{\partial \mathbf{k}}$

**Table A2.2:** Analogy to mechanics.

the trajectory satisfies the Euler-Lagrange equation

$$\frac{d}{dt} \frac{\partial \mathcal{L}}{\partial \dot{\mathbf{r}}} = \frac{\partial \mathcal{L}}{\partial \mathbf{r}}. \quad (\text{A2.2})$$

Using the Legendre transformation from the Lagrangian to the Hamiltonian  $H = \frac{\partial \mathcal{L}}{\partial \dot{\mathbf{r}}} \dot{\mathbf{r}} - \mathcal{L} = \mathbf{p} \dot{\mathbf{r}} - \mathcal{L}$ , the action integral [A2.1](#) can be rewritten as

$$S(t, \mathbf{r}) = \int_{t_0}^t \mathbf{p} \dot{\mathbf{r}} dt - \int_{t_0}^t H(\mathbf{p}(t), \mathbf{r}(t), t) dt = \int_{\mathbf{r}_0}^{\mathbf{r}} \mathbf{p} d\mathbf{r} - \int_{t_0}^t H dt, \quad (\text{A2.3})$$

where  $\mathbf{r}_0 = \mathbf{r}(t_0)$  and we used the fact  $d\mathbf{r} = \dot{\mathbf{r}} dt$ . Since, in general, any line integral along some path from  $(t_0, \mathbf{r}_0)$  to  $(t, \mathbf{r})$  can be written as

$$S(t, \mathbf{r}) = \int_{t_0}^t \frac{\partial S}{\partial t} dt + \int_{\mathbf{r}_0}^{\mathbf{r}} \frac{\partial S}{\partial \mathbf{r}} d\mathbf{r}, \quad (\text{A2.4})$$

by equating the corresponding terms between equations [\(A2.3\)](#) and [\(A2.4\)](#), we conclude that

$$\frac{\partial S}{\partial t} + H\left(t, \mathbf{r}, \frac{\partial S}{\partial \mathbf{r}}\right) = 0 : \begin{cases} \frac{\partial S}{\partial \mathbf{r}} = \mathbf{p}, & (\text{A2.5a}) \\ \frac{\partial S}{\partial t} + H(t, \mathbf{r}, \mathbf{p}) = 0, & (\text{A2.5b}) \end{cases}$$

where the last equation after replacing the momentum from the first equation becomes the Hamilton-Jacobi equation, which is the first-order partial differential equation (PDE) and hence can be reduced to ordinary differential equations (ODEs) using the method of characteristics, cf. [Appendix 3.B](#).

In this mechanistic context, we can revisit the earlier derivation of the eikonal equation in [§1.1](#). In analogy with geometric optics, we know that the sound traveling between points  $A$  and  $B$  follows a path that minimizes the total time  $T$  elapsed, which can be written as a line integral:

$$T = \int_A^B dt = \int_A^B \frac{n}{c_0} dl, \quad (\text{A2.6})$$

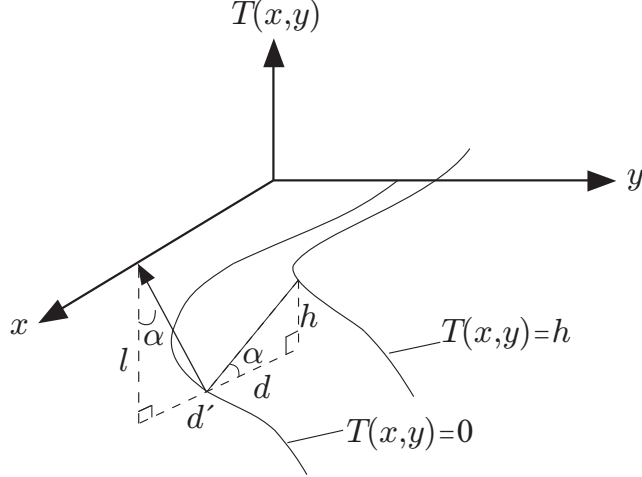


**Figure A2.1:** A geometric view of an advancing front.

where  $n = k_0/k = c_0/c$  is the refractive index of an inhomogeneous medium and  $dl$  is the differential element of displacement along the path. Writing  $c_0T \equiv S$  and  $dl = |\dot{\mathbf{r}}|dt$ , where  $|\dot{\mathbf{r}}| = \sqrt{\dot{x}^2 + \dot{y}^2 + \dot{z}^2}$ , for the above line integral we get

$$S = \int_{t_0}^t n(\mathbf{r})|\dot{\mathbf{r}}| dt, \quad (\text{A2.7})$$

minimization of which should give the path  $\mathbf{r}(t)$  joining points  $A$  and  $B$ . Considering the integrand as a Lagrangian  $\mathcal{L} = n(\mathbf{r})|\dot{\mathbf{r}}|$ , we can determine the momentum  $\mathbf{p} = \partial\mathcal{L}/\partial\dot{\mathbf{r}}$ , which satisfies  $|\mathbf{p}|^2 = n^2$ , while the corresponding Hamiltonian  $H = \mathbf{p} \cdot \dot{\mathbf{r}} - \mathcal{L}$  vanishes identically. Hence,

$$S = \int_{t_0}^t \mathcal{L} dt = \int_{t_0}^t \mathbf{p} \cdot \dot{\mathbf{r}} dt \Rightarrow \nabla S = \mathbf{p}, \quad \frac{\partial S}{\partial t} = 0, \quad (\text{A2.8})$$

and therefore we recover the eikonal equation  $|\nabla S|^2 = n^2(\mathbf{r})$ .

Finally, since the eikonal equation arises in the context of front (surface) propagation, its meaning should be purely geometric, which is easy to see by considering the curve evolution in the  $(x, y)$  plane described by the equation  $\frac{\partial \mathbf{C}}{\partial t} = v \mathbf{n}$ , where  $\mathbf{C}$  is the vector of curve point coordinates,  $\mathbf{n}$  the unit normal vector, and  $v$  is the speed of the front at each point of the plane. Let  $T(x, y)$  be a graph of the solution surface, cf. figure A2.1, i.e. the level sets of which are the evolved curves (fronts) or the time at which the curve crosses a point  $(x, y)$  in the plane. As follows from the figure, the

speed of the front is given by  $v(x, y) = \frac{d}{h} = \frac{1}{\tan \alpha} = \frac{1}{d'} = \frac{1}{|\nabla T|}$ , which means that  $T(x, y)$  satisfies the eikonal equation  $|\nabla T| v = 1$ .

## 2.B Electromagnetic shock wave generator

The setup in figure A2.2 consists of five functional parts detailed below: (a) an electromagnetic shock tube assembly as well as (b) charging, triggering, measuring, and capturing units; the latter is discussed in §2.1.1.1.

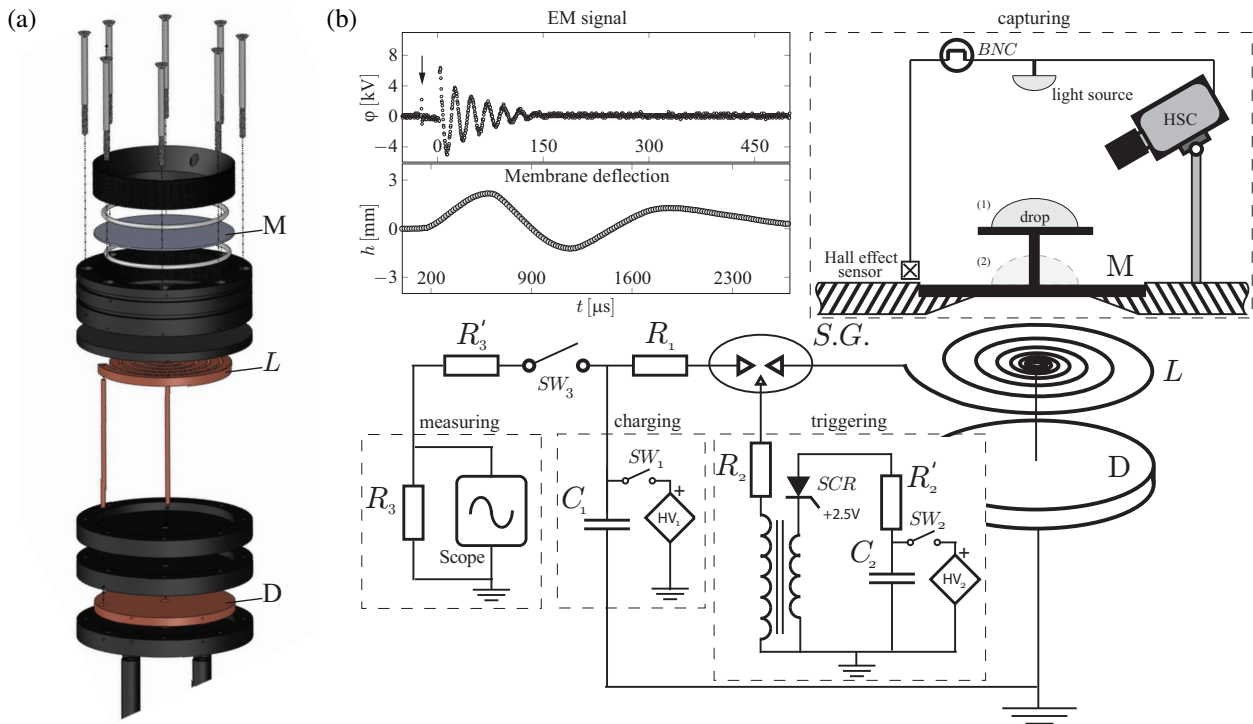


**Figure A2.2:** Schematics of the experimental setup. (a) Exploded view of the EMSWG gun, which consists of a slab spiral coil  $L = 1 \mu\text{H}$  mounted on the face of an acoustically hard, electrically insulated base and is separated by a thin insulating layer from an opposing metallic membrane  $M$ , a thick copper disk  $D$ , and a copper membrane ( $D = \varnothing 76 \text{ mm}$ ) which are assembled in a case made of Delrin. The slab spiral coil is of outer diameter 97 mm and has 5 turns with square cross section ( $6.25 \times 6.25 \text{ mm}$ ) with the gap between two sequence turns being 3.1 mm. A thick copper disk ( $\varnothing 125 \times 12.5 \text{ mm}$ ) is placed underneath the flat spiral coil to damp undesired EM field oscillations. Smooth copper membrane (alloy 110) of different thicknesses  $h_0 = 0.034 - 0.5 \text{ mm}$  is clamped in a close proximity above the flat spiral coil at 6.25 mm distance. (b) Electrical circuit. Inset shows examples of a scaled main signal in the circuit and the corresponding measured membrane deflection trajectory. Initial energy and membrane thickness are 390 J and 0.1 mm, respectively. The delay between membrane deflection and EM oscillations is due to the inertia of the former; for the same reason the membrane trajectory does not follow the EM oscillations.

*An electromagnetic shock tube.* Discharging the capacitor bank into the coil builds up a substantial transient current and hence electromagnetic field in the coil, which in turn induces eddy currents in both the metal membrane  $M$  (a load-bearing element on which a liquid drop of varying volume is placed) and in a thick copper disk  $D$ . According to Lenz's law, the direction of the eddy current always opposes the primary current (in the coil) that produced it. Next, these two opposite currents induce a Lorentz force which repels the membrane away from the coil. Also the eddy current in the thick copper disk  $D$  generates a secondary magnetic field which opposes the primary one and damps the undesired magnetic field to some extent. The acceleration of the membrane produces a pressure wave in the medium on top of the membrane such as in the drop sitting on the membrane. If the acceleration is rapid, the pressure wave will steepen, as it propagates, due to the nonlinearities in the medium and a shock wave will form. The peak EM pressure in the vicinity of the membrane can be estimated from  $p_{\max} = 2\mu_0 n^2 I_{\max}^2 / D^2$ , where  $I_{\max}$  is the peak discharge current,  $D$  the diameter,  $n$  the number of turns in the slab coil, and  $\mu_0$  the permeability of the free space (Eisenmenger, 1962). Thus the peak emitted pressure pulse is proportional to the square of the maximum current. To maximize the pressure in the near field of the membrane one should increase the turns density  $n$  on the slab coil, which, however, increases the coil inductance  $L$  and thus reduces the maximum current  $I_{\max}$ . The parameters of the circuit were chosen to achieve a fast decaying EM oscillatory behavior, which is confirmed by the oscillogram of the current in the inset of figure A2.2b. The membrane deflection shows the expected natural frequency oscillations. In fact, as one can see from this inset, the form of EM signal is not crucial<sup>13</sup> as it operates on a much shorter time scale compared to that defined by the circular plate dominant natural frequency  $\omega_M \sim h_0 (Y/\rho)^{1/2} / D$ , where  $Y = 128$  GPa is the Young modulus and  $\rho = 8960$  kg m<sup>-3</sup> the density of the copper. Use of membranes of different thicknesses  $h_0 = 0.034, 0.1, 0.17, \text{ and } 0.5$  mm allowed us to operate when  $\tau_M = 2\pi/\omega_M$  could be either much longer or comparable to the essential timescales of the drop dynamics (Appendix 2.C)

---

<sup>13</sup>Indeed, the oscillator  $\ddot{x} + \omega_M^2 x = \delta_D(t)$  driven by the delta-function  $\delta_D(t)$  signal behaves as  $x(t) \sim t H(t)$  at early times, i.e. in the same fashion as in the inset of figure A2.2b. For the same reason and due to the screening effect of the copper membrane we can neglect any influence on surface tension by the EM field.

– this makes the phenomena already complex enough even without the fluid-structure interaction present in drop impacts on soft membranes (Howland *et al.*, 2016; Chantelot *et al.*, 2018a).

*Electrical circuit and components.* Experiments were carried out with the apparatus sketched in figure A2.2b. Two 10 kV, 10  $\mu$ F capacitors  $C_1$  (Arizona Capacitors, LK100-106YND) are charged with a high voltage power supply  $HV_1$  (Matsusada, EQ-30P1-LG) to the desired voltage  $\varphi = 8.7 - 12.5$  kV. Upon charging, the high voltage power supply is disconnected and a trigger pulse (20 kV) is sent to a sealed spark gap  $S.G.$  (Del Mar Photonics, RU-78-TSG), which guarantees repeatability of the experiments compared to an in-house constructed spark, which is prone to changes in the ambient humidity and temperature since the physical mechanism of a spark gap operation is based on streamer initiation and propagation across the gap, as well as subsequent heating to form the arc channel decreasing the spark gap resistance and thus leading to the capacitor discharge (Williams & Peterkin, 1989). Also, extremely short risetime of sparkgaps (Lehr *et al.*, 1999) enables accurate timing necessary for constructing a time series from delayed snapshots. The trigger pulse releases the energy stored in the capacitor, which is then delivered to a flat spiral coil. Circuit elements are connected with short lengths of aluminum bar or braided copper wire, so that the stray inductance of the circuit excluding the EMSWG unit was kept to a minimum of 535 nH. To reach a variety of peak pressures  $p_{\max}$ , different  $h_0$  and initial stored energies in capacitors ( $E = \frac{1}{2} C \varphi^2 = 250, 390, 500, 750, 1000$  J) were used<sup>14</sup>.

*Measuring/discharge circuit.* To ensure the repeatability of the experiment a secondary circuit, consisting of  $R'_3 = 5$  M $\Omega$  (Ohmite 588-MOX-H-025004FE) and  $R_3 = 50$  k $\Omega$ -10 W resistors as well as an oscilloscope (Tektronix TDS 2024B), was connected in parallel to the main circuit in order to measure a scaled signal. In each run, voltage across the 50 k $\Omega$  resistor was recorded using the oscilloscope and a Tektronix P2220 voltage probe with attenuation factor of 10X. A sample measured signal for sequence capacitor configuration charged to 12.5 kV is shown in the inset of figure A2.2b: just before the main signal there is a small peak with a maximum amplitude of  $\sim 2$  kV

---

<sup>14</sup>To do that, we used different combinations of two 10 kV, 10  $\mu$ F capacitors. To have 250 and 390 J energy in the capacitors, we connected them in sequence and charged to 10 kV and 12.5 kV, respectively. In the case of 500 J, a single capacitor was charged to 10 kV. And, in order to have 750 and 1000 J energies, capacitors were connected in parallel and charged to 8.7 and 10 kV, respectively.

which corresponds to the trigger signal (shown with arrow). After each experiment a remaining charge in the capacitors was precisely measured using the same type of circuit as shown in figure [A2.2b](#), but with different values of the two resistors,  $R'_3 = 500 \Omega$  (Ohmite 20J500E) and  $R_3 = 50 \Omega$  (20J50RE), connected in sequence with the capacitor. The energy remaining in the capacitors ranged only from 0.1 J in the 250 J runs to 0.5 J in the 1000 J runs.

*The triggering circuit* includes two capacitors  $C_2$  (EPCOS, B43564A5108M000), a thyristor (Powerex, T600121804BT), a transformer (Del Mar Photonics, TT511A), a  $R_2 = 10 \text{ W-}500 \Omega$  resistor (Ohmite 20J500E), and a high voltage power supply  $HV_2$  (Stanford Research System, PS325/2500V-25W). To generate a trigger pulse, capacitors were charged up to 400 V and then disconnected from a high voltage power supply. The thyristor, used in our setup instead of a mechanical switch which would be prone to non-repeatability due to sparks at  $O(10^2)$  V, is controlled by receiving a 2.5 V pulse on its own trigger lead, enabling the delivery of the capacitors' energy to the transformer. Measured voltage across the primary winding of the transformer showed that the voltage at the input was around 200 V, which the transformer boosted up to  $\sim 20$  kV. This output voltage provides the trigger pulse to induce breakdown in the sealed spark gap, which eventually delivers the main capacitor  $C_1$  energy to the flat spiral coil  $L$ .

## 2.C Summary of characteristic time and length scales

The drop dynamics is governed by several factors: compressibility, capillarity, viscous diffusion, and inertia. Each of these processes is characterized by associated time and length scales estimated in table [A2.3](#) based on the available data for the temperatures close to our experimental conditions. Since the kinematics data indicate that  $V_{\max}$  and  $a_{\max}$  are interrelated, we may chose to express all relevant scales either in terms of the acceleration  $a = a_{\max}$  or velocity  $V = V_{\max}$ . For concreteness, in table [A2.3](#) we use only acceleration. Characteristic sessile drop radius  $R_0$  is taken to be equal to the radius of a sphere having the volume equal to that of the drop.

Process	Time scale	[s]	Length scale	[cm]
Inertia	$\tau_a^d = (R_0/a)^{1/2}$	$1.6 \cdot 10^{-4}$	$R_0$	0.25
Compressibility	$\tau_c^d = R_0/c_0$	$(1.7; 2.1; 1.3) \cdot 10^{-6}$	$R_0$	0.25
	$\tau_{\text{tensile}} = \zeta/[K]$	$O(10^{-12}; 10^{-12}; 10^{-10})$		
	$\tau_{\text{shear}} = \mu/G_\infty$	$O(10^{-13}; O(10^{-13}; 10^{-10})$		
Viscosity	$\tau_v^d = R_0^2/\nu$	$7.0; 4.1; 5.6 \cdot 10^{-3}$	$R_0$	0.25
	$\tau_a^v = (\nu/a^2)^{1/3}$	$(4.5; 5.3; 48.2) \cdot 10^{-6}$	$l_a^v = (\nu^2/a)^{1/3}$	$(2.0; 2.8; 232.1) \cdot 10^{-6}$
Surface tension	$\tau_\sigma^v = \nu^3/\gamma^2$	$1.4 \cdot 10^{-10}; 4.5 \cdot 10^{-9}; 0.56$	$l_\sigma^v = \nu^2/\gamma$	$(1.1; 8.3) \cdot 10^{-8}; 2.5 \cdot 10^{-2}$
	$\tau_\sigma^d = (R_0^3/\gamma)^{1/2}$	$(1.5; 2.4; 1.7) \cdot 10^{-2}$	$R_0$	0.25
	$\tau_\sigma^{v,d} = \nu R_0/\gamma$	$3.1 \cdot 10^{-5}; 1.4 \cdot 10^{-4}; 5.6 \cdot 10^{-2}$	$R_0$	0.25
	$\tau_a^\sigma = (\gamma/a^3)^{1/4}$	$(1.6; 1.3; 1.5) \cdot 10^{-5}$	$l_a^\sigma = (\gamma/a)^{1/2}$	$(2.7; 1.7; 2.2) \cdot 10^{-5}$

**Table A2.3:** Characteristic time and spatial scales for a (water, ethanol, glycerol) drop of radius  $R_0 = 0.25$  cm, surface tension  $\sigma = (0.072, 0.022, 0.063)$  N m<sup>-1</sup> at 25°C (Lide, 2006-2007), density  $\rho = (998, 789, 1261)$  kg m<sup>-3</sup> at 20°C (Lide, 2006-2007), acceleration  $a = 10^5$  m s<sup>-2</sup>, sound speed  $c_0 = (1479, 1170, 1923)$  m s<sup>-1</sup> at 20°C (Pryor & Roscoe, 1954; Giacomini, 1947; Association, 1963), dynamic viscosity  $\mu = (0.89, 1.2, 1410) \cdot 10^{-3}$  Pa s at 20°C (Lide, 2006-2007), kinematic viscosity  $\nu = \mu/\rho$ , the second (volume) viscosity  $\zeta = (2.4, 3.2, 1490) 10^{-3}$  Pa s at 17.4°C (Liebermann, 1949; Han *et al.*, 2008),  $[K] = K_\infty - K_0 = O(K_\infty)$  with static  $K_0$  and dynamic  $K_\infty = (2.19, 0.9, 4.34)$  GPa volume elastic moduli at 20°C (Shaughnessy *et al.*, 2005), as well as dynamic shear modulus  $G_\infty = (2.44, 1.02, 3.5)$  GPa at 25°C (Rodnikova, 2007). For brevity we introduce  $\gamma \equiv \sigma/\rho$ .

## 2.D SW reflection from plane interface

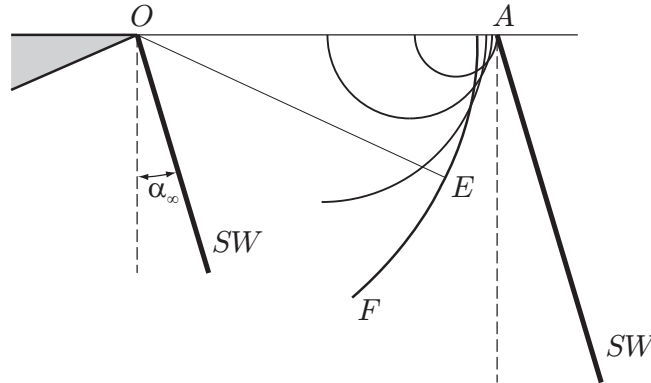


**Figure A2.3:** Reflection of a shock wave from a free surface (OA).

Since SW naturally interacts with free interfaces in the phenomena under consideration let us review SW reflection from interface in the simplest situation when both the interface and a SW are plane, cf. figure A2.3: a plane shock (compression) wave hits the free interface at time  $t = 0$  at the point  $O$  with the angle of incidence  $\alpha_\infty$  measured between the SW front and the normal to the

interface. In the acoustic approximation we find that the point of SW-interface intersection  $A$  moves along the free interface with velocity  $c / \cos \alpha_\infty$ , where  $a_0$  is the speed of sound in liquid. At each point of the free surface, at the moment of SW passage, there is formation of a rarefaction wave, at the front of which the pressure drops to zero. The front of each of such waves is half-cylinder with the axis coinciding, at the moment of the rarefaction wave formation, with the line of the SW intersection with the free surface. The envelope of the fronts of these cylindrical waves forms the front of the reflected wave  $AE$ . At the point  $E$  this front becomes the circle arc  $EF$  corresponding to the first rarefaction wave formed at the point  $O$ . To determine the angle of reflection  $\beta$ , i.e. the angle between the plane of the reflected wave  $AE$  and the normal to the free surface, notice that  $\cos \beta = OE/OA = \cos \alpha_\infty$ , which means that  $\beta = \alpha_\infty$ . The angle at which the velocity of point  $A$  equals to the velocity of the front of ‘rarefaction wave’ (wave of lowering pressure) is denoted as critical  $\alpha_*$ . Hence, there are two key regimes of reflections: *regular*  $\alpha_\infty > \alpha_*$ , when rarefaction waves arising on the free surface do not disturb the front of the SW because they cannot outrun their source, and *irregular*,  $\alpha_\infty < \alpha_*$  when rarefaction waves interact with the front of the SW by deforming (bending) the original shape of the SW front and reducing the pressure in it. This transition from regular to irregular reflection is analogous to the SW reflection from a solid in which transition from regular to Mach reflection takes place, so that a triple point is initiated consisting of incident shock, reflected shock, and a Mach stem along with its corresponding slip surface (Liepmann & Roshko, 2002). The same behavior is observed in SW reflection from liquid interfaces (Sembian *et al.*, 2016). The region of their interaction near the point  $A$  can be understood in the moving frame of reference from the point of view of the Prandtl-Meyer flow (Liepmann & Roshko, 2002).

## 2.E Image processing

To do image processing, a sequence of photos were used as input of code. As an illustration, the image processing for 45% wt glycerol-water solution is presented here. Following steps have been done for each time stamp, but shown here for 1000  $\mu s$ . First, resize image from  $256 \times 256$  to

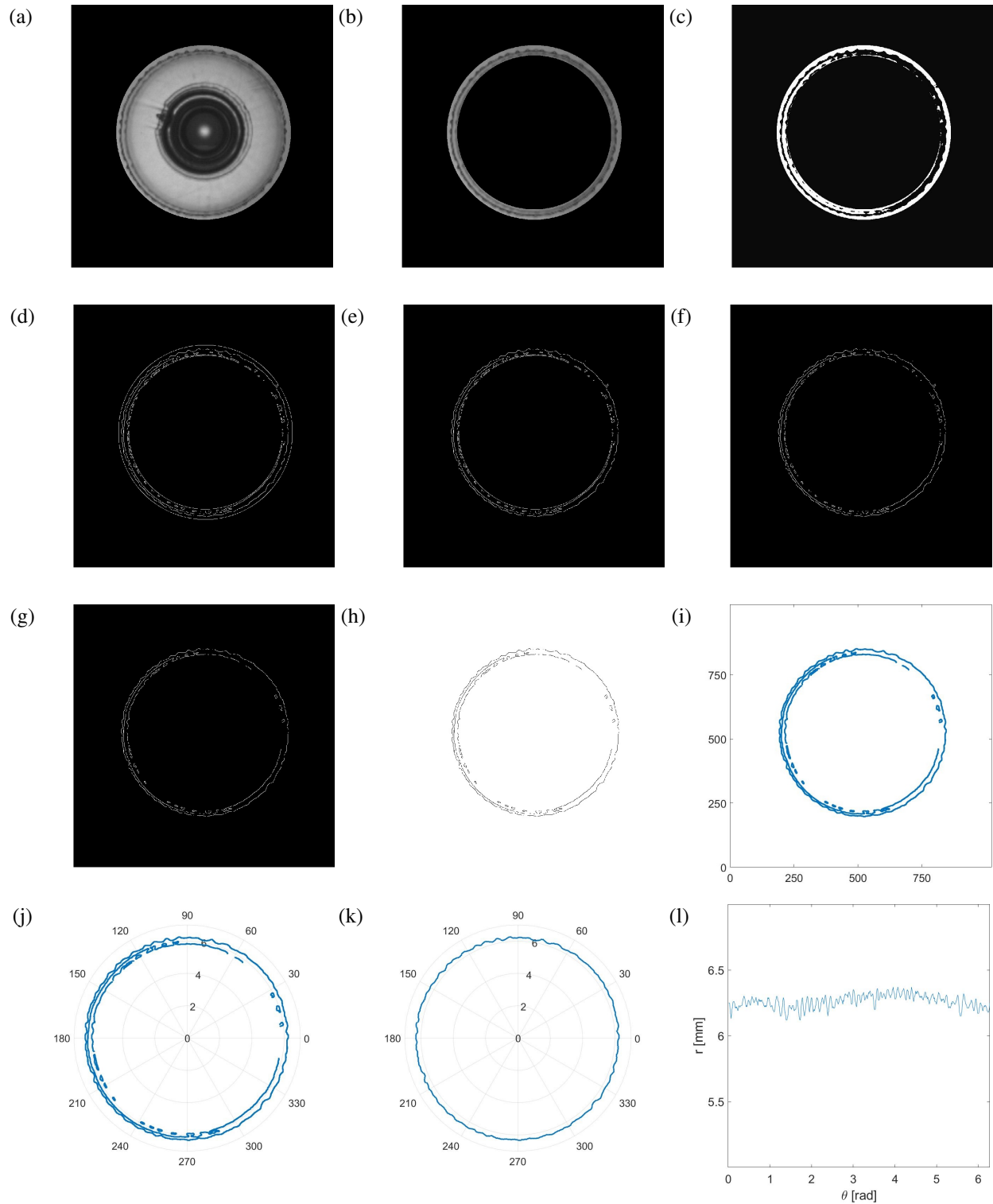


**Figure A2.4:** Image processing: (a) crop the frame to a circular frame; (b) crop the frame to a ring including the crown rim; (c) intensity changed; (d) edge detection; (e) frame outer edge removal; (f) frame inner edge removal; (g) small object removal; (h) switch background to white; (i) coordinate of objects in the image; (j) switch from a  $1024 \times 1024$  pixels to polar coordinate; (k) coordinate of the crown rim; (l) radius vs  $\theta$ .

1024 × 1024: this helps to find small object in more details. Next, crop the image to a ring shape frame, cf. figure A2.4a. Frame has to be such that to contain rim of the crown. Next, change the intensity of the rim, and then detect edge of the crown, cf. figure A2.4d. Edge detection function finds the inner and outer edge of the ring shape frame as shown in above image. In the next step, the code removes two circular lines correspond to inner and outer diameter of the ring shape frame. Remove small objects with size less than 30 pixels, cf. figure A2.4g. Switch image background to white and find coordinate of the of objects in image. Switch to polar coordinate. Code will search from 0 to  $2\pi$  to keep the outer diameter of the crown. In each angle it looks for point which is in more distance from the origin and remove all other points which are closer to the origin. After doing this, the code finds about 5000 points which these points form the diameter of the crown that we are looking for. Plot in radius vs  $\theta$ . Local maximum of radius shows number of fingers.

## 2.F Data fit

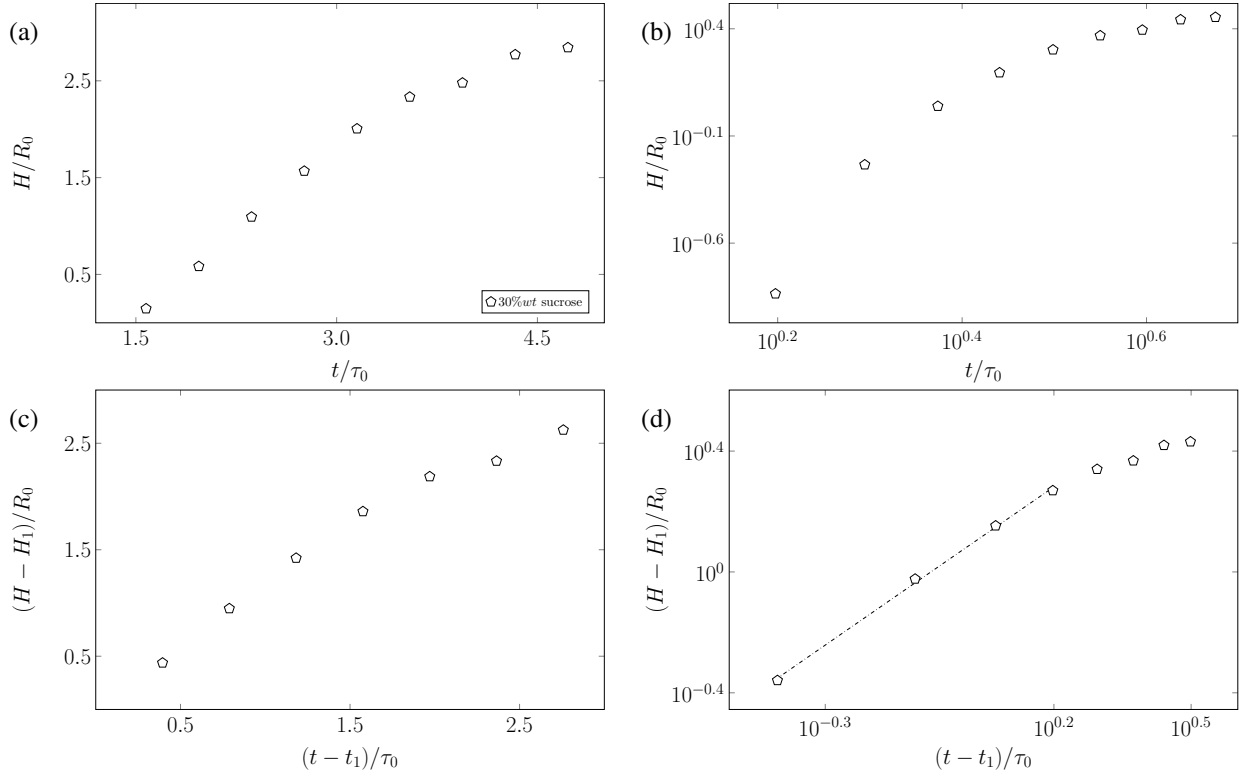


**Figure A2.5:** Procedure of curve fitting for non-dimensional height of 30% wt water-sucrose solution vs non-dimensional time (Figure 2.13(d)). Figure (a): original experimental data in non-dimensional form. Figure (b): log-log plot of the non-dimensional data. Figure (c): data shifted to the origin. To do shift each data set was subtracted by the amount of first element of that vector. Figure (d): curve fit in log-log scale of the shifted data. To do the curve fit  $\hat{H} - \hat{H}_1 = \beta(\hat{t} - \hat{t}_1)^\alpha$  was considered as a function and then  $\alpha$  and  $\beta$  determined. Terms  $\hat{H}$  and  $\hat{t}$  show radius and time in the non-dimensional form. Also,  $\hat{H}_1$  and  $\hat{t}_1$  represent the first data point of the non-dimensional radius and time, respectively.

Data acquired from experiments seem to follow the power-law, but the function  $y = ax^b$  is applicable when data points pass through the origin. To shift the data sets to the origin, each data set was subtracted by the first data point in the data set. After shifting to the origin, data were fitted by function  $y = ax^b$ , where  $y$  shows the values on the vertical axis and  $x$  shows the values of the horizontal axis. Values of  $a$  and  $b$  were found through data fit procedure. An example of the procedure has been presented in Figure A2.5 to find fitted curve to non-dimensional crown height with respect to non-dimensional time in 30% wt water-sucrose solution.

## 2.G Acoustic reflection and refraction

To understand the basics of shock wave reflection and refraction from a free interface, one may appeal to the limit of weak shock waves, which become acoustic waves. In terms of *acoustic impedance*  $z = \rho c$  measured in Rayles and representing the ratio of acoustic pressure to particle velocity in the 1D case (Kinsler *et al.*, 1999), the reflection coefficient at the interface between two media, for an acoustic wave incident (from media 1) at the angle  $\theta_1$  with respect to the vector normal to the interface, reads

$$\Gamma = \frac{z_2/z_1 - \sqrt{1 - (n-1) \tan^2 \theta_1}}{z_2/z_1 + \sqrt{1 - (n-1) \tan^2 \theta_1}}, \text{ where } n = \left(\frac{c_1}{c_2}\right)^2, \quad (\text{A2.9})$$

which for normal incidence,  $\theta_1 = 0$ , reduces to  $\Gamma = (z_2 - z_1) / (z_2 + z_1)$ . Taking the values of acoustic impedance for air  $z_2 = 415$  Rayles and for water  $z_1 = 1.48 \cdot 10^6$  Rayles, i.e. when incident wave propagates in water and reflects from the interface with air, we find  $\Gamma \simeq -1$ , that is the interface resembles a pressure release boundary, i.e. when the reflected wave receives a  $180^\circ$  phase shift – in the context of a SW reflection we say that the reflected wave is a rarefaction wave (RW). If, however,  $\Gamma = +1$ , which takes place when  $z_2 \gg z_1$ , the interface behaves as a rigid boundary – again, in the context of a SW reflection we say that the reflected wave is a SW.

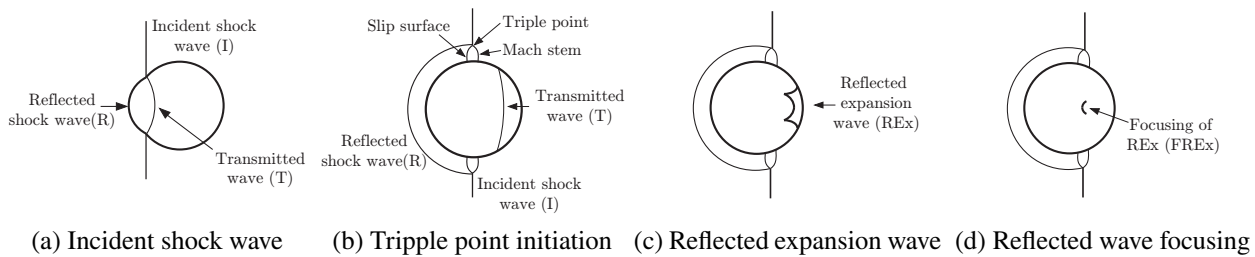


**Figure A2.6:** Shadowgraph images of a shock wave hitting a water column (Sembian *et al.*, 2016).

With reference to figure A2.6, when the incident shock wave (I) hits the water column, it gets reflected (R), diffracted, and transmitted (T) at the upstream interface (cf. figure A2.6a). When the incident is a shock/compression wave, the transmitted wave will also be a shock/compression

wave; however the reflected wave may either be an expansion or a shock wave depending on the acoustic impedance, defined as  $Z = \rho c$  where  $c$  is the speed of sound, as the continuity in pressure and velocity across the interface should be satisfied. Since  $Z_{air} < Z_{water}$ , the reflected wave is a shock wave. When a planar incident shock wave encounters a cylindrical convex surface, a regular reflection occurs as long as the angle of incidence is above a certain critical value, the so-called detachment angle. When the angle of incidence becomes less than the detachment angle, a transition from regular to Mach reflection takes place. A triple point is initiated consisting of incident shock, reflected shock, and a Mach stem along with its corresponding slip surface (cf. figure A2.6b). When reaching the downstream water-air interface, the transmitted shock gets reflected as an expansion wave, REx (cf. figure A2.6c), since  $Z_{water} > Z_{air}$ . Due to the column's downstream concave boundary the reflected expansion wave focuses at a point, FREx, (cf. figure A2.6d) creating “negative pressures.”

## 2.H On identification of detachment and disintegration times

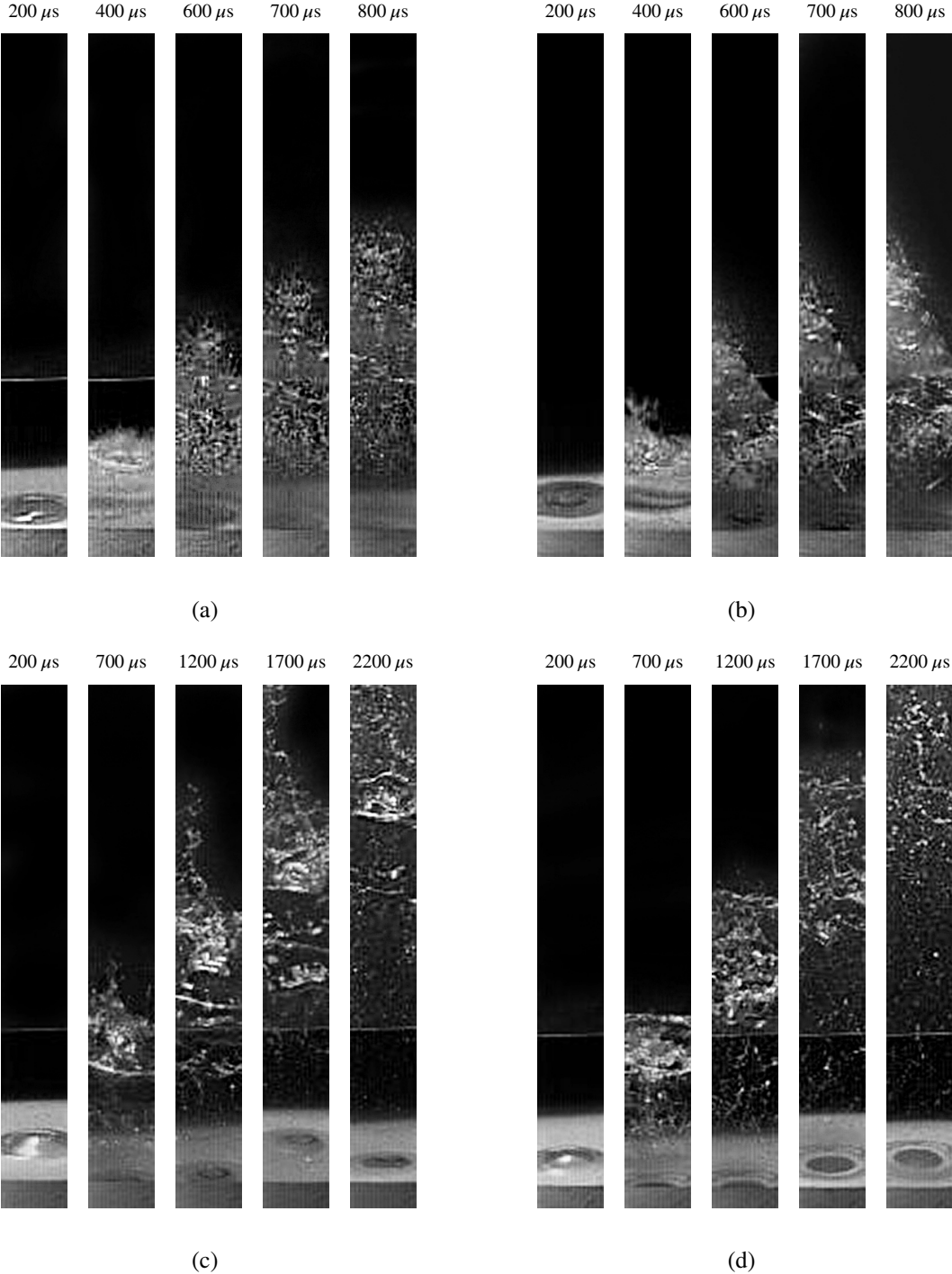


**Figure A2.7:** Disintegration time of different liquids in the cupola regime. Figure (a) to (d) correspond to water, 22% wt water-ethanol, 80% wt water-glycerol, and 50% wt water-sucrose, respectively. Membrane thickness, initial energy of the capacitors, and the droplet size were fixed and equal to 0.17 mm, 1000J, and 50  $\mu$ l, respectively. Disintegration time of water, 22% wt water-ethanol, 80% wt water-glycerol, and 50% wt water-sucrose are 800  $\mu$ s, 725  $\mu$ s, 1850  $\mu$ s, and 1375  $\mu$ s, respectively. Physical image size is 6  $\times$  48 mm<sup>2</sup>.

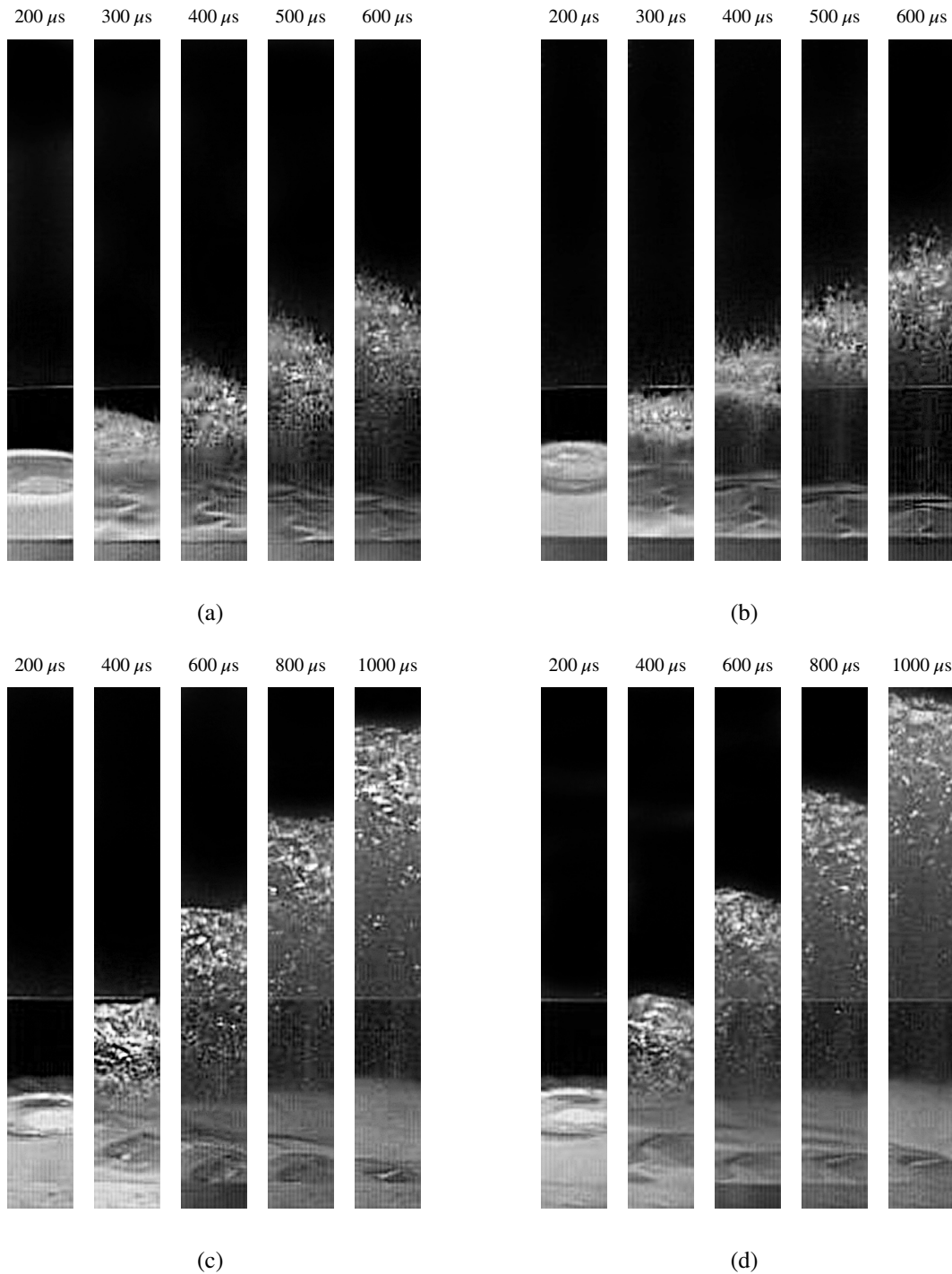


**Figure A2.8:** Disintegration time of different liquids in the direct atomization regime. Figure (a) to (d) correspond to water, 22% wt water-ethanol, 80% wt water-glycerol, and 50% wt water-sucrose, respectively. Membrane thickness, initial energy of the capacitors, and the droplet size were fixed and equal to 0.034 mm, 1000 J, and 50  $\mu\text{l}$ , respectively. Disintegration time of water, 22% wt water-ethanol, 80% wt water-glycerol, and 50% wt water-sucrose are 350  $\mu\text{s}$ , 325  $\mu\text{s}$ , 575  $\mu\text{s}$ , and 575  $\mu\text{s}$ , respectively. Physical image size is 6  $\times$  48 mm<sup>2</sup>.

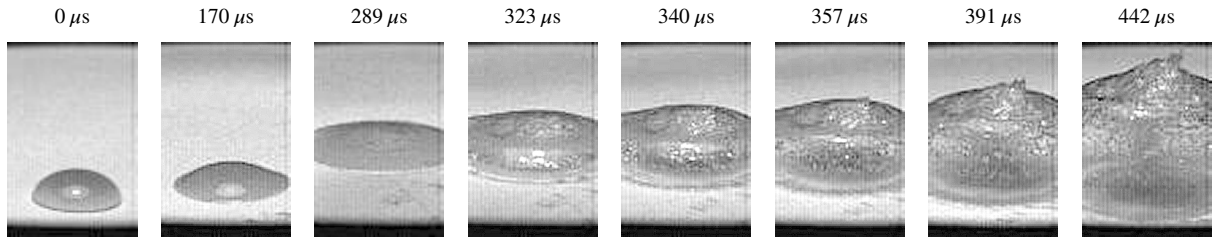


**Figure A2.9:** 50% wt water-sucrose liquid droplet detachment from the membrane in the cupola regime. Detachment time is  $323 \mu\text{s}$ . Membrane thickness, initial energy of the capacitors, and the liquid droplet size were fixed and equal to  $0.17 \text{ mm}$ ,  $1000 \text{ J}$ , and  $50 \mu\text{l}$ , respectively. Physical image size is  $6 \times 9 \text{ mm}^2$ .

## 2.I Stain detection via image processing

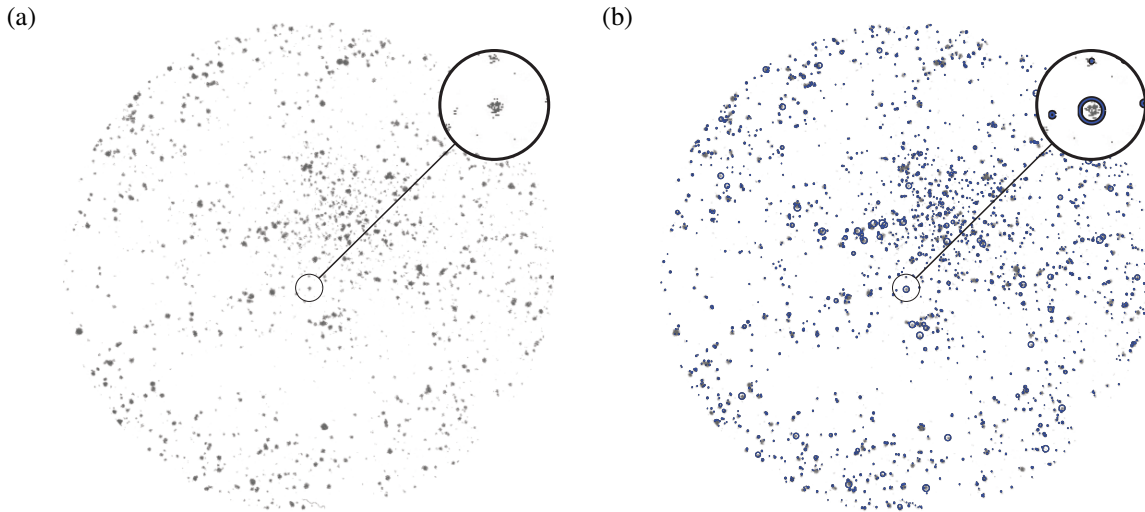


**Figure A2.10:** Hough transform on stains to determine the radii of the microdroplets. (a) scanned and enhanced image of the microdroplets distribution on the Whatman paper; (b) implementing Hough transform to fit circles to stains and acquiring coordinates of the centers and radii of circles. Applying this procedure to the scanned images, probability distribution of microdroplets' radii were analyzed and recorded. The images that are shown in this figure are for DI water experiment. The membrane thickness, liquid droplet size, capacitors' energy were fixed and equal to  $0.034 \text{ mm}$ ,  $25 \mu\text{l}$ ,  $1000 \text{ J}$ , respectively.

The purpose of the image processing in this section is to find radii of the microdroplets in the direct atomization regime. Different liquids were employed to study the effect of the viscosity and surface tension on the size of the microdroplets. The whole procedure is divided in two sections: the experimental procedure and the analysis via image processing.

In the experimental section, to be able to visualize the microdroplets, red food-colour was added to the liquids (< 1% wt). Whatman paper (grade 1<sup>15</sup>) placed 200 mm away from the membrane surface and parallel to it. By running experiment and atomization of the liquid droplet, microdroplets hit the Whatman paper and make stains on the paper. Then, the membrane and the Whatman paper were replaced for the next experiment. After doing experiments and collecting papers, they were scanned to get high resolution images of the stains.

In the image processing section, high resolution images were used as an input for a Matlab code. In the Matlab code, Hough transform used to fit circles to stains in the images. Using Hough transform we could find radii and centers of circles/stains in pixels. The next step was to translate these radii in pixels to radii of the microdroplets in meters. In atomization process, a liquid droplet breaks to a number of microdroplets, therefore we can write

$$\Omega = \sum_{i=1}^n \frac{4}{3} \pi r_i^3, \quad (\text{A2.10})$$

which  $\Omega$ ,  $n$ , and  $r_i$  are initial volume of the droplet (25  $\mu\text{l}$  in all cases), number of stains on the paper (each stain correspond to a microdroplet), and radius of  $i^{\text{th}}$  microdroplet in meters. Also, it was assumed that after atomization, all microdroplets hit the Whatman paper and we consider the following formula

$$\Omega = \xi \sum_{i=1}^n \pi [k(r_{pxl})_i]^2, \quad (\text{A2.11})$$

where  $k$  is a coefficient that scales radii from pixels to meters and  $(r_{pxl})_i$  is the radius of  $i^{\text{th}}$  stains in pixels. Constant  $\xi$  demonstrates the amount of penetration of the microdroplets in the paper, thus has the length dimension. From equation (A2.11) it was found that

$$\xi k^2 = \Omega / \sum_{i=1}^n \pi [(r_{pxl})_i]^2. \quad (\text{A2.12})$$

---

<sup>15</sup>Diameter: 150 mm, medium porosity (as per manufacturer specification for grade 1 Whatman paper, 10.5 seconds takes to pass 0.155 m<sup>3</sup> air from 1 m<sup>2</sup> surface area of the paper).

Now by equating the right hand side of equations (A2.10) and (A2.11) we find

$$\frac{4}{3}\pi(r_i)^3 = \xi k^2 \pi [(r_{pxl})_i]^2 \Rightarrow r_i = \left(\frac{3}{4}\xi k^2\right)^{1/3} [(r_{pxl})_i]^{2/3}. \quad (\text{A2.13})$$

which the value of  $\xi k^2$  is substituted from equation (A2.12). Using equation (A2.13) we could find the radius of the microdroplets in spherical form.

# Chapter 3

## Folds on soap films

Soap films have been not only the object of children’s play, but also the subject of scientific research since the time of Leonardo Da Vinci. Earlier systematic experimental studies of bursting soap films using high-speed flash photography (McEntee & Mysels, 1969) revealed a precursor wave preceding the expanding hole, with a disturbed region of shrinking film material in between. Mysels referred to this wave and the disturbed region as the “shock wave” and the “aureole”, respectively. These observations have overturned some misconceptions regarding the bursting process in earlier theoretical and experimental works (Dupré, 1867; Plateau, 1873), which concluded that a rolled up rim collected all of the disappearing film, leaving the rest of the film undisturbed and thus served as a basis for Taylor’s work. Frankel & Mysels (1969) qualitatively interpreted this as a shock wave in the surfactant film and showed that any significant aureole preceding the rim of the expanding hole in a punctured soap film is related to large changes in surface tension as the film shrinks and thickens. In this chapter we will report and interpret new phenomena associated with the aureole and accidentally discovered in our laboratory – the formation of folds on retracting soap films.

### 3.1 Experiments

#### 3.1.1 Materials and methods

Below we discuss the details of experimental platform in §3.1.1.1 and the soap solutions preparation using surfactant in §3.1.1.2.

### 3.1.1.1 Experimental setup components

The main components of the experimental setup to generate a flat soap film include the soap film frame, withdrawal apparatus, soap film thickness measurement system, soap film release electrical circuit, and high-speed visualization. For each component, exhaustive details are provided to have a complete picture of the experiments. The experimental platform should be capable of (a) allowing the creation of a flat soap film in a reasonably short time as the soap film lifetime is on the order of a minute, (b) eliminating any artifacts that may influence test conditions and results accordingly, and (c) creating a precisely repeatable electrical signal for the purpose of the soap film release by Joule heating of the film boundaries.

*Soap film frame.* The customized frame assembly and the details of each of the components are shown in figure 3.1. The frame is capable of adjusting different aspect ratios of a rectangular geometry  $l_1 \times l_2$ ; however in all experiments square frame ( $l_1 = l_2 \equiv l$ ) have been employed with a length  $l$  of 50 mm on each side. The soap film is formed on a continuous conducting wire which is strung around four aluminum posts (E/Z connectors DU-BRO brand). The wire ends are held in place using a clamp, which is manually adjusted to have a tensioned and straight wire frame during the experiments. Two different configurations of the wire in the corners have been used to study the effect of sharp (G) and curved (H) corners on the outcome of the soap film patterns.

Even though in previous experimental studies on soap film a variety of materials has been employed to build a frame including glass (McEntee & Mysels, 1969; Evers *et al.*, 1996) and plastics (Berg *et al.*, 2005), due to the required impulse heating in our experiments we must use a conductive material. Lyklema *et al.* (1965) used a nickel-chromium alloy with the diameter of  $12.5 \mu\text{m}$  for the formation of soap film and Momsen *et al.* (1989) showed that NiChrome (NiC) 60 is a great choice for surface tension measurements by Wilhelmy plate method. In only one study it has been reported that NiC alloy is not an appropriate material to be used for a soap film frame, which might be due to the requirement of long soap film lifetime ( $\sim 1000$  s) in their experiments (Berg *et al.*, 2005). The material of the metal wire was the same in all the experiments, because implementing a single type material allows one to minimize the variation in the surface properties of the wire such as rough-

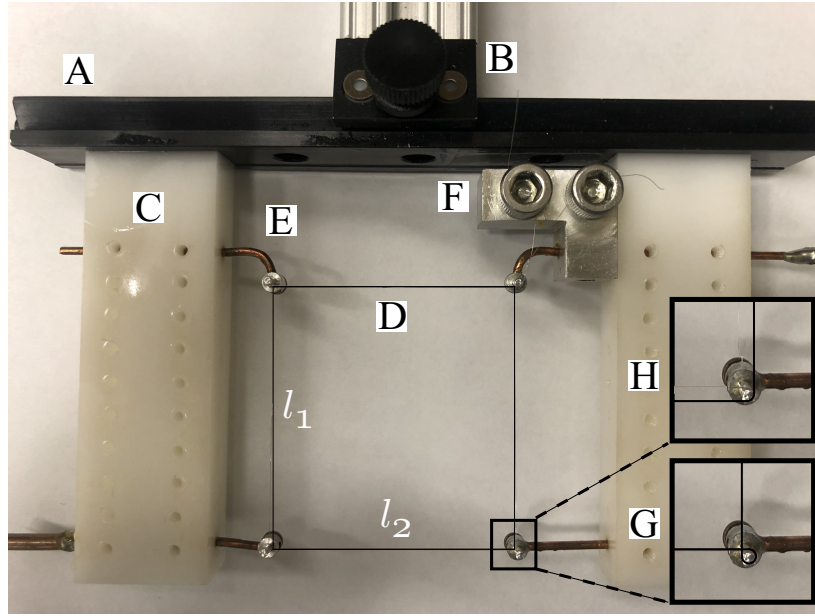


**Figure 3.1:** Frame configuration used for holding and releasing soap films. A miniature optical rail (A) is employed to position and fix two Delrin blocks (C) that house four copper rods (E). An aluminum post (E/Z Connector, Du-Bro) is fixed at the end of each copper rod (E) around which the continuous wire (D) is wrapped to form the metal soap film frame. The beginning and end of the wire are held by the clamp (F) in order to tighten the wire frame. Two wire configurations at the corners are shown in the insets (G,H). The sliding clamp (B) connects the entire frame structure to the rotating arm (L) of the withdrawal apparatus, cf. figure 3.2.

ness, age, and coatings, which cause a noticeable variation on boiling heat transfer characteristics due to influence on the nucleation site density (Rohsenow & Hartnett, 1973). Generally speaking, the effects of the mentioned characteristics are difficult to be determined precisely; however, they can affect the results of the boiling experiments (Lienhard, 1981). After all these considerations NiC 60 (Pelican Wire Company) with well-characterized properties (cf. table 3.1) is the material used in a soap film frame in our experiments.

wire gage	diameter	resistivity	density	specific heat
[ - ]	[ $\mu\text{m}$ ]	[ $\Omega\text{m}$ ]	[ $\text{kg m}^{-3}$ ]	[ $\text{J kg}^{-1}\text{K}^{-1}$ ]
40	79	$1.2 \times 10^{-6}$	8400	450

**Table 3.1:** Properties of NiChrome 60 wires (Incropera & DeWitt, 2002)

*Withdrawal apparatus.* The soap film withdrawal apparatus shown in figure 3.2 was designed and built to perform two major tasks: (a) to dip the frame assembly in a bath with soap solution and

withdraw it with known predefined speed (or, equivalently, to raise and lower the bath while keeping the frame stationary), and (b) to rotate the fresh soap film formed on the wire frame to a horizontal position. The horizontal orientation of the soap film was chosen to minimize gradual thinning due to gravity, which was already described by [Newton \(1704\)](#). Thus the goal of the second task is to create a uniform soap film compared to the vertically oriented one, in which the soap film is prone to drainage because of gravity ([Mysels \*et al.\*, 1959](#)), even though it is known to be stabilized by surfactants leading to the phenomena of marginal regeneration ([Nierstrasz & Frens, 1998, 1999](#)). Two precision stepper motor assemblies were required to complete these tasks. Referring to figure 3.2, the first assembly (A) is a stepper motor/lead screw combination (Velmex BiSlide), which is controlled and programmed by Velmex COSMOS software. This assembly enables one to move the bath downwards with precise velocity. Since the velocity of raising the soap bath has no effect on the soap film thickness, it was kept constant ( $9 \text{ mm s}^{-1}$ ) in the course of experiments. However, the range of velocity of lowering the soap bath, i.e. when a soap film is being created, was  $5\text{--}16 \text{ mm s}^{-1}$ . The second assembly (C) is a rotary stepper motor (Velmex B5990TS), which rotates the soap film frame  $90^\circ$  from vertical to the horizontal position and reverse. After the bath is lowered, the soap film is created on the frame, the stepper motor rotates the frame from vertical to the horizontal position, and after running an experiment, the stepper motor rotates the frame back to the vertical position to be ready for the next experimental run. Before running the next experiment, the wire frame is cleaned with a cotton swab to dry it out and remove the deposited chemicals – surfactant and glycerol – from the experiment. After  $\sim 1 \text{ s}$  of the frame being in the horizontal position, two steps take place in parallel (The delay is to let the soap film to be stabilized in the horizontal orientation and remove possible motions on the soap film surface caused in the rotation stage). First, the emitted light from the light source (D) passes through the optical diffuser (G) and soap film area (L) and is reflected into the camera (F) by the mirror (E). The high-speed camera (F) records the reflected image from the soap film area. Second, the power supply (I) sends a  $5 \text{ V}$  trigger signal to the *BNC* box (J), which, after a precisely predefined delay, sends a signal to the energy storage unit (K) and the high speed camera (F). Once the electrical box receives the signal, the thyristor releases

2.4 kV electrical pulse to the wire frame (for further details see the discussion of the electrical circuit below). By receiving the signal from the *BNC* box, the high-speed camera (F) starts and then stops recording after predefined delay in the camera controlling software. The time for the retraction of the soap film is  $< 10$  ms.

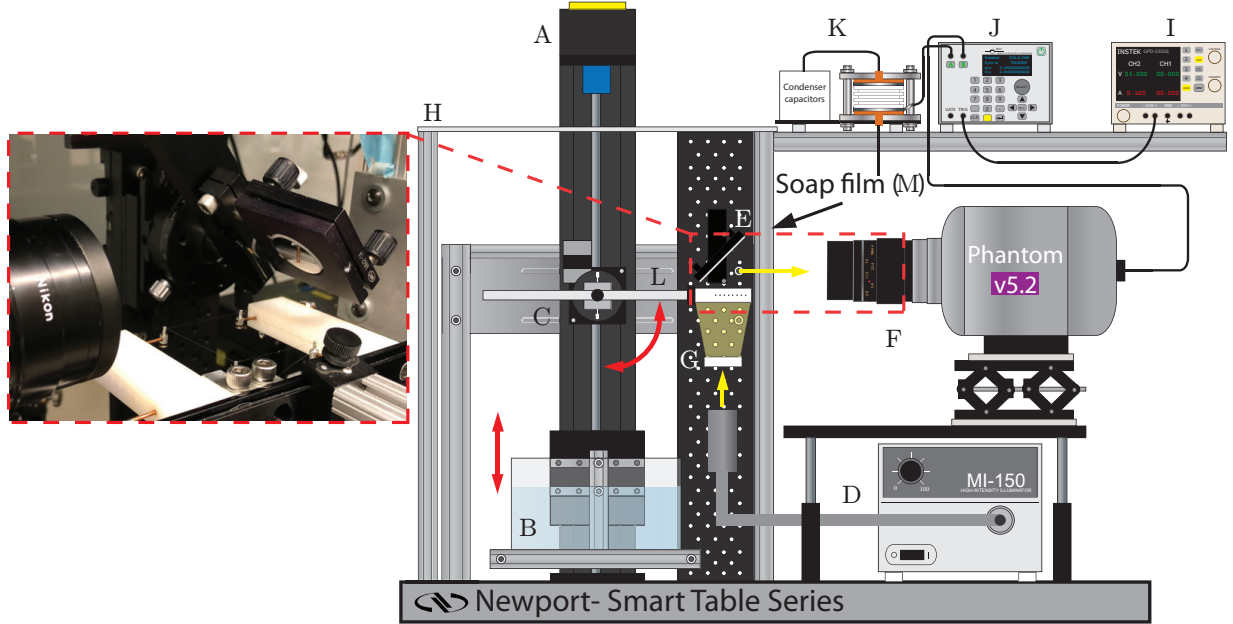


**Figure 3.2:** Experimental platform for the formation of a soap film from a metal frame. The stepper motor/lead screw combination (A) raises and lowers the soap bath (B). The wire frame assembly is screwed and fixed at the end of an arm (L) which is secured to a rotary stage (C). A light source (D) through an optical diffuser (E) illuminates the soap film area (M) and a high speed camera (G) records the phenomenon via a mirror (F) mounted at the angle of  $45^\circ$ . All components except the light source (D) and camera (G) are enclosed in an aluminium structure (H). The entire assembly is mounted on a anti-vibration table (Newport Corp. Smart series).

*Film thickness measurements.* Frankel’s law is often cited for the thickness of a uniform film created by vertical withdrawal of a wire frame in the gravity field with velocity  $V$  from a bath with surfactant solution having bulk viscosity  $\mu$  and surface tension  $\sigma$  (Mysels *et al.*, 1959)

$$h_\infty = 1.88 l_c Ca^{2/3}, \quad (3.1)$$

where  $h_\infty$  is the film thickness,  $l_c = \sqrt{\sigma/\rho g}$  the capillary length, and  $Ca = \mu V/\sigma$  the capillary number. Close examination of equation (3.1) shows that the film thickness is a function of fluid

properties (i.e. surface tension  $\sigma$ , viscosity  $\mu$ , and density  $\rho$ ) and the withdrawal speed  $V$ . Though Frankel's law can be applied to calculate film thickness in some occasions (Mysels & Cox, 1962), however it is not appropriate formula to calculate the thickness of soap film in our experimental situation. In particular, it has been reported that the thickness of soap film calculated by Frankel law (equation (3.1)) deviates from the experimental findings when  $Ca \gtrsim 10^{-3}$  (Adelizzi & Troian, 2004). The range of the capillary number  $Ca$  in our experiments is  $O(10^{-4} - 10^{-3})$ . The deviation can be caused by drainage when the soap frame is in a vertical position in the stage of withdrawal.

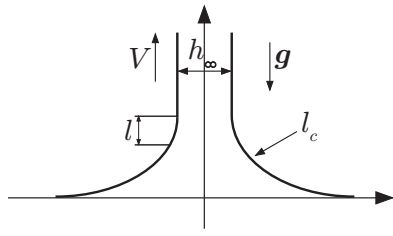


**Figure 3.3:** Soap film pulling.

To understand the origin of Frankel's law (3.1), note that the meniscus shape remains static (and hence undistorted) except for the region of size  $l \ll l_c$  in which all three forces due to viscosity, surface tension and gravity are in a dynamic equilibrium. Therefore, this region is called the *dynamic meniscus* region, i.e. the region influenced by dynamic effects, with the extent (in the soap film plane)  $l$  determined by the balance of capillary and viscous stresses and by matching the curvature of the static meniscus to that of the dynamic meniscus,

$$\mu \frac{V}{h_\infty^2} \sim \frac{\sigma/l_c}{l}, \quad \frac{h_\infty}{l^2} \sim l_c^{-1}.$$

Therefore,  $l \sim (h_\infty l_c)^{1/2}$  and  $h_\infty$  obeys (3.1). While Frankel's law has been tested over a wide range of bulk and surface viscosities (Mysels & Cox, 1962), it does demonstrate significant deviations when the surfactant film is not expected to be inextensible (though flexible) – the central assumption in the derivation of (3.1). In particular, the resulting presence of Marangoni stresses leads not only to the deviations from (3.1) similar to the film thickening effect in the Landau-Levich problem (cf. Mayer & Krechetnikov (2012) and references therein), but also to the deviations from the mass conservation (3.56) assumed in a number of works (Couder *et al.*, 1989). Also, at higher pulling velocities  $V$ , one can expect breakage of the surfactant rigid monolayer (Lal & di Meglio, 1994).

The steady retraction velocity of the soap film is directly related to the thickness of the soap film via the Taylor-Culick velocity  $U_{TC} = \sqrt{2\sigma/\rho h}$  (Culick, 1960; Taylor, 1959a). In many instances Frankel's law (Mysels *et al.*, 1959) can be used to calculate the uniform thickness of the soap film created by vertical withdrawal. For that, an independent film thickness measurement has been done for all test conditions, in particular in order to evaluate theoretically the terminal velocity of the soap film retraction and various wave propagation velocities and compare the results with experimental measurements. Measurement of the soap film thickness reported here were performed using a light source (Dolan Jenner MI-150) as a light emitter, and a collimating lens/fiber optic cable (Thorlabs M25L02) as a light collector of the transmitted light through the soap film, which sends an optical signal to UV-VIS spectrometer (Ocean Optics USB4000-UV-VIS). A detailed explanation of the soap film thickness measurement is reported in Appendix 3.A. For each test condition, the measurement was performed three times and the average value reported as the film thickness. The maximum deviation from the average was  $\sim 1 \mu\text{m}$  in all cases.

*Electrical circuit and components.* Once the frame along with the soap film on it is in the horizontal position, the soap film is ready to be released by impulsive Joule heating of the frame wire (Mayer & Krechetnikov, 2017). The required energy for the impulsive heating is stored in a capacitor and delivered to the wire through a thyristor in a single high voltage electric pulse. A schematic diagram of the electrical circuit used in the experimental setup is shown in figure 3.4. The leads connecting the conducting soap film frame to the circuit such that the frame forms two parallel resistors with resistance equivalent to the wire of length  $(l_1 + l_2)$  and resistivity of  $1.2 \times 10^{-6} \Omega \text{m}$  (see table 3.1) with the total resistance  $R_f$  (of the parallel resistors). Two high voltage capacitors which are connected in sequence C (Condenser Products MQP105-5MN-1 mF 5KV) are charged with a high voltage power supply  $HV_1$  (Matsusada, EQ-30P1-LG) to the desired value  $\varphi = 2.4 \text{KV}$ . Upon charging the capacitor, a power supply  $V_1$  (Instek GPD-3303S) sends a 5 V electric signal to a pulse/delay generator *BNC* (Berkeley Nucleonics Corp, Model 575). After some delay, precisely set by the *BNC*, a 5 V trigger pulse is sent to the high-speed camera (Phantom V5.2) and the thyristor (Astrol Electronics AG, AC-10140-001). The camera starts recording by receiving the

trigger pulse and the thyristor closes the circuit and delivers the energy stored in the capacitor to the wire frame. To ensure the repeatability of the experiment a measurement circuit consisting of  $R'_3 = 1 \text{ k}\Omega$  (Ohmite 40J1K0E) and  $R_3 = 10 \Omega$  (NTE 10W010LF) resistors, a voltage probe (Tektronix P2220), and an oscilloscope (Tektronix TDS 2024B) was made. The electrical pulse is measured across  $R_3$  resistor: a sample of the measured pulse is presented in figure 3.4.

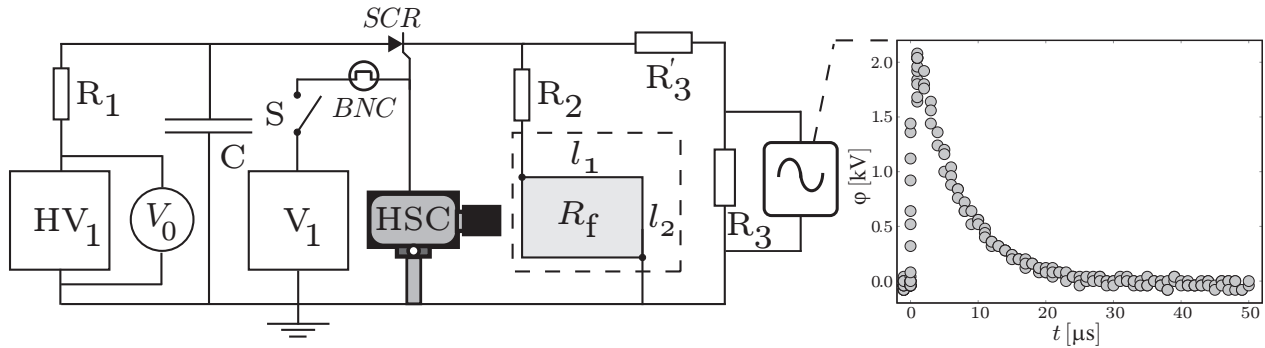


**Figure 3.4:** Schematic of the electrical circuit used for the controlled release of planar soap films. Discharging capacitor  $C$ , charged to voltage  $V_0$ , through the wire frame gives rise to Joule heating and releases the soap film. Actuation of the discharge process is started by sending a  $5 \text{ V}$  trigger signal from DC power supply  $V_1$ . Inset shows an example of the measured electric signal in the circuit.

*Visualization components.* The retraction of soap films was recorded at different frame rates (3000 – 5000 fps), exposure times ( $\sim 30 - 100 \mu\text{s}$ ), and resolutions using a Phantom v5.2 digital high speed camera (Vision Research) with 35 mm and 55 mm Nikkor lens. The back lighting technique has been used in all experiments.

### 3.1.1.2 Soap solutions

Soap solutions were prepared from mixtures of ultrapure water (Millipore Direct-Q 3UV-R), glycerol, and an anionic surfactant Sodium Dodecyl Sulfate (SDS) (Sigma-Aldrich 75746) with a purity of  $\geq 99\%$ . The latter was chosen as a surfactant for several reasons, one was that SDS is well-characterized and used in a number of fluid interface studies (Mysels & Cox, 1962; Lyklema *et al.*, 1965; McEntee & Mysels, 1969; Evers *et al.*, 1996; Huibers & Shah, 1997; Berg *et al.*, 2005). It should be mentioned that some studies used commercial detergents to make soap films, for instance Dreft<sup>®</sup> (Lhuissier & Villermaux, 2009b,a), Dawn<sup>®</sup> (Prasad & Weeks, 2009), and other “unreported”

(Liebman *et al.*, 1968) detergents. Unlike the commercial detergents, which include some unknown additives, reliable properties of SDS are well determined. Therefore using SDS enables us to be confident about the reproducibility of the experimental results. Relevant properties of SDS are summarized in table 3.2.

molecular weight	288.38 gm/mol
critical micelle concentration (CMC), $C_{\text{CMC}}$	8.3 mM
surface tension at CMC, $\sigma_{\text{CMC}}$	38 mN/m
maximum surface density, $\Gamma_{\infty}$	$3 \times 10^{-6} \text{ mol/m}^2$
bulk diffusivity, $D$	$8 \times 10^{-10} \text{ m}^2/\text{s}$
adsorption coefficient, $k_a$	$0.64 \times 10^{-5} \text{ m/s}$
desorption coefficient, $k_d$	$5.9 \text{ s}^{-1}$

**Table 3.2:** Properties of sodium dodecyl sulfate surfactant (Krechetnikov & Homsy, 2005; Fernandez *et al.*, 2005)

A basic set of experiments was performed to determine an optimal soap solution in the laboratory condition. Ranges of glycerol concentrations  $C_g$  (5–20 %wt), SDS concentrations (0.5–1.25 CMC), and soap frame withdrawal velocities ( $5 - 16 \text{ mm s}^{-1}$ ) were explored throughout the course of experiments, though not with the goal to find the most stable conditions for soap film lifetime. This allows one to study the effect of the soap film thickness, viscosity, and surface tension on the kinematics of the soap film retraction as well as on transition from no shock wave to the shock wave pattern.

### 3.1.2 Experimental results

To study the effect of surface tension, viscosity and soap film thickness on shock wave propagation on a planar soap film, we used various concentrations of glycerol (5, 10, 15, 20, and 25 %wt) and SDS (0.5, 0.625, 0.75, 0.875, 1, and 1.25 CMC) to prepare soap solution. Since the thickness of the soap film is related to the withdrawal velocity  $V$  from the soap bath (Mysels *et al.*, 1959), five different withdrawal velocities in the range  $5 - 16.1 \text{ mm s}^{-1}$  were used for each soap solution in the course of experiments. These solutions and withdrawal velocities were deliberately chosen to

achieve a wide range of viscosities 1.16 – 2.13 mPa·s, surface tensions 35 – 47.6 mN·m<sup>-1</sup>, and soap film thicknesses 4.6 – 19.3 μm.

### 3.1.2.1 Mapping of the regimes

First, experiments were performed to identify the key patterns of collapsing soap films, as shown in figure 3.5. The 35 mm Nikon lens was used to record the entire soap film time sequence images via the high-speed camera. Based on experimental observations, two outcome patterns were distinguished: (a) shock wave pattern and (b) no shock wave pattern. In the shock wave pattern, shock lines along the soap film diagonal are formed about 1 ms after that the soap film was released by a high voltage electrical pulse. Shock lines propagate along the diagonal until they merge at the center of the film, cf. figure 3.5a. In the no shock wave pattern, the soap film simply retracts with the microdroplets dispatched from the soap film boundaries. It is notable that the case of no shock wave pattern corresponds to the soap film retracting faster than that in the shock wave pattern case, which is especially distinguishable in the image captured at 6460 μs time frame by comparing surface area of the soap films.

As a next step, a number of experiments was carried out to understand the transition between the no shock wave and shock wave regimes. For that, the soap solution properties and withdrawal speed were varied as described earlier. The maps are presented in the right column of figure 3.6. Maps of the transition in terms of glycerol concentration  $C_g$  with respect to the soap film thickness  $h$ , are shown in the right column of figure 3.6. The variation in the soap film thickness on the horizontal axis is due to variation in the bath lowering speed. By increasing SDS concentration, the thickness of the soap film would decrease, and the resultant pattern would be of a no shock wave rather than a shock wave pattern. In the left column, the change of the soap film thickness with respect to velocity  $V$  is shown on the log-log scale. Also in each plot the film thickness calculated by Frankel's law  $h_\infty$  (Mysels *et al.*, 1959)

$$h_\infty = 1.88 l_c C a^{2/3} \quad (3.2)$$

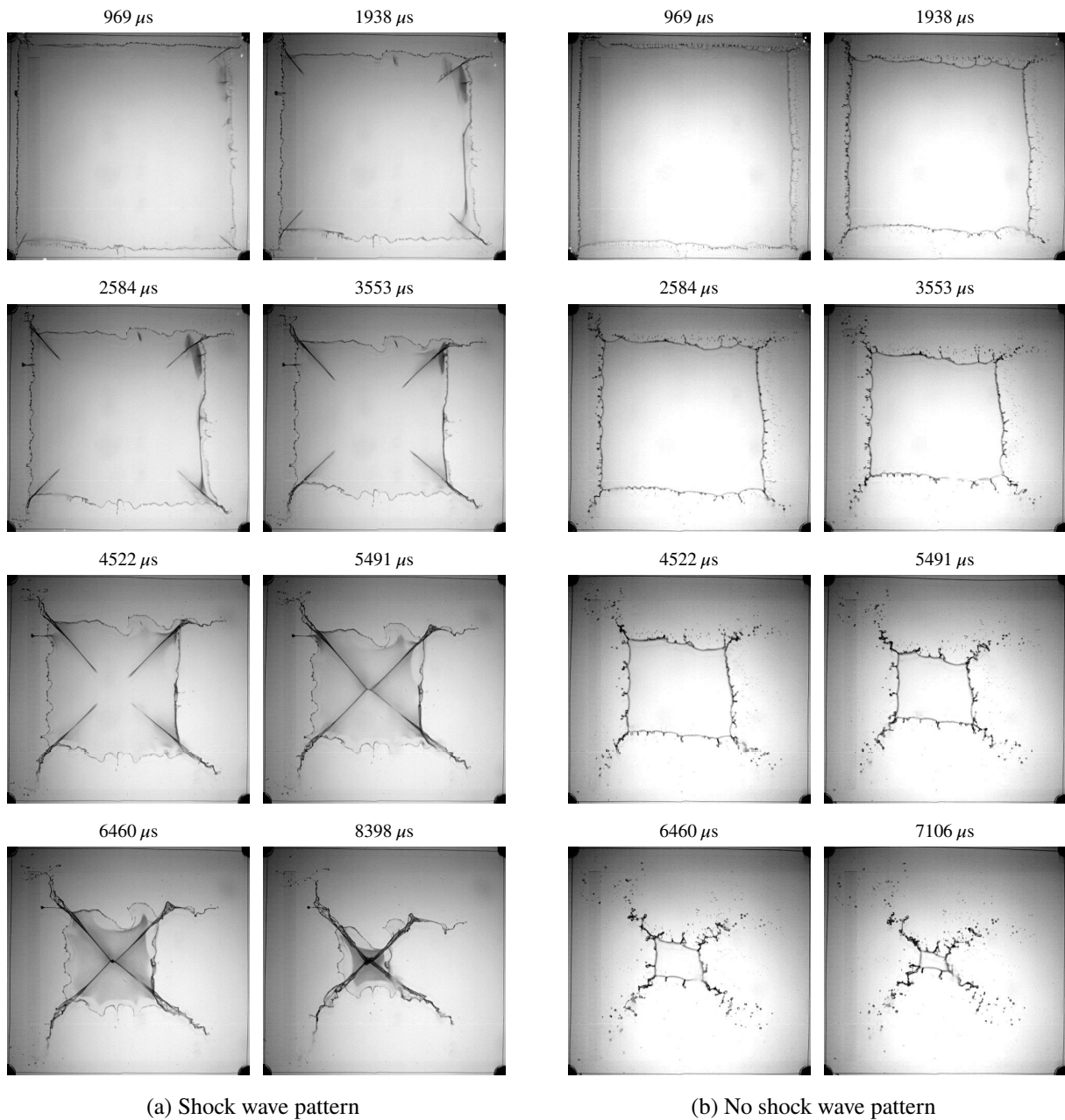


**Figure 3.5:** (a) Time sequence of the soap film retraction with developing shock pattern on the surface of the film. Soap film solution properties: 0.5 CMC of SDS, 20% wt glycerol. Withdrawal velocity and film thickness are  $12.4 \text{ mm s}^{-1}$  and  $16.9 \text{ }\mu\text{m}$ , respectively. (b) Time sequence of the soap film retraction without shock pattern. Soap film solution properties: 1.25 CMC of SDS, 20% wt glycerol. Withdrawal velocity and film thickness are  $12.4 \text{ mm s}^{-1}$  and  $8.5 \text{ }\mu\text{m}$ , respectively. Physical image size in both (a,b) is  $50 \times 50 \text{ mm}^2$ .

is added, where  $l_c = \sqrt{\sigma/\rho g}$  is the capillary length and  $Ca = \mu V/\sigma$  the capillary number: the solid and dashed lines correspond to the smallest and largest viscosity of the soap film solutions reported in each plot, respectively. As one can see, there is significant deviation between the measured data

points and the prediction by Frankel’s law. The deviation increases with increasing the surfactant concentration.

Lastly, in a rectangular geometry, i.e. when the soap film frame is not exactly square, we can observe the formation of a bridge, cf. figure 3.7, at the moment when the acoustic wave fronts from the vertical (in the image) sides side of the soap film experience a heads-on collision.

### 3.1.2.2 Key velocities

Dynamics of the collapsing soap film is dictated by the soap solution properties (viscosity, surface tension, etc.) and the thickness of the soap film (Brenner & Gueyffier, 1999; Savva & Bush, 2009; Couder *et al.*, 1989; Mysels *et al.*, 1959). In order to study the effect of these parameters on the retraction and shock wave propagation velocities two sets of experiments were carried out: (a) when the concentration of the surfactant was fixed at 0.5 CMC while the concentration of glycerol was changed between 5 – 25 %wt, and (b) when the concentration of glycerol was fixed at 20 %wt while the concentration of SDS was changed between 0.5 – 1.25 CMC. To have an adequate resolution in the recorded movies for the purpose of image processing, a high-speed camera with a 55 mm Nikon-Nikkor lens was employed and focused on the lower right quadrant of the soap film area. The recorded time-sequence images of both regimes are presented in figure 3.8.

The soap film retraction and shock wave propagation velocities were extracted from the recorded movies, with the help of two separate in-house image processing codes that were developed in MATLAB, and are presented in figures 3.9a and 3.9b for the first set of experiments and in figures 3.9c and 3.9d for the second set of experiments. In both cases, five withdrawal velocities were implemented in the course of experiments. In figures 3.9a and 3.9c one dimensional wave propagation velocity on the soap film surface and retraction velocity of the soap film edge are shown with white and black symbols, respectively. The theoretical estimates of the retraction terminal velocity are done with the Taylor-Culick formula  $U_{TC} = \sqrt{2\sigma/\rho h}$  and are represented with gray symbols.

Marangoni wave propagation velocity obeys  $\sqrt{2E/\rho h}$ , where  $E$  is the Marangoni elasticity of the soap film (Couder *et al.*, 1989). By fitting to the experimental data points of shock wave propa-

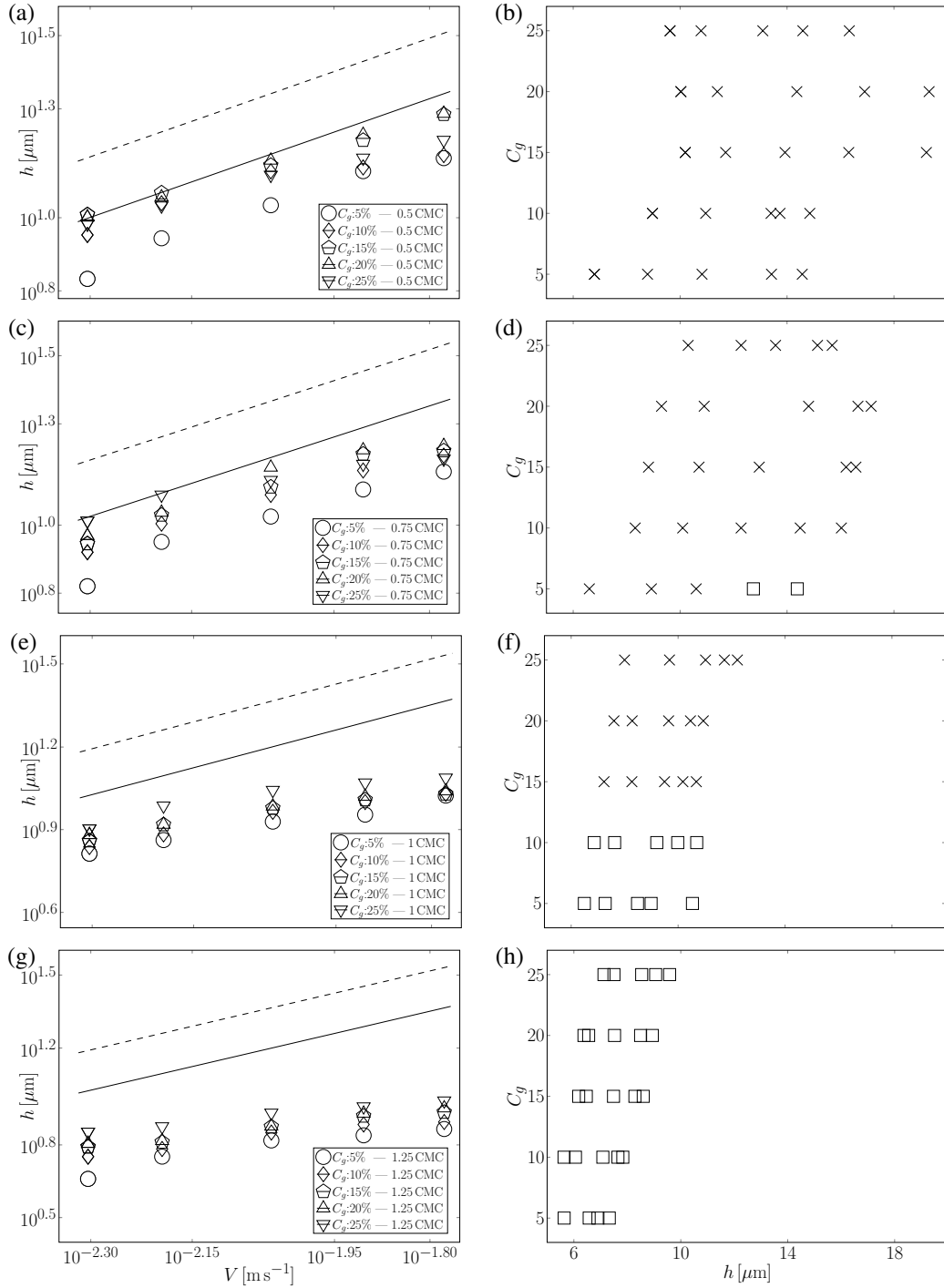


**Figure 3.6:** Maps of shock wave and no shock wave patterns for different concentrations of surfactant and glycerol. First to fourth rows correspond to 0.5, 0.75, 1, and 1.25 CMC of surfactant ( $\geq 99.5\%$  purity), respectively. Left column shows measured soap film thickness  $h$  with respect to the soap film withdrawal velocity  $V$ . Solid and dashed lines correspond to the calculated soap film thickness via Frankel's law (3.2) for the smallest and largest viscosity of the soap film solutions reported in each plot. Right column shows the map of the regimes in terms of glycerol concentration  $C_g$  with respect to the soap film thickness. Symbols  $\times$  and  $\square$  correspond to shock wave and no shock wave patterns, respectively.

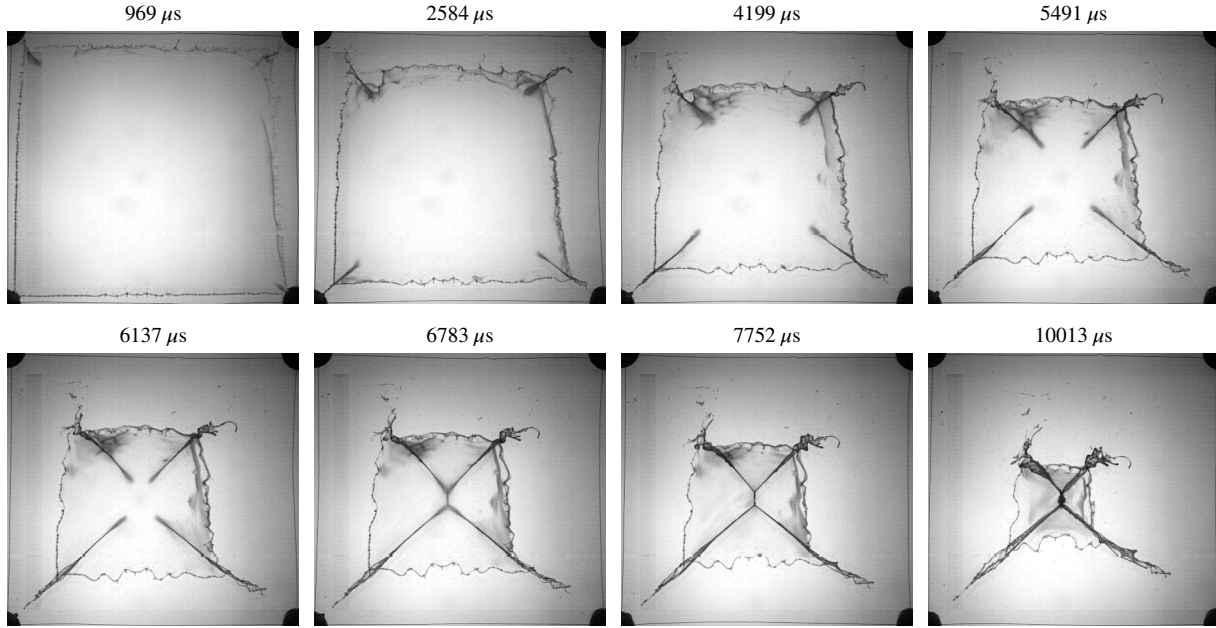
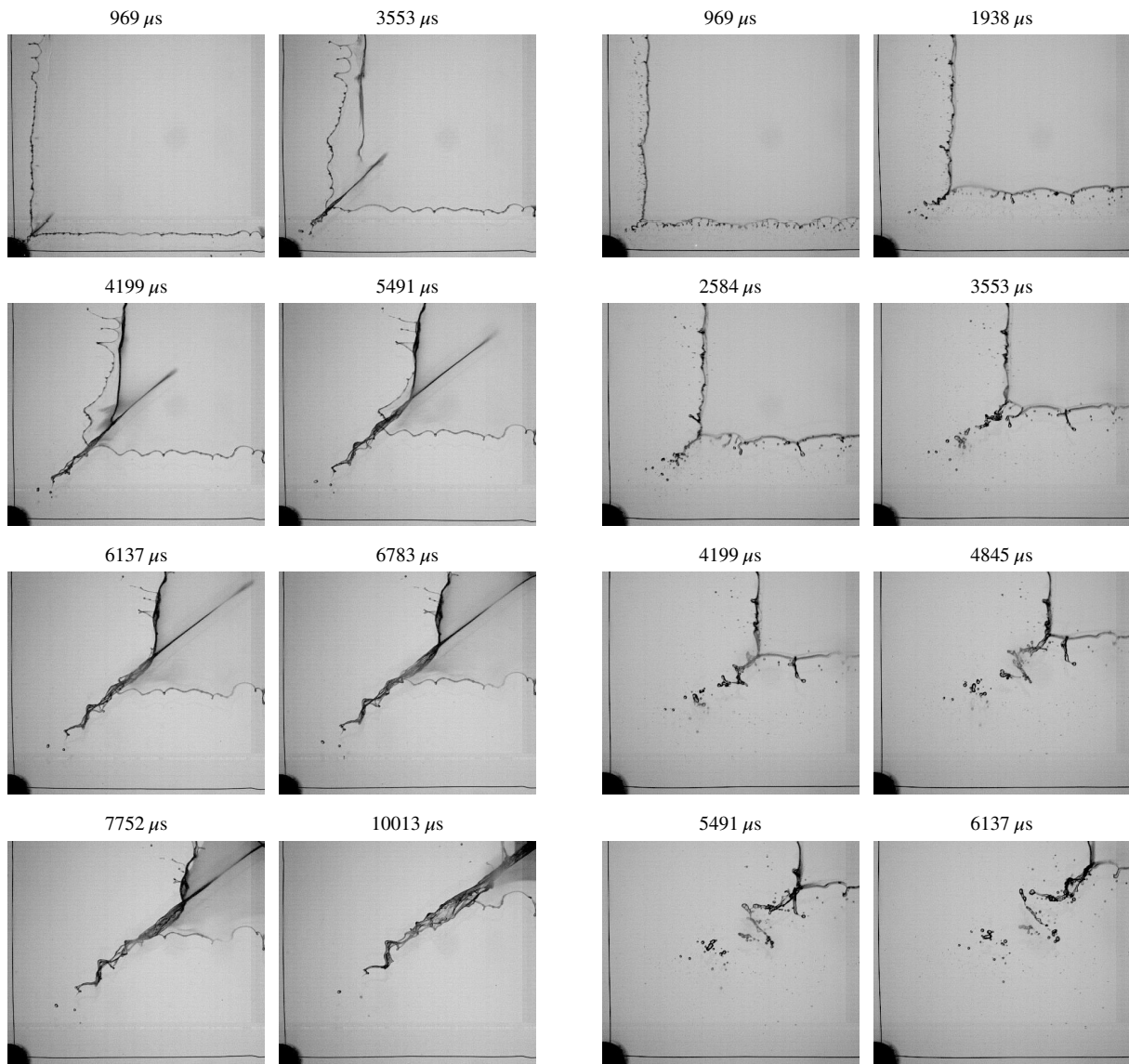


**Figure 3.7:** A time sequence of images showing the formation of a bridge in a rectangular soap film geometry. Soap film solution properties: 0.5 CMC of SDS, 5% wt glycerol. Withdrawal velocity and film thickness are  $16.1 \text{ mm s}^{-1}$  and  $14.6 \text{ }\mu\text{m}$ , respectively. Physical image size is  $50 \times 50 \text{ mm}^2$ .

gation velocity, we can calculate the elasticity of the soap film. Plots in the right column of figure 3.9 demonstrate the ratio of one dimensional wave propagation velocity to one dimensional soap film retraction velocity  $U_{TC}$  with respect to the soap film thickness. As shown in figure 3.9d, by increasing the concentration of SDS, the ratio of wave propagation velocity to soap film retraction velocity approaches unity. At a higher concentration of the surfactant (1.25 CMC) the shock wave pattern was not observed (figure 3.6h), which confirms that by increasing the surfactant concentration the no shock wave pattern is observed rather than the shock wave one. Since there was no shock wave lines on 1.25 CMC of SDS soap films, data for this concentration cannot be shown in figure 3.9c.

We should also note that for the two concentrations of surfactant (0.875 and 1 CMC) a dark region (areola) is developed along with shock line propagation on the soap film surface while for low concentrations (0.5 and 0.625 CMC) we did not observe any dark regions (figures 3.5a and 3.8a).



(a) Shock pattern

(b) No shock pattern

**Figure 3.8:** (a) Time sequence of the soap film retraction with developing shock pattern on the surface of the film with the camera zoomed on a quarter of the soap film area. Soap film solution properties: 0.5 CMC of SDS, 20% w glycerol. Withdrawal velocity and film thickness are  $12.4 \text{ mm s}^{-1}$  and  $16.9 \mu\text{m}$ , respectively. (b) Time sequence of the soap film retraction without shock pattern. Soap film solution properties: 1.25 CMC of SDS, 20% w glycerol. Withdrawal velocity, film thickness, and capacitor voltage are  $12.4 \text{ mm s}^{-1}$  and  $8.5 \mu\text{m}$ , respectively. Physical image size is  $22 \times 19 \text{ mm}^2$ .

Lastly, we would like to mention the relation of the observed wave propagation to the nature of surfactant molecules, which have one polar end and one non-polar end and therefore form a monolayer at the interface between a polar substance such as water and a nonpolar one such as oil

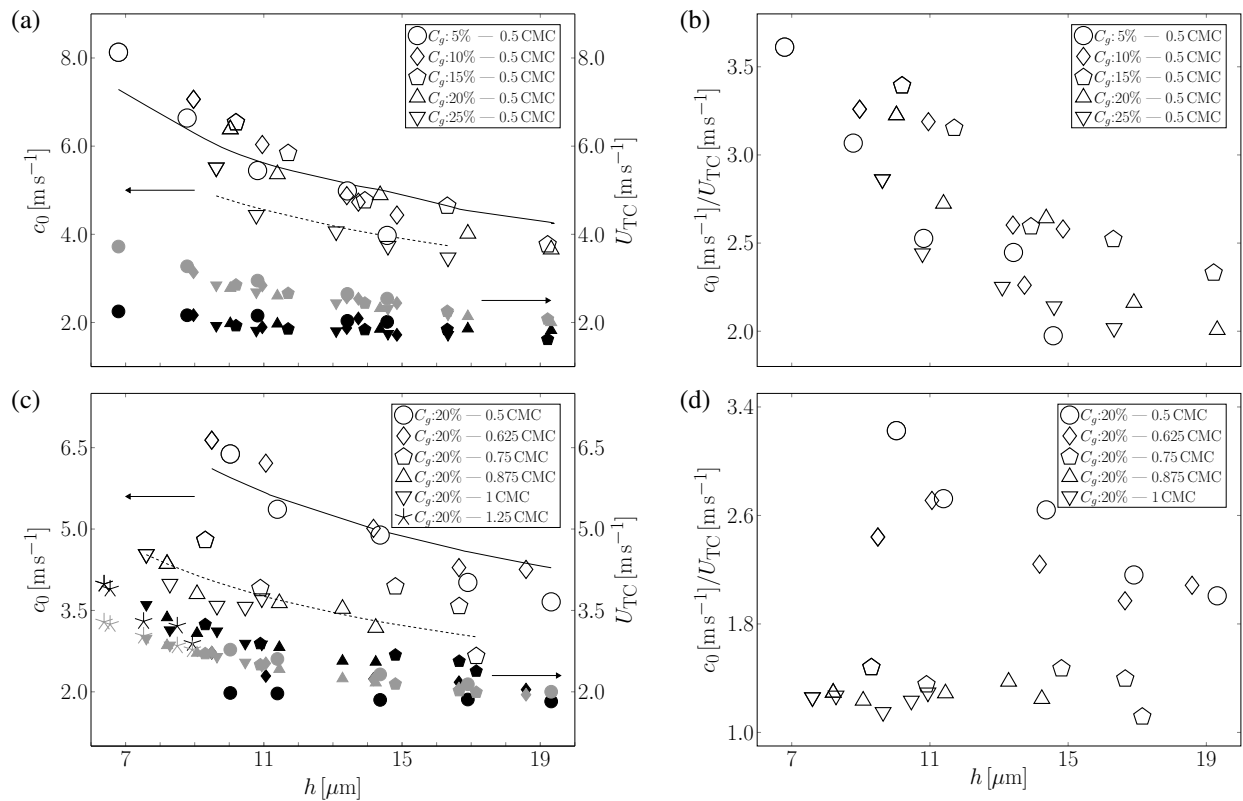


**Figure 3.9:** Wave propagation velocity  $c_0$  and soap film retraction velocity  $U_{TC}$  for different soap films. (a) Wave propagation and soap film retraction velocities for 0.5 CMC of SDS with respect to the soap film thickness. Five concentrations of glycerol (5, 10, 15, 20, and 25%wt) have been used and for each concentration five different withdrawal velocities have been applied which resulted in 25 different soap film thicknesses. The solid line is a fitted curve  $c_0 = \sqrt{2E/\rho h}$  to 5, 10, 15, and 20%wt glycerol data points yielding  $E = 0.182 \text{ N m}^{-1}$  and the dashed line is fitted curve to 25%w glycerol data points producing  $E = 0.121 \text{ N m}^{-1}$ ; here  $E$ ,  $\rho$ , and  $h$  are the soap film elasticity, density, and thickness, respectively. White and black symbols represent the wave propagation and the soap film retraction velocities, respectively. Gray symbols correspond to the Taylor-Culick terminal retraction velocity of the soap film  $U_{TC} = \sqrt{2\sigma/\rho h}$ , where  $\sigma$  is surface tension of the soap film. (b) Ratio of the wave propagation velocity to the soap film retraction velocity with respect to the soap film thickness for the cases that have been presented in (a). (c) The wave propagation and the soap film retraction velocities for different soap films with glycerol concentration fixed at 20 %wt. Surfactant concentration is changed in this set of experiments from 0.5 to 1.25 CMC. The solid line is fitted curve to 0.5 and 0.625 CMC wave propagation data points yielding  $E = 0.186 \text{ N m}^{-1}$  and the dashed line is fitted curve to 0.75, 0.875, and 1 CMC wave propagation velocity data points yielding  $E = 0.082 \text{ N m}^{-1}$ . (d) Ratio of the wave propagation velocity to the soap film retraction velocity with respect to the soap thickness for the cases shown in (c).

or air. The one molecule surfactant monolayer separates the two substances and reduces surface tension, which is why such monolayers in our lungs make it easier for us to breathe as the reduced surface tension requires less energy to breathe. As it happens in our experiments on collapsing soap films, under compression a surfactant monolayer may experience a mechanical instability, similar

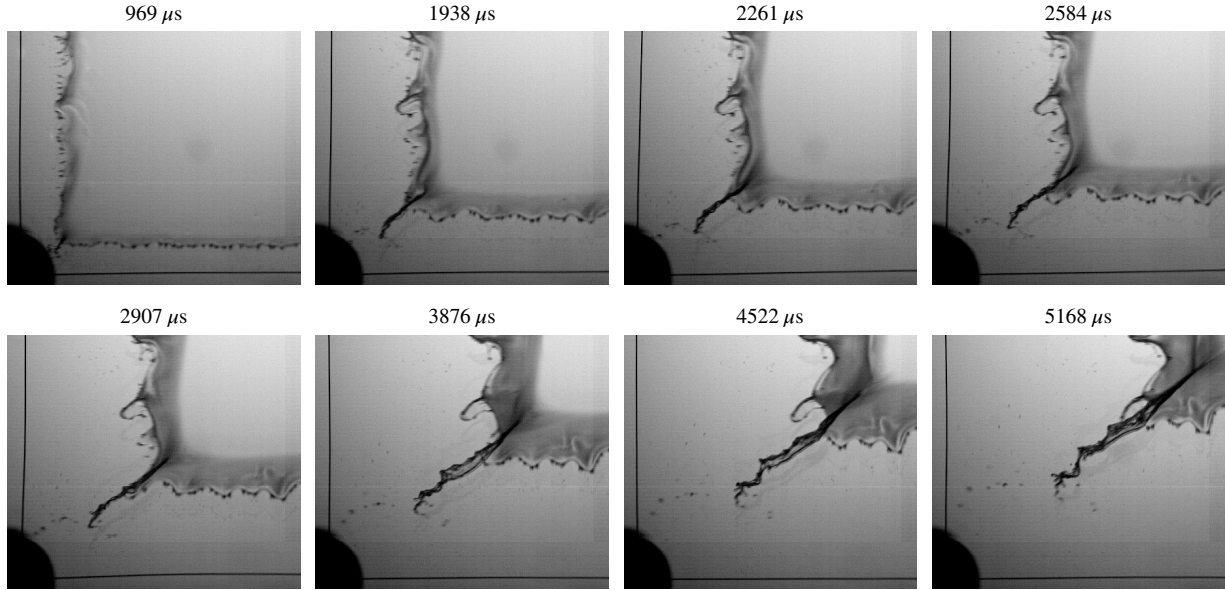


**Figure 3.10:** Time sequence of the soap film retraction to show the appearance of dark region on the soap film surface with the camera zoomed on a quarter of the soap film area. Dark region develops as the shock wave tip develops on the soap film surface. Soap film solution properties: 0.875 CMC of SDS, 20% wt glycerol. Withdrawal velocity and film thickness are  $9.1 \text{ mm s}^{-1}$ ,  $11.4 \text{ }\mu\text{m}$ , respectively. Physical image size is  $22 \times 19 \text{ mm}^2$ .

to the buckling instability of a beam or a plate, with the wavelength of the surface undulations in the range of  $1 - 10 \text{ }\mu\text{m}$  (Milner *et al.*, 1989; Saint-Jalmes & Gallet, 1998) and amplitude of a few nanometers. The velocity of the associated wave propagation in surfactant monolayers is dictated by their compressibility and could be on the order of  $10^2 \text{ m s}^{-1}$  (Griesbauer *et al.*, 2009). Obviously, while we cannot observe nanometer amplitude deformations on the soap film surface, the optical properties of the surfactant monolayer change drastically under compression, which leads to the observable “areola”. Because of the surfactant used in our experiments (SDS), its monolayer compressibility properties allow for significantly lower wave propagation velocities comparable to the edge retraction ones thus enabling the discovery reported here: transition from no-shock wave to shock wave regime.

### 3.1.2.3 The corner effect

In order to demonstrate the effect of the soap film frame corner, a few experiments were conducted on sharp and curved corners using a soap solution of 1 CMC of SDS and 20% w glycerol. The time

sequence of the images are shown in figure 3.11. Figure 3.11a shows the soap film retraction in the sharp  $90^\circ$  angle corner configuration and figure 3.11b demonstrates the retraction pattern in the case of the curved  $90^\circ$  corner configuration. Evidently, the curvature of the frame corner directly affects the outgoing soap film pattern: the shock wave pattern is observed in the sharp  $90^\circ$  corner while in the case of the curved  $90^\circ$  corner no shock pattern is observed in the course of retraction of the soap film.

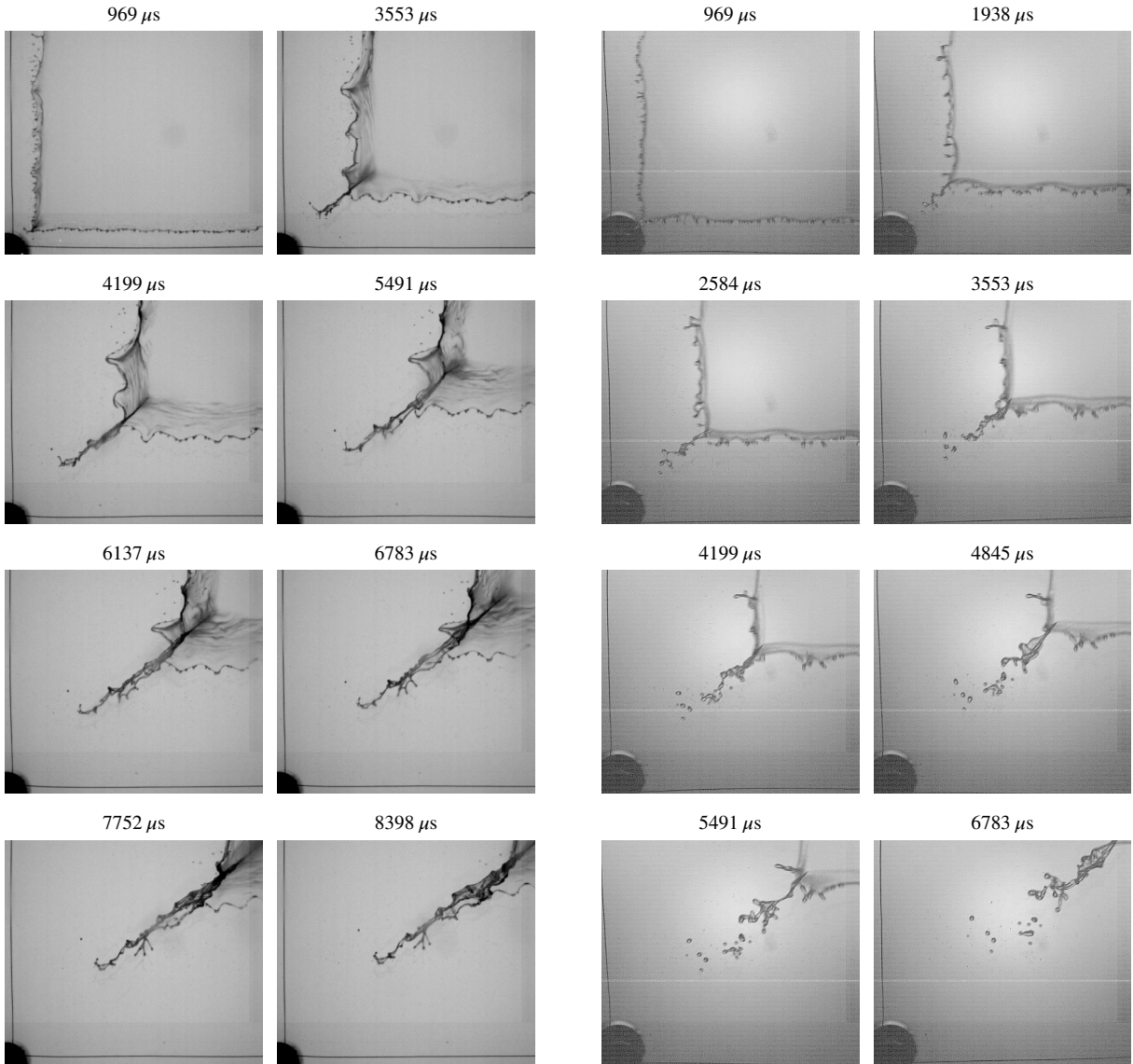
## 3.2 Theory

In what follows, first we use the basics of geometric acoustics (§1.1) to deduce qualitatively the behavior of acoustic waves on the soap film and to explain the origin of folds along the diagonal of a collapsing soap film. Given the experimental observation that there is an areola – a wave preceding the retracting soap film edge – in §3.2.1.2 we will revisit the classical theory (§3.2.1.1) in order to develop proper equations governing the velocity and thickness of the collapsing soap film, since these variables are crucial for the proper interpretation of the wave propagation (§3.2.2) superimposed on the evolving in time base state, which will lead to a succinct understanding of the origin of the observed folds in §3.2.3.

### 3.2.1 Soap film dynamics

#### 3.2.1.1 Classical theory of Taylor (1959c)

Let us first review the classical derivation by Taylor (1959c) of a retracting soap film edge forming a blob, generalized here to the case when not only the blob is moving, but also the sheet in front of it is moving as well, though with a different speed  $v_s$ . With reference to figure 3.12a, we can write



(a) Sharp 90° corner

(b) Curved 90° corner

**Figure 3.11:** Time sequence of the soap film retraction to show the effect of frame corner with the camera zoomed on a quarter of the soap film area. In the time sequence shown in (a) the corners of the frame are sharp 90° while in the set of images shown in (b) the frame corners are curved 90°. Soap film solution properties: 1 CMC of SDS, 20% wt glycerol. Withdrawal velocity and film thickness are  $\sim 12.4 \text{ mm s}^{-1}$  and  $10.5 \text{ }\mu\text{m}$ , respectively. Physical image size is  $\sim 22 \times 19 \text{ mm}^2$ .

down the momentum conservation for a system with variable mass<sup>1</sup>:

$$m(t) \frac{dv_r}{dt}(t) = [v_s(t) - v_r(t)] \frac{dm}{dt} + F_{\text{ext}}, \quad (3.3)$$

<sup>1</sup>This form of momentum conservation follows from the computation of the total change of momentum  $\delta(m v_r)$  over time  $\delta t$  as per figures 3.12a and 3.12b:  $\delta(m v_r) = [m(t) + \delta m(t)] v_r(t + \delta t) - [m(t) v_r(t) + \delta m(t) v_s(t)] \approx m(t) \frac{dv_r}{dt} \delta t + \delta m(t) [v_r(t) - v_s(t)]$ , i.e. it involves the relative velocity  $v_r - v_s$  of the escaping or incoming mass.

with the force  $\mathbf{F}_{\text{ext}}$  (per unit length) acting on the rim calculated via:

$$\mathbf{F}_{\text{ext}} = \int_C \sigma (\nabla \cdot \mathbf{n}) \mathbf{n} dl, \quad (3.4)$$

where  $\mathbf{n}$  is the normal vector to the interface, and with the help of the first of the Frenet-Serret formulas (Spivak, 1999) the integrand can be simplified to  $(\nabla \cdot \mathbf{n}) \mathbf{n} = d\mathbf{t}/dl$  with  $\mathbf{t}$  being the tangent vector and  $l$  the arclength along the interface, resulting in

$$\mathbf{F}_{\text{ext}} = \int_C \sigma \frac{d\mathbf{t}}{dl} dl = \sigma (\mathbf{t}_1 - \mathbf{t}_2) = 2\sigma \mathbf{e}_x, \quad (3.5)$$

i.e.  $F_{\text{ext}} = 2\sigma$  in equation (3.3). As follows from comparing figures 3.12a and 3.12b, the mass increase over time  $\delta t$  is  $\delta m(t) = \rho h_\infty [v_r(t) - v_s(t)] \delta t$ , which allows us to determine the mass time rate of change  $dm/dt$  in (3.3). From mass conservation, the blob mass at time  $t$  is

$$m(t) = \rho h_\infty x_r(t). \quad (3.6)$$

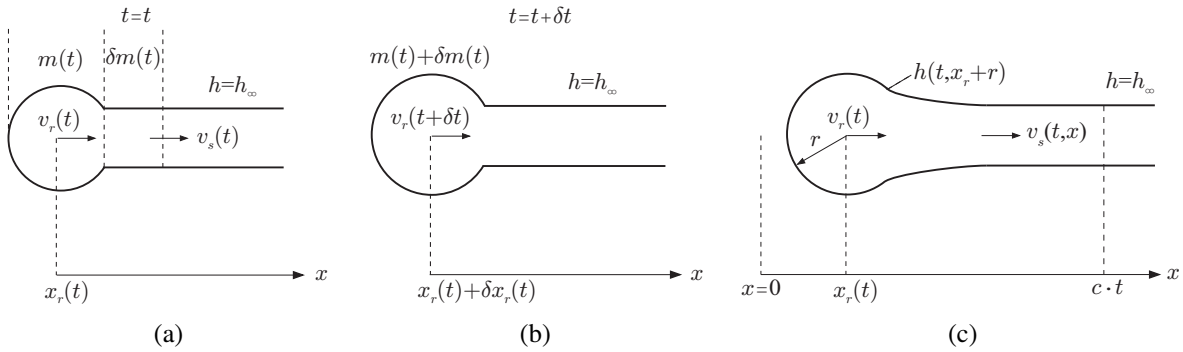


**Figure 3.12:** (a,b) Taylor's derivation; (c) new configuration.

If  $v_s \equiv 0$ , then momentum conservation (3.3) along with the blob mass expression (3.6) reduce to the classical Taylor formula:

$$\rho h_\infty \frac{d}{dt} \left[ x_r \frac{dx_r}{dt} \right] = 2\sigma, \quad (3.7)$$

possessing some interesting properties, which are usually not highlighted, but will be relevant for our subsequent general derivation. Since initially the soap film is at rest, the initial condition supplied to the above equation reads:

$$t = 0 : x_r = x_0, v_r = 0, \quad (3.8)$$

thus implying from (3.7) that as  $t \rightarrow 0$  the initial acceleration is infinite:

$$x_r \frac{d^2 x_r}{dt^2} = \frac{2\sigma}{\rho h_\infty} \neq 0, \quad (3.9)$$

which becomes possible due to infinitely small initial mass  $m(t) \rightarrow 0$  as  $t \rightarrow 0$ . Physically, of course, this is due to the fact that finite surface tension force acting on the edge from the right is not balanced by any force on the left (free edge). Taylor's equation (3.7) also allows one to immediately to determine the final speed of retraction once acceleration  $d^2 x_r / dt^2$  vanishes:

$$v_{TC} = \sqrt{2\sigma / \rho h_\infty}, \quad (3.10)$$

known as the Taylor-Culick speed, which can also be seen by formal integration of (3.7) with initial conditions (3.8):

$$v_r(t) = \frac{v_{TC}}{\sqrt{1 + \frac{x_0^2}{v_{TC}^2 t^2}}} \rightarrow v_{TC} \text{ as } t \rightarrow \infty. \quad (3.11)$$

The above formula indicates that the characteristic inviscid time  $\tau_{\text{inv}}$  of establishing  $v_{\text{TC}}$  is  $h_{\infty}/v_{\text{TC}}$ , which is clearly the inviscid characteristic time scale (Savva & Bush, 2009). If viscous effects are taken into account (Brenner & Gueyffier, 1999), then there is also a viscous (Stokes) length scale  $l_{\text{vis}} = \nu/v_{\text{TC}}$ , so that the associated viscous time scale becomes  $l_{\text{vis}}/v_{\text{TC}} = \mu h_{\infty}/2\sigma$ . For comparison, in the case of water soap film of thickness  $10 \mu\text{m}$ ,  $\tau_{\text{inv}} = 10^{-5}$  s, while  $\tau_{\text{vis}} = 10^{-7}$  s meaning that viscous effects are not important once  $v_{\text{TC}}$  is established – this fact is also confirmed by the corresponding estimated Reynolds number  $Re = v_{\text{TC}}h_{\infty}/\nu = 10^2$ .

Equation (3.7) can be rewritten by taking into account that  $d/dt = v_r d/dx$ :

$$\frac{d}{dx} \left( \frac{1}{2} m v_r^2 \right) + \frac{1}{2} \frac{dm}{dx} v_r^2 = 2\sigma, \quad (3.12)$$

integration of which with respect to  $x$  from 0 to  $x_r$  furnishes

$$2\sigma x_r = \frac{1}{2} \rho h_{\infty} x_r v_r^2 + \frac{1}{2} \rho h_{\infty} \int_0^{x_r} v_r^2 dx, \quad (3.13)$$

indicating that the surface energy on the left is converted not only into the kinetic one of the rim, but also into the second term on the right – its physical meaning amounts to doing the work against capillary pressure force inside the blob in order to inject mass  $\delta m$  into the blob over time  $\delta t$ , cf. figures 3.12a and 3.12b<sup>2</sup>. In the limit when the Taylor-Culick velocity is established, the latter term becomes equal to the kinetic energy of the rim resulting in the energy balance:

$$2\sigma x_r = \rho h_{\infty} x_r v_r^2. \quad (3.14)$$

This derivation highlights the mistake made by Dupré (1867), who assumed that the surface energy is converted into kinetic energy only.

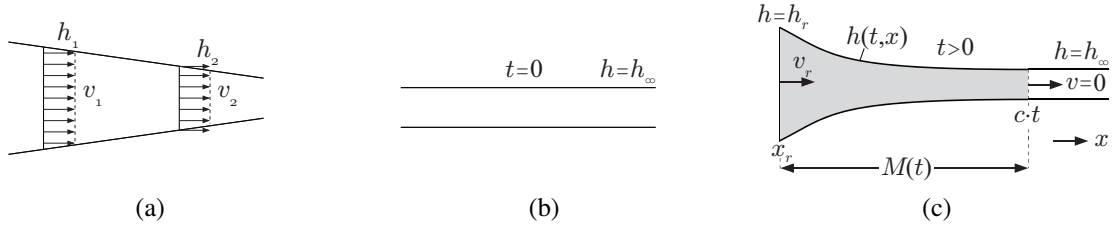


**Figure 3.13:** (a) Steady flow, (b,c) unsteady flow.

### 3.2.1.2 Generalized theory

The above analysis by [Taylor \(1959c\)](#) assumed that while the blob is moving with speed  $v_r$ , the sheet in front of it is not affected by the blob motion: this is justified only if the speed of propagation of disturbances along the soap film does not exceed the edge retraction speed. In the case of our phenomena, it is clear that in some regimes there is a front of disturbances overrunning the edge retraction very much like in rubber band/elastica retraction ([Mason, 1963](#); [Vermorel et al., 2007](#)): this region ahead of the soap film edge is now affected by the soap film dynamics and cannot be considered stationary bringing us to the picture in figure 3.12c and generalized analysis is developed here.

The key complication of this new situation, compared to the Taylor analysis, is that both the film thickness and the sheet velocity become functions of the time  $t$  and position  $x$  along the soap film,  $v_s(t, x)$  and  $h(t, x)$ , i.e. the ordinary differential equation (ODE) problem becomes of the partial differential equation (PDE) type due to its distributed character. In addition to the blob mass, which is still calculated according to  $m(t) = \rho h_\infty x_r(t)$  and can be assumed of circular cylinder shape of radius  $r$  determined from the mass conservation  $\pi r^2 = h_\infty x_r(t)$ , we also have to take into account the total affected mass  $M(t)$ , which includes both the blob and the deformed soap film profile ahead of it up to the position  $x = ct$ :

$$M(t) = \rho c t h_\infty = m(t) + \rho \int_{x_r+r}^{ct} h(t, x) dx, \quad (3.15)$$

<sup>2</sup>The interpretation is similar to the propulsion of a rocket, in which pressure forces of the exhaust gases do the work to propel the rocket.

where at the upper limit of integration  $h(t, ct) = h_\infty$  and at the lower limit can be assumed  $h(t, x_r + r) \approx 2r$ , but the latter assumption does not help one to determine the soap film thickness distribution. The nontriviality of the above mass conservation form can be seen by comparing to the steady state flow in a channel or soap film, which thickness profile does not vary in time, cf figure 3.13a, leading to the simple mass conservation form relating velocities and thicknesses at different locations:

$$v_1 h_1 = v_2 h_2. \quad (3.16)$$

In our situation, however, the mass conservation has an integral form reflecting the fact that the affected mass brought into motion changes with time due to signal propagation with speed  $c$  and, as opposed to the configuration in figure 3.13a, the flow velocity vanishes at  $x = ct$ , where the film thickness is finite and non-zero,  $h(t, ct) = h_\infty$ .

The momentum conservation (3.3) applied to the situation in figure 3.12c reads

$$\rho h_\infty x_r(t) \frac{d^2 x_r}{dt^2} = -\rho h(t, x_r + r) \left[ \frac{dx_r}{dt} - v_s(t, x_r + r) \right]^2 + F_{\text{ext}}, \quad (3.17)$$

with the surface tension force  $F_{\text{ext}}$  acting on the blob should now take into account that it acts at some angle to the  $x$ -axis, which can be found from the soap film thickness profile  $h(t, x_r + r)$ . While equation (3.17) can be rewritten in terms of the blob radius  $r(t)$ , it still contains boundary values of unknown functions  $h(t, x_r + r)$  and  $v_s(t, x_r + r)$ .

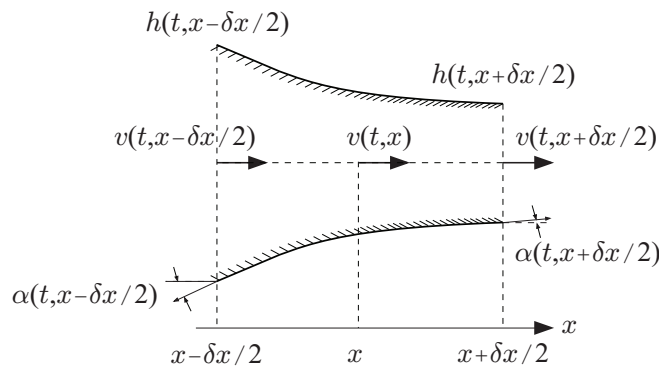


**Figure 3.14:** Element of an evolving soap film.

In order to determine the distribution of soap film thickness and velocity ahead of the blob, let us appeal to the local analysis of the soap film element of mass  $\delta m$  in figure 3.14. In the system of coordinates moving with the element of mass  $\delta m$ , the mass conservation reflects the fact that  $\delta m = \text{const}$ :

$$\delta m \approx \frac{h\left(t, x - \frac{\delta x}{2}\right) + h\left(t, x + \frac{\delta x}{2}\right)}{2} \delta x(t) \approx h(t, x) \delta x(t), \quad (3.18)$$

while its deformation during travel accounts for the balance of mass fluxes:

$$\frac{\partial h}{\partial t}(t, x) \delta x = v\left(t, x - \frac{\delta x}{2}\right) h\left(t, x - \frac{\delta x}{2}\right) - v\left(t, x + \frac{\delta x}{2}\right) h\left(t, x + \frac{\delta x}{2}\right), \quad (3.19)$$

leading to the mass conservation in the differential form

$$\frac{\partial h}{\partial t} = -h \frac{\partial v}{\partial x}. \quad (3.20)$$

The momentum conservation reads

$$\delta m \frac{dv}{dt}(t, x) = 2\sigma \left\{ \cos \left[ \alpha \left( t, x + \frac{\delta x}{2} \right) \right] - \cos \left[ \alpha \left( t, x - \frac{\delta x}{2} \right) \right] \right\}. \quad (3.21)$$

Taylor expanding the above expression and using equation (3.18) for the mass of the element we arrive at

$$h(t, x) \frac{\partial v}{\partial t}(t, x) = -2\sigma \sin [\alpha(t, x)] \frac{\partial \alpha}{\partial x} \approx -2\sigma \alpha(t, x) \frac{\partial \alpha}{\partial x} \quad (3.22)$$

for small deformations of the soap film (in particular, small angles  $\alpha$ ), where we also take into account that we work in the Lagrangian frame of reference thus replace the total (material) derivative with partial one. The angle  $\alpha$  can be related to the film thickness profile via:

$$\frac{\partial h}{\partial x} = -\tan \alpha \approx -\alpha, \quad (3.23)$$

again for small  $\alpha$ 's.

Since the presence of the blob is not crucial for our considerations and, indeed, there are cases in soap film dynamics when blob is not formed – for example in highly viscous films (Debrégeas *et al.*, 1995) in which an “instantaneous” thickening of the film is observed due to elastic propagation – we can consider the simpler situation in figures 3.13b and 3.13c. The total mass conservation (3.15) is then simplified as  $m(t) \equiv 0$ . The resulting initial-boundary value problem in Lagrangian coordinates becomes

$$h \frac{\partial v}{\partial t} = -2\sigma \frac{\partial h}{\partial x} \frac{\partial^2 h}{\partial x^2}, \quad (3.24a)$$

$$\frac{\partial h}{\partial t} = -h \frac{\partial v}{\partial x}, \quad (3.24b)$$

$$\int_{x_r}^{ct} \frac{\partial h}{\partial t} dx = h(t, x_r) v_r, \quad v_r \equiv v(t, x_r) = \frac{dx_r}{dt} \quad (3.24c)$$

$$t = 0 : h = h_\infty, v = 0, x_r = 0, \quad (3.24d)$$

$$x = ct : h_x = 0, h = h_\infty, v = 0. \quad (3.24e)$$

By inspection, it is easy to establish that the solution of the first two equations with the prescribed initial conditions would be trivial unless we take into account the nontrivial fact about the initial acceleration pointed out earlier in the context of Taylor’s derivation (3.9) rewritten here in the newly adopted variables

$$x_r \frac{\partial v}{\partial t} = \frac{2\sigma}{\rho h_\infty}; \quad (3.25)$$

this initial kick provides evolution of retracting soap film with deforming thickness profile in our case. It may seem unusual that the initial condition is posed in terms of acceleration (3.25), while the highest order derivative in the corresponding momentum equation (3.24a) is of the same order – the resolution of this apparent paradox is in that equation (3.24a) cannot be considered in isolation, but only as part of a second-order system of two equations (3.24a) and (3.24b).

In summary, the key qualitative observations from the derived initial-boundary value problem (3.24) is that the film is thickening monotonically with  $x$  in the interval  $x \in [x_r, ct]$ ; since, obviously,  $\partial v/\partial x < 0$ , from (3.24b) we get  $\partial h/\partial t > 0$  consistent with (3.24c), while (3.24a) tells us that  $\partial v/\partial t > 0$  since  $\partial h/\partial x < 0$  and  $\partial^2 h/\partial x^2 > 0$ , as per figure 3.14.

### 3.2.1.3 Numerical solution of one and two dimensional shock wave propagation models

Conservative form of one dimensional theoretical model (3.24) of the soap film retraction problem, which is rewritten here in Eulerian coordinates and non-dimensionalized based on the undisturbed film parameters:

$$h \rightarrow h_\infty h, \quad v \rightarrow v_\infty v, \quad x \rightarrow h_\infty x, \quad t \rightarrow \frac{h_\infty}{v_\infty} t, \quad (3.26)$$

takes the form

$$\frac{\partial h}{\partial t} + \frac{\partial (hv)}{\partial x} = 0, \quad (3.27a)$$

$$\frac{\partial (hv)}{\partial t} + \frac{\partial}{\partial x} \left[ h (v^2 + \hat{c}^2) + \frac{1}{2} \left( \frac{\partial h}{\partial x} \right)^2 \right] = 0, \quad (3.27b)$$

where  $\hat{c} = c/v_\infty$  and  $v_\infty \equiv v_{TC}(h_\infty)$ . Initial and boundary conditions read

$$t = 0 : \quad x_r(0) = 0, \quad h(0, x) = 1, \quad v_r(0) = 1, \quad (3.28a)$$

$$x = x_r : \quad v_r = \sqrt{h_\infty/h_r}, \quad \int_{x_r}^{\hat{c}t} h(t, x) dx = \hat{c}t, \quad (3.28b)$$

where  $x_r$  and  $v_r$  correspond to the soap film edge position and velocity, respectively.

In order to discretize the continuity equation (3.27a), finite difference method is implemented as follows

$$\frac{(h_i^n - h_i^{n-1})}{\Delta t} + \frac{(h_{i+1}^{n-1} u_{i+1}^{n-1}) - (h_i^{n-1} u_i^{n-1})}{\Delta x} = 0, \quad (3.29)$$

which is a backward scheme in time. Indices  $n$  and  $i$  correspond to time stamp and spatial mesh number, respectively. Using this discretization, the thickness of the soap film  $h_i^n$  is calculated based on the information at time stamp  $(n - 1)$ . Next, we discretize the momentum equation (3.27b) by implementing the same scheme as the one used for the continuity equation:

$$\frac{(hv)_i^n - (hv)_i^{n-1}}{\Delta t} + \frac{\left( h_i^n \left( (v_i^{n-1})^2 + \hat{c}^2 \right) + \frac{1}{2} (h_x)_i^n \right) - \left( h_{i-1}^n \left( (v_{i-1}^{n-1})^2 + \hat{c}^2 \right) + \frac{1}{2} (h_x)_{i-1}^n \right)}{\Delta x} = 0. \quad (3.30)$$

Using equation (3.30), we find  $v_i^n$  with the help of information on  $v$  at time stamp  $(n - 1)$  and  $h$  at time stamp  $n$ . The discretized equations are solved in MATLAB for 100 mesh nodes in  $x$  direction. Since the implemented scheme is an explicit one, we should make sure that the Courant number  $C = U\Delta t/\Delta x$  is less than one ( $C < 1$ ) to guarantee convergence of the solution. Parameter  $U$  in the Courant number is the maximum velocity in the system. By considering the Courant condition for maximum velocity  $U = \hat{c} \sim 2$ , time step  $\Delta t$  and spatial step  $\Delta x$  are chosen to be 0.1 and 1, respectively. Figure 3.15 shows the solution of the system after 80 time steps.

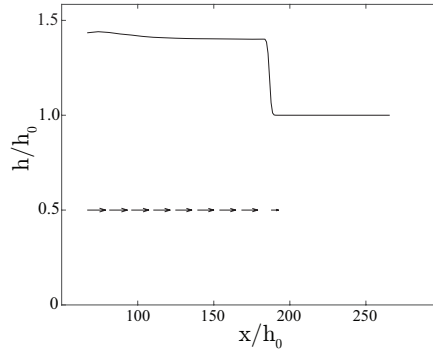


**Figure 3.15:** Shock wave and velocity field distribution on the soap film. Thickness of the soap film  $h$  at initial time equals to 1 over all the soap film. With passing time, the thickness of soap film increases up to  $\sim 1.4$  on the edge and then shock wave starts to propagate from the edge of the soap film toward its center. There is a steep decrease in the thickness of the film at  $\sim x/h_0 = 180$  which is a shock front. The shock front propagates on the soap film with the speed  $\hat{c}$ . Arrows show the velocity field distribution along the shock affected area. Velocity magnitude is at maximum on the boundary and slightly decreases towards the center of the soap film. Close to the shock front the magnitude of the velocity vectors decreases considerably.

Similarly, conservative form of the system of equations in two dimensional model of the soap film reads

$$\frac{\partial h}{\partial t} + \frac{\partial}{\partial x} (hu) + \frac{\partial}{\partial y} (hv) = 0, \quad (3.31a)$$

$$\frac{\partial}{\partial t} (hu) + \frac{\partial}{\partial x} (hu^2 + F) + \frac{\partial}{\partial y} (huv) = 0, \quad (3.31b)$$

$$\frac{\partial}{\partial t} (hv) + \frac{\partial}{\partial x} (huv) + \frac{\partial}{\partial y} (hv^2 + F) = 0, \quad (3.31c)$$

where  $u$  is the  $x$ -component and  $v$  is the  $y$ -component of the velocity field in the  $(x, y)$  soap film plane and  $F = \frac{1}{2} (h_x^2 + h_y^2 + \hat{c}^2 h)$ . Initial and boundary conditions are defined as

$$t = 0 : x_r(0, y) = 0, y_r(x, 0) = 0, h(x, y) = 1, u_r(0, y) = 1, v_r(x, 0) = 1, \quad (3.32a)$$

$$x = x_r(t) : u_r = \sqrt{\frac{h_\infty}{h_r}}, \quad y = y_r(t) : v_r = \sqrt{\frac{h_\infty}{h_r}}. \quad (3.32b)$$

In order to solve this two dimensional model numerically, it is discretized as appropriate for solving non-linear systems of hyperbolic conservative equations (Toro, 1999). In the Cartesian coordinates one can rewrite these equations as:

$$W_t + G(W)_x + H(W)_y = 0, \quad (3.33)$$

where  $G$  and  $H$  are non-linear functions of  $W$ :

$$W = \begin{bmatrix} h \\ hu \\ hv \end{bmatrix}, G = \begin{bmatrix} hu \\ hu^2 + F \\ huv \end{bmatrix}, H = \begin{bmatrix} hv \\ huv \\ hv^2 + F \end{bmatrix}, \quad (3.34)$$

For each equation, first we solve by sweeping in the  $x$  direction

$$W_{i,j}^{n+\frac{1}{2}} = W_{i,j}^n + \frac{\Delta t}{\Delta x} (G_{i-1,j}^n - G_{i,j}^n), \quad (3.35)$$

and then sweep in the  $y$  direction as is common in splitting schemes (Toro, 1999):

$$W_{i,j}^{n+1} = W_{i,j}^{n+\frac{1}{2}} + \frac{\Delta t}{\Delta y} \left( H_{i,j-1}^n - H_{i,j}^n \right); \quad (3.36)$$

here index  $n$  stands for the time stamp and indices  $i$  and  $j$  stand for mesh numbers in the  $x$  and  $y$  directions, respectively. For the two dimensional system of equations, the Courant number is defined as

$$C = \frac{U \Delta t}{\Delta x} + \frac{V \Delta t}{\Delta y} < 1, \quad (3.37)$$

where  $U$  and  $V$  are maximum velocities in  $x$  and  $y$  direction, respectively. By considering the Courant condition, time step  $\Delta t$ , spatial step  $\Delta x$  in the  $x$  direction, and spatial step  $\Delta y$  in the  $y$  direction are chosen to be 0.1, 1, and 1, respectively. The results of the numerical simulation after performing 80 time steps are shown in figure 3.16.

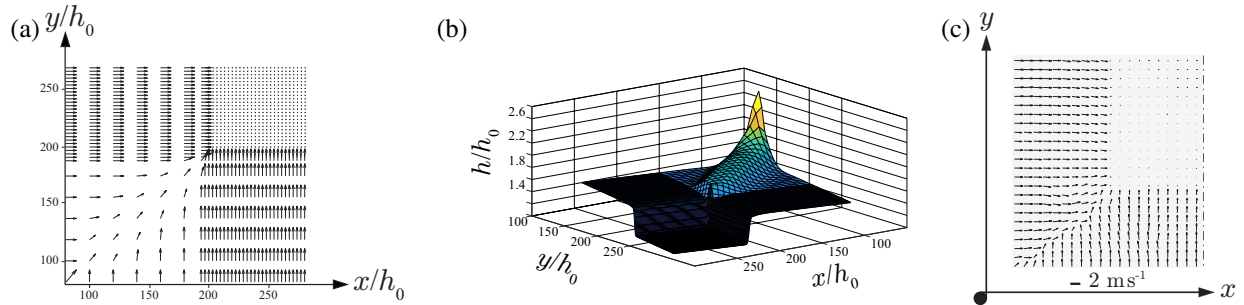


**Figure 3.16:** (a) Numerical result for the velocity field on the soap film in presence of a shock wave. (b) Changes of the soap film thickness due to the shock wave propagation in the soap film. On the diagonal, the soap film is folded and forms a bell shape profile. (c) The PIV image is acquired 2.4 ms after receiving the triggering pulse. Time difference between two PIV images is  $100 \mu\text{s}$ . The size of the gray area (PIV image) is  $19.8 \times 22 \text{ mm}$ .

Findings of the numerical simulation confirm the experimental observations. First, velocity field distribution (cf. figure 3.16a) is in good agreement with the experimental PIV velocity field measurements in figure 3.16c. Second, As shown by solving Eikonal equation and observations in the experiment, there is a fold on the diagonal of the soap film as a result of wave propagation (cf. figure 3.16b).

## 3.2.2 Waves on soap films

### 3.2.2.1 Taylor's inviscid analysis

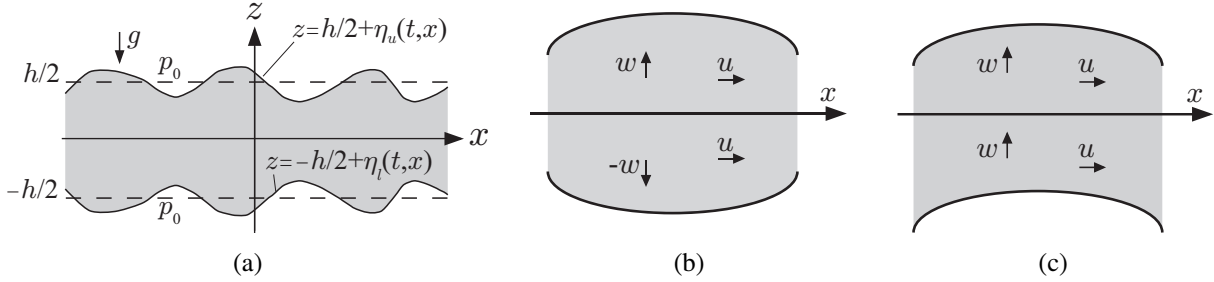


**Figure 3.17:** Waves on a soap film: (a) coordinate setup, (b) symmetric and (c) antisymmetric waves.

Before dwelling on viscous and Marangoni effects, let us first set the stage by reviewing the classical analysis by [Taylor \(1959a\)](#) of waves in an initially stationary free film in the inviscid potential flow approximation using the configuration shown in figure 3.17a. The upper interface is given by  $z = \frac{h}{2} + \eta_u(t, x)$  with the associated normal and tangent vectors, and curvature:

$$\mathbf{n} = \frac{\nabla F}{|\nabla F|} = \frac{-\mathbf{i}\eta_x + \mathbf{k}}{\sqrt{1 + \eta_x^2}}, \quad \mathbf{t} = \frac{\nabla F}{|\nabla F|} = \frac{\mathbf{i} + \mathbf{k}\eta_x}{\sqrt{1 + \eta_x^2}}, \quad \nabla \cdot \mathbf{n} = -\frac{\eta_{xx}}{(1 + \eta_x^2)^{3/2}}, \quad (3.38)$$

respectively, where  $F = z - \frac{h}{2} - \eta_u(t, x)$ ; similar expressions hold for the lower interface  $z = -\frac{h}{2} + \eta_l(t, x)$ , though the analysis will prove to be sufficient to develop only for the upper interface despite that in general both interfaces can move independently. In the above geometric setting, the problem

formulation reads:

$$\frac{\partial u}{\partial x} + \frac{\partial w}{\partial z} = 0, \quad (3.39a)$$

$$\frac{\partial u}{\partial t} + u \frac{\partial u}{\partial x} + w \frac{\partial u}{\partial z} = -\frac{1}{\rho} \frac{\partial p}{\partial x}, \quad (3.39b)$$

$$\frac{\partial w}{\partial t} + u \frac{\partial w}{\partial x} + w \frac{\partial w}{\partial z} = -\frac{1}{\rho} \frac{\partial p}{\partial z} - g, \quad (3.39c)$$

$$z = \frac{h}{2} + \eta_u(t, x) : \frac{\partial \eta}{\partial t} + u \frac{\partial \eta}{\partial x} = w, \quad (3.39d)$$

$$z = \frac{h}{2} + \eta_u(t, x) : p = p_0, \quad (3.39e)$$

with similar boundary conditions at the lower interface; here  $p_0$  is the atmospheric pressure. To simplify the bulk momentum equations, note that the hydrostatic pressure  $p_h = -\rho g z + \text{const.}$  Letting  $p_h|_{z=h/2} = p_0$ , we find  $\text{const} = p_0 + \rho g h/2$  and hence the dynamic pressure can be expressed as

$$p(t, x, z) = p_h + p'(t, x, z), \text{ where } p_h = p_0 + \rho g \left( \frac{h}{2} - z \right). \quad (3.40)$$

Then the momentum equations read

$$\frac{\partial u}{\partial t} + u \frac{\partial u}{\partial x} + w \frac{\partial u}{\partial z} = -\frac{1}{\rho} \frac{\partial p'}{\partial x}, \quad (3.41a)$$

$$\frac{\partial w}{\partial t} + u \frac{\partial w}{\partial x} + w \frac{\partial w}{\partial z} = -\frac{1}{\rho} \frac{\partial p'}{\partial z}, \quad (3.41b)$$

and the perturbation pressure  $p'$  at the upper interface assumes the value

$$z = \frac{h}{2} + \eta_u(t, x) : p' = \rho g \eta(t, x) + \sigma \nabla \cdot \mathbf{n}. \quad (3.42)$$

If the flow is initially irrotational, then based on Kelvin's theorem it continues to be so at later times and thus the ansatz  $\mathbf{v} = (u, w) = \nabla\phi$  simplifies the Euler problem (3.39)a-c to<sup>3</sup>

$$-\frac{h}{2} + \eta_l < z < \frac{h}{2} + \eta_u : \quad \Delta\phi = 0, \quad (3.43a)$$

$$-\frac{h}{2} + \eta_l < z < \frac{h}{2} + \eta_u : \quad \frac{\partial\phi}{\partial t} + \frac{1}{2}(\nabla\phi)^2 + \frac{p'}{\rho} = 0, \quad (3.43b)$$

while the boundary conditions reduce to

$$z = \frac{h}{2} + \eta_u : \quad \frac{\partial\eta}{\partial t} + \frac{\partial\phi}{\partial x} \frac{\partial\eta}{\partial x} = \frac{\partial\phi}{\partial z}, \quad (3.44a)$$

$$z = \frac{h}{2} + \eta_u : \quad p' = \rho g \eta(t, x) + \sigma \nabla \cdot \mathbf{n}. \quad (3.44b)$$

Since we are interested in the small amplitude wave solutions of the above system, it is sufficient for this purpose to consider its linearized version and thus, for convenience, to decompose the solution into symmetric (figure 3.17b) and anti-symmetric (figure 3.17c) parts, which based on the obvious symmetries of the velocity components indicated in those figures lead to the following requirements on the velocity potential (and streamfunction  $\psi$  as well defined via  $u = \psi_z$  and  $w = -\psi_x$ , which is shown here for future use):

$$\text{symmetric :} \quad \phi(t, x, -z) = \phi(t, x, z), \quad \psi(t, x, -z) = -\psi(t, x, z), \quad (3.45a)$$

$$\text{antisymmetric :} \quad \phi(t, x, -z) = -\phi(t, x, z), \quad \psi(t, x, -z) = \psi(t, x, z). \quad (3.45b)$$

In order to solve the linearized problem we take the Fourier transform defined as  $\hat{\phi}(t, z; k) = \int_{\mathbb{R}} \phi(t, x, z) e^{-ikx} dx$ , thus leading to the following problem in the Fourier space

$$-\frac{h}{2} < z < \frac{h}{2} : \quad \frac{d^2\hat{\phi}}{dz^2} - k^2\hat{\phi} = 0, \quad (3.46a)$$

---

<sup>3</sup>In this derivation it is convenient to consider the momentum equation in the vector form  $\partial\mathbf{v}/\partial t + (\mathbf{v} \cdot \nabla)\mathbf{v} = -\nabla p'/\rho$ , so that the vector equality  $(\mathbf{v} \cdot \nabla)\mathbf{v} = \frac{1}{2}\nabla(\mathbf{v} \cdot \mathbf{v}) - \mathbf{v} \times (\nabla \times \mathbf{v})$  and integration with respect to spatial coordinates leads to the Euler-Lagrange integral (3.43b), where we put the constant of integration (which in general can be a function of time) to be zero without loss of generality since the velocity potential is defined up to any function of time.

$$z = \pm \frac{h}{2} : \begin{cases} \frac{\partial \hat{\phi}}{\partial t} + \left( g + \frac{\sigma}{\rho} k^2 \right) \hat{\eta} = 0, & (3.46b) \\ \frac{\partial \hat{\eta}}{\partial t} = \frac{\partial \hat{\phi}}{\partial z}, & (3.46c) \end{cases}$$

where we linearized not only the equations, but also the boundary locations to non-perturbed positions. Notably, the boundary conditions in (3.46) can be reduced to a single equation in the Fourier space:

$$z = \pm \frac{h}{2} : \frac{\partial^2 \hat{\phi}}{\partial t^2} + \left( g + \frac{\sigma}{\rho} k^2 \right) \frac{\partial \hat{\phi}}{\partial z} = 0. \quad (3.47)$$

The solution of the Laplace equation (3.46a) in a finite width strip can be written as a sum of symmetric and antisymmetric parts

$$\hat{\phi}(t, z; k) = C_s(t; k) \cosh kz + C_a(t; k) \sinh kz. \quad (3.48)$$

Solving for each part separately, from the boundary condition (3.47) at  $z = \pm h/2$  we get the oscillator equations for the amplitudes  $C_s$  and  $C_a$ , e.g. for the symmetric part:

$$\frac{d^2 C_s}{dt^2} + \left( g + \frac{\sigma}{\rho} k^2 \right) k \tanh \left( \frac{kh}{2} \right) C_s = 0, \quad (3.49)$$

meaning that the frequency of symmetric waves  $\omega_s^2 = \left( g + \frac{\sigma}{\rho} k^2 \right) k \tanh \left( \frac{kh}{2} \right)$ , i.e. it is the boundary conditions which determine the frequency, while the Laplace equations defines the spatial structure (decay) of the solution away from the boundaries; similarly, the frequency of antisymmetric waves is rendered to be  $\omega_a^2 = \left( g + \frac{\sigma}{\rho} k^2 \right) k \coth \left( \frac{kh}{2} \right)$ . These are the classical results obtained by Taylor (1959a).

In the phenomena under consideration, we are going to be interested in the waves of length  $\lambda$  substantially shorter than the capillary length  $l_c = \sqrt{\sigma/\rho g}$ , which means that we can safely neglect the gravity contribution, but sufficiently longer than the soap film thickness, so that both  $\tanh \left( \frac{kh}{2} \right)$

and  $\coth\left(\frac{kh}{2}\right)$  are close to unity. If we consider the monochromatic waves of a specific wavelength  $\lambda = 2\pi/k$ , it is appropriate to speak of their phase speed  $v = \omega/k$ , which in the symmetric and antisymmetric cases read:

$$v_s \approx k \sqrt{\frac{\sigma h}{2\rho}}, \quad (3.50a)$$

$$v_a \approx \sqrt{\frac{2\sigma}{\rho h}}, \quad (3.50b)$$

i.e. the symmetric (peristaltic) modes are dispersive, while the antisymmetric ones are non-dispersive propagating with the same speed regardless of the wavelength – moreover, this speed coincides with the Taylor-Culick one for the edge retraction (3.10)!

### 3.2.2.2 Surfactant surface kinetics and material behavior

Taylor's analysis above neglected the presence of a surfactant, without which a soap film cannot exist, which leads to an extra set of equations governing surfactant transport. Hence, to close the system of equations, we need to describe the evolution of the surface tension  $\sigma$  that enters the problem through the surface stress balance. The surface tension is considered as a function of surface excess  $\Gamma/\Gamma_\infty$  scaled by the saturation concentration  $\Gamma_\infty$  (strictly speaking,  $\Gamma_\infty$  is different from that  $\Gamma_{\max}$  corresponding to the critical micelle concentration (CMC)  $C_{\max}$ ), which is known as the Frumkin equation – a model for the material behaviour:

$$\sigma = \sigma_0 + RT\Gamma_\infty \ln\left(1 - \frac{\Gamma}{\Gamma_\infty}\right), \quad (3.51)$$

where  $R$  is the perfect gas constant,  $T$  the temperature, and the last term is often called the spreading (surface) pressure  $f$  of the surfactant. As mentioned above, in the case of a soluble surfactant, the sorption kinetics is modelled by a Langmuir isotherm, which at equilibrium  $d\Gamma/dt = 0$  is given by (3.53) with  $\Gamma = \Gamma_0$  and  $c = c_0$  being the interfacial and bulk concentrations at equilibrium. The Frumkin equation in the equilibrium case becomes the von Szyskowski equation. At low concen-

trations (compared to CMC), equation (3.51) reduces to a perfect gas law:

$$\sigma = \sigma_0 - \Gamma RT \equiv \sigma_a - \sigma_r \Gamma, \quad (3.52)$$

which is the simplest equation of state for the surface tension, where  $\sigma_a$  is the surface tension in the absence of surfactant and  $\sigma_r$  accounts for the elasticity of the film.

While in the non-equilibrium case there is a dependence of the kinetic constants on concentration (Chang & Franses, 1992), one can approximate the non-equilibrium surfactant dynamics with the Langmuir-Hinshelwood equation, valid below  $C_{\max} = 8.3 \text{ mM}$ , for the surfactant surface concentration  $\Gamma$ :

$$\frac{d\Gamma}{dt} = k_a c \left( 1 - \frac{\Gamma}{\Gamma_{\max}} \right) - k_d \Gamma, \quad (3.53)$$

with  $k_a = 0.64 \cdot 10^{-5} \text{ m s}^{-1}$ ,  $k_d = 5.87 \text{ s}^{-1}$ , and the Langmuir constant  $K_L = k_a/k_d \Gamma_{\max} = 0.11 \frac{\text{m}^3}{\text{mol}}$  calculated based on the analysis in Chang *et al.* (1992) of the data by Elworthy & Mysels (1966). Therefore, the typical time of adsorption  $t_a = \Gamma_{\max}/(k_a c)$  is  $< 1 \text{ s}$ , for the range of concentrations  $c \leq C_{\max}$ , and the time of desorption  $t_d = k_d^{-1} < 0.2 \text{ s}$ . In equilibrium, the chemical potential of the soap molecules are equal in the bulk and in the surface phase, which imposes a relation between  $\Gamma_1$  and  $c_1$ . For concentrations significantly below the CMC,  $\Gamma \ll \Gamma_{\max}$ , this relation can be taken as linear,

$$\Gamma = K c, \quad (3.54)$$

where  $K \equiv k_a/k_d$  is a coefficient with the dimension of a length that may be interpreted as the virtual thickness of the interface in terms of soap molecule adsorption. Since soap molecules, composed of a hydrophilic polar head and a hydrophobic carbon tail, tend to be absorbed at the surface,  $K$  is large, e.g. of the order of  $4 \mu\text{m}$  for sodium dodecyl sulfate (SDS) following Rusanov & Krotov (1979).

We shall assume that the flux  $j$  is dictated by an adsorption-desorption process given by a first-order kinetics using the linearized version of (3.53) for  $\Gamma \ll \Gamma_{\max}$ :

$$j = (Kc - \Gamma) / \tau \equiv \frac{d\Gamma}{dt} = k_d \left[ \frac{k_a}{k_d} c - \Gamma \right], \quad (3.55)$$

where  $\tau = k_d^{-1}$  is the adsorption-desorption time, which may be large too (from an order of  $10^2$  s for a pure single surfactant agent and  $Kc$  is the instantaneous equilibrium surface density, so that the equilibrium equation (3.54) does not apply.

### 3.2.2.3 Soap film elasticity

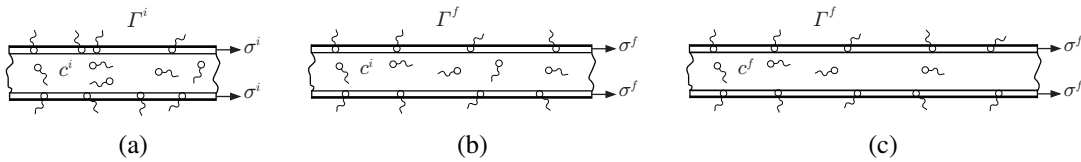


**Figure 3.18:** Evolution of a soap film under an increase of the applied tension (Couder *et al.*, 1989; Chomaz, 2001): (a) initial state, (b) instantaneous response (Marangoni elasticity), (c) long-time response (Gibbs elasticity).

First, one needs to consider the process by which a soap film is created. The film is usually formed by dipping a wire frame and withdrawing it from the bath with surfactant solution of concentration  $c_0$ . The film itself is composed of a bulk phase and a double surface phase which may exchange soap molecules, cf. figure 3.18a. Its surface concentration  $\Gamma_1$  and the bulk concentration  $c_1$  of the interstitial fluid are linked by the mass conservation

$$c_0 = c_1 + 2\Gamma_1/h, \quad (3.56)$$

where  $c_0$  is the total concentration of soap, given by the initial solution in the bath from which the film has been made.

Thin liquid films made from aqueous solutions of surface-active material demonstrate a resistance against thinning by extension, which can be interpreted as film elasticity. This property is

similar to a Young's modulus of a solid material in that it represents the ratio between the stress increase and the corresponding extension. The increased stress in the extended film can be attributed to depletion of surface-active material in the extended surfaces and in the contacting film liquid – the process, which accounts for the foaming properties of the soap film solutions. The contribution of this surfactant transport effect to the film elasticity is time dependent, since the depletion of surface-active material near the extended film surface is counteracted by transport of surfactant from the film liquid and, more slowly, from further-removed parts of the system.

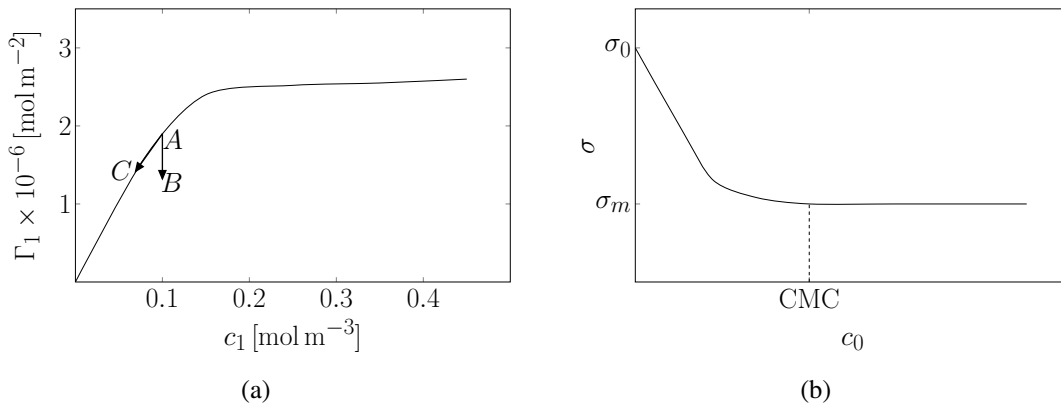


**Figure 3.19:** (a) Adsorption isotherm: the surface concentration  $\Gamma_1$  of soap molecules adsorbed at the interface as a function of the volumetric concentration  $c_1$  in the bulk of the fluid. (b) The isothermal dependence of the surface tension  $\sigma$  on the concentration  $c_0$  of the solution.

A local stretching of the soap film disturbs the equilibrium between  $\Gamma_1$  and  $c_1$ . Figure 3.18 illustrates the stretching of a soap film initially at equilibrium, when the tension force applied to the film is increased from  $\sigma^i$  to  $\sigma^f$  in (b) or (c). If this happens over times shorter than the adsorption-desorption time  $\tau$  (figure 3.18b), the flux of molecules from the bulk fluid to the surface is negligible, so that the same number of surfactant molecules initially present at the interface are now distributed over a larger area: path A-B in figure 3.19a showing that as the surface of the film increases, the surface soap concentration  $\Gamma$  decreases from its initial value  $\Gamma^i$  until it reaches the final value  $\Gamma^f$ . Over these short times, the initial chemical equilibrium given by  $Kc^i - \Gamma^i = 0$  is violated and soap molecules begin to migrate from the bulk to the surface. In the course of this migration process, the film continues to elongate slowly since  $j$  is positive and  $\Gamma$  increases from the value  $\Gamma^i$  by the

imposed constant tension applied to the film. This fast time response of the film is usually named as the Marangoni elasticity. For times larger than the adsorption-desorption time  $\tau$  (figure 3.18c),  $j$  vanishes and the new equilibrium given by  $Kc^f - \Gamma^f = 0$  is reached: path A-C in figure 3.19a. Under the condition of slow film stretching compared to the time scale  $\tau$ , the elasticity is of the Gibbs type<sup>4</sup> with (dilatational) modulus of a thin film defined in analogy to the Young modulus (Prins *et al.*, 1967; Rusanov & Krotov, 1979) as the response of the surface tension to a fractional increase of the area  $A$  of a surface element<sup>5</sup>

$$E = \frac{2d\sigma}{d \ln A}. \quad (3.57)$$

Formula (3.57) amounts to the following behavior: an increase in the area  $A$  of a patch of the film, which inevitably accompanies film thinning, causes the surfactant molecules surface concentration to dilute and the surface tension  $\sigma$  to increase thus providing a restoring force. In view of Lucassen *et al.* (1970) the modulus (3.57) contains an elastic part (immediate response of surface tension) and a viscous part (delayed response). Using incompressibility of the interstitial fluid, expression (3.57) can be rewritten as

$$E = -2A \frac{df}{dA} = -2h \frac{d\sigma}{dh}. \quad (3.58)$$

For example, the Gibbs elasticity  $E_G$  found from (3.57) proves to be

$$E_G = \frac{2E_M K}{h + 2K}, \quad (3.59)$$

which, for example, for a  $2 \mu\text{m}$  thick film of a dilute solution of SDS gives  $E_G = 30 \times 10^{-3} \text{ N/m}$  for small concentrations when the linear relationship (3.54) applies, the Marangoni elasticity is simply

---

<sup>4</sup>The transition between the Marangoni and the Gibbs elasticity is also affected by the time scale  $\tau_D = h^2/D$  which characterizes the diffusive motion of soap molecules through the film thickness, i.e. for the same surfactant films of different thicknesses may behave differently. For example, if the diffusion coefficient is  $D = 4 \times 10^{-6} \text{ cm}^2/\text{s}$ , for films  $1 \mu\text{m}$  thick  $\tau_D$  is of the order of 0.01 s.

<sup>5</sup>There is an alternative definition (Edwards *et al.*, 1991) of the Gibbs elasticity  $E = -d\sigma/d \ln \Gamma$ , which is equivalent to (3.57) (without factor of two) only for an insoluble monolayer and at large surface Peclet number.

double of the surface pressure:

$$E_M = 2f = 2RT\Gamma_1, \quad (3.60)$$

where  $\Gamma_1$  can be found from (3.54) and (3.56) resulting in

$$\Gamma_1 = c_0 \frac{hK}{h + 2K}. \quad (3.61)$$

In the limit of thin films,  $h \ll 2K$ , i.e. when the interstitial fluid is too thin to provide soap molecules to the interfaces,  $E_G \approx E_M$ .

#### 3.2.2.4 Elasticity waves in soap films: phenomenological model

The fact that elasticity can be calculated as a number without detailed modeling of surfactant transport brings about the possibility of a simple calculation of the speed of the corresponding “sound” waves in a soap film. First, let us neglect damping effects in the soap film evolution. Also, because of the disparate scales of the thickness  $h$  of the film and the soap film extension  $L \gg h$ , we may assume that the velocity is in the film plane and uniform in depth (plug flow). In this approximation, the mass and momentum conservation laws can be easily written for a soap film element:

$$\frac{Dh}{Dt} = -h \operatorname{div} \mathbf{u}, \quad (3.62a)$$

$$\frac{D\mathbf{u}}{Dt} = -\frac{E(h)}{\rho h^2} \nabla h, \quad (3.62b)$$

where the latter equation follows from the Newton second law for the soap film element balancing the inertia and elastic forces (due to surface tension gradients):

$$\rho h \frac{D\mathbf{u}}{Dt} = 2\nabla \sigma, \quad (3.63)$$

	Soap film	Compressible flow
Continuity equation	$\frac{Dh}{Dt} = -h \operatorname{div} \mathbf{u}$	$\frac{D\rho}{Dt} = -\rho \operatorname{div} \mathbf{u}$
Momentum equations	$\frac{D\mathbf{u}}{Dt} = -\frac{E(h)}{\rho h^2} \nabla h$	$\frac{D\mathbf{u}}{Dt} = -c^2 \frac{\nabla \rho}{\rho}$

**Table 3.3:** Analogy between soap film and compressible flow dynamics (Wen & Lai, 2003).

where we may express the surface tension force acting on two soap film interfaces using (3.58) as

$$2\nabla\sigma = 2\frac{d\sigma}{dh}\nabla h = -\frac{E(h)}{h}\nabla h. \quad (3.64)$$

The direct comparison of the system (3.62) with that for compressible barotropic  $p = p(\rho)$  fluid flow in table 3.3 tells us that the speed of “sound” propagation is  $c = \sqrt{E/\rho h}$ . Using the Marangoni elasticity value  $E_M = 2f = 80 \times 10^{-3}$  N/m we find  $c = 4$  m/s in a  $10 \mu\text{m}$  thick film, and  $c = 13$  m/s in a  $1 \mu\text{m}$  thick film. The existence of elasticity-mediated speed of propagation, similar to that for sound speed, provides the means for generating shock waves in soap films – the subject, which is still of wide appeal (Wen & Lai, 2003; Wen *et al.*, 2003; Tran *et al.*, 2009; Kim & Mandre, 2017).

### 3.2.2.5 Effect of viscosity and elasticity on soap film waves

Let us now consider the 2D version of the problem, ignoring the  $y$ -coordinate in the soap film plane. Since in the presence of viscosity the flow field can no longer be assumed potential, it must include the vorticity part via the Helmholtz decomposition (Arfken & Weber, 2005):

$$\mathbf{v} = \nabla\phi + \nabla \times \boldsymbol{\psi}, \quad (3.65)$$

where  $\boldsymbol{\psi} = \mathbf{j}\psi$  is the vector stream-function and  $\nabla = \mathbf{i}\partial_x + \mathbf{k}\partial_z$ , where  $\mathbf{i}$ ,  $\mathbf{j}$ ,  $\mathbf{k}$  are unit vectors in the  $x$ ,  $y$ , and  $z$  directions, respectively. Component-wise, the velocity then reads

$$u = \phi_x + \psi_z, \quad w = \phi_z - \psi_x. \quad (3.66)$$

As a result, neglecting gravity based on earlier considerations in §3.2.2.1, the linear problem of wave propagation on a quiescent soap film decomposes into the potential part:

$$\Delta\phi = 0, \quad (3.67a)$$

$$\frac{\partial\phi}{\partial t} + \frac{p}{\rho} = 0, \quad (3.67b)$$

and the viscous part:

$$\frac{\partial\psi}{\partial t} - \nu\Delta\psi = 0. \quad (3.68)$$

Based on the symmetries (3.45), the antisymmetric solution of the above system for  $\phi$  and  $\psi$  can be sought in the form

$$\phi = C_a \sinh(kz) e^{i(\omega_a t - kx)} + \text{c.c.}, \quad (3.69a)$$

$$\psi = D_a \cosh(mz) e^{i(\omega_a t - kx)} + \text{c.c.}, \quad (3.69b)$$

where  $m^2 = k^2 + i\omega_a/\nu$  and, as before in the inviscid case, the frequency  $\omega_a$  is dictated by the interfacial boundary conditions; the symmetric solution (3.45a) for  $\phi$  and  $\psi$  is found by changing  $\sinh$  to  $\cosh$  and vice versa. The pressure is then determined from the linearized Euler-Lagrange equation (3.67b). The dynamic boundary conditions simplify, in the linear approximation, to

$$p + \sigma\eta_{xx} = 2\mu w_x, \quad (3.70a)$$

$$\sigma_x = \mu(u_z + w_x), \quad (3.70b)$$

while the kinematic boundary condition becomes:

$$\frac{\partial\eta}{\partial t} = w. \quad (3.71)$$

There are two ways to deal with the Marangoni term  $\sigma_x$  in the tangential boundary condition (3.70b): (i) to model this term as elastic, and (ii) to account for the surfactant dynamics, which would require solving additional surfactant transport equations. In what follows, we will consider and compare both approaches.

First, following Lucassen *et al.* (1970) and more recently Acharige *et al.* (2014), equation (3.70b) can be rewritten as

$$\tilde{E} \xi_{xx} = \mu (u_z + w_x), \quad (3.72)$$

where  $\tilde{E} = d\sigma/d \ln A$ , i.e. half that of (3.57)<sup>6</sup> and  $\xi$  is the displacement of the interface in the  $x$ -direction. In such a formulation one does not need to model the surfactant dynamics as long as the dilational modulus  $\tilde{E}$  can be measured as was recently done by Acharige *et al.* (2014); in fact,  $\tilde{E}$  proves to be complex  $\tilde{E} = \tilde{E}' + i\tilde{E}''$  with real part being “in-phase” and imaginary “out-of-phase” components (Edwards *et al.*, 1991).

To start with the derivation of a dispersion relation, we can simplify the involved boundary conditions. From (3.70a) and (3.67b) with the use of (3.66) we deduce

$$-\rho\phi_t + \sigma\eta_{xx} = 2\mu (\phi_{zx} - \psi_{xx}), \quad (3.73)$$

which after the Fourier transform in  $x$  becomes

$$\sigma k^2 \hat{\eta} = 2\mu (ik\hat{\psi}_z - \hat{\phi}_{zz}) - \rho\hat{\phi}_t, \quad (3.74)$$

while (3.71) in the Fourier space yields  $\hat{\eta}_t = \hat{\phi}_z - ik\hat{\psi}$ , which together with the above expression produces

$$\sigma k^2 (\hat{\phi}_z - ik\hat{\psi}) = 2\mu (ik\hat{\psi}_{tz} - \hat{\phi}_{tzz}) - \rho\hat{\phi}_{tt}. \quad (3.75)$$

---

<sup>6</sup>convention used by many authors including Lucassen *et al.* (1970); Rusanov & Krotov (1979); Kim & Mandre (2017) cited here.

The tangential boundary condition (3.70b) with  $\sigma_x = \tilde{E} \xi_{xx}$  and  $\xi_t = \phi_x + \psi_z$  in turn furnishes

$$\hat{\xi}_t = ik\hat{\phi} + \hat{\psi}_z, \quad (3.76a)$$

$$-\frac{\tilde{E}}{\mu}k^2\hat{\xi} = \hat{\psi}_{zz} + k^2\hat{\psi} + 2ik\hat{\phi}_z. \quad (3.76b)$$

Considering one frequency harmonic

$$\hat{\phi} = \hat{\phi}^\omega e^{i\omega t}, \quad \hat{\psi} = \hat{\psi}^\omega e^{i\omega t}, \quad \hat{\xi} = \hat{\xi}^\omega e^{i\omega t}, \quad (3.77)$$

we can reduce (3.75,3.76) to the following system

$$-\rho\omega^2\hat{\phi}^\omega + \sigma k^2 (\hat{\phi}_z^\omega - ik\hat{\psi}^\omega) = -2\mu\omega (k\hat{\psi}_z^\omega + i\hat{\phi}_{zz}^\omega), \quad (3.78a)$$

$$\hat{\psi}_{zz}^\omega + k^2\hat{\psi}^\omega + 2ik\hat{\phi}_z^\omega = i\frac{\tilde{E}}{\mu\omega}k^2 (ik\hat{\phi}^\omega + \hat{\psi}_z^\omega). \quad (3.78b)$$

First, let us consider the effect of viscosity on the dispersion relation in absence of film elasticity, i.e.  $\sigma_x = 0$  in (3.70b) or  $\tilde{E} = 0$  in (3.78). In the case of antisymmetric waves, i.e. when velocity potential and stream-function are represented via

$$\hat{\phi}^\omega = A \sinh kz, \quad \hat{\psi}^\omega = B \cosh mz, \quad (3.79)$$

the system (3.78) leads to the dispersion relation

$$\frac{\omega}{k} = \sqrt{\frac{2\sigma}{\rho h}}, \quad (3.80)$$

i.e. the waves are non-dispersive and frequency does not depend on viscosity, which may seem counter-intuitive as viscosity should lead to the waves decay – this is because in the linear wave approximation in the antisymmetric (bending) wave there is not much relative motion of fluid elements and hence viscous stresses would appear only at the next order of approximation compared to the

symmetric waves, where viscosity proves to contribute at the leading order due to more substantial fluid elements deformation. Note that the wavenumber  $m$  (in  $z$ -direction) of the vorticity mode is complex now.

Second, let us consider the symmetric mode

$$\hat{\phi}^\omega = A \cosh kz, \quad \hat{\psi}^\omega = B \sinh mz, \quad (3.81)$$

in the presence of elasticity. The same system (3.78) leads to the dispersion relation

$$\omega^2 - 4ivk^2\omega - \left( \frac{\sigma h}{2\rho} k^4 + \frac{2\tilde{E}}{\rho h} k^2 \right) = 0, \quad (3.82)$$

which does exhibit dependence on viscosity (contributing to the imaginary part of  $\omega$  responsible for the decay). In the absence of viscous effects, there are two limiting frequencies and corresponding phase velocities:

$$\omega = k^2 \sqrt{\frac{\sigma h}{2\rho}} \Rightarrow v_s = k \sqrt{\frac{\sigma h}{2\rho}}, \quad (3.83a)$$

$$\omega = k \sqrt{\frac{2\tilde{E}}{\rho h}} \Rightarrow v_{se} = \sqrt{\frac{2\tilde{E}}{\rho h}}, \quad (3.83b)$$

where the first one corresponds to (3.50a) determined by Taylor (1959a) and the second one is due to the film elasticity: as shown below in §3.2.2.6, the latter (elastic) mode is dominant. Strictly speaking, keeping elasticity while neglecting viscosity is non-physical because viscosity is required to balance Marangoni stresses (Landau & Lifshitz, 1987) as is evident from the tangential part of the dynamic boundary condition (3.70b). Therefore, the right way to interpret formula (3.83b) is for small, but non-zero viscosity  $\mu$ .

### 3.2.2.6 Symmetric modes

The motion of a peristaltic (symmetric) mode involves two possible processes of change in the local film thickness. The first one  $(\partial h / \partial t)_f$  is due to the internal viscous flows from one region to the

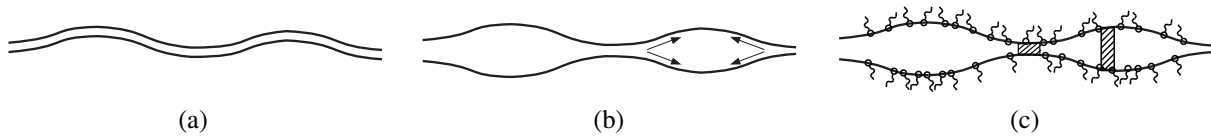


**Figure 3.20:** Waves in a soap film: (a) antisymmetric, (b) Taylor symmetric and (c) elastic symmetric.

other related, as in films of pure water, to variations of the Laplace pressure, cf. figure 3.20b. In the second one, the changes  $(\partial h/\partial t)_s$  due to the elastic stretching of the surface films in the antinodes, cf. figure 3.20c. To evaluate the order of magnitude of the ratio of these two effects, let us first estimate  $(\partial h/\partial t)_f$  using Trouton's formula (Trouton, 1906) for the rate of uniform deformation of a viscous medium:

$$\frac{dL}{dt} = \frac{FL}{3\mu S}, \quad (3.84)$$

where  $L$  is the length of the element being deformed,  $S$  its cross-sectional area,  $\mu$  the dynamic viscosity of the liquid, and  $F$  the force applied to the cross-section. In our case, using the incompressibility condition we find

$$\frac{1}{L} \frac{dL}{dt} = -\frac{1}{h} \frac{dh}{dt}, \quad (3.85)$$

and using for the force  $F = S\Delta p$ , where  $\Delta p$  is the pressure difference for the perturbed and non-perturbed regions in the soap film, we obtain

$$\left(\frac{\partial h}{\partial t}\right)_f = -\frac{h\Delta p}{3\mu}. \quad (3.86)$$

To determine the rate of changing the film thickness due to inner flows in the region of higher pressure, we use Reynolds' formula (Reynolds, 1886) describing the hydrodynamics of the flow between two approaching parallel solid disks of radius  $R$ :

$$\frac{d}{dt} \left( \frac{1}{h^2} \right) = \frac{4\Delta p}{3\mu R^2}, \quad (3.87)$$

application of which to our situation with  $R \simeq \lambda$  being the wavelength, yields

$$\left(\frac{\partial h}{\partial t}\right)_s = -\frac{h^3 \Delta p}{\mu \lambda^2}. \quad (3.88)$$

Altogether, the ratio of the involved two effects (Rusanov & Krotov, 1979) can be estimated as

$$\left(\frac{\partial h}{\partial t}\right)_f / \left(\frac{\partial h}{\partial t}\right)_s \sim \frac{h^2}{\lambda^2}, \quad (3.89)$$

which is a small quantity in our case. As a result, the pure symmetrical (Taylor) mode (3.50a) can be neglected in the soap films, and the waves are the elastic waves (3.83b), where the variation of thickness are related to variation of the surface density of the surfactant molecules, cf. figure 3.20c. We have to emphasize that so far the derivation was based on phenomenological modeling of soap film elasticity. Next, we will take on a more rigorous approach.

### 3.2.2.7 Soap film dynamics: problem statement

With reference to figure 3.17a we can now formulate a complete problem of soap film dynamics (Fast, 2005) taking into account the surfactant transport and three-dimensionality of the problem. Introducing the notations for 3D velocity vector  $\mathbf{v} = (u, v, w)$  and gradient  $\nabla = \mathbf{i}\partial_x + \mathbf{j}\partial_y + \mathbf{k}\partial_z$ , as well as their 2D counterparts in the soap film  $(x, y)$ -plane velocity  $\mathbf{u} = (u, v)$  and gradient  $\nabla_{\parallel} = \mathbf{i}\partial_x + \mathbf{j}\partial_y$ , the corresponding equations in the bulk are

$$-\frac{h}{2} + \eta_l(t, x, y) < z < \frac{h}{2} + \eta_u(t, x, y) : \begin{cases} \nabla \cdot \mathbf{v} = 0, & (3.90a) \\ \frac{\partial \mathbf{v}}{\partial t} + (\mathbf{v} \cdot \nabla) \mathbf{v} = -\frac{1}{\rho} \nabla p + \nu \nabla^2 \mathbf{v}, & (3.90b) \\ \frac{\partial c}{\partial t} + (\mathbf{v} \cdot \nabla) c = D \nabla^2 c, & (3.90c) \end{cases}$$

and at the interface

$$z = \frac{h}{2} + \eta_u(t, x, y) : \left\{ \begin{array}{l} \frac{\partial \eta}{\partial t} + \mathbf{u} \cdot \nabla_{\parallel} \eta = w, \quad (3.91a) \\ -\mathbf{n} \cdot (\mathbf{P}_1 - \mathbf{P}_2) \cdot \mathbf{n} = 2\mathcal{H}\sigma, \quad (3.91b) \\ -\mathbf{t} \cdot (\mathbf{P}_1 - \mathbf{P}_2) \cdot \mathbf{n} = \mathbf{t} \cdot \nabla_s \sigma, \quad (3.91c) \\ \frac{\partial \Gamma}{\partial t} + \nabla_s \cdot (\mathbf{u}_s \Gamma) + \Gamma (\nabla_s \cdot \mathbf{n}) (\mathbf{v} \cdot \mathbf{n}) = D_s \nabla_s^2 \Gamma + j, \quad (3.91d) \end{array} \right.$$

where  $\mathbf{P}$  is the stress tensor expressed in terms of the rate-of-strain tensor  $\mathbf{D}$ :

$$\mathbf{P} = -p\mathbf{I} + \left( \zeta - \frac{2}{3}\mu \right) (\mathbf{I} : \mathbf{D}) \mathbf{I} + 2\mu \mathbf{D}(\mathbf{v}), \quad \text{with } \mathbf{D}(\mathbf{v}) = \frac{1}{2} [\nabla \mathbf{v} + (\nabla \mathbf{v})^T], \quad (3.92)$$

which in the incompressible flow case simplifies since  $\zeta = \frac{2}{3}\mu$ ; here  $\nabla_s = \mathbf{I}_s \cdot \nabla$  is the surface gradient, which can be expressed in terms of the surface idemfactor

$$\mathbf{I}_s = \mathbf{I} - \mathbf{nn} = \frac{1}{1 + \eta_x^2 + \eta_y^2} \begin{pmatrix} 1 + \eta_y^2 & -\eta_x \eta_y & \eta_x \\ -\eta_x \eta_y & 1 + \eta_x^2 & \eta_y \\ \eta_x & \eta_y & \eta_x^2 + \eta_y^2 \end{pmatrix}, \quad (3.93)$$

where  $\mathbf{nn}$  is a dyadic tensor formed by juxtaposing a pair of normal to the interface vectors  $\mathbf{n}$ , so that

$$\nabla_s = \frac{1}{1 + \eta_x^2 + \eta_y^2} \begin{pmatrix} (1 + \eta_y^2)\partial_x - \eta_x \eta_y \partial_y + \eta_x \partial_z \\ -\eta_x \eta_y \partial_x + (1 + \eta_x^2)\partial_y + \eta_y \partial_z \\ \eta_x \partial_x + \eta_y \partial_y + (\eta_x^2 + \eta_y^2)\partial_z \end{pmatrix}; \quad (3.94)$$

$j = -D\mathbf{n} \cdot \nabla c$  is the flux of soap from the bulk film to the surface, which in the case of first order kinetics is given by (3.55) and follows from the linearized (for low concentrations  $\Gamma \ll \Gamma_{\infty}$ )

Langmuir-Hinshelwood equation

$$j = k_a c - k_d \Gamma \equiv (Kc - \Gamma) / \tau, \text{ with } \tau = k_d^{-1}, K = k_a / k_d, \quad (3.95)$$

while the surfactant material behavior  $\sigma(\Gamma)$  is described by the linearized Frumkin equation of state

$$\sigma = \sigma_0 - RT\Gamma \equiv \sigma_a - \sigma_r \Gamma, \text{ where } \sigma_r = -\sigma_\Gamma(0) = RT. \quad (3.96)$$

The coefficients  $D$  and  $D_s$  are the bulk and surface diffusivities of a surfactant, respectively; and  $\mathbf{u}_s = \mathbf{I}_s \cdot \mathbf{v}$ , which in general is different from  $\mathbf{u}$  in the  $(x, y)$ -plane

$$\mathbf{u}_s = \frac{1}{1 + \eta_x^2 + \eta_y^2} \begin{pmatrix} (1 + \eta_y^2)u - \eta_x \eta_y v + \eta_x w \\ -\eta_x \eta_y u + (1 + \eta_x^2)v + \eta_y w \\ \eta_x u + \eta_y v + (\eta_x^2 + \eta_y^2)w \end{pmatrix}. \quad (3.97)$$

The interface  $\eta(t, x, y)$  geometry is given by the normal and tangent vectors:

$$\mathbf{n} = \frac{\nabla S}{|\nabla S|} = \frac{-\mathbf{i}\eta_x - \mathbf{j}\eta_y + \mathbf{k}}{\sqrt{1 + \eta_x^2 + \eta_y^2}}, \quad \mathbf{t}_1 = \frac{\mathbf{i} + \mathbf{k}\eta_x}{\sqrt{1 + \eta_x^2 + \eta_y^2}}, \quad \mathbf{t}_2 = \frac{\mathbf{j} + \mathbf{k}\eta_y}{\sqrt{1 + \eta_x^2 + \eta_y^2}}, \quad (3.98)$$

respectively, where  $S = z - \frac{h}{2} - \eta(t, x, y)$  and, notably, the tangent vectors are not unit. The surface mean curvature with this choice of coordinates computes to

$$2\mathcal{H} \equiv \nabla \cdot \mathbf{n} = \nabla_s \cdot \mathbf{n} = \frac{-\eta_{xx}(1 + \eta_y^2) + 2\eta_x \eta_y \eta_{xy} - \eta_{yy}(1 + \eta_x^2)}{(1 + \eta_x^2 + \eta_y^2)^{3/2}}. \quad (3.99)$$

### 3.2.2.8 Soap film dynamics: non-dimensional equations

Using non-dimensionalization for the time, coordinates and velocities:

$$t \rightarrow \frac{L}{U}t, (x, y) \rightarrow L(x, y), z \rightarrow h_\infty z, \mathbf{u} \rightarrow U\mathbf{u}, w \rightarrow \epsilon U w, \quad (3.100)$$

where  $\epsilon = h_\infty/L$  and the scaling for  $w$  follows from the continuity equation, and the following non-dimensionalization for the rest of variables:

$$p \rightarrow \frac{\epsilon \sigma_m}{L} p, \Gamma \rightarrow \Gamma_m \Gamma, c \rightarrow C_m c, \sigma \rightarrow \sigma_m \sigma, \quad (3.101)$$

where the scalings with index  $m$  stand for the mean values of interfacial and bulk concentrations obeying the relations  $K C_m - \Gamma_m = 0$  as well as surface tension  $\sigma_m = \sigma_0 - \sigma_r \Gamma_m$ ; note that because the dilute case is considered  $\Gamma \ll \Gamma_\infty$ , scaling with respect to  $\Gamma_\infty$  and  $\sigma_0$  is less convenient since  $K C_\infty \neq \Gamma_\infty$  in view of the linearized character of the Frumkin equation (3.51) used here. As a result of non-dimensionalization we will naturally arrive at the following non-dimensional complexes:

$$Re = \frac{UL}{\nu}, Sc = \frac{\nu}{D}, Sc_s = \frac{\nu}{D_s}, \lambda = \frac{L}{U\tau}, Ma_M^2 = \frac{\rho h_\infty U^2}{\sigma_r \Gamma_m}, Ma_\sigma^2 = \epsilon^{-2} \frac{\rho h_\infty U^2}{\sigma_m}, \quad (3.102)$$

which are the Reynolds, bulk and surface Schmidt, relaxation, Marangoni and capillary (bending) Mach numbers, respectively. The corresponding non-dimensional equations in the bulk read

$$\left\{ \begin{array}{l} \nabla_{\parallel} \cdot \mathbf{u} + \frac{\partial w}{\partial z} = 0, \quad (3.103a) \\ \frac{\partial \mathbf{u}}{\partial t} + (\mathbf{u} \cdot \nabla_{\parallel}) \mathbf{u} + (w \partial_z) \mathbf{u} = -\frac{1}{Ma_\sigma^2} \nabla_{\parallel} p + \frac{1}{Re} \left( \nabla_{\parallel}^2 + \epsilon^{-2} \partial_z^2 \right) \mathbf{u}, \quad (3.103b) \\ \frac{\partial w}{\partial t} + (\mathbf{u} \cdot \nabla_{\parallel}) w + (w \partial_z) w = -\frac{\epsilon^{-2}}{Ma_\sigma^2} \frac{\partial p}{\partial z} + \frac{1}{Re} \left( \nabla_{\parallel}^2 + \epsilon^{-2} \partial_z^2 \right) w, \quad (3.103c) \\ \frac{\partial c}{\partial t} + (\mathbf{u} \cdot \nabla_{\parallel}) c + (w \partial_z) c = \frac{1}{Re Sc} \left( \nabla_{\parallel}^2 + \epsilon^{-2} \partial_z^2 \right) c, \quad (3.103d) \end{array} \right.$$

and the corresponding non-dimensional interfacial conditions are:

$$\frac{\partial \eta}{\partial t} + \mathbf{u} \cdot \nabla_{\parallel} \eta = w, \quad (3.104a)$$

$$p - 2\mathcal{H}\sigma = \frac{Ma_{\sigma}^2}{Re} \frac{2}{1 + \epsilon^2(\eta_x^2 + \eta_y^2)} \left\{ -\nabla_{\parallel} \cdot \mathbf{u} - \eta_x u_z - \eta_y v_z \right. \\ \left. + \epsilon^2 \left[ \eta_x^2 u_x + \eta_y^2 v_y + \eta_x \eta_y (u_y + v_x) - \eta_x w_x - \eta_y w_y \right] \right\}, \quad (3.104b)$$

$$-\epsilon^2 \frac{Re}{Ma_M^2} \Gamma_x = \frac{1}{\sqrt{1 + \epsilon^2(\eta_x^2 + \eta_y^2)}} \left\{ u_z + \epsilon^2 \left[ -\eta_x^2 u_z + w_x - \eta_x \eta_y v_z \right. \right. \\ \left. \left. - 2\eta_x (u_x - w_z) - \eta_y (u_y + v_x) \right] - \epsilon^4 \left[ \eta_x^2 w_x + \eta_x \eta_y w_y \right] \right\}, \quad (3.104c)$$

$$-\epsilon^2 \frac{Re}{Ma_M^2} \Gamma_y = \frac{1}{\sqrt{1 + \epsilon^2(\eta_x^2 + \eta_y^2)}} \left\{ v_z + \epsilon^2 \left[ -\eta_y^2 v_z + w_y - \eta_x \eta_y u_z \right. \right. \\ \left. \left. - 2\eta_y (v_y - w_z) - \eta_x (u_y + v_x) \right] - \epsilon^4 \left[ \eta_y^2 w_y + \eta_x \eta_y w_x \right] \right\} \quad (3.104d)$$

where we took into account that  $\sigma_x = -\sigma_r \Gamma_x$  and similarly for  $\sigma_y$ ; also

$$2\mathcal{H} \rightarrow \frac{\epsilon}{L} 2\mathcal{H}, \quad 2\mathcal{H} = -\nabla_{\parallel}^2 \eta + O(\epsilon^3). \quad (3.105)$$

The non-dimensional interfacial surfactant transport becomes

$$\frac{\partial \Gamma}{\partial t} + \nabla_s \cdot (\mathbf{u}_s \Gamma) + \Gamma (\nabla_s \cdot \mathbf{n}) (\mathbf{v} \cdot \mathbf{n}) = \frac{1}{Re S c_s} \nabla_s^2 \Gamma + j, \quad (3.106)$$

with  $j = \lambda(c - \Gamma)$  and the surface gradient scaled with respect to  $L^{-1}$ :

$$\nabla_s = \frac{1}{1 + \epsilon^2(\eta_x^2 + \eta_y^2)} \begin{pmatrix} \partial_x + \eta_x \partial_z + \epsilon^2 \left[ \eta_y^2 \partial_x - \eta_x \eta_y \partial_y \right] \\ \partial_y + \eta_y \partial_z + \epsilon^2 \left[ \eta_x^2 \partial_y - \eta_x \eta_y \partial_x \right] \\ \epsilon \left[ \eta_x \partial_x + \eta_y \partial_y + (\eta_x^2 + \eta_y^2) \partial_z \right] \end{pmatrix}, \quad (3.107)$$

and the interfacial velocity scaled with respect to  $U$ :

$$\mathbf{u}_s = \frac{1}{1 + \epsilon^2(\eta_x^2 + \eta_y^2)} \begin{pmatrix} u + \epsilon^2 [\eta_y^2 u - \eta_x \eta_y v + \eta_x w] \\ v + \epsilon^2 [\eta_x^2 v - \eta_x \eta_y u + \eta_y w] \\ \epsilon [\eta_x u + \eta_y v] + \epsilon^3 (\eta_x^2 + \eta_y^2) w \end{pmatrix}. \quad (3.108)$$

### 3.2.2.9 Soap film dynamics: asymptotic expansion

In order to simplify the complete system formulated in the previous subsection, let us expand all dependent variables in series of  $\epsilon^2$ , e.g. in-plane velocity:

$$\mathbf{u} = \mathbf{u}^0 + \epsilon^2 \mathbf{u}^1 + \dots, \quad (3.109)$$

and similarly for other variables, with the idea to derive equations governing continuity, momentum, and surfactant transport in the soap film  $(x, y)$ -plane only.

First, let us deal with the hydrodynamic part of the problem. The tangential components (3.104c, 3.104d) of the dynamic boundary condition at the leading order impose

$$\mathbf{u}_z^0 = 0, \quad (3.110)$$

thus implying no  $z$ -dependence  $\mathbf{u}^0 = \mathbf{u}^0(t, x, y)$ . As a result, by integration the continuity equation (3.103a) we find the  $z$ -component of velocity

$$w^0 = -z \nabla_{\parallel} \cdot \mathbf{u}^0, \quad (3.111)$$

as a result of which the kinematic condition (3.104a) can be expressed as

$$\frac{\partial \eta^0}{\partial t} + \mathbf{u}^0 \cdot \nabla_{\parallel} \eta^0 = -\eta^0 \nabla_{\parallel} \cdot \mathbf{u}^0 \Rightarrow \frac{\partial \eta^0}{\partial t} + \nabla_{\parallel} \cdot (\eta^0 \mathbf{u}^0) = 0. \quad (3.112)$$

The normal component (3.104b) of the dynamic boundary condition at the leading order produces:

$$p^0 + \nabla_{\parallel}^2 \eta^0 = -\frac{2Ma_{\sigma}^2}{Re} \nabla_{\parallel} \cdot \mathbf{u}^0, \quad (3.113)$$

At the order  $O(\epsilon^2)$  the momentum equation (3.103b) in the  $(x, y)$ -plane after integration with respect to  $z$  once and evaluation at  $z = \eta^0$  reads

$$\frac{1}{Re} \mathbf{u}_z^1 = \eta^0 \left[ \frac{\partial \mathbf{u}^0}{\partial t} + (\mathbf{u}^0 \cdot \nabla_{\parallel}) \mathbf{u}^0 + \frac{1}{Ma_{\sigma}^2} \nabla_{\parallel} p^0 + \frac{1}{Re} \nabla_{\parallel}^2 \mathbf{u}^0 \right], \quad (3.114)$$

and the tangential components (3.104c) and (3.104d) of the dynamic boundary conditions are

$$u_z^1 = -\frac{Re}{Ma_M^2} \Gamma_x^0 + 2\eta_x^0 u_x^0 + \eta_y^0 (u_y^0 + v_x^0) + \eta^0 (\nabla_{\parallel} \cdot \mathbf{u}^0)_x + 2\eta_x^0 \nabla_{\parallel} \cdot \mathbf{u}^0, \quad (3.115a)$$

$$v_z^1 = -\frac{Re}{Ma_M^2} \Gamma_y^0 + 2\eta_y^0 v_y^0 + \eta_x^0 (u_y^0 + v_x^0) + \eta^0 (\nabla_{\parallel} \cdot \mathbf{u}^0)_y + 2\eta_y^0 \nabla_{\parallel} \cdot \mathbf{u}^0, \quad (3.115b)$$

the combination of which with the momentum equation (3.114) at  $z = \eta^0$  and the normal component (3.113) of the dynamic boundary condition yields the system

$$Re \left[ \eta^0 \frac{D_{\parallel} u^0}{Dt} + \frac{1}{Ma_M^2} \Gamma_x^0 - \frac{\eta^0}{Ma_{\sigma}^2} \nabla_{\parallel}^2 \eta_x^0 \right] = 2\partial_x \left[ \eta^0 (u_x^0 + \nabla_{\parallel} \cdot \mathbf{u}^0) \right] + \partial_y (\eta^0 u_y^0 + \eta^0 v_x^0), \quad (3.116a)$$

$$Re \left[ \eta^0 \frac{D_{\parallel} v^0}{Dt} + \frac{1}{Ma_M^2} \Gamma_y^0 - \frac{\eta^0}{Ma_{\sigma}^2} \nabla_{\parallel}^2 \eta_y^0 \right] = 2\partial_y \left[ \eta^0 (v_y^0 + \nabla_{\parallel} \cdot \mathbf{u}^0) \right] + \partial_x (\eta^0 u_y^0 + \eta^0 v_x^0), \quad (3.116b)$$

where  $D_{\parallel}/Dt = \partial/\partial t + \mathbf{u}^0 \cdot \nabla_{\parallel}$ .

Next, let us adapt the surfactant transport equations to the soap film dynamics. The interfacial surfactant transport equation (3.106) at the leading order simplifies to

$$\frac{\partial \Gamma^0}{\partial t} + \nabla_{\parallel} \cdot (\mathbf{u}^0 \Gamma^0) = \frac{1}{Re Sc_s} \nabla_{\parallel}^2 \Gamma^0 + \lambda (c^0 - \Gamma^0), \quad (3.117)$$

where we took into account that  $2\mathcal{H} = O(\epsilon)$  and  $\nabla_s = \nabla_{\parallel} + O(\epsilon)$ . The transport equation for the bulk (interstitial) concentration (3.103d) at the leading order produces

$$c_{zz}^0 = 0, \quad (3.118)$$

implying no  $z$ -dependence  $c^0 = c^0(t, x, y)$ , while at the order  $O(\epsilon^2)$  we find

$$\frac{1}{Re Sc} \partial_z^2 c^1 = \frac{\partial c^0}{\partial t} + (\mathbf{u}^0 \cdot \nabla_{\parallel}) c^0 - \frac{1}{Re Sc} \nabla_{\parallel}^2 c^0, \quad (3.119)$$

which can be integrated with the corresponding (linearized) boundary condition

$$z = \eta^0 : \frac{1}{Re Sc} \partial_z c^1 = \lambda K^* (c^0 - \Gamma^0), \quad (3.120)$$

where  $K^* = K/h_{\infty}$ , leading to

$$\eta^0 \left[ \frac{\partial c^0}{\partial t} + (\mathbf{u}^0 \cdot \nabla_{\parallel}) c^0 - \frac{1}{Re Sc} \nabla_{\parallel}^2 c^0 \right] = \lambda K^* (c^0 - \Gamma^0). \quad (3.121)$$

In summary, defining the in-plane rate-of-strain tensor  $\mathbf{D}_{\parallel} = [\nabla_{\parallel} \mathbf{u}^0 + (\nabla_{\parallel} \mathbf{u}^0)^T] / 2$ , the resulting system of equations governing the soap film dynamics can be written (dropping superscripts) in the conservative form

$$\frac{\partial (\eta \mathbf{u})}{\partial t} + \nabla_{\parallel} \cdot (\eta \mathbf{u} \mathbf{u}) = -\frac{1}{Ma_M^2} \nabla_{\parallel} \Gamma + \frac{h}{Ma_{\sigma}^2} \nabla_{\parallel}^3 \eta + \nabla_{\parallel} \cdot \left\{ \frac{2\eta}{Re} [\mathbf{D}_{\parallel} + \mathbf{I} (\nabla_{\parallel} \cdot \mathbf{u})] \right\}, \quad (3.122a)$$

$$\frac{\partial \eta}{\partial t} + \nabla_{\parallel} \cdot (\eta \mathbf{u}) = 0, \quad (3.122b)$$

$$\frac{\partial \Gamma}{\partial t} + \nabla_{\parallel} \cdot (\Gamma \mathbf{u}) = -\lambda (\Gamma - c) + \frac{1}{Sc_s Re} \nabla_{\parallel}^2 \Gamma, \quad (3.122c)$$

$$\frac{\partial (\eta c)}{\partial t} + \nabla_{\parallel} \cdot (\eta c \mathbf{u}) = \lambda K^* (\Gamma - c) + \frac{\eta}{Sc_s Re} \nabla_{\parallel}^2 c. \quad (3.122d)$$

With the above systematically derived model for the soap film dynamics, we can not only justify the phenomenologically deduced system (3.62), but also compute the wave velocities on the

surface of a symmetrically perturbed soap film made of an insoluble surfactant. Considering small perturbations superimposed on a quiescent base state  $\mathbf{u} = \mathbf{0} + (u', 0)$ ,  $\eta = 1 + \eta'$ , and  $\Gamma = 1 + \Gamma'$ , we get the system of linearized equations

$$\frac{\partial u'}{\partial t} = -\frac{1}{Ma_M^2} \Gamma'_x + \frac{1}{Ma_\sigma^2} \eta'_{xxx} + \frac{4}{Re} u'_{xx}, \quad (3.123a)$$

$$\frac{\partial \eta'}{\partial t} + u'_x = 0, \quad (3.123b)$$

$$\frac{\partial \Gamma'}{\partial t} + u'_x = 0, \quad (3.123c)$$

which reduces to the single equation for the velocity perturbation

$$u'_{tt} = \frac{1}{Ma_M^2} u'_{xx} - \frac{1}{Ma_\sigma^2} u'_{xxxx} + \frac{4}{Re} u'_{txx}. \quad (3.124)$$

Neglecting dissipation (the last term in the above equation), we get two limiting types of waves:

$$Ma_M, Re \rightarrow \infty : u'_{tt} = -\frac{1}{Ma_\sigma^2} u'_{xxxx} \Rightarrow \omega = \frac{k^2}{Ma_\sigma^2}, \quad (3.125a)$$

$$Ma_\sigma, Re \rightarrow \infty : u'_{tt} = \frac{1}{Ma_M^2} u'_{xx} \Rightarrow \omega = \frac{k}{Ma_M}, \quad (3.125b)$$

where the former corresponds to the peristaltic dispersive modes (3.50a) determined by Taylor (1959a) and the latter corresponds to the elasticity waves (3.83b) calculated earlier phenomenologically and thus justifies its usage in interpreting the experimental data.

### 3.2.3 Acoustics on soap film: eikonal equation and key findings

Let us try to achieve understanding of the fold formation (1.27a) in the soap film dynamics with the help of a single eikonal equation:

$$\psi_x^2 + \psi_y^2 = \left(\frac{\omega}{c}\right)^2 \equiv n^2, \quad (3.126)$$

subject to the boundary conditions

$$x = 0 : \psi_x = k_0, \psi_y = 0, \quad (3.127a)$$

$$y = 0 : \psi_x = 0, \psi_y = k_0. \quad (3.127b)$$

In the context of geometric acoustics, if the phase  $\psi(x, y)$  is a solution of the eikonal equation, the level curves  $\psi(x, y) = \text{const}$  represent wavefronts, whereas the characteristic base curves  $x(s, \tau)$  and  $y(s, \tau)$  for fixed  $\tau$  represent acoustic rays. The intensity of the acoustic field in geometric acoustics is characterized by the convergence or divergence of the acoustic rays: as the rays converge the intensity increases. If there is a focal point  $(x_0, y_0)$  at which the rays converge or diverge from it, it corresponds to a singular point representing a point of high intensity of acoustic field. For example, a cylindrical wave

$$\psi(x, y) = \psi_0 + n\sqrt{(x - x_0)^2 + (y - y_0)^2}, \quad (3.128)$$

is a singular solution of the above eikonal equation – it clearly satisfies equation (3.126) except at the initial point  $(x_0, y_0)$  where the derivative  $\psi_x$  and  $\psi_y$  are singular. Another region of high intensity of acoustic field is given by the caustic curves which are envelopes of the characteristic base curves or the acoustic rays – the solutions of the eikonal equation break down at the caustic curves as well.

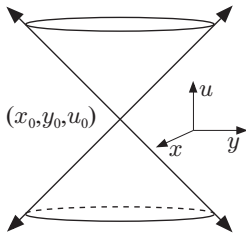


**Figure 3.21:** Mach cone.

Defining the implicit nonlinear first-order PDE (3.126) as  $F = p^2 + q^2 - n^2(x, y) = 0^7$  with  $p = \psi_x$  and  $q = \psi_y$ , and using the method of characteristics (Appendix 3.B) we get the system of five equations

$$\frac{dx}{ds} = 2p, \quad \frac{dy}{ds} = 2q, \quad \frac{d\psi}{ds} = 2n^2, \quad (3.129a)$$

$$\frac{dp}{ds} = 2nn_x, \quad \frac{dq}{ds} = 2nn_y. \quad (3.129b)$$

<sup>7</sup>The relationship (3.126),  $p^2 + q^2 = n^2$ , is the equation for the Monge cone, which is a right circular cone if  $n = \text{const}$  and making an angle  $\tan^{-1} \frac{1}{n}$  with the  $u$ -axis. Since the Monge cone is just the union of all acoustic rays passing through the point  $(x_0, y_0, u_0)$ , it is just the Mach cone, cf. figure 3.21.

If we are going to evolve from one of the sides of the soap film corner, say from  $y = 0$ , then the corresponding initial conditions can be parameterized as

$$x(0, \tau) = \tau, \quad y(0, \tau) = 0, \quad \psi(0, \tau) = 0, \quad p(0, \tau) = 0, \quad q(0, \tau) = k_0, \quad (3.130)$$

which obviously satisfy the non-characteristic condition as the transformation from  $(x, y)$  to  $(s, \tau)$  is non-degenerate since the Jacobian of that transformation

$$J(s, \tau) = \begin{vmatrix} \frac{\partial x}{\partial s} & \frac{\partial x}{\partial \tau} \\ \frac{\partial y}{\partial s} & \frac{\partial y}{\partial \tau} \end{vmatrix} = -2k_0 \neq 0. \quad (3.131)$$

Introducing  $\mathbf{r} = (x, y)$ , from the characteristic system (3.129) we deduce the ‘‘Newton’’ equation for ray evolution

$$\frac{1}{2} \frac{d^2 \mathbf{r}}{ds^2} = \nabla (n^2). \quad (3.132)$$

Since the vector tangent to the ray is  $\mathbf{t} = d\mathbf{r}/ds$  and  $\|d^2\mathbf{r}/ds^2\| = \kappa(s)$  is the curvature of the ray curve, then in the presence of inhomogeneous refraction index  $n = n(x, y)$  the ray bends in the direction of the positive gradient  $\nabla n$ . On the soap film diagonal,  $\nabla n$  is discontinuous and thus the curvature is singular!

Now, if we take into account the motion of the soap film itself with some velocity field  $\mathbf{u}$ , the steady-state eikonal equation (3.126) modifies to (since  $\omega = \text{const}$ ):

$$\omega = c |\nabla \psi| + \mathbf{u} \cdot \nabla \psi. \quad (3.133)$$

While the general nonlinear case can be formally considered, in order to make the implications of the presence of the soap film flow transparent, let us treat the case  $|\mathbf{u}| \ll c$ , which leads to the

characteristic system

$$\frac{dx}{ds} = 2(p + nu), \quad \frac{dy}{ds} = 2(q + nv), \quad \frac{d\psi}{ds} = 2 [n^2 - n(up + vq)], \quad (3.134a)$$

$$\frac{dp}{ds} = 2nn_x + 2n_x(up + vq) + 2n(u_x p + v_x q), \quad (3.134b)$$

$$\frac{dq}{ds} = 2nn_y + 2n_y(up + vq) + 2n(u_y p + v_y q).$$

Analysis similar to the case without the flow leads to the following “Newton’s” equations:

$$\frac{1}{2} \frac{d^2 x}{ds^2} = \frac{dp}{ds} + \frac{dn}{ds} u + n \frac{du}{ds}, \quad (3.135a)$$

$$\frac{1}{2} \frac{d^2 y}{ds^2} = \frac{dq}{ds} + \frac{dn}{ds} v + n \frac{dv}{ds}, \quad (3.135b)$$

or, in the vector form

$$\frac{1}{2} \frac{d^2 \mathbf{r}}{ds^2} = \frac{d}{ds} \mathbf{p} + \frac{dn}{ds} \mathbf{v} + n \frac{d\mathbf{v}}{ds}, \quad (3.136)$$

where  $\mathbf{p} = (p, q)$  and the first term on the right-hand side can be summed up from the corresponding characteristic equations

$$\frac{1}{2} \frac{d}{ds} \mathbf{p} = n \nabla n + (up + vq) \nabla n + n(p \nabla u + q \nabla v). \quad (3.137)$$

Next, taking into account the equalities

$$up + vq = \frac{1}{2}(ux_s + vy_s) - n(u^2 + v^2), \quad (3.138a)$$

$$p \nabla u + q \nabla v = \frac{1}{2}(x_s \nabla u + y_s \nabla v) - n(u \nabla u + v \nabla v), \quad (3.138b)$$

along with the vector form of some of their elements  $ux_s + vy_s = \mathbf{t} \cdot \mathbf{u}$  and  $x_s \nabla u + y_s \nabla v = \mathbf{t} \cdot \nabla \mathbf{u}$ , we arrive at

$$\frac{1}{2} \frac{d^2 \mathbf{r}}{ds^2} = \nabla (n^2) + \nabla n \mathbf{t} \cdot \mathbf{u} + n \mathbf{t} \cdot \nabla \mathbf{u} + \frac{d}{ds} (n \mathbf{u}); \quad (3.139)$$

in the notation  $\mathbf{t} \cdot \nabla \mathbf{u}$  we took into account the usual properties of vector-tensor product:

$$\mathbf{t} \cdot \nabla \mathbf{u} = (x_s, y_s) \begin{pmatrix} u_x & u_y \\ v_x & v_y \end{pmatrix} = x_s (\mathbf{i}u_x + \mathbf{j}u_y) + y_s (\mathbf{i}v_x + \mathbf{j}v_y). \quad (3.140)$$

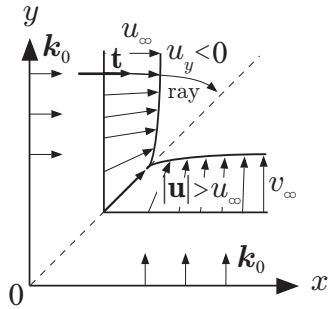


**Figure 3.22:** Velocity field.

The first term on the right of equation (3.139) shows the effect consistent with the conclusion drawn above from (3.132), i.e. that the ray bends towards the direction of decreasing sound speed (increasing refraction index), the second term amplifies the first term effect as  $\mathbf{t} \cdot \mathbf{u} > 0$ , the third term seems to suggest bending towards the transversal increase of along the ray velocity, e.g. if  $\mathbf{t} = (x_s, 0)$  and  $u_y > 0$  as per figure 3.22, then the ray initially propagating in the  $x$ -direction will bend in the positive  $y$ -direction. The positive sign of  $u_y$  is due to the

collision of the soap film flows on the diagonal and mass conservation: increasing film thickness on the diagonal leads to the decrease of the flow velocity. The last term in (3.139) is also positive since towards the diagonal not only  $n$  is increasing, but also the total in-plane velocity  $\mathbf{u}$  despite that the  $x$ -component  $u$  is decreasing. With the above understanding of the individual effects of all four terms on the right-hand side of (3.139), there is a more universal way to treat them. Namely, the first term is of the potential field nature due to its gradient structure, while the last three terms, when rewritten in the tensor notation and after taking into account that  $d/ds = \mathbf{t} \cdot \nabla$ , can be combined as

$$\nabla_j n t_i u^i + n t_i \nabla_j u^i + t_i \nabla_i (n u^j) = t_i [\nabla^j (n u_i) + \nabla_i (n u^j)], \quad (3.141)$$

where we took into account that the gradient is a covariant vector, while velocity is contravariant. The expression in parentheses on the right-hand side of (3.141) can be recognized as the in-plane stress tensor  $\tau_i^j \equiv \nabla^j(nu_i) + \nabla_i(nu^j)$ , though weighted with the refraction index  $n$ . The presence of the latter is not essential as even for  $n \equiv 1$ , the flow field in the soap film has a dynamic effect on acoustic rays.

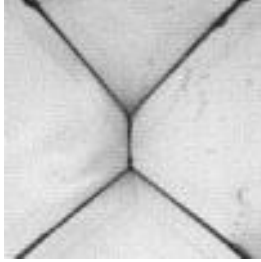


**Figure 3.23:** The bridge formation (cf. figure 3.7).

Applying this to the collapsing soap film we can conclude that the soap film flow will bend the rays towards the diagonal. In conclusion, all these effects – sound speed decreasing towards the diagonal as per (3.83b) since the film thickness  $h$  is larger on the diagonal as well as the soap film flow (§3.2.1.2) – seem to suggest that in the realm of our soap film acoustics, the rays will bend towards the diagonal of the soap film. As experimental observations indicate and, as consistent with the general theory of PDEs, the singularity at the corner (point  $O$  in figure 3.22), at which the eikonal equation is not valid, propagates along the diagonal and this singularity is also intensified by the convergence of acoustic rays emanating from retracting soap film edges towards the soap film diagonal. Having said that, the propagating acoustic fronts are capable of developing a SW-like structure even without the singularities in the initial data: indeed, figure (3.23) clearly shows that given enough time for the acoustic fronts evolution upon collision they produce similar singular structure of the bridge type, which connects the shock waves emanating from the singular corners of the soap film. The nature of the bridge formation upon collision of acoustic fronts in figure 3.23 is easy to understand as the waves propagating with a lower “sound” speed in the bridge area (due to increasing soap film thickness) are being caught up by faster traveling waves from behind.

# Appendices

## 3.A Optical film thickness measurements

Since soap film thickness is a determining factor in our analysis, to be confident about the data analysis and interpretation, soap film thickness was measured directly for all test conditions in this study via optical interference method. Referring to figure A3.1a, a collimated broad band light source (Dolan Jenner MI-150) (A) emits light through the soap film (B). On the other side of the soap film, a collimating lens (C), which is connected to a fiber optical cable (Thorlabs M25L02) (D), collects the transmitted light intensity and sends signals to a UV-VIS spectrometer (Ocean Optics USB-UV-VIS) (E). The spectrometer is connected to a PC (F) and data are recorded via SpectaSuite software: two examples of the observed signal are presented in figure A3.1b. Multiple maxima and minima are observed in the light signal (in the range of wavelengths  $\sim 500 - 650$  nm) that are used to calculate the soap film thickness as explained below. To make sure that the measured thicknesses are reasonably close to the ones in the experiments on shock wave formation, the thickness measurement procedure starts 1 s after that the soap frame is turned into the horizontal position. This is the time gap that the soap film is relaxed after getting in the horizontal position and before receiving the 2.4 kV trigger pulse to be released in free collapsing state.

The soap film thickness  $h_\infty$  is related to the wavelength  $\lambda$  of the transmitted light intensity through the soap film using equation:

$$h_\infty = (N/2n) \left[ (1/\lambda_1) - (1/\lambda_2) \right]^{-1}, \quad (\text{A3.1})$$

where  $N$  and  $n$  are number of cycles and refractive index of the soap solution, respectively. Parameters  $\lambda_1$  and  $\lambda_2$  are the wavelength values of any maxima or minima (Hecht, 2002). In equation (A3.1) the refractive index is assumed to be constant across all the soap film and equal to the re-

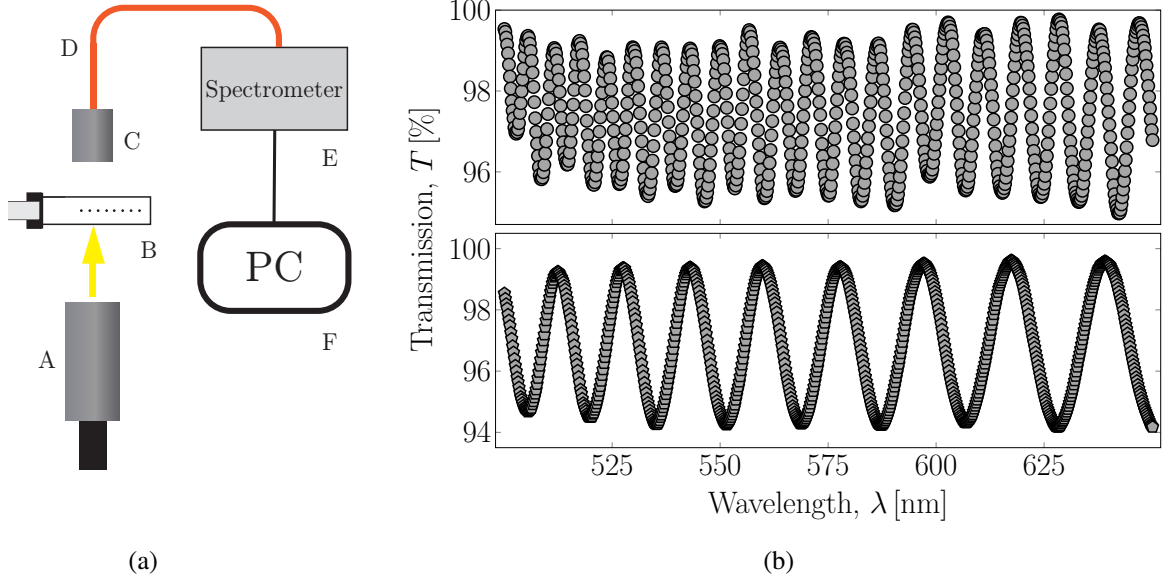


**Figure A3.1:** (a) Schematic of the soap film thickness measurement assembly. (b) Two samples of light intensity signal collected with the UV-VIS spectrometer. The top data set corresponds to a thick soap film compared the bottom data set for a thin soap film (calculated film thicknesses are provided in figure A3.2).

fractive index of soap solution  $n = 1.33$  (Huibers & Shah, 1997; Berg *et al.*, 2005). Considering the recorded light intensity signal we can modify equation (A3.1) as follows

$$h_{\infty} = (N/2n) \left[ (1/\lambda_0) - (1/\lambda_N) \right]^{-1}, \quad (\text{A3.2})$$

where  $\lambda_0$  represents the starting wavelength value from which all successive wavelength values  $\lambda_n$  are counted. Rearranging equation (A3.2) in the form

$$N = h_{\infty} \left\{ 2n \left[ (1/\lambda_0) - (1/\lambda_N) \right] \right\}, \quad (\text{A3.3})$$

helps one to find film thickness from the linear curve fit, as the only unknown in the experimental data is  $h_{\infty}$ . An example of the result of this approach using the data from figure A3.1 is shown in figure A3.2. The slope of the linear fitted curve equals to the film thickness  $h_{\infty}$ .

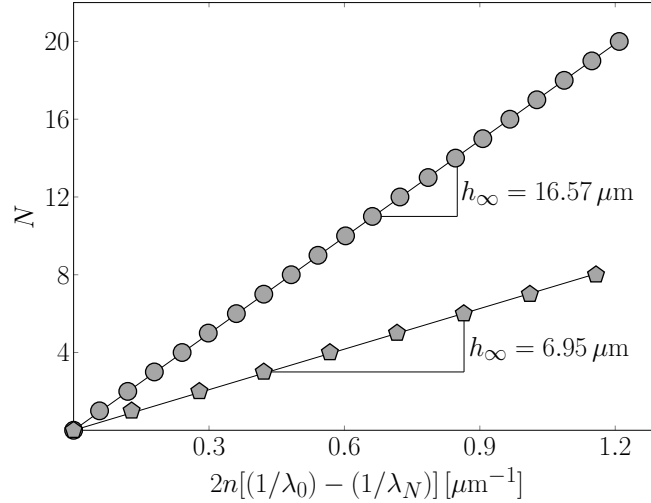


**Figure A3.2:** Soap film thicknesses determined from the light transmission data in figure A3.1 using equation (A3.2). Film thickness  $h_\infty$  corresponds to the slope of the linear curve fit of the data. The number of oscillations (cf. figure A3.1b) within a given range of wavelengths increases with the thickness of the film.

### 3.B Method of characteristics

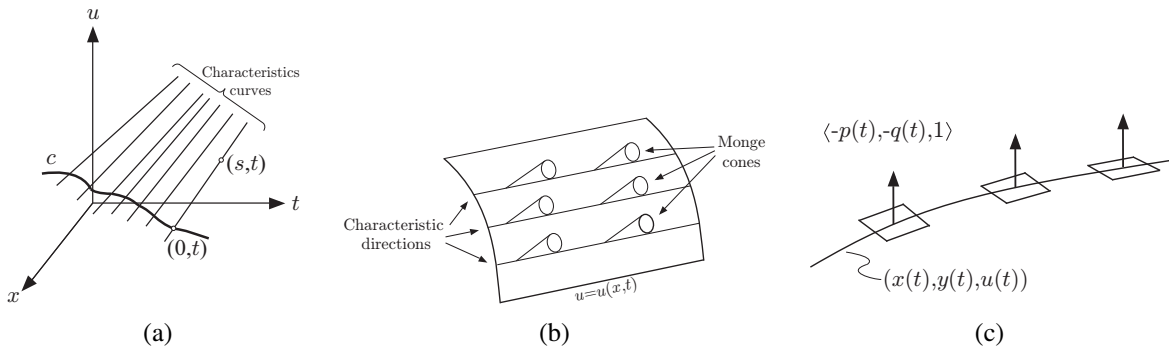


**Figure A3.3:** Method of characteristics for nonlinear first-order PDEs: (a) construction of the integral surface, (b) the Monge cones, (c) the initial strip.

The exposition here is a condensed and clarified version of those in [McOwen \(2002\)](#) and [Zauderer \(2006\)](#). Let us consider a nonlinear first order PDE in its most general form:

$$F(x, t, u, u_x, u_t) = 0, \tag{A3.4}$$

where we let  $p = u_x$  and  $q = u_t$  for convenience of notation and require  $F_p^2 + F_q^2 \neq 0$  for equation (A3.4) to be nontrivial. A solution  $u = u(x, t)$  of (A3.4) defines an integral surface over  $(x, t)$ -plane,

the normal vector to which is  $[p, q, -1]$ . Then for a given point  $(x_0, t_0, u_0)$ , equation (A3.4) defines a relation  $q = q(p)$ , which may not be unique, but we assume that a branch of possible solutions can be chosen. Then the normal vector  $[p, q(p), -1]$  at  $(x_0, t_0, u_0)$  defines a family of tangent planes

$$H(x, t, u, p, q) = (u - u_0) - p(x - x_0) - q(p)(t - t_0) = 0, \quad (\text{A3.5})$$

which envelope a cone, known as the Monge cone, constructed by eliminating  $p$  from (A3.5) and the envelope condition<sup>8</sup>

$$\frac{\partial H}{\partial p} = -(x - x_0) - \frac{dq}{dp}(p)(t - t_0). \quad (\text{A3.6})$$

The contact (intersection) of the Monge cones with the integral surface  $u = u(x, t)$  determines the field of directions on that surface known as the characteristic directions, cf. figure A3.3b.

With the above geometric understanding, we are in the position to construct characteristic equations. First, note that equation (A3.4) at  $(x_0, t_0, u_0)$  implies

$$\frac{dF}{dp} = \frac{\partial F}{\partial p} + \frac{dq}{dp}(p) \frac{\partial F}{\partial q} = 0, \quad (\text{A3.7})$$

which gives  $q'(p) = -F_p/F_q$  and hence from (A3.6) we find

$$\frac{x - x_0}{F_p} = \frac{t - t_0}{F_q}, \quad (\text{A3.8})$$

which together with (A3.5) produces

$$\frac{u - u_0}{t - t_0} = p \frac{x - x_0}{t - t_0} + q = \frac{pF_p + qF_q}{F_q}, \quad (\text{A3.9})$$

---

<sup>8</sup>Let us consider a family of curves with each curve  $C_p$  defined by an implicit equation  $F(x, t; p) = 0$  with  $p$  being a parameter. The envelope of the family  $C_p$  is then defined as a set of points  $(x, t)$  for which equations  $F(x, t; p) = 0$  and  $\partial F(x, t; p)/\partial p = 0$  are simultaneously satisfied.

or, altogether,

$$\frac{x - x_0}{F_p} = \frac{t - t_0}{F_q} = \frac{u - u_0}{pF_p + qF_q}, \quad (\text{A3.10})$$

where the denominators are constants evaluated at  $(x_0, t_0, u_0)$  on the integral surface. Hence, the above equation defines the characteristic directions:

$$\frac{dx}{ds} = F_p, \quad (\text{A3.11a})$$

$$\frac{dt}{ds} = F_q, \quad (\text{A3.11b})$$

$$\frac{du}{ds} = pF_p + qF_q. \quad (\text{A3.11c})$$

The curves generated by (A3.11) must be chosen such that they lie on a single surface  $u = u(x, t)$ , i.e. we need to determine the values that  $p[x(s), t(s)]$  and  $q[x(s), t(s)]$  must have along the curves  $x = x(s)$ ,  $t = t(s)$ ,  $u = u[x(s), t(s)]$  on that surface. By differentiating  $p$  and  $q$  and using (A3.11) we find

$$\frac{dp}{ds} = p_x x'(s) + p_t t'(s) = p_x F_p + p_t F_q, \quad (\text{A3.12a})$$

$$\frac{dq}{ds} = q_x x'(s) + q_t t'(s) = q_x F_p + q_t F_q. \quad (\text{A3.12b})$$

To simplify the last set of equations, let us differentiate (A3.4) with respect to  $x$  and  $t$ :

$$\frac{dF}{dx} = F_x + F_u p + F_p p_x + F_q q_x = 0, \quad (\text{A3.13a})$$

$$\frac{dF}{dt} = F_t + F_u q + F_p p_t + F_q q_t = 0, \quad (\text{A3.13b})$$

which together with (A3.12) and the fact that  $p_t = q_x$  produce

$$\frac{dp}{ds} = -F_x - F_u p, \quad (\text{A3.14a})$$

$$\frac{dq}{ds} = -F_t - F_u q. \quad (\text{A3.14b})$$

The five equations (A3.11,A3.14) constitute the characteristic equations for (A3.4) with the solutions called “characteristic strips” since the specification of  $p$  and  $q$  provides infinitesimal pieces of the tangent planes along the curve  $(x(s), t(s), u(s))$ , cf. figure A3.3c.

Finally, the initial value problem for (A3.4) requires that the integral surface  $u = u(x, t)$  contain the initial curve  $C$ , cf. figure A3.3a, which can be described parametrically as

$$x = x(\tau), \quad t = t(\tau), \quad u = u(\tau), \quad (\text{A3.15})$$

so that the solution to (A3.4) can be considered in the form  $x = x(s, \tau)$ ,  $t = t(s, \tau)$ ,  $u = u(s, \tau)$  with  $s = 0$  corresponding to (A3.15). However, in order to solve the system (A3.11,A3.14), in addition to (A3.15) we need initial conditions for  $p = p(\tau)$  and  $q = q(\tau)$ . One equation for that purpose is given by (A3.4), i.e.

$$F [x = x(\tau), t = t(\tau), u = u(\tau), p(\tau), q(\tau)] = 0, \quad (\text{A3.16})$$

which states that tangent planes along the initial curve  $C$  are tangent to the Monge cone at the corresponding point on  $C$ , while the other equation follows from the requirement that these tangent planes must fit together smoothly along  $C$  like the scales of a fish:

$$\frac{du}{d\tau}(\tau) = p(\tau) \frac{dx}{d\tau}(\tau) + q(\tau) \frac{dt}{d\tau}(\tau), \quad (\text{A3.17})$$

naturally known as the strip condition.

# Chapter 4

## Conclusions

In the presented dissertation, we studied both experimentally and theoretically the acoustic singularity phenomena interacting with liquid interfaces, in one case (impulse-driven drop) leading to cavitation and drop disintegration and in the other (soap film) to shock-wave formation in subsonic regimes, i.e. when the flow velocity is less than the one of acoustic wave propagation.

Besides extensive experimental measurements performed in the context of both phenomena, proper theoretical interpretation of the occurring singularities was deduced. In the case of impulse-driven drop we studied pressure amplification (should it be positive or negative) near the cusp resulting from the rarefaction wave focusing. In the case of the soap film phenomena, we deduced new evolution equations for the soap film thickness and velocity field, analyzed their solutions and interpreted fold formation with the help of eikonal equation incorporating the soap film flow.

Also, qualitative insights developed with the help of geometric acoustics and singularity theory provide adequate interpretation of the explored physical phenomena. However, quantitatively accurate modeling will require development of nonlinear analytical approaches and problem formulations taking into account realistic boundary conditions as well as numerical techniques, which would be indispensable should one target application of these phenomena in real world.

# Bibliography

- ABRAMOWITZ, M. & STEGUN, I. A. 1965 *Handbook of mathematical functions: with formulas, graphs, and mathematical tables*. Dover, New York.
- ACHARIGE, S. K., ELIAS, F. & DEREK, C. 2014 Soap film vibration: origin of the dissipation. *Soft Matter* **10**, 8341–8348.
- ADELIZZI, E. A. & TROIAN, S. M. 2004 Interfacial slip in entrained soap films containing associating hydrosoluble polymer. *Langmuir* **20**, 7482 – 7492.
- ALEKSEEV, V. B., ZALKIND, V. I., ZEIGARNIK, YU. A., MARINICHEV, D. V., NIZOVSKII, V. L. & NIZOVSKII, L. V. 2015 On the nature of bimodal drop distribution over sizes under superheated water atomization. *High Temperature* **53**, 214–216.
- ARFKEN, G. B. & WEBER, H. J. 2005 *Mathematical methods for physicists*. Academic Press: San Diego.
- ARNOLD, V. I. 2003 *Catastrophe Theory*. Springer.
- ASHGRIZ, N. 2011 *Handbook of Atomization and Sprays*. Spriger.
- ASSOCIATION, GLYCERINE PRODUCER'S 1963 *Physical properties of glycerine and its solutions*. Gulf Publishing Company.
- AUBIN, D. 2004 Forms of explanation in the catastrophe theory of René Thom: topology, morphogenesis, and the structuralism. In *Growing explanations: historical perspective in the sciences of complexity* (ed. M. N. Wise), pp. 95–130. Duke University Press.

- BANG, B. H., AHN, C. S., KIM, D. Y., LEE, J. G., KIM, H. M., JEONG, Y. T., AL-DEYAB, W. S. YOON S. S., YOO, J. H., YOON, S. S. & YARIN, A. L. 2016 Breakup process of cylindrical viscous liquid specimens after a strong explosion in the core. *Physics of Fluids* **28**, 094105.
- BENDER, C. M. & ORSZAG, S. A. 1999 *Asymptotic methods and perturbation theory*. Springer.
- BEREZIN, O. A. & GRIB, L. A. 1960 Irregular reflection of a plane shock wave in water from a free surface. *Zh. Prikl. Mekh. Tekh. Fiz.* **2**, 34–39.
- BERG, S., ADELIZZI, E. A. & TROIAN, S. M. 2005 Experimental study of entrainment and drainage flows in microscale soap films. *Langmuir* **21**, 3867 – 3876.
- BERRY, M. V. 1976 Waves and Thom's theorem. *Advances in Physics* **25**, 1–26.
- BILLINGSLEY, P. 1995 *Probability and Measure*. John Wiley & Sons.
- BOWDEN, F. P. & FIELD, J. E. 1964 The brittle fracture of solids by liquid impact, by solid impact, and by shock. *Proc. R. Soc. London Ser. A* **282**, 331–352.
- BRENNEN, C. E. 1995 *Cavitation and bubble dynamics*. Oxford University Press.
- BRENNER, M. P. & GUEYFFIER, D. 1999 On the bursting of viscous sheets. *Phys. Fluids* **11**, 737–739.
- BUCHAL, R. N. & KELLER, J. B. 1960 Boundary layer problems in diffraction theory. *Commun. Pure Appl. Math.* **XIII**, 85–114.
- CAMUS, J.-J. 1971 A study of high speed liquid flow in impact and its effect on solid surfaces. PhD thesis, Cambridge Univ.
- CAUPIN, F. 2005 Liquid-vapor interface, cavitation, and the phase diagram of water. *Phys. Rev. E* **71**, 051605.
- CHANG, C.-H. & FRANCES, E. I. 1992 Modified Langmuir-Hinshelwood kinetics for dynamic adsorption surfactants at the air/water interface. *Colloids and Surfaces* **69**, 189–201.

- CHANG, C.-H., WANG, N.-H. L. & FRANSES, E. I. 1992 Adsorption dynamics of single and binary surfactants at the air/water interface. *Colloids and Surfaces* **62**, 321–332.
- CHANTELOT, P., CLANET, M. COUX C. & QUÉRÉ, D. 2018a Drop trampoline. *Euro. Phys. Lett.* **124**, 24003.
- CHANTELOT, P., COUX, M., DOMINO, L., PYPE, B., CLANET, C., EDDI, A. & QUÉRÉ, D. 2018b Kicked drops. *Phys. Rev. Fluids* **3**, 100503.
- CHOMAZ, J.-M. 2001 The dynamics of a viscous soap film with soluble surfactant. *J. Fluid Mech.* **442**, 387–409.
- COHEN, R. D. 1991 Shattering of a liquid drop due to impact. *Proc. Roy. Soc. Lond. A* **435**, 483–503.
- COLE, J. D. & COOK, L. P. 1986 *Transonic Aerodynamics*. North Holland.
- COUDER, Y., CHOMAZ, J.-M. & RABAUD, M. 1989 on the hydrodynamics of soap films. *Physica D* **37**, 384–405.
- COULOUVRAT, F. 2000 Focusing of weak acoustic shock waves at a caustic cusp. *Wave Motion* **32**, 233–245.
- CULICK, F. E. C. 1960 Comments on a ruptured soap film. *J. Appl. Phys.* **31**, 1128–1129.
- DEBRÉGEAS, G., MARTIN, P. & BROCHARD-WYART, F. 1995 Viscous bursting of suspended films. *Phys. Rev. Lett.* **75**, 3886–3889.
- DEEGAN, R. D., BRUNET, P. & EGGERS, J. 2008 Complexities of splashing. *Nonlinearity* **21**, C1–C11.
- DION, S., HEBERT, C. & BROUILLETTE, M. 2009 Comparison of methods for generating shock waves in liquids. In *Shock waves* (ed. K. Hannemann & F. Seiler), pp. 851–856. Springer, Berlin.
- DRAZIN, P. G. & REID, W. H. 2004 *Hydrodynamic stability*. Cambridge University Press, Cambridge.

- DUEZ, C., YBERT, C., CLANET, C. & BOCQUET, L. 2007 Making a splash with water repellency. *Nature Physics* **3**, 180–183.
- DUPRÉ, M. A. 1867 Sixième memoire sur la theorie mécanique de la chaleur. *Ann. Chim. Phys.* **4**, 194–220.
- EDWARDS, D. A., BRENNER, H. & WASAN, D. T. 1991 *Interfacial transport processes and rheology*. Butterworth-Heinemann.
- EISENMENGER, W. 1962 Elektromagnetische Erzeugung von eben Druckstößen in Flüssigkeiten. *Acustica* **12**, 185–202.
- ELWORTHY, P. H. & MYSELS, K. J. 1966 The surface tension of sodium dodecylsulfate solutions and the phase separation model of micelle formation. *J. Colloid Interface Sci.* **21**, 331–347.
- EROGLU, H. & CHIGIER, N. 1991 Initial drop size and velocity distributions for airblast coaxial atomizers. *J. Fluids Eng.* **113**, 453–459.
- EVERS, L. J., SHULEPOV, S. Y. & FRENS, G. 1996 Rupture of thin liquid films from Newtonian and viscoelastic liquids. *Faraday Discuss.* **104**, 335 – 344.
- FAST, P. 2005 A viscous compressible model of soap film flow and its equivalence with the Navier-Stokes equations , arXiv: Preprint UCRL-JRNL-214578.
- FERNANDEZ, J., KRECHETNIKOV, R. & HOMSY, G. M. 2005 Experimental study of a surfactant-driven fingering phenomenon in a Hele-Shaw cell. *J. Fluid Mech.* **527**, 197 – 216.
- FIELD, J. E., DEAR, J. P. & OGREN, J. E. 1989 The effects of target compliance on liquid drop impact. *J. Appl. Phys.* **65**, 533–540.
- FRANKEL, S. & MYSELS, K. J. 1969 The bursting of soap films. II. A theoretical study. *J. Phys. Chem.* **73**, 3029–3038.
- FRENKEL, J. 1955 *Kinetic theory of liquids*. Dover Publications.

- GIACOMINI, A. 1947 Ultrasonic velocity in ethanol-water mixtures. *J. Acous. Soc. Am.* **19**, 701–702.
- GONOR, A. L. & RIVKIND, V. YA. 1982 Drop dynamics. In *Advances in science and engineering. Fluid mechanics, Vol. 17*, pp. 86–159. VINITI, Moscow.
- GRIESBAUER, J., WIXFORTH, A. & SCHNEIDER, M. F. 2009 Wave propagation in lipid monolayers. *Biophysical J.* **97**, 2710–2716.
- GUIRAUD, J.-P. 1965 Acoustique géométrique, bruit balistique des avions supersoniques et focalisation (geometrical acoustics, ballistic noise of supersonic aircraft and focusing). *J. Mec.* **4**, 215–267.
- HABIBI, H. & KRECHETNIKOV, R. 2015 Shock wave-droplet interaction. Poster P0028 in the Gallery of Fluid Motion at the 68th Annual Meeting, American Physical Society, Division of Fluid Dynamics, Boston, Massachusetts, 22-24 November.
- HALL, M. J. 1970 Use of the stain method in determining the drop-size distributions of coarse liquid sprays. *Trans. A.S.A.E.* **41**, 33–37.
- HAN, A., LU, W., PUNYAMURTULA, V. K., X. CHEN, F. B. SURANI & T. KIM, Y. QIAO 2008 Effective viscosity of glycerin in a nanoporous silica gel. *J. Appl. Phys.* **104**, 124908.
- HARARI, R. & SHER, E. 1998 Bimodal drop size distribution behavior in plain-jet airblast atomizer sprays. *Atomization and Sprays* **8**, 349–362.
- HECHT, E. 2002 *Optics - 4th Edition*. Pearson - Addison Wesley.
- HOWLAND, C. J., ANTKOWIAK, A., RAFAEL CASTREJÓN-PITA, J., HOWISON, S. D., OLIVER, J. M., STYLE, R. W. & CASTREJÓN-PITA, A. A. 2016 It's harder to splash on soft solids. *Phys. Rev. Lett.* **117**, 184502.
- HSIANG, L.-P. & FAETH, G. M. 1992 Near-limit drop deformation and secondary breakup. *Int. J. Multiphase Flow* **18**, 635–652.

- HUIBERS, P. D. T. & SHAH, D. O. 1997 Multispectral determination of soap film thickness. *Langmuir* **13**, 5995 – 5998.
- INCROPERA, F. P. & DEWITT, D. P. 2002 *Introduction to Heat Transfer 4th Edition*. John Wiley & Sons.
- JOSEPH, D. D., BELANGER, J. & BEAVERS, G. S. 1999 Breakup of a liquid suddenly exposed to a high-speed airstream. *Int. J. Multiphase Flow* **25**, 1263–1303.
- JOSEPH, D. D., HUANG, A. & CANDLER, G. V. 1996 Vaporization of a liquid drop suddenly exposed to a high-speed airstream. *J Fluid Mech.* **318**, 223–236.
- JOSSERAND, C. & THORODDSEN, S. T. 2016 Drop impact on a solid surface. *Annu. Rev. Fluid Mech.* **48**, 365–391.
- JOSSERAND, C. & ZALESKI, S. 2003 Droplet splashing on a thin liquid film. *Phys. Fluids* **15**, 1650–1657.
- JOUKOWSKY, N. E. 1899 On hydraulic jump in water pipes. *Bull. Polytech. Soc.* **5**, 1–36.
- VON KARMAN, T. H. 1929 The impact on seaplane floats during landing. *Tech. Rep.* 321. NACA.
- KEDRINSKII, V. K. 1993 Nonlinear problems of cavitative disintegration of liquid at explosive loading. *Zh. Prikl. Mekh. Tekh. Fiz.* **34**, 74–91.
- KEDRINSKII, V. K., BESOV, A. S. & GUTNIK, I. E. 1997 Inversion of a two-phase state of a liquid under a pulse loading. *Dokl. RAN* **352**, 477–479.
- KEDRINSKII, V. K. & CHERNOBAEV, N. N. 1992 One-dimensional projection of a liquid shell by an explosive charge. *J. Appl. Mech. Tech. Phys.* **33**, 851–856.
- KEDRINSKII, V. K., MAKAROV, A.I., VAN DOORN, E. & BOREL, H. 2005 Research of viscosity effect on the dynamics of the motion of liquid drop with its shock-wave load. In *XVI Session of the Russian Acoustical Society*, pp. 18–21. Russian Acoustical Society, Moscow.

- KIM, I. & MANDRE, S. 2017 Marangoni elasticity of flowing soap films. *Phys. Rev. Fluids* **2**, 082001.
- KINSLER, L. E., FREY, A. R., COPPENS, A. B. & SANDERS, J. V. 1999 *Fundamentals of acoustics*. Wiley, New York.
- KNOBLOCH, E. & KRECHETNIKOV, R. 2015 Problems on time-varying domains: formulation, dynamics, and challenges. *Acta Appl. Math.* **137**, 123–157.
- KOLMOGOROV, A. N. 1941 On the log-normal distribution of particles sizes during break-up process. *Dokl. Akad. Nauk. SSSR XXXI*, 99–101.
- KOMABAYASI, M., GONDA, T. & ISONO, K. 1964 Life time of water drops before breaking and size distribution of fragment droplets. *J. Met. Soc. Japan* **42**, 330–340.
- KONENKOV, YU. K. 1975 Interaction of a liquid layer with a membrane during the initial stage of impact. *Fluid Dynamics* **10**, 837–841.
- KRECHETNIKOV, R. 2009 Rayleigh-Taylor and Richtmyer-Meshkov instabilities of flat and curved interfaces. *J. Fluid Mech.* **625**, 387–410.
- KRECHETNIKOV, R. 2010 Stability of liquid sheet edges. *Phys. Fluids* **22**, 092101.
- KRECHETNIKOV, R. 2017 Stability of a growing cylindrical blob. *J. Fluid Mech.* **827**, R3.
- KRECHETNIKOV, R. & HOMSY, G. M. 2005 Experimental study of substrate roughness and surfactant effects on the Landau-Levich law. *Phys. Fluids* **17**, 102108.
- KRECHETNIKOV, R. & HOMSY, G. M. 2009 Crown-forming instability phenomena in the drop splash problem. *J. Colloid Interface Sci.* **331**, 555–559.
- KUZNETSOV, V. P. 1970 Equations of nonlinear acoustics. *Sov. Phys. Acoust.* **16**, 467–470.
- LAL, J. & DI MEGLIO, J.-M. 1994 Formation of soap films from insoluble surfactants. *J. Colloid Interface Sci.* **164**, 506–509.

- LAMB, H. 1932 *Hydrodynamics*. Cambridge University Press.
- LANDAU, L. D. & LIFSHITZ, E. M. 1986 *Theory of elasticity*. Oxford, Pergamon Press.
- LANDAU, L. D. & LIFSHITZ, E. M. 1987 *Fluid mechanics*. Pergamon, New York.
- LEFEBVRE, A. H. & MCDONELL, V. G. 2017 *Atomization and Sprays*. CRC Press, Taylor & Francis Group.
- LEHR, J. M., BAUM, C. E., PRATHER, W. D. & TORRES, R. J. 1999 Fundamental physical considerations for ultrafast spark gap switching. In *Ultra-Wideband Short Pulse Electromagnetics 4* (ed. E. Heyman, B. Mandelbaum & J. Shiloh), pp. 11–20. New York: Plenum Press.
- LENARD, P. 1904 Uber Regen. *Meteorologische Zeitschrift* **21**, 248–262.
- LESSER, M. B. 1981 Analytic solutions of liquid-drop impact problems. *Proc. R. Soc. Lond. A* **377**, 289–308.
- LHUISSIER, H. & VILLERMAUX, E. 2009a Destabilization of flapping sheets: The surprising analogue of soap films. *C. R. Mechanique* **337**, 469 – 480.
- LHUISSIER, H. & VILLERMAUX, E. 2009b Soap films burst like flapping flags. *Phys. Rev. Lett.* **103**, 054501.
- LIDE, D. R. 2006-2007 *Handbook of chemistry and physics*. Taylor and Francis.
- LIEBERMANN, L. N. 1949 The second viscosity of liquids. *Physical Review* **75**, 1415–1422.
- LIEBMAN, I., CORRY, J. & PERLEE, H. E. 1968 Rupture mechanism of a liquid film. *Science* **161**, 373 – 375.
- LIENHARD, J. H. 1981 *A Heat Transfer Book*. Prentice-Hall.
- LIEPMANN, H. W. & ROSHKO, A. 2002 *Elements of Gas Dynamics*. Dover Publications.

- LIU, J., VU, H., YOON, S. S. & JEPSEN, R. A. 2010 Splashing phenomena during liquid droplet impact. *Atomization and Sprays* **20**, 297–310.
- LUCASSEN, J., VAN DEN TEMPEL, M., VRIJ, A. & HESSELINK, F. 1970 Waves in thin liquid films i. the different modes of vibration. *Proc K Ned Akad Wetensch B* **73**, 109–124.
- LUDWIG, D. 1966 Uniform asymptotic expansions at a caustic. *Commun. Pure Appl. Math.* **XIX**, 215–250.
- LYKLEMA, J., SCHOLTEN, P. C. & MYSELS, K. J. 1965 Flow in thin liquid films. *J. Phys. Chem.* **69**, 116 – 123.
- MASON, P. 1963 Finite elastic wave propagation in rubber. *Proceedings of the Royal Society of London. Series A* **272**, 315–330.
- MATHESON, A. J. 1971 *Molecular acoustics*. Wiley.
- MAYER, H. C. & KRECHETNIKOV, R. 2012 Landau-levich flow visualization: revealing the flow topology responsible for the film thickening phenomena. *Phys. Fluids* **24**, 052103.
- MAYER, H. C. & KRECHETNIKOV, R. 2017 Liquid film dewetting induced by impulsive joule heating. *Phys. Rev. Fluids* **2**, 094003.
- MAYER, H. C. & KRECHETNIKOV, R. 2018 Flat plate impact on water. *J. Fluid Mech.* **850**, 1066–1116.
- MCENTEE, W. R. & MYSELS, K. J. 1969 The bursting of soap films. I. An experimental study. *J. Phys. Chem.* **73**, 3018–3028.
- MCOWEN, R. 2002 *Partial differential equations: methods and applications*. Pearson.
- MILNER, S. T., JOANNY, J.-F. & PINCUS, P. 1989 Buckling of langmuir monolayers. *Europhys. Lett.* **9**, 495–500.

- MOMSEN, W. E., SMABY, J. M. & BROCKMAN, H. L. 1989 The suitability of nichrome for measurement of gas-liquid interfacial tension by the Wilhelmy method. *J. Colloid Inter. Sci.* **135**, 547 – 552.
- MORTIMER, B. J. P. & SKEWS, B. W. 1996 An electromagnetic liquid shock wave generator for the production of a pulsed water jet. *J. Acoust. Soc. Am.* **100**, 3548–3553.
- MUNDO, C., SOMMERFELD, M. & TROPEA, C. 1995 Droplet-wall collisions: experimental studies of the deformation and breakup process. *Int. J. Multiphase Flow* **21**, 151–173.
- MYSELS, K. J. & COX, M. C. 1962 An experimental test of frankel's law of film thickness. *J. Colloid Sci.* **17**, 136–145.
- MYSELS, K. J., SHINODA, K. & FRANKEL, S. 1959 *Soap Films: Studies of Their Thinning*. Pergamon.
- NEWTON, I. 1704 *Opticks*. London.
- NIERSTRASZ, V. A. & FRENS, G. 1998 Marginal regeneration in thin vertical liquid films. *Journal of Colloid and Interface Science* **207**, 209–217.
- NIERSTRASZ, V. A. & FRENS, G. 1999 Marginal regeneration and the Marangoni effect. *Journal of Colloid and Interface Science* **215**, 28–35.
- PEARCEY, T. 1946 The structure of an electromagnetic field in the neighbourhood of a cusp of a caustic. *Philosophical Magazine and Journal of Science (London, Edinburgh, and Dublin)* **37**, 311–317.
- PEREGRINE, D. H. 1981 The fascination of fluid mechanics. *J. Fluid Mech.* **106**, 59–80.
- PILCH, M. & ERDMAN, C. A. 1987 Use of break-up time data and velocity history data to predict the maximum size of stable fragments for acceleration-induced break-up of a liquid drop. *Int. J. Multiphase Flow* **13**, 741–757.

- PLATEAU, J. 1873 *Statique expérimentale et théorique des liquides soumis aux seules forces moléculaires*. Gauthier Villars, Paris.
- PLESSET, M. S. & WHIPPLE, C. G. 1974 Viscous effects in Rayleigh-Taylor instability. *Physics of Fluids* **17**, 1–7.
- PRASAD, V. & WEEKS, E. R. 2009 Flow fields in soap films: Relating surface viscosity and film thickness. *Phys. Rev. E* **80**, 026309.
- PRINS, A., ARCURI, C. & VAN DEN TEMPEL, M. 1967 Elasticity of thin liquid films. *J. Colloid Interface Sci.* **24**, 84–90.
- PRYOR, A. W. & ROSCOE, R. 1954 Velocity and absorption of sound in aqueous sugar solutions. *Proc. Phys. Soc. B* **67**, 70–81.
- RENARDY, Y., POPINET, S., DUCHEMIN, L., RENARDY, M., ZALESKI, S., JOSSERAND, C., DRUMRIGHT-CLARKE, M. A., RICHARD, D., CLANET, C. & QUÉRÉ, D. 2003 Pyramidal and toroidal water drops after impact on a solid surface. *J. Fluid Mech.* **484**, 69–83.
- REYNOLDS, O. 1886 On the theory of lubrication and its application to Mr. Beauchamp tower's experiments, including an experimental determination of the viscosity of olive oil. *Philosophical Transactions of the Royal Society of London* **177**, 157–234.
- RIOBOO, R., TROPEA, C. & MARENCO, M. 2001 Outcomes from a drop impact on solid surfaces. *Atomization and Sprays* **11**, 155–165.
- RODNIKOVA, M. N. 2007 A new approach to the mechanism of solvophobic interactions. *J. Mol. Liquids* **136**, 211–213.
- ROHSENOW, W. M. & HARTNETT, J. P. 1973 *Handbook of Heat Transfer*. McGraw-Hill.
- ROI, N. A. 1970 Pulsed electrodynamic radiators. *Sov. Phys. Acoustics* **16**, 94–100.

- ROSALES, R. R. & TABAK, E. G. 1998 Caustics of weak shock waves. *Physics of Fluids* **10**, 206–222.
- ROUX, D. C. D. & COOPER-WHITE, J. J. 2004 Dynamics of water spreading on a glass surface. *J. Colloid Interface Sci.* **277**, 424–436.
- RUDENKO, O. V. & KHOKHLOVA, V. A. 2009 Historical aspects of the khokhlov-zabolotskaya equation and its generalizations. *J. Acoust. Soc. America* **126**, 2200.
- RUSANOV, A. I. & KROTOV, V. V. 1979 Gibbs elasticity of liquid films, threads, and foams. *Progr. Surf. Membrane Sci.* **13**, 415–524.
- SAINT-JALMES, A. & GALLET, F. 1998 Buckling in a solid langmuir monolayer: light scattering measurements and elastic model. *Eur. Phys. J. B* **2**, 489–494.
- SAVVA, N. & BUSH, J. W. M. 2009 Viscous sheet retraction. *J. Fluid Mech.* **626**, 211–240.
- SEMBIAN, S., LIVERTS, M., TILLMARK, N. & APAZIDIS, N. 2016 Plane shock wave interaction with a cylindrical water column. *Phys. Fluids* **28**, 056102.
- SHARP, D. H. 1984 An overview of Rayleigh-Taylor instability. *Physica D* **12**, 3–18.
- SHAUGHNESSY, E. J., KATZ, I. M. & SCHAFFER, J. P. 2005 *Introduction to fluid mechanics*. Oxford University Press.
- SIMPKINS, P. G. & BALES, E. L. 1972 Water-drop response to sudden accelerations. *J. Fluid Mech.* **55**, 629–639.
- SPIVAK, M. 1999 *A Comprehensive Introduction to Differential Geometry*. Publish or Perish, Inc.
- STEBNOVSKII, S. V. & CHERNOBAEV, N. N. 1986 Energy threshold for impulsive failure of a liquid volume. *J. Appl. Mech. Tech. Phys.* **27**, 51–54.
- STEBNOVSKII, S. V. & CHERNOBAEV, N. N. 1987 Influence of the dynamics of loading of a liquid volume on the mechanism of its failure. *Zh. Prikl. Mekh. Tekh. Fiz.* **5**, 134–138.

- STOW, C. D. & HADFIELD, M. G. 1981 An experimental investigation of fluid flow resulting from the impact of a water drop with an unyielding dry surface. *Proc. Roy. Soc. Lond. A* **373**, 419–441.
- STRASBERG, M. 1956 Undissolved air cavities as cavitation nuclei. In *Cavitation in hydrodynamics*, *Proc. Sympos. Nat. Phys. Lab.*, pp. 1–13.
- TAIT, P. G. 1888 Report on some physical properties of fresh water and seawater. In *The Voyage of H.M.S. Challenger, Vol. II*, pp. 1–76. London.
- TAYLOR, G. I. 1949 The shape and acceleration of a drop in a high-speed air stream. In *The scientific papers of G. I. Taylor* (ed. G. K. Batchelor), pp. 457–464. Cambridge University Press, Cambridge.
- TAYLOR, G. I. 1959a The dynamics of thin sheets of fluid. II. Waves on fluid sheets. *Proc. R. Soc. London, Ser. A* **253**, 296–312.
- TAYLOR, G. I. 1959b The dynamics of thin sheets of fluid. II. Waves on fluid sheets. *Proc. R. Soc. London, Ser. A* **253**, 296–312.
- TAYLOR, G. I. 1959c The dynamics of thin sheets of fluid. III. Disintegration of fluid sheets. *Proc. R. Soc. London, Ser. A* **253**, 313–321.
- THEOFANOUS, T. G. & LI, G. J. 2008 On the physics of aerobreakup. *Phys. Fluids* **20**, 052103.
- THOM, R. 1954 Quelques propriétés globales des variétés différentiables. *Commentarii Mathematici Helvetici* **28**, 17–86.
- THOM, R. 1956 Un lemme sur les applications différentiables. *Bol. Soc. Mat. Mexicana* **2**, 59–71.
- THORODDSEN, S. T. 2002 The ejecta sheet generated by the impact of a drop. *J. Fluid Mech.* **451**, 373–381.
- TORO, E. F. 1999 *Riemann Solvers and Numerical Methods for Fluid Dynamics*. Springer, Manchester.

- TRAN, T., CHAKRABORTY, P., GIOIA, G., STEERS, S. & GOLDBURG, W. 2009 Marangoni shocks in unobstructed soap-film flows. *Phys. Rev. Lett.* **103**.
- TROUTON, F. T. 1906 On the coefficient of viscous traction and its relation to that of viscosity. *Proceedings of the Royal Society of London. Series A* **77**, 426–440.
- VERMOREL, R., VANDENBERGHE, N. & VILLERMAUX, E. 2007 Rubber band recoil. *Proceedings: Mathematical, Physical and Engineering Sciences* **463**, 641–658.
- WANG, A.-B. & CHEN, C.-C. 2000 Splashing impact of a single drop onto very thin liquid films. *Phys. Fluids* **12**, 2155–2158.
- WASSERMANN, G. 1974 *Stability of unfoldings, Springer Mathematical Notes, Vol. 393*. Springer.
- WEN, C. Y., CHANG-JIAN, S. K. & CHUANG, M. C. 2003 Analogy between soap film on one-dimensional motion and gas dynamics. II. Experiments of shock waves in soap films. *Experiments in Fluids* **34**, 130–180.
- WEN, C. Y. & LAI, J. Y. 2003 Analogy between soap film and gas dynamics. I. Equations and shock jump conditions. *Experiments in Fluids* **34**, 107–114.
- WIGGINS, S. 2003 *Introduction to applied nonlinear dynamical systems and chaos*. Springer.
- WILLIAMS, P. F. & PETERKIN, F. E. 1989 Triggering in trigatron spark gaps: a fundamental study. *J. Appl. Phys.* **66**, 4163.
- WILSON, D. A., HOYT, J. W. & MCKUNE, J. W. 1975 Measurement of tensile strength of liquid by explosion technique. *Nature* **253**, 723–725.
- WORTHINGTON, A. M. 1877a On the forms assumed by drops of liquids falling vertically on a horizontal plate. *Proc. Roy. Soc. Lond.* **25**, 261–272.
- WORTHINGTON, A. M. 1877b A second paper on the forms assumed by drops of liquids falling vertically on a horizontal plate. *Proc. Roy. Soc. Lond.* **25**, 498–503.

WORTHINGTON, A. M. 1895 *The splash of a drop*. London.

YAKIMOV, YU. L. 1973 Influence of atmosphere at falling of bodies on water. *Izv. Akad. Nauk SSSR, Mekh. Zhidk. Gaza* **5**, 3–6.

YARIN, A. L. 2006 Drop impact dynamics: splashing, spreading, receding, bouncing ... *Annu. Rev. Fluid Mech.* **38**, 159–192.

YARIN, A. L. & WEISS, D. A. 1995 Impact of drops on solid surfaces: self-similar capillary waves, and splashing as a new type of kinematic discontinuity. *J. Fluid Mech.* **283**, 141–173.

ZAUDERER, E. 2006 *Partial differential equations of applied mathematics*. Wiley-Interscience.

ZHANG, L. V., BRUNET, P., EGGERS, J. & DEEGAN, R. D. 2010 Wavelength selection in the crown splash. *Phys. Fluids* **22**, 122105.